

Roman Keding

CO-DIFFUSED BACK-CONTACT BACK-JUNCTION SILICON SOLAR CELLS

Fraunhofer Institute for Solar Energy Systems ISE

SOLARE ENERGIE- UND SYSTEMFORSCHUNG /
SOLAR ENERGY AND SYSTEMS RESEARCH

Co-diffused Back-Contact Back-Junction Silicon Solar Cells

Roman Keding

FRAUNHOFER VERLAG

Contact:

Fraunhofer Institute for Solar Energy Systems ISE
Heidenhofstrasse 2
79110 Freiburg
Phone +49 761/4588-5150
Fax +49 761/4588-9342
E-Mail info@ise.fraunhofer.de
URL www.ise.fraunhofer.de

Bibliographic information published by Die Deutsche Bibliothek

The Deutsche Bibliothek lists this publication in the Deutsche Nationalbibliografie;
detailed bibliographic data is available in the Internet at [<http://dnb.d-nb.de>](http://dnb.d-nb.de).

D 25

Zugl.: Freiburg, Univ., Diss., 2015

Book Series: »Solare Energie- und Systemforschung / Solar Energy and Systems Research«

Printing and Bindery:

Mediendienstleistungen des
Fraunhofer-Informationszentrum Raum und Bau IRB, Stuttgart

Printed on acid-free and chlorine-free bleached paper.

All rights reserved; no part of this publication may be translated, reproduced, stored in a retrieval system, or transmitted in any form or by any means, electronic, mechanical, photocopying, recording or otherwise, without the written permission of the publisher.

Many of the designations used by manufacturers and sellers to distinguish their products are claimed as trademarks. The quotation of those designations in whatever way does not imply the conclusion that the use of those designations is legal without the consent of the owner of the trademark.

© by Fraunhofer Verlag, 2015, ISBN 978-3-8396-0905-7

Fraunhofer Information-Centre for Regional Planning and Building Construction IRB
P.O. Box 80 04 69, D-70504 Stuttgart
Nobelstrasse 12, D-70569 Stuttgart
Phone +49 (0) 7 11/9 70-25 00
Fax +49 (0) 7 11/9 70-25 07
E-Mail verlag@fraunhofer.de
URL www.verlag.fraunhofer.de

Co-diffused Back-Contact Back-Junction Silicon Solar Cells

Dissertation

zur Erlangung des Doktorgrades
der Technischen Fakultät
der Albert-Ludwigs-Universität Freiburg im Breisgau

vorgelegt von
Roman Johannes Keding

Fraunhofer Institut für Solare Energiesysteme
Freiburg im Breisgau

2015

Dekan:
Prof. Dr. Georg Lausen

Erstgutachter:
Prof. Dr. Holger Reinecke
Zweitgutachter:
Prof. Dr. Gerhard Willeke

Vorsitzender der Prüfungskommission:
Prof. Dr. Leonhard Reindl
Beisitzer:
Prof. Dr. Moritz Diehl

Tag der Disputation: 19.06.2015

Institut für Mikrosystemtechnik
Technische Fakultät der Albert-Ludwigs-Universität Freiburg

Abstract

The thesis is dedicated to a sophisticated silicon solar cell, denoted as back contact back junction (BC-BJ) solar cell, which features a metal free front side, no shading losses as a consequence, and, therefore, a relatively high efficiency potential. In terms of costs per wattpeak, the high efficiency potential can only be advantageous if additional process costs are limited to a minimum. The unique selling point of the BC-BJ solar cell developed here is that the desired process sequence includes a so-called co-diffusion module which enables the integration of all the required doped surfaces in only one single temperature step and, accordingly, offers a great reduction in process costs and costs per wattpeak, respectively.

The co-diffusion modules of interest feature a combination of three solid dopant sources as well as two solid dopant sources and a gaseous dopant source. Solid dopant sources, in this case boron- (BSG) and phosphorus-doped silicate glass (PSG) layers, are deposited by means of plasma enhanced chemical vapor deposition (PECVD), whereas phosphoryl chloride (POCl_3) is utilized as a gaseous dopant source. The process related parameters are optimized in order to provide compatibility of the single processes with each other while also being in accordance with the special requirements of a BC-BJ solar cell. It will be shown that the combination of solid and gaseous dopant sources is only possible by protecting the solid dopant sources with an additional silicon oxide (SiO_x) layer, adapting the dopant concentration in the solid dopant sources, and keeping the oxygen content during diffusion as low as possible.

BC-BJ solar cells (active area = 4 cm^2) are manufactured on Czochralski (Cz) grown *n*-type material by introducing a base line process which utilizes industrially scalable inkjet patterning modules and the highly innovative co-diffusion modules. First generation solar cells feature a conversion efficiency up to 20.5 %, whereas those cells are based on a process sequence with a second thermal step (drive-in). During the development of the latter cell, several modifications of the base line process are discussed. These are the impact of the silicon material, the passivation layers, emitter formation, doping-structure, and metallization. The evaluation of the doping-structure shows that the omission of the gap region has economical and physical advantages. By introducing the POCl_3 related co-diffusion module in the base line process without drive-in, the efficiency of 20.5 % is maintained, but the process costs and cost per wattpeak, respectively, decrease drastically. Second generation solar cells feature an optimized base line process without drive-in and an efficiency up to 21.1 % (± 0.2 %, absolute efficiency deviation of 25 small-size cells on one industrial-size wafer). Simulations predict a realistic short-term improvement in efficiency exceeding 23.1 %.

Kurzfassung

Die Thesis widmet sich einer hochwertigen Silicium Solarzelle, bezeichnet als Rückseitenkontakt (RSK) Solarzelle, welche keine Vorderseitmetallisierung und verknüpfte Abschattungsverluste impliziert und daher ein hohes Wirkungsgradpotential aufweist. In Anbetracht der Kosten per Wattpeak ist das hohe Wirkungsgradpotenzial der Zelle nur von Vorteil, wenn zusätzliche Prozesskosten auf ein Minimum beschränkt werden können. Das Alleinstellungsmerkmal der hier entwickelten Zelle ist ein in die Prozesslinie integriertes simultanes Diffusionsmodul, welches die gleichzeitige Dotierung aller notwendigen Hochdotierungen in einem einzigen Hochtemperaturschritt ermöglicht. Die fokussierte Zelle erlaubt daher eine enorme Reduzierung der Prozesskosten bzw. Kosten per Wattpeak.

Die simultanen Diffusionsmodule von Interesse beinhalten eine Kombination von drei festen Dotierstoffquellen sowie zwei feste und eine gasförmige Dotierstoffquelle. Feste Dotierstoffquellen, diese sind Bor- (BSG) und Phosphor-dotierte Silikatglas (PSG) Schichten, werden mit der Plasma unterstützten Gasphasenabscheidung (PECVD) abgeschieden, wobei Phosphoroxychlorid (POCl_3) als gasförmige Dotierstoffquelle eingesetzt wird. Die prozessrelevanten Parameter werden hinsichtlich der gegenseitigen Anwendbarkeit der Einzelprozesse und der speziellen Anforderungen der RSK Solarzelle optimiert. Es wird gezeigt dass eine Kombination von festen und gasförmigen Dotierstoffquellen möglich ist, wenn feste Dotierstoffquellen durch eine Siliciumoxid (SiO_x) Schicht geschützt werden, die Dotierstoffkonzentration in der festen Quelle angepasst wird und der Sauerstoffgehalt während der Diffusion auf ein Minimum reduziert wird.

Mit einer Basis Prozesslinie, welche auf die industrierelevante Inkjet Technologie und die innovativen simultanen Diffusionsmodule zurückgreift, werden RSK Solarzellen (aktive Fläche = 4 cm^2) auf Czochralski (Cz) gewachsenen *n*-Typ Siliciumscheiben hergestellt. Zellen in erster Generation zeigen einen Wirkungsgrad von bis zu 20.5 %, wobei die Zellen auf einem zweiten Temperaturschritt (Eintreiben) basieren. Während der Entwicklung der erwähnten Zelle werden verschiedenen Modifikationen der Basis Prozesslinie untersucht. Diese sind der Einfluss des Silicium Materials, der Passivierungsschichten, der Emitter Formation, der Dotierungsstruktur, und der Metallisierung. Die Evaluation der Dotierungsstruktur zeigt, dass eine Substitution des Gap-Bereichs mit ökonomischen und physikalischen Vorteilen verknüpft ist. Die Anwendung des simultanen Diffusionsmoduls mit POCl_3 in der Prozesslinie ohne Eintreiben ermöglicht die Einhaltung des Wirkungsgrads von 20.5 %, aber eine drastische Reduzierung der Prozesskosten bzw. Kosten per Wattpeak. Zellen in zweiter

Generation basieren auf einer optimierten Basis Prozesslinie und zeigen einen Wirkungsgrad von 21.1 % (± 0.2 %, absolute Abweichung des Wirkungsgrads von 25 kleinen Zellen auf einem industrierelevanten, großformatigen Substrat). Simulationen prognostizieren eine kurzfristige, realistische Wirkungsgradsteigerung der Zellen bis zu 23.1 %.

Table of Contents

Table of Contents	i
1 Introduction.....	1
1.1 Motivation and focus of the thesis	1
1.2 Thesis outline	2
2 Physics of silicon solar cells	5
2.1 Semiconductor physics	5
2.1.1 Semiconductor	5
2.1.2 Intrinsic semiconductor	6
2.1.3 Extrinsic semiconductor	7
2.1.4 Charge carrier transport.....	9
2.1.5 Generation and recombination	11
2.1.6 <i>pn</i> -junction	13
2.1.7 Two-diode model	16
2.2 Back-Contact Back-Junction silicon solar cells.....	19
2.2.1 Design and working principle	19
2.2.2 Critical effects	21
2.2.3 Advantages/disadvantages and conversion efficiency.....	23
2.2.4 Cell characterization.....	25
3 Material and applied technologies	29
3.1 Wafer material	29
3.2 Wet chemical cleaning.....	32
3.3 Deposition	33
3.3.1 Plasma enhanced chemical vapor deposition	33
3.3.2 Plasma enhanced atomic layer deposition	34
3.3.3 Physical vapor deposition	35
3.3.4 Inkjet printing.....	36
3.4 Diffusion.....	38
3.4.1 Thermal diffusion.....	38
3.4.2 Solubility of boron and phosphorus in silicon.....	41
3.5 BC-BJ processing	42
3.5.1 Base line process.....	42
3.5.2 Cost reduction by co-diffusion	46
4 Co-diffusion processes	49
4.1 Challenge.....	49
4.2 Formation of boron-doped surfaces from BSG layers	51

4.2.1	Sample preparation and characterization.....	51
4.2.2	Results and discussion.....	54
4.3	Formation of phosphorus-doped surfaces from PSG layers.....	60
4.3.1	Sample preparation and characterization.....	60
4.3.2	Results and discussion.....	62
4.4	Formation of phosphorus-doped surfaces with POCl_3	66
4.4.1	Sample preparation and characterization.....	66
4.4.2	Results and discussion.....	69
4.5	Emitter formation in POCl_3 based co-diffusion processes	73
4.5.1	Sample preparation and characterization.....	73
4.5.2	Results and discussion.....	75
4.6	Chapter summary.....	80
5	Co-diffused back-contact back-junction solar cells.....	83
5.1	Challenge.....	83
5.2	Characterization of the base line process	83
5.3	Influence of material on cell performance	89
5.3.1	Motivation.....	89
5.3.2	Cell preparation and characterization	89
5.3.3	Results and discussion.....	91
5.4	Influence of passivation scheme on cell performance.....	96
5.4.1	Motivation.....	96
5.4.2	Cell preparation and characterization	97
5.4.3	Results and discussion.....	98
5.5	Influence of B-dopant source on cell performance	105
5.5.1	Motivation.....	105
5.5.2	Cell preparation and characterization	105
5.5.3	Results and discussion.....	106
5.6	Influence of cell structure on cell performance.....	111
5.6.1	Motivation.....	111
5.6.2	Cell preparation and characterization	111
5.6.3	Results and discussion.....	114
5.7	Influence of metal thickening on cell performance.....	120
5.7.1	Motivation.....	120
5.7.2	Cell modification and characterization.....	121
5.7.3	Results and discussion.....	121
5.8	Chapter summary.....	124
6	Process simplification and efficiency improvement.....	127

6.1	Challenge.....	127
6.2	Process simplification by co-diffusion with POCl_3	129
6.2.1	Motivation.....	129
6.2.2	Cell preparation and characterization.....	130
6.2.3	Results and discussion.....	132
6.3	Efficiency improvement	138
6.3.1	Motivation.....	138
6.3.2	Cell preparation and characterization.....	138
6.3.3	Results and discussion.....	140
6.4	Chapter summary.....	145
7	Loss analysis of the best cell	147
7.1	Motivation	147
7.2	Simulation parameters	148
7.3	Results and discussion	149
7.4	Conversion efficiency estimation	153
8	Summary	157
9	Outlook	161
10	Deutsche Zusammenfassung	163
	Bibliography	169
	List of Constants, Symbols and Acronyms.....	179
	List of Publications.....	187
	Danksagung	191

1 Introduction

1.1 Motivation and focus of the thesis

The only constant in life is change. Due to the growing world population, which is mainly driven by the Far East and Africa [1], the world energy demand has been increasing drastically for years [2]. Fossil fuels, which are predicted to be fully used up in the next 100 to 200 years [3], cannot fully provide the energy demand of the future. Moreover, the generation of usable energy by fossil fuels is driven by combustion reactions contaminating the earth's atmosphere with greenhouse gases which are responsible for the global climate change [4] and all the related consequences such as the global rise in temperature [5]. Covering the growing energy demand with new installations of nuclear power plants generating energy by exothermic nuclear processes such as nuclear fission would simultaneously lead to a remarkable increase in risk of steadily appearing nuclear disasters. The nuclear disasters of Chernobyl in 1986 and Fukushima in 2011 led to radioactive contaminations with terrible consequences for the world, nature, animals, and humans [6]. Additionally, the storage of nuclear waste in a safe environment over thousands of years cannot absolutely be guaranteed [7]. There is only one solution for a safe future and a sustainable energy supply all over the world: High-tech products featuring low energy consumption, which are supplied with renewable energies like solar irradiation, wind power, and bio mass.

A simple calculation underlines the extreme potential of solar irradiation to be one of the key energy sources in the future. Besides the infinite availability of solar irradiation, the sun submits a power of $1.7 \cdot 10^{17}$ J per second to earth [8]. This corresponds to a power of $1.5 \cdot 10^{21}$ kWh per year. When considering the annual energy consumption of the whole world in 2010 of $1.7 \cdot 10^{17}$ kWh [9], the sun could have supplied this global consumption in around 50 minutes. Due to the high availability of silicon in the crust of the earth [10] and the steady progress in semiconductor technologies since 1950 [11], wafer based silicon solar cells might be key transducers enabling the highly efficient, extensive, save, and direct conversion of solar energy into electricity (photovoltaics, PV).

By focusing on industrial solar cell fabrication, the ratio of costs per watt peak has to be lowered. This can be achieved by increasing the solar cell conversion efficiency and by decreasing the overall solar cell costs, including material costs, process costs, and costs related to the module assembly [12]. One very promising approach allowing for a strong increase in conversion efficiency is the concept of a back-contact back-junction

(BC-BJ) solar cell exploiting the potential of a sun-facing solar cell side without metal contacts and, in turn, without any shading losses. Since the assembly of this sophisticated type of solar cell is related to a high process complexity and high process costs, the market breakthrough of BC-BJ solar cells can only be achieved with innovative processes. The first aim of this work is the development of a so called co-diffusion process that would be eminently innovative, because of the number of cost-intensive thermal steps that could be strongly reduced through it. The second aim of this work is to fabricate a highly efficient BC-BJ solar cell which features a process sequence that would implement the developed co-diffusion process. The combination of the co-diffusion process and the BC-BJ solar cell is believed to feature a remarkable potential in decreasing the costs per watt peak of wafer based silicon solar cells and, consequently, have a high relevance for industrial applications.

1.2 Thesis outline

In **chapter 2**, the working principle and basic equations of semiconductors are introduced. In addition, the utilization of semiconductors as a photosensitive device or rather as a BC-BJ solar cell is discussed. Since this work aims at co-diffusion, special attention is given to the characteristics of a doped semiconductor. The generation and separation of excess carriers by differently doped surfaces is explained as well. The BC-BJ Solar cell is introduced by discussing the design and the working principle, critical effects, advantages and disadvantages of the cell structure, and the presentation of actual solar cell efficiencies. The chapter concludes with the introduction of characterization methods used for the analysis of cells fabricated in this work.

In **chapter 3**, the focus is set on the material and the applied process technologies. In the case of material, the utilization of monocrystalline silicon, which is fabricated according to the Czochralski process, is discussed. Moreover, the advantage of a silicon wafer featuring an *n*-type base doping is explained. In the case of the applied process technologies, wet chemical cleaning, deposition techniques, and thermal diffusion are introduced. The chapter concludes with a demonstration of the favored base line process and a presentation of the economic advantage of co-diffusion compared to sequential diffusion.

Before a BC-BJ solar cell can be processed, co-diffusion processes needed to be evaluated in this work. **Chapter 4** presents some BC-BJ cell related challenges of co-diffusion and significant characteristics of co-diffusion which are detected on special samples. The process development is performed by analyzing boron and phosphorus diffusion from the utilized dopant sources separately. In order to combine solid and gaseous dopant sources in one thermal process, a modification of solid

dopant sources and the gaseous phase during the thermal process is qualified. The sample characterization within this chapter focuses on the electrical conductance of the realized doped surfaces.

Chapter 5 deals with the integration of the co-diffusion processes developed in chapter 4 into the desired base line process presented in chapter 3. In order to improve the conversion efficiency of the BC-BJ solar cell step by step, the influence of single modifications of the base line process (featuring only solid dopant sources) on the conversion efficiency is demonstrated. The modifications of the base line process include a variation of the material, the passivation scheme, the boron-dopant source, and the doping-structure. The presentation of surface recombination related to the realized doped surfaces is carried out in the variation of the passivation scheme. The chapter concludes with a modification of the cell metallization in order to increase the efficiency of the best BC-BJ solar cell presented in chapter 5.

Chapter 6 is divided into the main sections referred to as process simplification and efficiency improvement. In both cases, a new base line process is utilized which features a modified doping-structure that would enable a drastic decrease in process costs. In fact, the presented BC-BJ cells are free of a gap region. Within the scope of the process simplification, the process costs of the new base line process are further decreased by combining a gaseous dopant source with two solid dopant sources. The demonstrated cell is the one with the highest cost-reduction potential processed in this work. In the context of the efficiency improvement, such as in chapter 5, solid dopant sources are utilized during co-diffusion. The process sequence of the BC-BJ cell considers all the process modifications demonstrated in chapter 5 which led to a gain in conversion efficiency. Consequently, the BC-BJ cell with the highest conversion efficiency achieved in this work is demonstrated in this section.

In order to guide the way for future investigations concerning the developed BC-BJ solar cell, a loss analysis of the best solar cell is presented in **chapter 7**. Moreover, a simulation of a BC-BJ cell is carried out which combines the most promising surface properties extracted in this work and, thus, a realistic estimation of the short term efficiency improvement. An estimation of the long term efficiency improvement is carried out by joining simulation results, experiment results, and the potential of a solar cell structure featuring a highly insulating rear side passivation.

2 Physics of silicon solar cells

This chapter deals with a discussion of semiconductor principles helping to understand silicon doping and the working principle of solar cells. Subsequently, the special characteristics of the solar cell in question, the BC-BJ solar cell, are introduced.

The discussions in this chapter are based on the text books from Goetzberger [13], Sze [14], Göbel [15], and Green [16].

2.1 Semiconductor physics

2.1.1 Semiconductor

Crystalline materials feature a periodically arranged lattice with a high concentration of atoms. Single atoms are known to feature discrete energy states which are occupied by electrons or not. Due to the high concentration of atoms in a crystalline material, discrete energy states of neighboring atoms overlap leading to the formation of so-called energy bands. These energy bands are known as valence and conductive band. Electrons which occupy energy states in the valence band are immobile and, as a consequence, do not contribute to the electrical conductivity of a crystalline material. In the other case, electrons which occupy energy states in the conductive band are mobile and, therefore, contribute to the conductivity of a crystalline material. The two energy bands might be split by energy states which cannot be occupied by electrons. The amount of these states denoted to as forbidden states are quantified by the band gap energy E_g . According to the value of the band gap energy, crystalline materials are divided into conductors, semiconductors, and insulators. In the case of a conductor, for example a metal, the valence band and the conductive band overlap ($E_g = 0$ eV). As a consequence, electrons in the valence band can easily be transferred to the conductive band. As the name reveals, conductors feature a very high electrical conductivity. An insulator indicates a high band gap energy ($E_g > 10$ eV). Thus, most of the electrons occupy energy states in the valence band and, accordingly, insulators feature a very low electrical conductivity. In this work, semiconductors are utilized to fabricate solar cells. A semiconductor exhibits a band gap energy between the band gap energy of a conductor and an insulator. By providing energy, electrons which occupy states in the valence band are transferred to the conductive band. In turn, the electrical conductivity of a semiconductor can be manipulated. Silicon features a E_g of 1.1 eV. As a result, the energy of light or rather the energy of a photon featuring a wavelength lower than

1127 nm is sufficient to transfer an electron from the valence band to the conductive band and, therefore, is able to significantly manipulate the electrical conductivity of a semiconductor. The latter effect is known as the so-called photoelectric effect and the base principle of a silicon solar cell. The following sections deals with the difference between an intrinsic and an extrinsic semiconductor.

2.1.2 Intrinsic semiconductor

Intrinsic semiconductors feature a conductivity which is manipulated by thermal energy. At a temperature of 0 K, all electrons in silicon occupy energy states of the valence band. As a consequence, the semiconductor is not conductive. With increasing temperature, the mean energy of electrons increases to such an extent that electrons are transferred from the valence to the conductive band and, therefore, contribute to the electrical conductivity. The transfer of an electron from the valence to the conductive band is connected to the generation of an electron vacancy in the valence band. Since the electrons of neighboring atoms can occupy the generated electron vacancy, the electron vacancy is mobile and, hence, contributes to the conductivity as well. In the following, electron vacancies are denoted to as holes.

Based on the latter settings, the conductivity σ of a crystalline material is expressed according to the following equation,

$$\sigma = \sigma_n + \sigma_p = q(\mu_n n + \mu_p p) \quad (2-1)$$

with the conductivity of electrons σ_n and holes σ_p , the elementary charge q , the mobility of μ_n and holes μ_p , and the carrier concentration of mobile electrons n and holes p .

In order to calculate the temperature T dependent concentration of electrons and holes in a semiconductor, the following equations are utilized,

$$n = \int_{E_C}^{E_{Max}} F(E) \cdot N(E) dE \quad (2-2)$$

$$p = \int_{E_{Min}}^{E_D} (1 - F(E)) \cdot N(E) dE \quad (2-3)$$

with the energy dependent density of energy states $N(E)$, the energy dependent probability of an electron to occupy a certain energy state $F(E)$, the lower conductive

energy band edge E_C and the upper valence band edge E_D . By using Fermi-Dirac statistics for $F(E)$,

$$F(E) = \frac{1}{1 + \exp\left(\frac{E - E_F}{k_B T}\right)} \quad (2-4)$$

with the Boltzmann constant k_B and the Fermi energy E_F , the electron and hole concentration are expressed as follows,

$$n = N_C \exp\left(\frac{E_F - E_C}{k_B T}\right) \quad (2-5)$$

$$p = N_V \exp\left(\frac{E_V - E_F}{k_B T}\right) \quad (2-6)$$

with the effective density of energy states in the conduction N_C and the valence band N_V . The Fermi energy, also denoted as Fermi level, indicates the energy state occupied by electrons with a probability of 50 %. In the case of an intrinsic semiconductor featuring a pairwise generation of electrons and holes, the Fermi level is located in the center of the energy band gap. Finally, the intrinsic carrier concentration n_i are expressed according to the following equation:

$$n_i^2 = np \quad (2-7)$$

The so-called mass action law is a fundamental equation which is also valid for extrinsic semiconductors.

2.1.3 Extrinsic semiconductor

Compared to intrinsic semiconductors, extrinsic semiconductors feature an additional conductivity which is caused by doping. Doping means the introduction of dopants into semiconductors acting as either donors or acceptors. In the following, silicon is utilized as semiconductor material.

Silicon features four electrons in the outer atomic shelve. By substituting a silicon atom in the silicon lattice with a phosphorus atom featuring five electrons in the outer atomic shelve, one electron is left over and, as a consequence, weekly bonded to the phosphorus atom. The thermal energy available at room temperature is absolutely sufficient to ionize phosphorus, mobilize the weekly bonded electron, and,

consequently, transfer the weekly bonded electron to the conduction band. Thus, phosphorus acts like a donor. After ionization, phosphorus is positively charged. In the band diagram, the low ionization energy of acceptors is considered, by integrating an additional energy state, the donor level E_D , near the valence band edge.

By substituting a silicon atom in the silicon lattice with a boron atom featuring three electrons in the outer atomic shelve, an electron vacancy is generated. At room temperature, the mean electron energy of silicon atoms in the surrounding of the regarded boron atom is sufficient to occupy the generated electron vacancy. This behavior is related to an ionization of the boron atom, a mobilization of a hole, and, consequently, a transfer of a hole to the valence band. Thus, boron acts like an acceptor. After ionization, boron is negatively charged. In the band diagram, the low ionization energy of acceptors is considered, by integrating an additional energy state, the acceptor level E_A , near the valence band edge.

In this work so-called n -type silicon wafers are utilized as an extrinsic semiconductor. Those wafers feature a high amount of donors. By assuming that all donors are ionized and that the corresponding electron concentration exceeds the intrinsic carrier concentration over several orders of magnitude, the following approximation is valid,

$$n \approx N_D \quad (2-8)$$

with the donor concentration (N_D). According to the mass action law (2-7), the related hole concentration is calculated as follows:

$$p \approx \frac{n_i^2}{N_D} \quad (2-9)$$

In values, a n -type silicon wafer with a base resistivity of $3 \Omega\text{cm}$ features a donor concentration N_D of $1.6 \cdot 10^{15} \text{ cm}^{-3}$. For the calculation of N_D , the carrier and dopant concentration dependent charge carrier mobility after Klaassen et al. [17] was taken into account. At room temperature, the intrinsic carrier concentration n_i of the regarded wafer is $8.5 \cdot 10^9 \text{ cm}^{-3}$ [18, 19]. For the calculation of n_i , the temperature dependence of the band gap after Green et al. [20] and the dopant concentration dependent band gap narrowing after Schenk at al. [21] were considered. Consequently, the extrinsically generated amount of electrons per volume is much higher than the intrinsically generated amount of electrons per volume. Finally, the hole concentration p can be calculated according to equation (2-9) and is $4.5 \cdot 10^4 \text{ cm}^{-3}$. Since the electron concentration exceeds the hole concentration by several orders of magnitude, the

conductivity of the wafer is mainly caused by mobile electrons and, as a consequence, the regarded wafer is denoted as *n*-type. Due to the high quantity of electrons compared to holes, electrons are denoted as majority charge carriers (short: majorities), whereas holes are denoted as minority charge carriers (short: minorities). Compared to the intrinsic semiconductor featuring a Fermi level in the center of the band gap, the extrinsic *n*-type semiconductor features a Fermi level which is shifted towards the conductive band edge. In the case of *p*-type wafers, holes are majority charge carriers and, compared to the intrinsic semiconductor, the Fermi level is shifted towards the valence band edge (compare Figure 2.1).

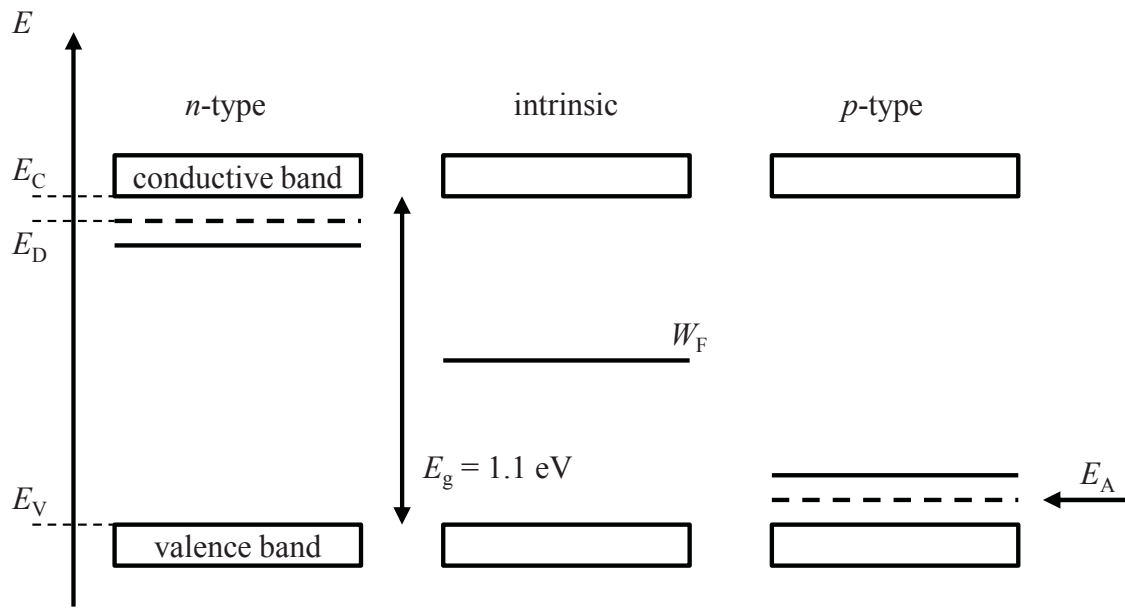


Figure 2.1 Band diagram of three separately regarded semiconductors. These are an intrinsic semiconductor (middle) and an extrinsic *n*-type (left) and *p*-type semiconductor (right). The depicted band gap energy E_g corresponds to the value of silicon. The position of the Fermi level E_F in the band gap depends on the semiconductor type.

2.1.4 Charge carrier transport

In general, charge carriers are transported by two major transport mechanisms: drift and diffusion. The drift current density of electrons $J_{\text{drift},n}$ and holes $J_{\text{drift},p}$ is described according to the following equations,

$$J_{\text{drift},n} = qn\mu_n \xi \quad (2-10)$$

$$J_{\text{drift},p} = qp\mu_p \xi \quad (2-11)$$

with the elementary charge q , the electron n and hole concentration p , the mobility of electrons μ_n and holes μ_h and the electrical field ξ . The drift current is enhanced by the impact of an electrical field on the charge carriers. The current density increases with increasing charge carrier concentration and mobility. Electrical fields are the result of a spatial variation in the electrical potential along a certain area denoted as potential gradient. In the band diagram, a potential gradient appears as a so-called band bending. The diffusion current density of electrons $J_{\text{diff},n}$ and holes $J_{\text{diff},p}$ is described according to the following equations,

$$J_{\text{diff},n} = qD_n \frac{dn}{dx} \quad (2-12)$$

$$J_{\text{diff},p} = -qD_p \frac{dp}{dx} \quad (2-13)$$

with the diffusion constant of electrons D_n and holes D_p . Thus, the diffusion current density is enhanced by the impact of a spatial variation in charge carrier concentration denoted as charge carrier gradient. The negative algebraic sign of the hole diffusion current density considers the different current direction of holes and electrons diffusing in the same direction. Moreover, the diffusion current density depends proportionally on the diffusion constant which is related to the temperature T and the charge carrier mobility, as the following equations reveal.

$$D_n = \frac{kT}{q} \mu_n \quad (2-14)$$

$$D_p = \frac{kT}{q} \mu_p \quad (2-15)$$

The relation between diffusion constant and carrier mobility is denoted as Einstein equation. Finally, the total current density of electrons and holes flowing through a semiconductor is expressed by the sum of the corresponding drift and diffusion current density.

$$J_n = q(n\mu_n\xi + D_n \frac{dn}{dx}) \quad (2-16)$$

$$J_p = q(p\mu_p\xi - D_p \frac{dp}{dx}) \quad (2-17)$$

2.1.5 Generation and recombination

The absorption of photons in silicon leads to the generation of electron hole pairs denoted as excess carriers. This statement is valid for direct semiconductors like gallium arsenide (GaAs) featuring a valence band maximum and a conductive band minimum at the same linear momentum. In the case of silicon, the valence band maximum and the conductive band minimum are located at different linear momentums. As a consequence, the transfer of an electron from the valence band maximum to the conductive band minimum is only possible if the excited atom additionally absorbs a phonon (potential energy of vibrations in the silicon lattice). Correspondingly, silicon is an indirect semiconductor.

If generated electron hole pairs are not separated from each other, recombination takes place. Recombination can happen by several mechanisms: radiative recombination, Auger recombination, and recombination via traps. In the following, the recombination mechanisms and the related equations are introduced briefly. For that, schematics of the recombination mechanisms are depicted in Figure 2.2.

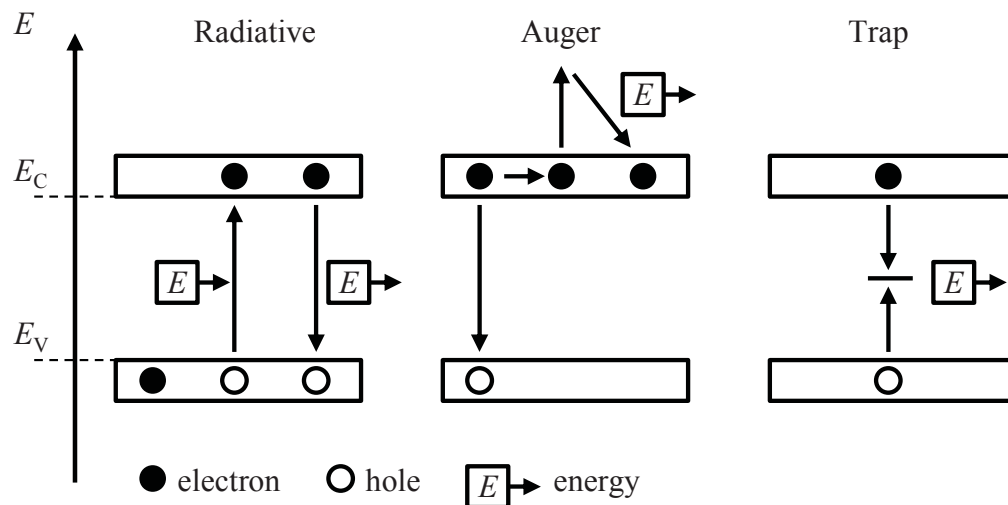


Figure 2.2 Recombination mechanisms according to radiative (left), Auger (middle) and trap recombination (right). The picture of radiative recombination includes the generation of an electron hole pair.

Radiative recombination

Radiative recombination is defined as the recombination of an electron in the conduction with a hole in the valence band by the emission of energy (photon). In the case of indirect semiconductors, the radiative recombination mechanism is rather improbable due to the different linear momentum of the valence band maximum and the conductive band minimum.

Auger recombination

Auger recombination means the interaction of three charge carriers. Figure 2.2, therefore, depicts the interaction of two electrons in the conductive and a hole in the valence band. Notice, that the interaction of two holes and one electron enables the same recombination mechanism. The first electron transfers energy to a second electron and recombines with the hole. The second electron is transferred to a higher energy state and, afterwards, transferred to the origin energy state by the emission of a phonon. Auger recombination is very probable if many charge carriers are available in the semiconductor.

Trap recombination

Impurities and defects in and at the surface of a semiconductor correspond to trap energy states in the band gap and are, therefore, very efficient recombination centers. The recombination is assumed to follow a two-step mechanism. Thus, an electron in the conduction band occupies the energy state in the band gap and, afterwards, recombines with a hole in the valence band. During this two-step mechanism energy is emitted.

The total recombination rate U , or rather the sum of the radiative recombination rate U_{rad} , the Auger recombination rate U_{Aug} , and the trap recombination rate U_{trap} , is expressed by the following equations,

$$U = U_{\text{rad}} + U_{\text{Aug}} + U_{\text{trap}} \quad (2-18)$$

$$U = (C_{\text{rad}} + (C_{\text{Aug},n}n + C_{\text{Aug},p}p) + \frac{v_{\text{th}}N_t}{\frac{n+n_1}{\phi_p} + \frac{p+p_1}{\phi_n}}) \cdot (np - n_i^2) \quad (2-19)$$

$$n_1 = N_C \exp\left(-\frac{E_C - E_t}{kT}\right)$$

$$p_1 = N_V \exp\left(-\frac{E_t - E_V}{kT}\right)$$

with the radiative recombination constant C_{rad} , the Auger recombination constant of electrons $C_{\text{Aug},n}$ and holes $C_{\text{Aug},p}$, the thermal velocity v_{th} , the trap density of a certain trap N_t , the energy state of the regarded trap E_t also denoted as trap level, and the capture cross section of the regarded trap to capture electrons ϕ_n and holes ϕ_p . The main statements to derive from these equations is that, first, the recombination rate increases with increasing carrier concentration, second, Auger recombination is

dominant in the case of high carrier densities, and, third, trap recombination is dominant in the case of low carrier densities. Moreover, the trap recombination rate increases with decreasing energy difference between the energy state of the regarded trap and the center of the band gap. The recombination rate can also be expressed by the carrier lifetime of electrons τ_n and holes τ_p ,

$$\tau_n = \frac{\Delta n}{U} \quad (2-20)$$

$$\tau_p = \frac{\Delta p}{U} \quad (2-21)$$

with the excess carrier concentration of electrons Δn and holes Δp . In the case of n -type material, the lifetime of holes needs to be high in order to reach a low recombination rate.

The charge carrier concentration in a specified volume of a semiconductor can only change with time if the sum of inflow, outflow, generation and recombination of charge carriers in the regarded volume is not zero. The latter correlation is mathematically expressed by the continuity equation,

$$\frac{dn}{dt} = \frac{1}{q} \frac{dJ_n}{dx} + G - U \quad (2-22)$$

$$\frac{dp}{dt} = -\frac{1}{q} \frac{dJ_p}{dx} + G - U \quad (2-23)$$

with the generation rate G . In a steady state, with the charge carrier concentration independent from time, a current gain out of the regarded volume is possible if the generation rate exceeds the recombination rate. Hence, In the case of solar cells, the recombination rate should be kept as low as possible.

2.1.6 pn -junction

Up to now, charge carriers are generated to recombine. In order to extract a current out of a semiconductor, charge carriers need to be separated from each other. This is accomplished by an electrical field as available in the space charge region (SCR) of a pn -junction. In the following, the working principle of a pn -junction in the non-illuminated and the illuminated state is discussed. The band diagram of the pn -junction in both states is depicted in Figure 2.3.

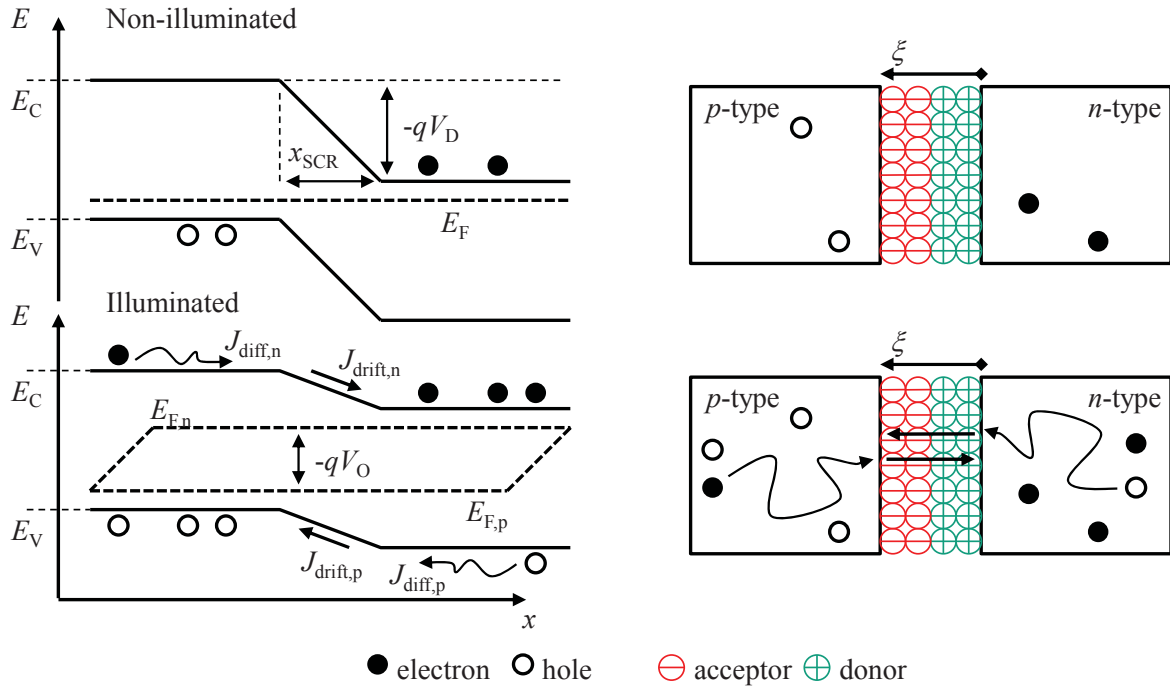


Figure 2.3 Band diagram of the pn-junction in the non-illuminated and the illuminated state (left) and schematic cross section of both states (right).

Separated p -type and n -type semiconductors feature different carrier densities. The p -type semiconductor features a high hole concentration, whereas the n -type semiconductor features a high electron concentration. After contacting both semiconductors with each other, the carrier concentration gradient enables a diffusion current from the p -type to the n -type semiconductor. Independent from the semiconductor type, the outflow of charge carriers leads to an ionization of the carrier related dopants and as a consequence, to a rise in potential gradient enhancing the drift current from the n -type to the p -type semiconductor. The potential gradient rises until diffusion current and drift current equalize each other. In this steady state, the Fermi energy of both semiconductors is on the same level, whereas, due to the available charges in the SCR and the corresponding electrical field, the electrical potential ($\phi = -E_C / q$) differs.

The drop in electrical potential V_D upon the SCR, denoted as diffusion voltage, is a function of the dopant concentration in the p -type N_A and the n -type semiconductor N_D .

$$V_D = \frac{k_B T}{q} \ln\left(\frac{N_A N_D}{n_i^2}\right) \quad (2-24)$$

The Poisson equation provides a relation between charges in the SCR, the electrical field, and the electrical potential,

$$-\frac{d^2\varphi}{dx^2} = \frac{d\xi}{dx} = \frac{q}{\varepsilon\varepsilon_0}(n - p + N_D - N_A) \quad (2-25)$$

with the dielectric constant in the semiconductor ε and the vacuum ε_0 , and, hence, allows for a deduction of the expansion of the space charge region x_{SCR} ,

$$x_{\text{SCR}} = \sqrt{\frac{2\varepsilon\varepsilon_0}{q} \left(\frac{1}{N_A} + \frac{1}{N_D} \right) (V_D - V_I)} \quad (2-26)$$

with the impressed voltage V_I . Notice that the equation is only valid for $V_D > V_I$. Therefore, the expansion of the space charge region decreases with increasing dopant concentration. By impressing a voltage, a spatial manipulation of the SCR is possible. In the illuminated state, the Fermi level is not sufficient to describe the quantity of electrons and holes in the semiconductor including the pn -junction. In order to consider excess carriers, the Fermi level has to be separated in quasi-Fermi levels expressing the hole $E_{F,p}$ and the electron concentration $E_{F,n}$. According to the band bending and the related electrical field of the SCR, excess carriers are separated from each other. Electrons generated in the p -type semiconductor diffuse into the SCR, drift towards the SCR, and reach the n -type semiconductor. Similarly, generated holes are transported from the n -type to the p -type semiconductor. As soon as excess carriers become majorities, the recombination probability decreases down to a minimum and, consequently, the regarded carriers contribute to the electrical power of the solar cell. The voltage V of the device is expressed according to the following equation.

$$V = \frac{E_{F,n} - E_{F,p}}{q} = \frac{k_B T}{q} \ln\left(\frac{np}{n_i^2}\right) \quad (2-27)$$

The maximum spreading of the quasi Fermi levels corresponds to the carrier dependent maximum open circuit voltage V_{OC} of a solar cell. As described above, the output current density is defined by the sum of the drift and the diffusion current density of the charge carriers.

2.1.7 Two-diode model

The structure of a diode consists of a p -type and an n -type semiconductor featuring a space charge region and is, consequently, similar to a simple solar cell structure. In the dark, diodes and solar cells feature a similar dependence of the output current density J on the impressed voltage V denoted as J - V curve. By implementing electric components like diodes in a circuit, the so-called two-diode model enables a simulation of the J - V curve of a simple solar cell. In the following, the diode equation is depicted and, afterwards, the 2-diode model is introduced.

Based on the continuous equation for holes (2-22) and electrons (2-23) and the Poisson equation (2-25), the diode equation can be deduced,

$$J = J_0 \left(\exp\left(\frac{qV}{n_{id}kT}\right) - 1 \right) \quad (2-28)$$

with the diode current density J , the impressed voltage V , and the dark saturation current density J_0 , and the ideality factor n_{id} . By assuming a diode with an infinite expansion and a voltage of 0 V, the current density corresponds to the dark saturation current density which is defined as,

$$J_0 = qn_i^2 \left(\frac{D_n}{L_n N_A} + \frac{D_p}{L_p N_D} \right) \quad (2-29)$$

with the effective diffusion length of electrons L_n and holes L_p . The diffusion lengths of holes and electrons are expressed by the following equations:

$$L_n = \sqrt{D_n \tau_n} \quad (2-30)$$

$$L_p = \sqrt{D_p \tau_p} \quad (2-31)$$

As a consequence, the dark saturation current density increases with decreasing lifetime and can be utilized to describe recombination current densities in the semiconductor.

The circuit of the two-diode model, consisting of a current source, two diodes (D1 and D2), and two resistors, is depicted in Figure 2.4. Diodes are utilized to present recombination losses, whereas resistors are utilized to present resistance losses.

The maximum current density achievable by the solar cell is expressed by the photo current density J_{ph} of the current source. Recombination losses in the silicon bulk and at the surfaces are expressed by the dark saturation current density J_{01} of D1 wired in

parallel to the output. Similarly, recombination losses in the space charge region are quantified by the dark saturation current density J_{02} of D2 wired in parallel as well. Resistance losses arising because of short circuits are expressed by the shunt resistance R_{Sh} of the parallel resistor. Resistance losses due to current flow are considered with the series resistance R_S of the resistor wired in series to the circuit output.

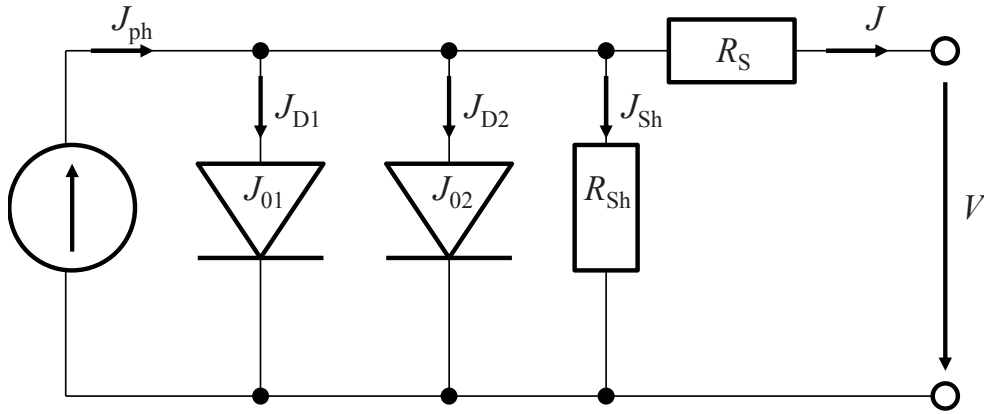


Figure 2.4 Electrical circuit of the two-diode model.

By utilizing Ohm's law, Kirchhoff's circuit laws [22] and the diode equation according to (2-28), the following equation describing the J - V curve of a solar cell can be deduced,

$$J(V) = J_{01} \left[\exp\left(\frac{q(V - JR_S)}{n_1 k_B T}\right) - 1 \right] + J_{02} \left[\exp\left(\frac{q(V - JR_S)}{n_2 k_B T}\right) - 1 \right] + \frac{V - JR_S}{R_{Sh}} - J_{ph} \quad (2-32)$$

with the ideality factor of the first n_1 and the second diode n_2 . Generally, the ideality factor of D1 ($n_1 = 1$) has been found to be lower than that of D2 ($n_2 \geq 2$). Thus, recombination in the space charge region is favored to be the dominating recombination mechanism for low voltages, whereas recombination at in the silicon bulk and at the surfaces is favored to be the one for high voltages. Beier et al. found that n_2 increases with decreasing material purity [23]. The special geometry of the BC-BJ related space charge region is assumed to feature an impact on n_2 as well.

Figure 2.5 depicts the J - V curve of a solar cell for a dark and an illuminated state. In the dark state, the J - V curve of the solar cell corresponds to the one of a forward-biased diode. In the illuminated state, the dark J - V curve shifts along the J axis. Negative values of the current density take into account the technical current direction from the n -type to the p -type semiconductor of the diode.

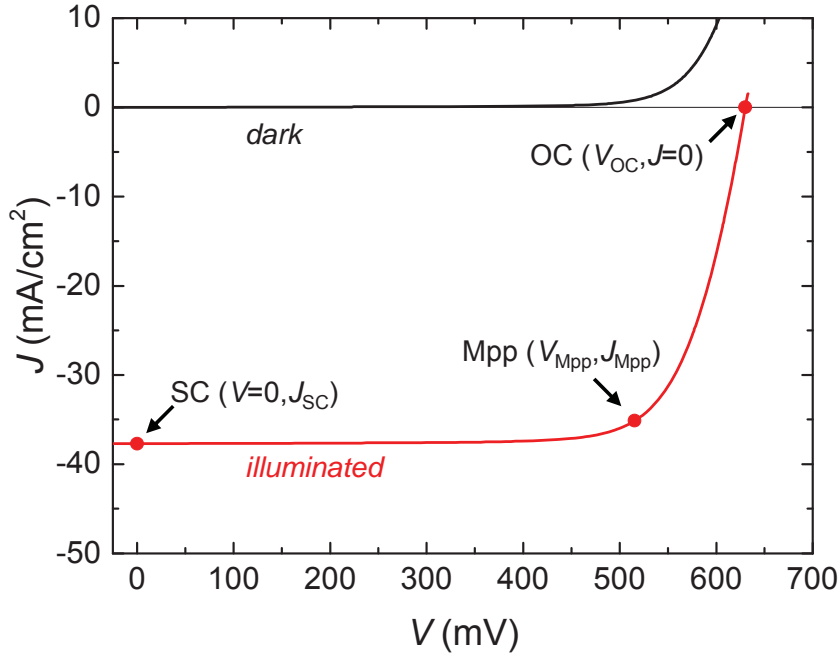


Figure 2.5 J - V curve of a solar cell for a dark and an illuminated state. The illuminated J - V curve and the solar cell performance, respectively, is described with the short circuit current density J_{SC} , the open circuit voltage V_{OC} , and the fill factor FF defining the MPP. The depicted J - V curve corresponds to a solar cell featuring a conversion efficiency η of 18.1 % ($J_{SC} = 37.7 \text{ mA/cm}^2$, $V_{OC} = 630.1 \text{ mV}$, $FF = 76.2 \%$). This corresponds to an output power at MPP P_{MPP} of 181 W/m^2 .

The main parameters describing the performance of a solar cell are highlighted in the illuminated J - V curve. These are the short circuit current density J_{SC} , the open circuit voltage V_{OC} , and the maximum power point (MPP) featuring a voltage V_{MPP} and a current density J_{MPP} . The fill factor is defined as,

$$FF = \frac{J_{MPP} V_{MPP}}{J_{SC} V_{OC}} \quad (2-33)$$

and the efficiency as,

$$\eta = \frac{P_{MPP}}{P_0} = \frac{J_{MPP} V_{MPP}}{P_0} = \frac{FF J_{SC} V_{OC}}{P_0} \quad (2-34)$$

with the power at the maximum power point P_{MPP} and the irradiated power P_0 under, for example, standard test conditions.

2.2 Back-Contact Back-Junction silicon solar cells

2.2.1 Design and working principle

Back-Contact Back-Junction (BC-BJ) solar cells are free of metallization at the front side and, as the name reveals, the *pn*-junction and the electrodes are located at the rear side. In the following, the design of the cell is introduced and described from the inside to the outside and the working principle of the cell is discussed.

Figure 2.6 depicts the photographic top view on the front and on the rear as well as the schematic cross section of the cell. The design of the BC-BJ solar cell was introduced in 1975 by Schwartz and Lammert [24].

The *n*-type silicon wafer indicates a textured front side and a planar rear side. By regarding the schematic cross section of the device, three differently doped surfaces are visible. These are the front surface field (FSF), the back surface field (BSF) and the emitter. In this work, the FSF and the BSF are phosphorus-doped, whereas the emitter is boron-doped. Woehl et al. proposed an *n*-type BC-BJ solar cell with an aluminum alloyed emitter [25]. To differentiate the higher dopant concentration of the FSF, the BSF, and the emitter compared to the dopant concentration in the *n*-type silicon wafer, the highly doped surfaces are indicated as n^+ -Si (BSF, FSF) and p^+ -Si (emitter). The BSF and the emitter are locally doped and separated by a so-called gap region. The realization of the gap region is usually related to an increase in process complexity. Cesar et al. propose a BC-BJ cell design without gap and, thus, a highly industrially relevant BC-BJ approach [26]. The front and the rear side are covered with passivation layers. In order to achieve a contact between silicon and electrodes, the passivation layer at the rear side is locally opened. By regarding the top view on the rear side of the solar cell, the electrodes contacting BSF and emitter are strictly separated or rather electrically insulated from each other. Both electrodes are indicated by several metal fingers leading to a so-called busbar. Thus, the electrodes feature a comb-shaped structure.

Due to the low reflection at the front side featuring a texture and an anti-reflection (AR) layer, most of the light is coupled into the wafer. In the wafer, the light or rather the energy of photons is absorbed and excess carriers are generated. Due to the wavelength dependent absorption length of silicon to absorb photons (compare Figure 2.7), most excess carriers are generated near the front side.

BC-BJ top view

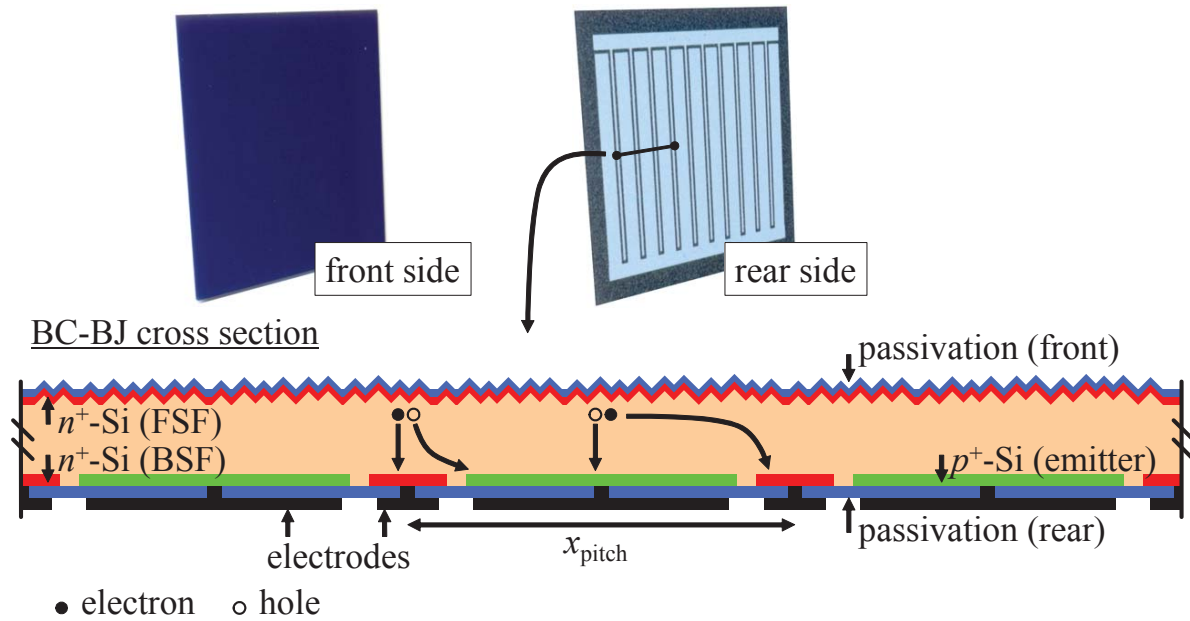


Figure 2.6 Photographic top view on the front and the rear side of the BC-BJ solar cell. A schematic cross section is depicted as well. Notice that the front side of the cell is free of metallization. Assumed diffusion path ways of excess carriers at particular positions are depicted as well.

The absorption length of photons increases with increasing wavelength. At a wavelength of 900 nm the absorption length is approximately 34 μm . As a consequence, all photons featuring a wavelength lower than 900 nm are absorbed close to the front side of the solar cell. After excess carrier generation, holes and electrons are separated. Holes diffuse through the wafer and are collected by the emitter and the connected electrode. Accordingly, electrons (majority charge carriers) diffuse through the wafer and are extracted by the BSF and the connected electrode. The diffusion path length is dependent upon the position of photon absorption and excess carrier generation, respectively. The cross section of the BC-BJ device highlights two extreme cases. In the first case, excess carriers are generated upon the BSF. Electrons can diffuse vertically to be extracted. Because of the location of the emitter, holes need to diffuse vertically and laterally to be collected by the emitter. Thus, the diffusion path length of holes is prolonged compared to the one of electrons. In the second case, electrons and holes are generated upon the emitter, holes diffuse vertically, and electrons diffuse vertically and laterally to be extracted. Thus, electrons feature a higher diffusion path length than holes.

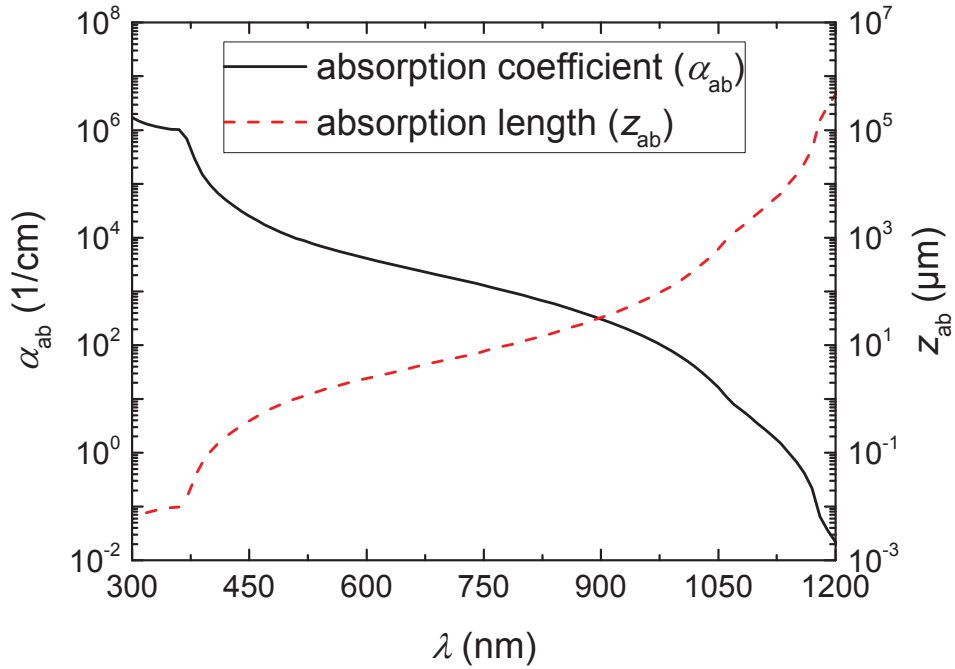


Figure 2.7 Absorption coefficient α_{ab} and length z_{ab} in dependence of the wavelength λ of a photon. Data is taken from [27].

2.2.2 Critical effects

Highly efficient BC-BJ cells exhibit a high front side passivation quality, a high material lifetime, a high emitter coverage, and a low distance between the contact opening of the emitter and the BSF. The latter distance equals the half width of the symmetry element of the cell denoted as pitch distance x_{pitch} (compare Figure 2.6).

Since, as discussed, most of the excess carriers are generated at the front side, the front side passivation quality needs to be very high in order to avoid a high recombination rate at the front side. By passivation layers enabling a strong saturation of silicon surface defects [28] and an FSF enabling an electrical shielding of the silicon surface [29], a high passivation quality of the front side is achievable. The phosphorus concentration in the FSF needs to be adjusted in order to limit additional interface [30] and Auger recombination [31, 32].

Compared to other solar cells, the BC-BJ cell is indicated by a high diffusion path length. In order to overcome that high diffusion path length, a high diffusion length is required. This is achieved by a material featuring a high lifetime and processes exhibiting a low impact on the bulk carrier lifetime. High material lifetimes are usually the result of a low impurity concentration and a low oxygen concentration disabling the formation of harmful silicon-oxygen related precipitates [33].

Due to the low lifetime and the corresponding low diffusion length of holes (minority charge carriers) compared to electrons (majority charge carriers), the emitter coverage should be high in order to provide a high minority collection probability of the cell. Moreover, the BSF should feature a low width in order to decrease the diffusion path length of holes generated upon the BSF. The recombination effect of minorities upon the BSF is denoted as electrical shading and was intensively studied in [34-36].

The pitch distance is related to the diffusion path length of electrons generated upon the emitter. With increasing pitch distance, the series resistance and, as a consequence, series resistance losses increase. Series resistance losses arising from the cell dimensions can be calculated according to the model of Kluska et al. [37]. Thus, the pitch distance needs to be kept as low as possible. Moreover, additional series resistance losses of cells featuring a comparably high pitch distance can be balanced by adjusting the phosphorus doping-level in the FSF.

Two tradeoffs need to be found in order to achieve a BC-BJ cell featuring a high efficiency. First, the phosphorus concentration in the FSF needs to be adapted in order to enable low recombination and resistance losses. Due to interface and Auger recombination, recombination losses increase, whereas, due to electrical conductivity, the series resistance losses decrease with increasing phosphorus concentration.

Second, the pitch distance needs to be adapted in order to provide low recombination and low series resistance losses. Due to the increasing emitter coverage, recombination losses decrease, whereas, due to increase in the lateral path length of majorities, the series resistance losses increase with increasing pitch distance.

2.2.3 Advantages/disadvantages and conversion efficiency

In the following, the advantages and disadvantages of the BC-BJ solar cell compared to other solar cells are listed.

Advantages

- Higher potential in conversion efficiency and, consequently, in costs per watt peak.
- The absence of the front metallization grid is connected to a strong decrease in optical losses. Additionally, the front side can be optimized in order to achieve a low recombination rate without considering the electrical properties of a metal-silicon contact.
- Due to the location of the metal grid on the rear side, the design of the metal grid can be varied in order to achieve low series resistance losses without considering optical shading losses.
- One side interconnection of BC-BJ cells during module assembly is related to a strong decrease in process complexity [38]. Moreover, the packaging density of cells interconnected in a module expressed by cells per area is higher.
- Attractive and uniform appearance of the finished BC-BJ modules.

Disadvantages

- Very high dependence of the conversion efficiency on the wafer quality. Material with a high purity is required. *In this work*, industrially relevant low-cost Cz-Si material is utilized.
- Due to additional process steps (three diffusion steps among other), the process sequences are complex and, usually, connected to high process costs. *In this work*, a co-diffusion process is introduced featuring a very high potential to decrease process costs.
- The conversion efficiency of the cell strongly depends on the minimum feature size and the alignment accuracy of the utilized patterning technique. Moreover, fatal shunts are possible between the electrodes at the rear side. *In this work*, the industrially feasible inkjet technology is utilized to achieve structures and to fulfil the high requirements of the BC-BJ solar cell.

Table 2.1 depicts the characteristic cell parameters, these are the open circuit voltage V_{OC} , the short circuit current density J_{SC} , the fill factor FF and the conversion efficiency η , of the best performing BC-BJ cells published up until now in dependence of the producer, the material, and the cell area A . The efficiency limit of the BC-BJ cell derived in [39] is presented as well. For the efficiency limit, a cell with ideal optics and

material properties was assumed. The calculation was done for a cell featuring an n -type base doping, a base resistivity of $1 \, \Omega\text{cm}$, and a thickness of $150 \, \mu\text{m}$.

Table 2.1 Best performing BC-BJ solar cells. Open circuit voltage V_{OC} , Short circuit current density J_{SC} , fill factor FF , and efficiency η in dependence of the producer, the material, and the cell area A .

Producer	Material	A (cm^2)	V_{OC} (mV)	J_{SC} (mA/cm^2)	FF (%)	η (%)
Panasonic [40]	Cz, n -type	143.7	740.0	41.8	82.7	25.6
Bosch [41]	Cz, n -type	243.4	676.2	41.6	78.5	22.1
Sunpower [42]	Cz, n -type	121.0	725.6	41.5	82.9	25.0
<i>Limit</i>			742.5	44.0	86.5	28.3

The highest efficiency on semi large-scale wafers was achieved by Panasonic. Panasonic exploits the potential of the very high passivation quality of amorphous silicon layers on crystalline silicon surfaces. Thus, the open circuit voltage of the cell approaches the calculated open circuit voltage limit. The highest efficiency on large-scale wafers featuring an edge length of $156 \, \text{mm}$ was achieved by Bosch. The highly doped surfaces of the cell have been processed by ion-implantation. The Sunpower Cooperation was founded in 1985 by Swanson in order to industrialize the BC-BJ solar cell. Thus, Sunpower certainly has the highest expertise in working on this solar cell concept. The technology that Sunpower utilizes to process solar cells is rather unclear. By integrating passivated metal contacts, the efficiency could be increased from $22.4 \, \%$ (Generation 2, [43]) up to $24.2 \, \%$ (Generation 3, [44]). By utilizing a process sequence referred to as SPWR Maxeon Gen III process, the conversion efficiency of the cell could be further increased up to $25.0 \, \%$. Up until now, Sunpower is the only company producing commercially available BC-BJ solar cell modules. Sunpower modules integrate 96 BC-BJ cells with an area of $155.1 \, \text{cm}^2$. These modules feature a conversion efficiency of up to $20.4 \, \%$ [44].

2.2.4 Cell characterization

The cells fabricated in this work are characterized by J - V measurements, Suns V_{OC} measurements and Quantum efficiency (QE) measurements.

J - V curve

The J - V measurements are carried out in order to plot the J - V curve and to determine the cell characteristic parameters: the short circuit current density J_{SC} , the open circuit voltage V_{OC} , the fill factor FF and the conversion efficiency η . The performance or rather the cell characteristic parameters are dependent on the irradiation intensity. In this work, solar cells are measured under standard test conditions also denoted as one sun conditions. Standard test conditions are defined in the IEC norm 60904-3 and imply a solar spectrum AM1.5G [45] with an irradiation power of 1000 W/cm^2 and a cell temperature of 25 C . The measurements were performed with a measurement chuck developed by Granek [39]. Accordingly, solar cells were characterized with an aperture featuring an opening size of 4 cm^2 .

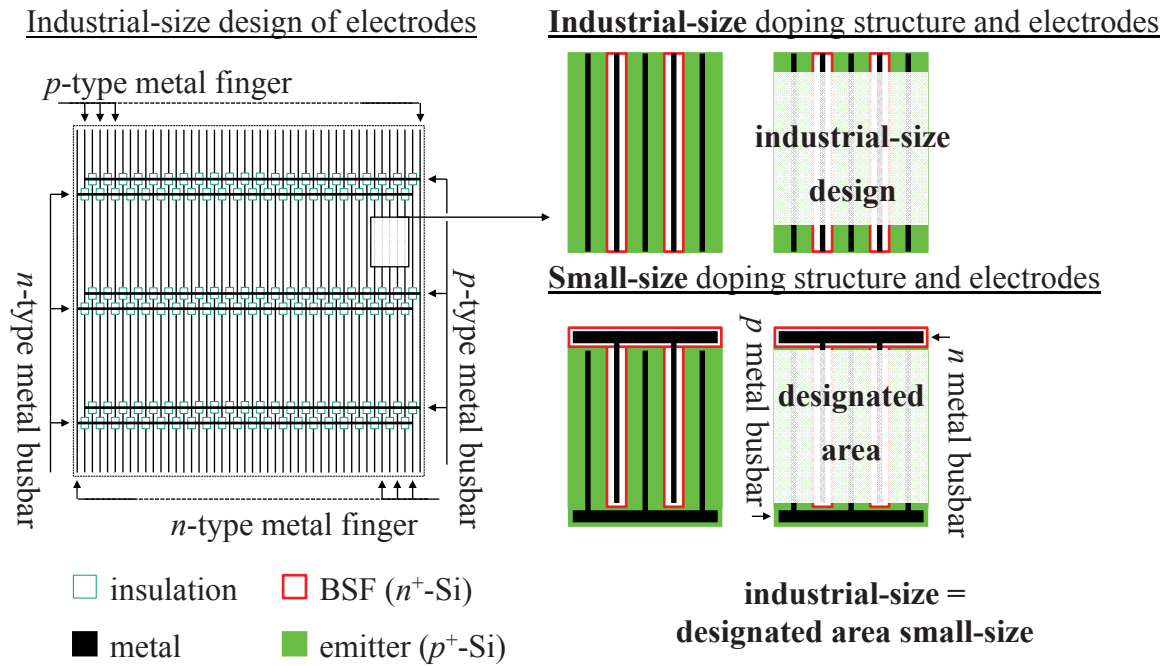


Figure 2.8 Desired industrial-size design of electrodes on the left as well as doping structure and electrodes of the industrial-size and the small-size cell on the right. Depicted are the schematic top views of the BC-BJ cell's rear side. In order to avoid the negative impact of the phosphorus-doped busbar (n^+ -Si), which is not available in the case of an industrial-size cell, on the cell performance, small-size cells are measured with the designated area.

In the case of n -type BC-BJ cells, the phosphorus-doped busbar might be related to a strong loss in short circuit current density arising from electrical shading. In this work, an industrial-size cell design without doped busbars is desired (compare Figure 2.8). Moreover, the shift of busbars away from the wafer edges enables a strong decrease in metal consumption. The industrial-size design was introduced by Mihailetschi et al. [46] and Galbiati et al. [47] in order to develop an industrial-size BC-BJ cell (239 cm^2), denoted as Zebra cell, featuring a maximum conversion efficiency of 21.0 %. In order to achieve a realistic efficiency estimation for the industrial-size solar cell, the busbars (doped busbars and metal busbars) of the fabricated small-size cells were shadowed during the J - V measurements. The area of a solar cell which is free of busbars is denoted as designated area [48].

Quantum efficiency

The quantum efficiency can be separated into external (EQE) and internal quantum efficiency (IQE). The EQE describes the cell conversion of irradiated power into electrical current. The IQE describes the cell conversion of absorbed photons into current. During quantum efficiency measurements, the contacts of the solar cell are short circuited. The EQE is dependent on optical and electrical losses. Optical losses are interface reflection losses, absorption losses in the thin layers, absorption losses due to silicon doping also denoted as free carrier absorption (FCA), and transmission losses at the rear and at the front side of the solar cell. Electrical losses are recombination losses. In contrast, the IQE is only dependent on transmission losses at the rear side and recombination losses.

By integrating the wavelength dependent $EQE(\lambda)$ over the wavelength (λ), the short circuit current density (J_{SC}) is calculated according to the following equation,

$$J_{SC} = \frac{q}{hc} \int_{\lambda=300\text{nm}}^{\lambda=1200\text{nm}} EQE(\lambda) I_0(\lambda) d\lambda \quad (2-35)$$

with the elementary charge q , the Planck constant h , the speed of light c , and the intensity of irradiated light I_0 which is given in $\text{W}/(\text{m}^2\text{nm})$.

By measuring the wavelength dependent reflection $R(\lambda)$ of the solar cell, the wavelength dependent internal quantum efficiency $IQE(\lambda)$ is calculated according to the following equation.

$$IQE(\lambda) = \frac{EQE(\lambda)}{(1 - R(\lambda))} \quad (2-36)$$

By analyzing quantum efficiency measurements, current losses are divided into losses arising from the short ($\lambda \leq 600$ nm), the middle ($600 \text{ nm} < \lambda \leq 900$ nm), and the long wave length range ($\lambda > 900$ nm). Thus, a differentiation of current losses at the front side, in the bulk, and at the rear side is possible as well.

Suns V_{OC}

Fill factor losses of a solar cell are divided into fill factor losses arising from the series resistance, from the leakage current, and non-ideal diode behavior. Fill factor losses due to leakage current are further divided into losses due to the shunt resistance and the dark saturation current density in the space charge region. An attribution of fill factor losses to the mentioned effects is possible by measuring the so called pseudo fill factor and calculating the ideal fill factor. In order to determine the pseudo fill factor, Suns V_{OC} measurements are performed [49]. By varying the light intensity, the characterized solar cell is irradiated under open circuit conditions. With the help of a reference cell measuring the intensity dependent current density and an estimation of the short circuit current density of the characterized solar cell, a pseudo J - V curve can be plotted which is independent from series resistance losses. The difference of the extracted pseudo fill factor and the fill factor $pFF - FF$ enables a characterization of series resistance losses. In turn, the total series resistance R_s is calculated according to the following equation,

$$R_s = \frac{pFF - FF}{pFF} \cdot \frac{V_{OC}}{J_{SC}} \quad (2-37)$$

with the open circuit voltage V_{OC} and the short circuit current density J_{SC} . The ideal fill factor FF_0 , which is dependent on temperature T and on the V_{OC} , is calculated according to the following equation,

$$FF_0 = \frac{\frac{qV_{OC}}{nkT} - \ln\left(\frac{qV_{OC}}{nkT} + 0.72\right)}{\frac{qV_{OC}}{nkT} + 1} \quad (2-38)$$

with the elementary charge q , the Boltzmann constant k , and the ideality factor. Due to the strong dependence of the V_{OC} on recombination losses at, among others, silicon

surfaces, the difference of the calculated ideal fill factor and the pseudo fill factor $FF_0 - pFF$ enables a characterization of losses arising from the leakage current and non-ideal diode behavior.

Series resistance losses in a BC-BJ solar cell depend on the cell design, the applied materials, and the doping-levels [37]. Especially the pitch distance of the solar cell might have a great impact on series resistance losses.

Losses due to leakage current can occur due to a contamination of the space charge region [50], incomplete metal contact separation [51], metal spiking through the space charge region [52], directly adjacent silicon surfaces featuring high doping-levels [53], and solar cells featuring an injection dependent bulk life time and surface recombination [54], whereby the latter effect might be caused by highly charged passivation layers influencing an inversion of charges in silicon.

3 Material and applied technologies

In the following, the applied wafer material, cleaning processes, deposition processes, and the principals of diffusion processes are introduced. The cleaning processes are discussed by utilizing the text books of Kern [55] and Reinhardt [56]. The discussion of the deposition processes is based on the text books of e.g. Ohring [57] and Lüth [58]. The mathematics of diffusion are compiled in e.g. the text book of Crank [59], whereas the text book of Fisher [60] provides a research compilation of impurity diffusion in silicon. The chapter finishes with a demonstration of the BC-BJ base line process used for cell fabrication and a calculation of the co-diffusion related cost-saving potential.

3.1 Wafer material

Most of the excess carriers of a back-contact back-junction silicon solar cell are generated close to the front side of the solar cell. As a consequence, minorities have to diffuse through the whole wafer to be collected by the emitter at the rear side. Since the diffusion length of minorities and the collection probability of the BC-BJ device, respectively, depend strongly on the bulk carrier lifetime, material selection as a first step to a working BC-BJ device is of importance. In this work, monocrystalline silicon wafers are used as base material. These wafers are fabricated according to crystal pulling, also denoted as the Czochralski process. In this process, a seed crystal is dipped into molten silicon. By rotating and pulling the seed crystal upwards, a large cylindrical ingot is extracted from the melt. By dissolving dopants like P and Sb, or B and Ga into the melt, silicon doping to n - or p -type is possible. Since the melt is contained in a silica crucible, the so-called Cz-Si (Cz, Czochralski) wafers generally contain a high oxygen concentration in the range of 10^{17} to 10^{18} cm⁻³. Details concerning the Czochralski process can be found in e.g. the text book [61].

A high amount of oxygen in silicon might lead to the formation of silicon oxygen (Si-O) defects. Depending on the stoichiometric configuration, these defects act as metastable electron donors, also known as thermal donors [62, 63], or as defects being harmful for the bulk carrier lifetime, also known as Si-O precipitates [64, 65]. Metastable electron donors can be dissociated in a thermal treatment, so that these special defects have only a temporal impact on the specific bulk resistivity. Si-O precipitates can form stable traps in the band gap of silicon and, in turn, act as recombination centers. Due to the enhanced growth rate of Si-O precipitates in silicon

at higher temperatures, these recombination centers can get even more effective. In microelectronics, thermally controlled Si-O precipitation is used to capture metal impurities from the silicon surface. The affinity of metal impurities to decorate Si-O precipitates induces a so-called denuded zone in the range of the active area [66]. In photovoltaics and especially in the case of bulk sensitive BC-BJ solar cells, Si-O precipitates are undesired and need to be avoided. A qualitative analysis of Si-O defects is possible by photo luminescence studies before and after thermal treatments [67].

In this work *n*-type Cz-Si wafers are used as base material for the BC-BJ solar cells. Compared to *p*-type, *n*-type material does not suffer from light induced degradation. Light induced degradation is generally caused by B-O complexes which appear especially in the case of high boron and oxygen concentrations [68].

Table 3.1 Recombination parameters including trap energy and capture cross sections of different impurities. Data is derived from [69].

Impurity	Type	E_t (eV)	ϕ_n (cm ²)	ϕ_p (cm ²)	$K = \phi_n / \phi_p$
Ti	Donor	$E_C-0.27$	$3.1 \cdot 10^{-14}$	$1.4 \cdot 10^{-15}$	22
	D. donor	$E_V+0.26$	$1.3 \cdot 10^{-14}$	$2.8 \cdot 10^{-17}$	460
V	D. donor	$E_V+0.36$	$5.0 \cdot 10^{-14}$	$3.0 \cdot 10^{-18}$	17000
Cr	Donor	$E_C-0.22$	$2.3 \cdot 10^{-13}$	$1.1 \cdot 10^{-13}$	2
Mo	Donor	$E_V+0.28$	$1.6 \cdot 10^{-14}$	$6.0 \cdot 10^{-16}$	30
Fe	Donor	$E_V+0.38$	$5.0 \cdot 10^{-14}$	$7.0 \cdot 10^{-17}$	700
Au	Acceptor	$E_C-0.55$	$1.4 \cdot 10^{-16}$	$7.6 \cdot 10^{-15}$	0.02
Zn	Acceptor	$E_V+0.33$	$1.5 \cdot 10^{-15}$	$4.4 \cdot 10^{-15}$	0.34
	D. acceptor	$E_C-0.47$	$1.3 \cdot 10^{-19}$	$6.6 \cdot 10^{-15}$	0.00002

Depending on the purity degree of the Cz-setup, also other impurities like carbon and metals might be dissolved in the ingot. In the latter case, *n*-type material has an additional advantage compared to *p*-type material. The lifetime depends strongly on the trap niveau of impurities in the band gap of silicon and on the capture cross section of these impurities. The capture cross section is a parameter describing the potential of impurities to trap holes or electrons. Impurities are divided into donors and acceptors. Donors are charged positively, attract electrons, and push away holes. Acceptors are charged negatively, attract holes, and push away electrons. For example Ti and Fe form donors, whereas Ti also appears as a double donor being doubly charged. Au and Zn form acceptors. Since in *n*-type silicon the diffusion length of holes and, hence, the

capture cross section of impurities to trap holes is crucial, n -type solar cells are less sensitive to a contamination with donors [69]. Table 3.1 lists recombination parameters of common impurities and the corresponding type, trap energy E_t energy and capture cross section for trapping holes ϕ_p and electrons ϕ_n as well as the so-called K -factor. Since many process setups are made of stainless steel, particular attention needs to be paid to Fe-contamination. Figure 3.1 depicts the impact of Fe on the injection dependent lifetime of n -type and p -type silicon. The calculation is based on the trap related term of equation (2-19) and the Fe data highlighted in Table 3.1.

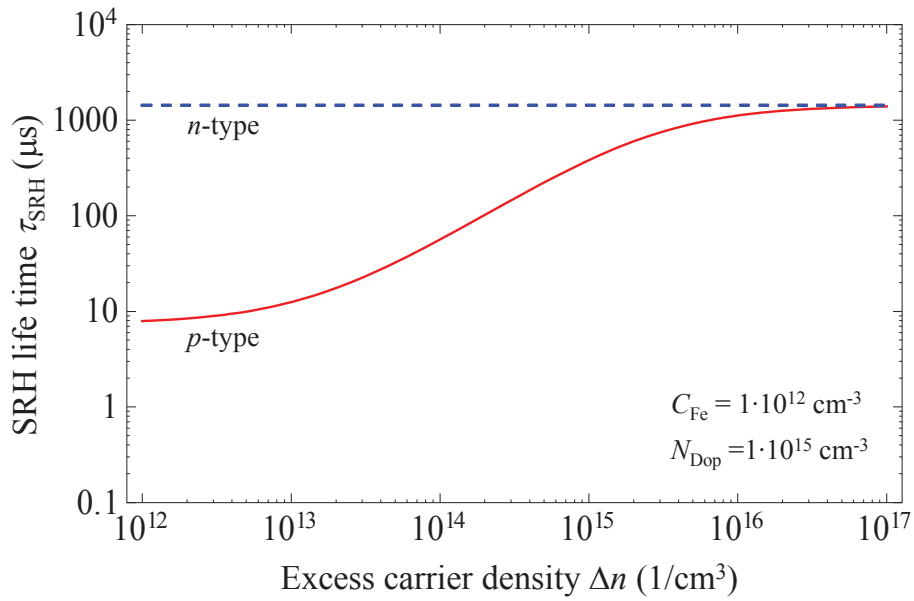


Figure 3.1 Shockley read hall (SRH) lifetime τ_{SRH} as a function of the excess carrier concentration Δn for an n -type and a p -type wafer in the case of iron contamination. The SRH lifetime corresponds to the life time limitation arising from traps.

The p -type wafer shows a strong lifetime dependence on the excess carrier concentration especially in the low injection range. The lifetime of the n -type wafer is independent from the excess carrier concentration in the considered range. For example, at an excess carrier concentration of 10^{14} cm^{-3} the lifetime of an n -type wafer is more than two orders of magnitude higher compared to the one of a p -type wafer. This is due to the low capture cross section of Fe donors to trap. By assuming wafer contamination with vanadium V, this lifetime difference would be even more distinctive. In the case of a contamination with zinc Zn, p -type material would be the better choice compared to n -type material.

3.2 Wet chemical cleaning

Ideally, solar cells are fabricated on quadratic wafers featuring an edge to edge length of 156 mm and a wafer thickness of 200 μm . According to these dimensions, the consideration of surface effects is of importance. For example, surface defects like silicon precipitates decrease the passivation quality, increase the dark saturation current density, and, finally, the open circuit voltage. Metal impurities located on the silicon surface diffuse into silicon, distribute homogeneously and decrease the bulk carrier life time, the diffusion length, and, finally, the short circuit current density. Dielectric residuals featuring a low electrical conductivity like silicon oxide prevent a low electrical contact between metallization and silicon, a low series resistance and, finally, low fill factors. Moreover, organic residuals on the silicon surface lead to an insufficient adhesion of thin layers on silicon or between thin layers. All the mentioned defects like precipitates, metal impurities, dielectric and organic residuals are removable by a cleaning process.

In the following, a brief introduction of the questioned cleaning procedures is carried out. In this discussion, the sensitive dependence of chemical reactions on, among other, temperature, pressure, ratio of components, and pH-values are not considered [55].

A wet chemical cleaning procedure consists of several independent cleaning steps, which are optimized for the removal of special contaminants. Usually, a cleaning procedure features a cleaning step oxidizing and cleaning the wafer surface, followed by a cleaning step removing the grown silicon oxide. These cleaning steps are carried out with a defined temperature and time. Before and after a cleaning step, wafers are rinsed in deionized water (DI- H_2O). In the following experiment, the cleaning steps of interest are the standard clean 1 (SC1), the standard clean 2 (SC2), diluted nitric acid (HNO_3) and diluted hydrofluoric acid (HF).

The SC1 is an alkaline solution consisting of ammonium hydroxide (NH_4OH), hydrogen peroxide (H_2O_2), and water (H_2O). The combination of the solutes induces a simultaneous oxidation and etching of the wafer surfaces. Thus, particles (also particle like organics) are underetched and dissolved, organics are oxidized and form soluble compounds, and metals are captured into the silicon oxide layer.

The SC2 is an acidic solution consisting of hydrochloric acid (HCl), H_2O_2 , and H_2O . The combination of the acidic and oxidative character leads to a protonation of metal bonds at the wafer surface as well as to a metal oxidation. The products of these reactions are all soluble in the chlorine rich solution. Generally, SC2 is very effective as the removal of heavy metals, alkalis, and metal hydroxides is aimed at.

Diluted HNO_3 is a solution combining acidic and oxidative character and is therefore an adequate choice, too, as the removal of organics and heavy metals is aimed at. Diluted HF allows for etching of grown silicon oxides including impurities captured during the oxide growth of the cleaning steps.

Table 3.2 Cleaning procedures of the RCA and the HNF clean.

<u>RCA</u>	<u>HNF</u>
Rinsing in DI- H_2O	Rinsing in DI- H_2O
SC1 ($T_{\text{SC1}} = 60^\circ\text{C}$, $t_{\text{SC1}} = 10$ min)	HNO_3 ($T_{\text{HNO}_3} = 110^\circ\text{C}$, $t_{\text{HNO}_3} = 10$ min)
Rinsing in DI- H_2O	Rinsing in DI- H_2O
HF-Dip ($T_{\text{HF}} = \text{RT}^\circ\text{C}$, $t_{\text{HF}} = 1$ min)	HF-Dip ($T_{\text{HF}} = \text{RT}^\circ\text{C}$, $t_{\text{HF}} = 1$ min)
Rinsing in DI- H_2O	Rinsing in DI- H_2O
SC2 ($T_{\text{SC2}} = 60^\circ\text{C}$, $t_{\text{SC2}} = 10$ min)	Drying
Rinsing in DI- H_2O	
HF-Dip ($T_{\text{HF}} = \text{RT}$, $t_{\text{HF}} = 1$ min)	
Rinsing in DI- H_2O	
Drying	

The cleaning procedures of interest in this work are the so-called RCA and the HNF clean. Process steps and parameters of the cleaning procedures of choice are depicted in Table 3.2. Multifunctional batch systems from Stangl (Semiconductor Equipment AG) and Goller are mainly utilized to perform wet chemical processes. Commercially available inline systems provide a wafer throughput of up to 7200 industrial-size wafers per hour.

3.3 Deposition

3.3.1 Plasma enhanced chemical vapor deposition

In order to deposit passivation layers and solid dopant sources, plasma enhanced chemical vapor deposition (PECVD) is carried out. Since the layer deposition is the result of a chemical reaction at the substrate surface, PECVD is denoted as a heterogenic deposition process. During deposition, a plasma state is utilized. The plasma state consists of dissociated gas molecules and the corresponding products. These are neutral molecules, excited molecules, ionized molecules, electrons, and radicals [70]. Due to the plasma state, the reaction energy required for chemical

reactions is strongly decreased and layer deposition is carried out at a lower temperature compared to other CVD techniques. The energy for plasma activation is provided electrically and/or inductively. During a plasma process, gas molecules are coupled into the process chamber, are activated to the plasma state, reactants (reactive molecules of the plasma) diffuse towards the substrate surface, migrate at the substrate surface, and react at the substrate surface. The products of the reactions are a deposited thin layer and by-products not incorporated in the thin layer. By products diffuse away from the substrates and are exhausted.

In dependence of the process parameters, the morphology of thin layers deposited by means of PECVD ranges from crystalline to amorphous. The porosity is adjustable as well. Due to the high availability of hydrogen in the plasma, layers usually incorporate a high amount of hydrogen and are, as a consequence, not stoichiometric correct.

In this work, several thin layers are deposited by means of PECVD, whereby the following reactive gases are utilized during the deposition process. Boron-doped silicate glass (BSG) layers are deposited by utilizing the gases diborane (B_2H_6), silane (SiH_4), and nitrous oxide (N_2O). Phosphorus-doped silicate glass (PSG) layers are deposited by substituting diborane with trimethyl phosphite (TMPi). TMPi is a liquid precursor injected to the process chamber with argon as carrier gas. Silicon oxynitride ($SiON_x$) layers are deposited by using silane and nitrous oxide as reactive gases. Due to the relatively high silane gas flow during deposition and the related high incorporation of silicon in the deposited layer, a silicon oxynitride film is often denoted as silicon rich. Anti-reflective silicon nitride (AR- SiN_x) layers are deposited by utilizing ammonia (NH_3) and silane as reactive gases.

The PECVD processes were primarily performed with a SINA XS setup from Roth und Rau. Depending on the process parameters, PECVD setups from Roth und Rau enable a wafer throughput of around 5000 industrial-size wafers per hour.

3.3.2 Plasma enhanced atomic layer deposition

Aluminum oxide (Al_2O_3) layers are deposited by means of plasma enhanced atomic layer deposition (ALD). The layer deposition is the result of chemical reactions at the silicon surface. Compared to PECVD, mono layers are deposited in a self-limiting deposition cycle. By repeating these deposition cycles, the thickness of the layers is precisely adjustable. The morphology of ALD layers is highly crystalline with a very low porosity. In the following, the ALD deposition cycle utilized to deposit an aluminum oxide monolayer is shortly introduced. For this, the findings published in [71] are utilized.

The deposition cycle is divided into a precursor, oxidation, and two purge steps carried out after the precursor and the oxidation step. During the complete deposition cycle, the valve used for injecting oxygen into the process chamber is open. During the precursor step, the valve used for injecting TMAI ($\text{Al}[\text{CH}_3]_3$) is open as well. The aluminum atom in TMAI connects to the oxygen atom in a silicon-oxide-hydrogen (Si-O-H) bond, the natural end-group of a silicon surface. This reaction proceeds until all Si-O-H bonds are transformed into Si-O-Al $[\text{CH}_3]_2$ bonds. In the following purge step, the TMAI valve is closed and remaining TMAI as well as by-products are exhausted. During the oxidation step, an oxygen plasma is shortly excited by a so-called inductively coupled plasma (ICP) source. The interaction of the highly reactive oxygen species with the modified end-group leads to a transformation of Si-O-Al $[\text{CH}_3]_2$ into Si-O-Al $[\text{OH}]_2$ bonds. Moreover, by cross linking of hydroxyl (OH) groups, neighboring Si-O-Al $[\text{OH}]_2$ bonds interconnect with each other. The oxidation step proceeds until all methyl groups (CH_3) are substituted by hydroxyl groups. In the following purge step, by-products are exhausted and the deposition cycle is completed. In this work, a semi-industrial ALD setup (InPassion LAB) from SolayTech was utilized to deposit Al_2O_3 layers. By assuming a deposition process featuring a temperature of 180-200°C, a deposition rate of 30 nm/min, and a layer thickness below 5 nm, a wafer throughput of around 100 industrial-size wafers per hour is achievable.

3.3.3 Physical vapor deposition

Metal electrodes are deposited by means of evaporation, a process belonging to the category physical vapor deposition (PVD). Compared to CVD, PVD coated thin layers are not the consequence of a chemical reaction at the substrate surface. The layer deposition has a physical origin. The evaporation process is differentiated into three steps. First, the ingot material is heated until evaporation. Second, the evaporated material diffuses towards the substrate. Third, the evaporated material condenses at the surface of the substrate, whereas the substrate is usually clamped into a cooled chuck. The ingot material is evaporated by resistance heating or by a focused high-energy electron beam. In order to achieve a homogenous layer deposition, evaporation is carried out in an evacuated chamber. The condensation of the evaporated material upon the substrate starts with nucleation, followed by nuclei growth, until coalescence of the growing nuclei.

Besides process pressure and surface topography, morphology and adhesion of the deposited layers depend strongly on the substrate temperature. In order to achieve a low porosity and a high adhesion of the layer on the substrate, the substrate temperature should be set higher than 0.45 times the material specific melting

point [72]. For example, pure aluminum, featuring a melting point of around 933 K, should be deposited with a substrate temperature higher than 420 K (147°C). In contrast, titanium, featuring a melting point of around 1998 K, should be deposited with a substrate temperature higher than 899 K (626°C). In this work, ingots consisting of aluminum-silicon alloy are utilized to deposit electrodes. Because the compounds feature a lower melting point than pure aluminum, the substrate temperature is set to relatively low temperatures.

In this work, electronic beam assisted evaporation is carried out by using the setup EV 1-10 from FerroTec. Industrially convertible in-line setups like the ATON 500 from applied materials enable a wafer throughput of around 1000 industrial-size wafers per hour.

3.3.4 Inkjet printing

Masking and etching is carried out to realize structures. Masking is performed by inkjet printing of an etch mask upon the layer which is chosen to be patterned. An organic, waxy media is utilized as etch mask. The ink features a very high robustness in wet chemical solutions containing HF. Since a large palette of thin layers - silicon oxide and silicon nitride layers among others - feature a high etch rate in wet chemical solutions containing HF, a pattern transfer of the inkjet printed etch mask into these layers is possible [73, 74].

The printing setup (Schmid, Inkjet DoD 300) consists of a printhead module, a printhead (Spectra, SE128AA30pl) and a substrate table. The printhead module consists of three separate ink reservoirs. The upper reservoir is utilized to melt the ink featuring a melting point of around 80°C. The middle reservoir collects the molten ink and supplies the bottom reservoir which is directly connected to the printhead. The printhead features 128 nozzles which are actuated simultaneously by an electrically deformable piezo membrane. By varying process parameters like, for example, the piezo voltage and the time dependent actuation of the piezo membrane, the droplet volume and the droplet speed is adjustable. The printhead module including the printhead is fixed, whereas the substrate table is movable. Moreover, the temperature of the substrate table is tunable and enables a manipulation of the droplet shape upon the printed substrate. Due to the special properties of the waxy ink, the development of the droplet shape upon the substrate is more dependent upon solidification than on wetting phenomena.

Figure 3.2 depicts several ink droplets which were printed on a saw-damage etched wafer featuring a silicon oxide layer on top. The images were recorded by using a scanning electron microscope (SEM). The droplets feature a diameter of around

50 μm . By assuming a succeeding etching process, areas covered with droplets would not be etched, whereas uncovered areas would be etched. According to the design of the utilized digital printing mask, the droplets can be shifted to each other and therefore an infinite quantity of patterns is easily achievable in several thin layers.

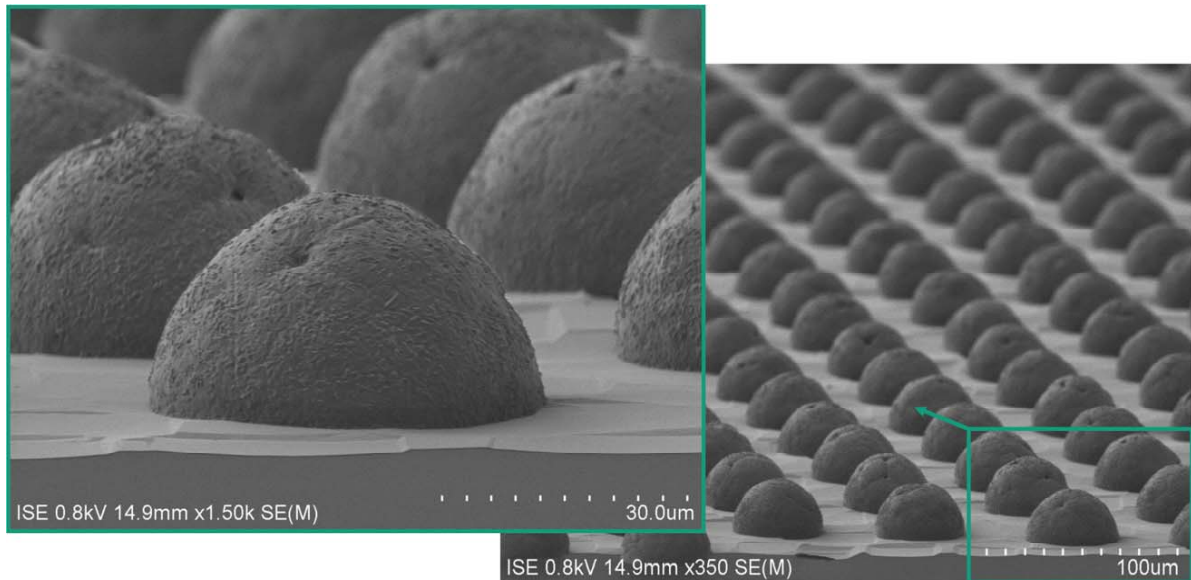


Figure 3.2 Images taken with a scanning electron microscope (SEM) of ink droplets after inkjet printing on a saw-damage etched silicon wafer featuring a silicon oxide layer on top. Pictures were taken and studied in the time parallel doctoral thesis of David Stüwe [75].

The printing accuracy of serially performed printing steps can be evaluated by performing the following experiment (Compare Figure 3.3). Utilizing a saw-damage etched silicon wafer (1), deposition of a thin layer upon a wafer (2), aligned printing of an etch mask upon the layer (3), etching the layer (4), removal of the etch mask (5), aligned printing of the same etch mask upon the patterned layer (6), evaluation of the accuracy with an optical microscope.

After sample preparation, the etched line and the printed line indicate a difference in line width of around 25 μm . Since the distance of the outer printed line to the outer etched line is equal on both sides, the difference in line width arises due to under etching effects. The alignment accuracy is very high and assumed to be lower than $\pm 10 \mu\text{m}$. Significant alignment inaccuracies because of distortional and rotational defects, for example, were not determinable. To sum up, the minimal feature size of around 50 μm and the accuracy of $\pm 10 \mu\text{m}$ underline the high compatibility of inkjet printing to the assembly of high resolution BC-BJ solar cells. Other mentionable advantages of inkjet printing compared to, for instance, screen printing are, first, processing without mechanical contact to the substrate and, second, the flexibility of

digital printing masks compared to screens. A mentionable disadvantage of inkjet printing is nozzle clogging.

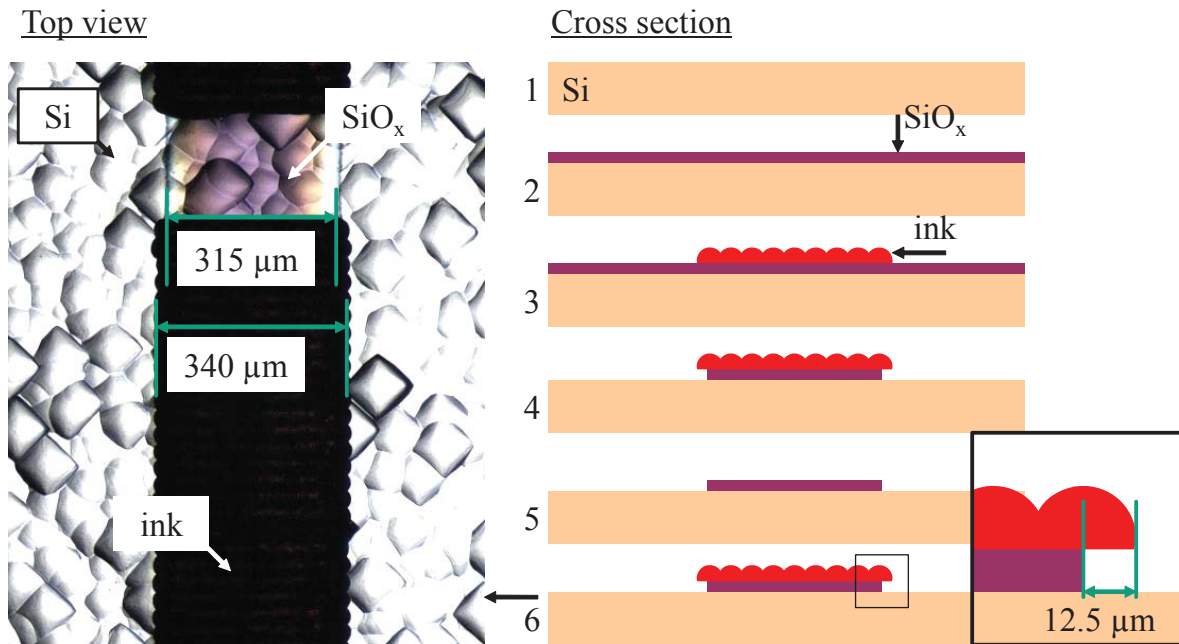


Figure 3.3 Demonstration of the alignment accuracy provided by the utilized inkjet printer. Top vie on the fabricated sample (left) and schematic cross sections depicting the process sequence utilized during sample fabrication (right).

For example Roth and Rau provides an inkjet printer (JETx) enabling a wafer throughput up to 2400 industrial-size wafers per hour. Moreover, only one missing droplet per 30000 wafers is expected. These developments demonstrate the growing feasibility of inkjet printers for solar cell mass production.

3.4 Diffusion

3.4.1 Thermal diffusion

Thermal diffusion of atoms in a material is described by the first and the second Fick's law. In the following Fick's laws are briefly introduced by discussing one-dimensional diffusion phenomena. Fick's first law is represented mathematically by the following equation,

$$J = -D \frac{dC}{dx} \quad (3-1)$$

with the current density J of the diffusing species (dopant), the concentration gradient of the dopant in the medium (dC/dx), the diffusion coefficient of the dopant in the material D which is mathematically defined according to the Arrhenius Law,

$$D = D_0 \exp\left(-\frac{E_a}{k_B T}\right) \quad (3-2)$$

with the Boltzmann constant k_B , the temperature T , the activation energy E_a , and the diffusivity D_0 . Consequently, dopant diffusion is driven by an inhomogeneous distribution of dopants in the material and is strongly influenced by temperature and the diffusion mechanism related diffusivity and activation energy of the particular dopant in the particular material. Moreover, the diffusion mechanism related diffusivity is a function of the dopant concentration. Boron diffuses via diffusion mechanisms related to silicon self-interstitials. The diffusion mechanism of phosphorus is dependent on the phosphorus concentration. For concentrations below 10^{20} cm^{-3} , phosphorus diffuses like boron via diffusion mechanisms related to silicon self-interstitials [76]. For concentrations higher than 10^{20} cm^{-3} , phosphorus is assumed to diffuse via diffusion mechanisms related to vacancies and interstitial sites [77]. By regarding a material consisting of two adjacent materials with a low (dopant receiver) and a high initial dopant concentration (dopant source), the diffusion of dopants takes place from the dopant source into the dopant receiver.

The diffusion time dependent change in dopant concentration in the material (dC/dt) due to diffusion is described with Fick's second law according to the following equation.

$$\frac{dC}{dt} = D \frac{d^2 C}{dx^2} \quad (3-3)$$

Thus, the dopant concentration at a position changes with time as long as dopant current densities around this position differ.

Based on Fick's laws and particular boundary conditions, two important cases of diffusion phenomena can be deduced: diffusion from infinite and finite dopant sources. In case of infinite dopant sources featuring an infinite amount of dopants, the time dependent progress of the dopant concentration profile in the dopant receiver $C(x,t)$ is described by the following equation.

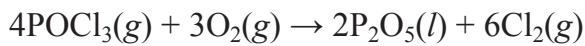
$$C(x,t) = C_s \operatorname{erfc} \frac{x}{2\sqrt{Dt}} \quad (3-4)$$

Where C_s is the dopant concentration at the interface between the dopant source and the dopant receiver. During diffusion, the dopant concentration at the interface is constant with time. In the case of finite dopant sources featuring a finite amount of dopants, $C(x,t)$ is expressed as follows:

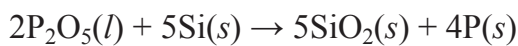
$$C(x,t) = \frac{DA}{\sqrt{\pi Dt}} \exp\left(-\frac{x^2}{4Dt}\right) \quad (3-5)$$

Where DA is the so called dopant assignment of the dopant source expressing the mathematical product of dopant concentration and layer thickness of the dopant source. In this thesis, the expression dopant content refers to the total amount of dopants in the dopant source. The dopant concentration at the interface between dopant source and receiver decreases with increasing diffusion time. The deduced dopant concentration profiles enable an adequate forecast of diffusion processes related to one diffusion mechanism, for instance boron. The concentration dependent diffusion mechanisms of phosphorus might lead to a so called kink and tail shape of the dopant concentration profile [77]. These profiles cannot be approximated by the deduced equations. In the case of BC-BJ solar cells, the course of the dopant concentration profiles of the FSF, the BSF, and the emitter has a strong impact on the solar cell performance.

In this work, PECVD BSG and PSG layers are utilized as solid dopant sources. A thermally grown PSG layer deposited in-situ in the diffusion process is utilized as well. Therefore, a quartz tube furnace is flooded with the reactive gases phosphoryl chloride (POCl_3), nitrogen (N_2), and oxygen (O_2). The deposition of the thermally grown PSG layer then occurs according to the following two-step reaction. At first, POCl_3 and O_2 react in the gas phase forming phosphorus pentoxide (P_2O_5) and gaseous chlorine (Cl_2).



A positive effect of chlorine is the high affinity to capture metallic impurities. Thus, the reaction has a potential to increase the wafer purity [78]. At second, P_2O_5 condenses at the silicon surface forming phosphorus-doped silicon oxide.



Besides the introduced two-step reaction, dry oxidation of silicon takes place as well. Consequently, the phosphorus concentration in the thermally grown PSG layer depends strongly on the utilized gas flow ratios of POCl_3 and O_2 during the diffusion process, as shown e.g. in [79]. Notice that POCl_3 is in truth a liquid. During processing POCl_3 is heated to the boiling point in a so called bubbler and injected into the process chamber by argon acting as carrier gas. In the following, POCl_3 is denoted as gaseous diffusion source.

3.4.2 Solubility of boron and phosphorus in silicon

The incorporation of silicon dopants in the silicon lattice is divided into the incorporation of so called active and inactive dopants [80]. Active dopants are located at regular sites of the silicon lattice, are ionized at room temperature, and contribute to the electrical conductivity of silicon. Inactive dopants are located at interstitial sites and do not contribute to the electrical conductivity of the semiconductor. Figure 3.4 depicts the temperature dependence of the active solubility limit of boron and phosphorus in silicon after Solmi et al. [81].

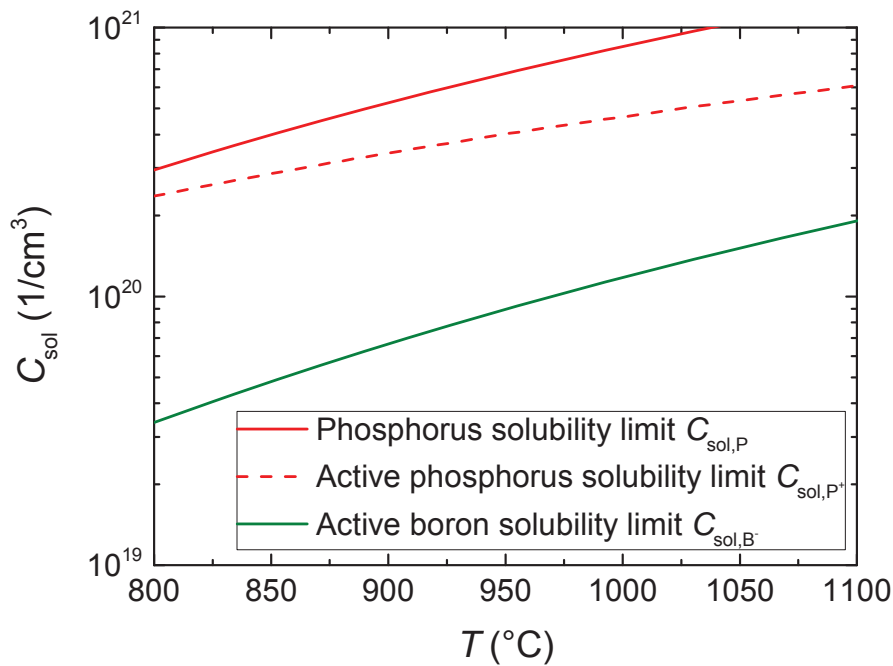


Figure 3.4 Solubility limit C_{sol} of active C_{sol,P^+} and inactive phosphorus $C_{sol,P}$ as well as active boron C_{sol,B^-} in dependence of the temperature T during a thermal diffusion process. The data is based on investigations performed by Solmi et al. [81].

The active solubility limit of boron and phosphorus increases with increasing temperature. At a temperature of 950°C, the active solubility limit of phosphorus $C_{\text{sol,P+}}$ is $4.0 \cdot 10^{20} \text{ cm}^{-3}$. In comparison, the active solubility limit of boron $C_{\text{sol,B-}}$ at the same temperature is $9.0 \cdot 10^{19} \text{ cm}^{-3}$. In the case of dopant concentrations exceeding the depicted active solubility limit, dopants are acting inactive. Moreover, a high quantity of inactive dopants at interstitial sites might lead to a formation of harmful precipitates. The highest dopant concentration during thermal diffusion usually occurs at the silicon surface and, in consequence, the formation of precipitates is a surface related effect. In the case of phosphorus diffusion with a diffusion temperature of 950°C, Si-P precipitation starts for a dopant concentration exceeding the critical value $C_{\text{sol,P}}$ of $6.7 \cdot 10^{20} \text{ cm}^{-3}$ [80]. In the case of boron, a differentiation between active and inactive dopants is unknown. Thus, precipitation can already occur for a dopant concentration slightly higher than the active solubility limit. The extensive spreading of boron related precipitates over the complete wafer surface is a commonly known issue in PV and denoted to as the formation of a boron rich layer (BRL) [82, 83]. Due to the following reasons, the precipitation of dopants during diffusion is undesired.

Compared to silicon, the crystal structure of precipitates differs [84, 85]. Consequently, the incorporation of precipitates induces dislocations in the silicon wafer and, hence, enables a negative impact on the bulk life time [86, 87]. Moreover, the availability of precipitates at the silicon surface is expected to decrease the surface passivation quality arising from the spatial separation of the passivation layer and the silicon surface and the corresponding incomplete deactivation of surface defects. The formation of a low-resistance contact between silicon and metallization as desired in a silicon solar cell is hindered by precipitates as well [88]. The removal of precipitates by pre-treatments after diffusion like low-temperature oxidation (LTO) and subsequent etching is not expected to completely anneal dislocations in the silicon bulk. Additionally, LTO processes are cost-intensive processes. It is assumed that a dopant concentration below the active solubility limit during the whole time span of the diffusion should lead to a prevention of dopant precipitation at the silicon surface. Such diffusion conditions are favored in this work and are expected to be achievable by adjusting the dopant concentration of the utilized dopant sources.

3.5 BC-BJ processing

3.5.1 Base line process

In this section, the base line process desired for BC-BJ cell processing is introduced. Therefore, Figure 3.5 depicts the cross section of the BC-BJ solar cell after every

process step. These cross sections correspond to the symmetry element of the solar cell and not to the complete wafer cross section. The dimensions are selected for visualization and are, therefore, not to scale.

The process sequence is divided into three process modules. These are ‘texturing’ (a), ‘co-diffusion’ (b), and ‘passivation and metallization’ (c). The complete process sequence of the base line process involves four patterning modules which are carried out in the same manner. In Figure 3.5 the patterning module ‘inkjet patterning’, which is used for patterning of thin layers and stacks, is shown exemplarily on the right hand side. Depicted is the so-called contact opening of the rear passivation. In the following, the base line process is described in detail.

Texturing

Monocrystalline silicon wafers are utilized as base material (a-1). The utilized material is grown according to the Czochralski (Cz) process and features a phosphorus (*n*-type) base doping. After damage etching and cleaning (a-1), the rear side of the wafers is coated with a silicon nitride layer (SiN_x) deposited by means of PECVD (a-2). The process parameters during PECVD are adjusted to deposit SiN_x layers with a thickness of around 125 nm. The deposited layer acts as a barrier against KOH solutions and, hence, enables a sufficient protection of the solar cell’s rear side during texturing processes. As a consequence, only the front side of the solar cell is textured during the alkaline texturing process (a-3). After texturing, the SiN_x layer on the rear side of the solar cell is removed in a wet chemical solution containing HF (a-4). After this process, the wafers feature a textured front side and a damage etched rear side.

Co-diffusion

Prior to the PECVD of a PSG/SiO_x stack on both sides of the wafer (b-1), an HNF-cleaning procedure is performed. To provide adequate diffusion conditions, the cleaning procedure before the co-diffusion module is of high importance. After PECVD, the first patterning module is carried out (b-2). Therefore, the PSG/SiO_x stack on the rear side is locally covered with an organic ink which is printed with the help of an inkjet printer. Since the corresponding ink mask defines the expansion of the BSF, the patterning module is referred to as BSF definition. The front side is protected with an additionally printed full area mask. After printing, etching is performed in a buffered etching solution containing HF. Patterning modules finish with the ink removal in acetone and isopropyl alcohol (IPA) and by removing organic residuals in a SC1 followed by a short HF-Dip.

After BSF definition, the rear side of the solar cells is PECVD coated with an additional SiO_x layer (b-3). During co-diffusion, this layer serves as a barrier against B-diffusion from the BSG layer into the wafer. After deposition of the SiO_x layer, the next patterning module is carried out (b-4). Therefore, the PSG/ SiO_x lines underneath the additionally deposited SiO_x are covered with overlapping ink lines. Since the corresponding ink mask defines the gap regions between emitter and BSF, the patterning module is referred to as gap definition. Again, the front side is protected with an additionally printed full area mask and, then, etching is performed in a buffered etching solution containing HF.

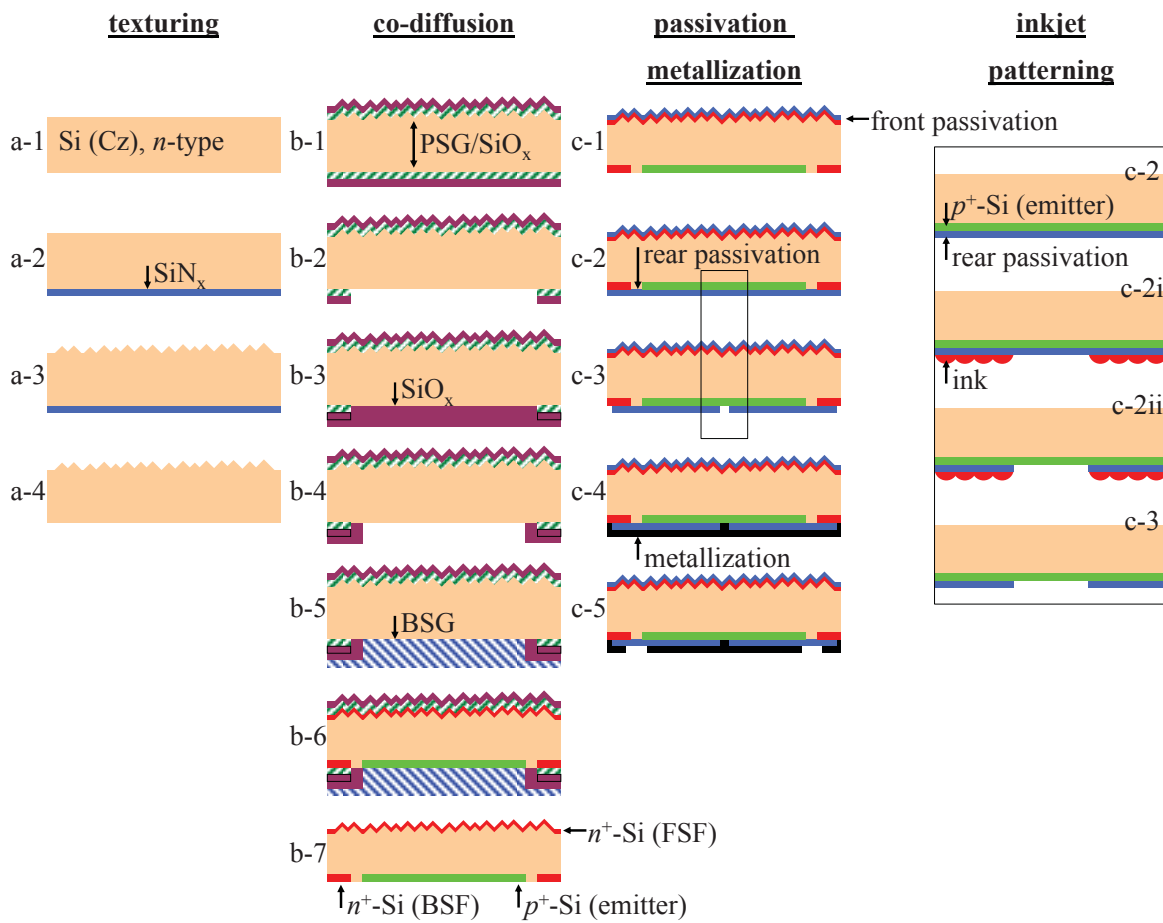


Figure 3.5 Base line process for the assembly of BC-BJ solar cells. The complete process sequence is divided into process modules. These are ‘texturing’, ‘co-diffusion’, and ‘passivation and metallization’. The patterning module referred to as ‘inkjet-patterning’ is depicted on the right hand side.

After patterning, a BSG layer acting as B-dopant source is deposited on the rear side of the cell (b-5) and, finally, a high temperature step is carried out enabling the co-diffusion process (b-6). If the solid dopant sources, these are the PSG/SiO_x stacks

and the BSG layer, feature an interface with silicon, the diffusion of dopants into silicon is accomplished. This leads to the formation of the FSF, the BSF and the emitter. After co-diffusion, the doped silicate glasses are etched back in a wet chemical process featuring diluted HF (b-7).

Passivation and metallization

Following the co-diffusion module, the process module passivation and metallization is performed. Therefore, the uncoated wafers are cleaned in an HNF-cleaning procedure. The HF-dip is carried out directly before the deposition of the front side passivation (c-1). In the base line process, the front side passivation is a PECVD layer stack consisting of a silicon rich silicon oxynitride (SiON_x) layer and a so-called anti reflection silicon nitride (AR- SiN_x) layer, as investigated by Seiffe et al. [89]. The SiON_x layer is optimized for surface passivation on P-doped surfaces. The AR- SiN_x layer is improved for reflection especially in combination with the additional SiON_x layer. To keep absorption losses as low as possible, the thickness of the SiON_x layer is below 5 nm, whereas the thickness of the AR- SiN_x layer is approximately 75 nm [90]. Prior to the deposition of the rear passivation, a short HF-dip is performed in order to obtain a perfectly clean surface. The etching time needs to be selected carefully, because the AR- SiN_x on the front is slightly etched as well. Immediately after the HF-dip, the rear side is coated with an aluminum oxide (Al_2O_3) layer deposited by means of plasma enhanced atomic layer deposition (ALD, c-2). The deposition cycles are adjusted to realize a layer thickness of around 5 nm. Layers with a thickness of around 5 nm were found to provide a high surface passivation quality on B-doped surfaces [91]. By protecting the Al_2O_3 layer with an additional PECVD AR- SiN_x layer, the rear passivation stack is finished. Subsequently, the next patterning module is performed (c-3). In this module, the passivation stack at the rear side is covered with an ink mask featuring line openings. Since these line openings define the location and the dimensions of the contact openings in the rear passivation stack, this patterning module is referred to as contact opening. Again, the front side is protected with an additionally printed full area mask. The pattern transfer is performed in a buffered etching solution containing HF.

To realize the cell electrodes, the rear side of the solar cell is coated with an aluminum silicon (Al-Si) alloy deposited by means of evaporation in an electronic beam configuration (c-4). The target material used during evaporation features an atomic silicon percentage of around 1 %. The layer thickness after deposition is approximately 3 μm . Finally, the last patterning module is performed (c-5). Therefore, the Al-Si layer at the rear side is locally covered with an ink mask allowing for the definition of the

electrodes electrically contacting the BSF and the emitter. To avoid short circuits, the width of the ink fingers are narrower than the width of the corresponding doped surfaces. The front side is covered with an additional ink mask. The pattern transfer is performed in a buffered etching solution featuring phosphoric, hydrochloric, and acetic acid. The patterning module is referred to as contact separation.

3.5.2 Cost reduction by co-diffusion

The highlight of the base line process is the co-diffusion module which allows for the simultaneous formation of all the required doped surfaces in only one single diffusion process and, as a consequence, features a high potential in order to decrease the process costs and to increase the cell efficiency. In this section, the introduced co-diffusion module is compared to a diffusion module based on sequentially performed diffusion processes [92-94]. In the following, an estimation of the diffusion module related process costs is performed by utilizing a cost calculation tool developed at the Fraunhofer ISE [95]. The process sequences of the regarded diffusion modules were arranged with the same process techniques (PECVD, Inkjet, Wet chemistry, thermal diffusion in a tube furnace). In the case of sequential diffusion, the locally doped surfaces at the rear side of the cell are assumed to be fabricated by utilizing pre-patterned diffusion barriers at the rear side of the cell during the diffusion step featuring a gaseous dopant source. The results of the cost calculation of sequential diffusion and co-diffusion are depicted in Table 3.3.

Table 3.3 Process sum and process costs of co-diffusion and sequential diffusion. The process sequences of the regarded diffusion modules were arranged with the same process techniques. These are PECVD, Inkjet, wet chemistry and diffusion in a tube furnace.

Process Type	Sequential diffusion		Co-Diffusion	
	Process steps	Cost / Wafer (€ct)	Process steps	Cost / Wafer (€ct)
PECVD	5	24.0	6	27.9
Inkjet	4	19.4	4	19.4
Wet chemistry	9	21.3	7	11.9
Diffusion	3	20.3	1	5.6
Sum	21	85.0	18	64.8

Since the process sum of sequential diffusion is higher than that of co-diffusion, co-diffusion enables a decrease in process complexity (number of process steps).

Moreover, co-diffusion enables a saving in process costs of 24 %_{rel.}. Independent from the diffusion module, the PECVD processes and the inkjet processes feature a high contribution to the sum of process costs. Generally, the costs of a single process strongly depend on the process related input parameters. Thus, the omission of PECVD and inkjet processes is the first, an optimization of PECVD and Inkjet processes in order to decrease the process costs is the second, the integration of cost-efficient process techniques like atmospheric pressure chemical vapor deposition (APCVD) and laser patterning the third option to improve the sum of process costs. In this work, the first option is of major interest. In a time parallel thesis at the Fraunhofer ISE, the APCVD technique was intensively studied by P. Rothhardt et al. in order to achieve a co-diffusion process applicable to bifacial solar cells [96]. Thus, cells with a maximum efficiency of 19.6 % could be achieved on industrially sized (239 cm²) *n*-type Cz-Si wafers with a co-diffusion module joining an APCVD BSG layer for emitter and POCl₃ for BSF formation.

Apart from the advantages in effort and costs, co-diffusion is known to exhibit physical advantages as well. First, due to the low number of high temperature steps, the risk of bulk contamination and precipitation is low [97]. Second, due to the simultaneous formation of doped surfaces on both sides of the wafer, impurity gettering is very effective [98]. The main challenge of co-diffusion is to form phosphorus- and boron-doped surfaces with different electrical properties in one thermal step. This challenge is accepted in this work and investigations are discussed in the following chapter.

4 Co-diffusion processes

The findings of chapter 4 concerning co-diffusion processes were partly published in the proceedings of the 27th (2010, Frankfurt, Germany) and the 29th European Photovoltaic Solar Energy Conference and Exhibition (2014, Amsterdam, Netherlands). Even more details can be studied in the thesis of Christian Roters (B.Eng. [99]) and Nauman bin Tanvir (M.Sc. [100]) whose research was supervised by the author of this thesis.

4.1 Challenge

In this chapter, the co-diffusion process is investigated. This sophisticated process enables simultaneous boron (B) and phosphorus (P) diffusion from several dopant sources in one single heat-treatment. Co-diffusion is especially advantageous for solar cells featuring more than one highly doped surface. The *n*-type back-contact back-junction (BC-BJ) silicon solar cell features three highly doped surfaces: the front surface field (FSF, n^+ -Si), the back surface field (BSF, n^+ -Si) and the emitter (p^+ -Si). On the one hand, the high number of doped surfaces integrated in the BC-BJ solar cell leads to an increase in complexity of co-diffusion processes compared with, for example, the bifacial cell featuring only two highly doped surfaces, on the other hand, the cost-saving potential of co-diffused BC-BJ cells is higher than that of other cell structures.

In the following, the investigated co-diffusion modules utilizing different dopant sources are introduced and, subsequently, the special requirements of a BC-BJ solar cell are discussed in regard to the doping-levels of the highly doped surfaces.

Figure 4.1 depicts the cross sections of the completed BC-BJ cell (left) and the investigated setups after the co-diffusion modules (right). The FSF covers the complete front side of the solar cell. The BSF and the emitter on the rear side are locally diffused. Two co-diffusion setups are of special interest. Both setups utilize a wafer featuring a pre-patterned stack consisting of a phosphorus-doped silicate glass (PSG) and a silicon oxide (SiO_x) layer overlaid with a boron-doped silicate glass (BSG) layer on the rear side. In the first case (Figure 4.1, co-diffusion setup A), the textured front side is coated with a solid PSG/ SiO_x stack. The diffusion is carried out in a process environment including nitrogen (N_2) and oxygen (O_2). In the second case (Figure 4.1, co diffusion setup B), the front side is uncoated and the diffusion is carried out in an adapted process environment featuring POCl_3 as a gaseous P-dopant source. Due to the omission of up to two PECVD steps, i.e. the PECVD of a PSG and a SiO_x layer at the

front side, this module enables a further decrease in process costs. In this work, PSG and SiO_x layers are deposited one after the other. Notice that for industrial applications, a PSG/ SiO_x stack can also be deposited in one single PECVD process.

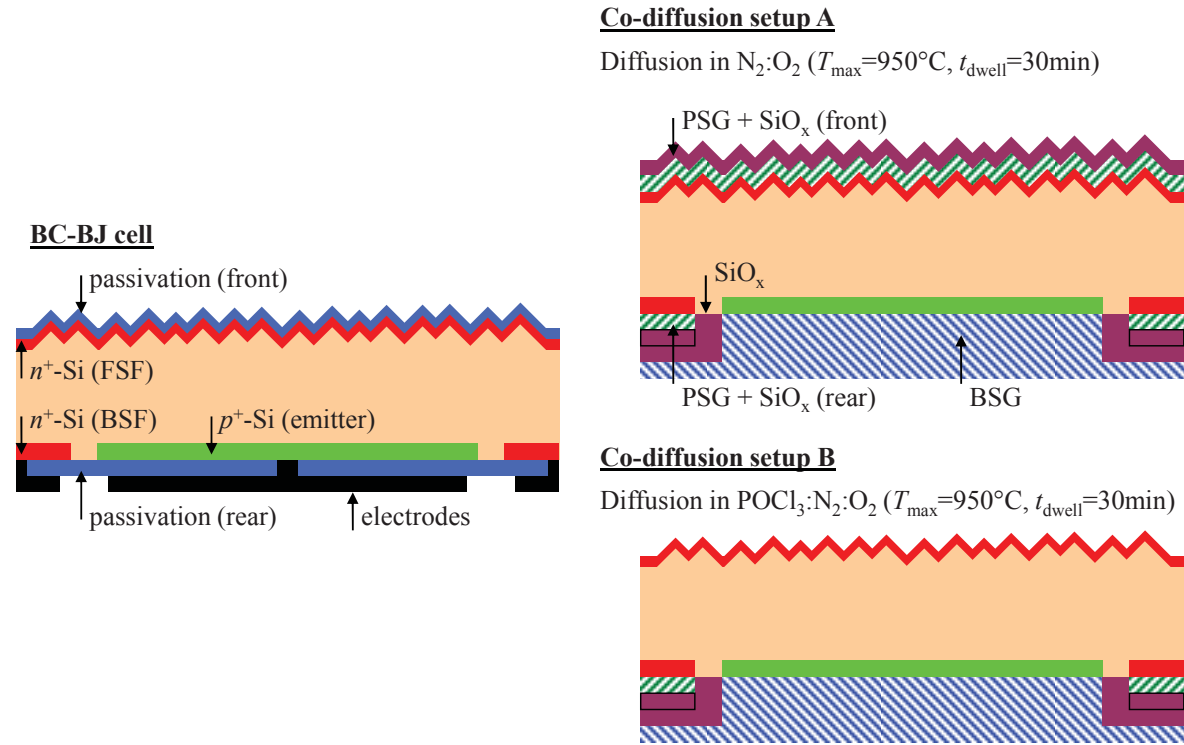


Figure 4.1 Schematic cross section of the BC-BJ solar cell (left) and the co-diffusion setups investigated in this work (right). Co-diffusion setup A utilizes a PSG/ SiO_x stack as the solid P-dopant source, whereas co-diffusion setup B uses POCl_3 as a gaseous P-dopant source for FSF formation. In both setups, a pre-patterned PSG/ SiO_x stack and an overlaying BSG layer are used as P- and B-dopant sources at the rear side.

The formation of the FSF is performed on textured surfaces. In order to achieve a trade-off between recombination and resistive losses, the FSF should feature a low doping-level allowing for an adequate passivation quality and lateral conductivity. For example, Granek et al. achieved a trade-off between recombination and resistive losses, by using an FSF with a phosphorus concentration of $4.5 \cdot 10^{19} \text{ cm}^{-3}$ and a depth of $0.38 \mu\text{m}$ [39]. Additionally, Granek et al. applied a drive-in process (dry oxidation, $T = 1050^\circ\text{C}$) in order to achieve an FSF with a phosphorus concentration of $3.8 \cdot 10^{18} \text{ cm}^{-3}$ and a depth of $1.44 \mu\text{m}$. The realization of the deep FSF is related to an increase in process costs and, consequently, not of special interest in this work. The formation of the BSF and the emitter is carried out on damage etched surfaces. In order to provide a trade-off between recombination, optical, and resistive losses, the BSF and emitter should feature doping-levels allowing for a high passivation quality, low free

carrier absorption, and low resistive electrical contacts. In the case of a low resistive aluminum-silicon contact, Schroeder et al. [101] suggest a boron concentration higher than 10^{17} cm^{-3} and a phosphorus concentration higher than 10^{19} cm^{-3} . Dopant concentrations exceeding these values should enable a contact lower than $2 \text{ m}\Omega\text{cm}^2$. The depth of the emitter should be high in order to avoid the penetration of the emitter by metal spikes. Since spiking depends on the thermal budget during and after deposition of aluminum, a value for the depth cannot be suggested. E.g. Fallisch et al. [52] determined a penetration depth of Al spikes into silicon of 450 nm as annealed with a temperature between 350 and 500°C and an annealing time of 5 minutes after PVD.

In co-diffusion, P- and B-diffusion take place simultaneously in one thermal process. The diffusion of dopants into silicon depends, as explained in section 3.4, on the dopant specific diffusivity and solubility limit. The major challenge is to find deposition processes or rather parameters for the application of dopant sources, which allow for an adjustment of the doping-level in silicon independent from the temperature during diffusion. Thus, in the following experimental part, all the diffusion processes are carried out at a given maximum temperature T_{max} of 950°C and a plateau time t_{plateau} of 30 min. Moreover, the diffusivity of dopants depends on the surface topography. Consequently, the impact of the topography on diffusion, especially in the case of BSF and FSF formation, is regarded as well.

The chapter is divided into four sections. First, the BSG deposition is investigated in order to achieve emitter adequate doping-levels. Second, the deposition of PSG/SiO_x stacks is investigated in order to achieve both BSF and FSF adequate doping-levels. Third, diffusion processes including POCl₃ are introduced and optimized in order to achieve FSF adequate doping-levels. The impact of the process environment during POCl₃ diffusion on solid dopant sources is then evaluated. Fourth, the BSG layer used as the dopant source for emitter formation is modified in order to be feasible in co-diffusion processes featuring POCl₃.

4.2 Formation of boron-doped surfaces from BSG layers

4.2.1 Sample preparation and characterization

A BSG layer is used as a solid dopant source for the formation of B-doped silicon surfaces. The deposition of BSG layers is performed with two different plasma enhanced chemical vapor deposition (PECVD) setups. The main difference between these setups is the way of plasma excitation. The first setup uses two opposite microwave generators. The microwaves are generated pulse-wise and coupled into the

process chamber by means of a linear antenna in order to electromagnetically provide the energy required to activate the plasma. In the following, this setup is called the MW-setup (MW, micro waves). The second setup uses two electrodes arranged like a plate capacitor. These electrodes are connected to an alternating voltage with a radio frequency of 13.56 MHz. The energy for plasma excitation is provided electrically. In the following this setup is called the EP-setup (EP, electrical power).

The samples used for the characterization of B-doped surfaces were processed in a symmetrical manner according to the flow chart illustrated in Figure 4.2. In the case of BSG-deposition with the MW-setup, FZ-Si wafers with a *p*-type base doping were utilized. These wafers featured a base resistivity of 0.5 Ωcm . In the case of BSG deposition with the EP-setup, the wafers featured a base resistivity of 10 Ωcm . To ensure surface conditions that occur in BC-BJ cells, all the wafers were saw-damage etched in diluted KOH ($c_{\text{KOH}} = 30\%$). After saw-damage removal, wafers to be processed in the MW-setup were laser diced into smaller samples with an area of $5 \times 5 \text{ cm}^2$ in order to provide a higher sample quantity. Before BSG deposition, all the samples were cleaned in an HNF-cleaning procedure.

During PECVD with the MW-setup, two major variations were performed. The first variation allows for evaluating the impact of the diborane gas flow $Q_{\text{B}_2\text{H}_6:\text{H}_2}$ on the boron doping-level in silicon after diffusion. Therefore, the $Q_{\text{B}_2\text{H}_6:\text{H}_2}$ was varied with 200, 300, 400, and 500 sccm. The thickness of the layers, adjusted by the carrier velocity v_{C} , was kept constant. The second variation enables a characterization of the boron doping-level dependence on the BSG layer thickness. Thus, the v_{C} was varied with 6, 9 18, and 36 cm/min. The $Q_{\text{B}_2\text{H}_6:\text{H}_2}$ was kept constant.

In the case of BSG deposition with the EP-setup, the impact of the silane gas flow Q_{SiH_4} on the boron doping-level in silicon was determined. For this, the Q_{SiH_4} was varied with 25, 50, 75, and 100sccm. By adjusting the deposition time during diffusion, the thickness of the layers h_{BSG} was kept constant.

According to the above mentioned variations, all the samples were coated with a BSG layer on both sides. Before the diffusion step was carried out, the samples were measured inductively to determine the base sheet resistance of the wafer. Detailed information concerning the inductive sheet resistance measurement can be found in e.g. [102]. Moreover, the layer thickness was determined by laser ellipsometry [103]. Subsequently, the diffusion was carried out in a quartz tube furnace. The temperature profile featured one temperature plateau with a maximum temperature T_{max} of 950°C and a plateau time t_{plateau} of 30 minutes. The diffusion environment of the tube included nitrogen and oxygen but only with very small concentrations. After diffusion, all the samples were measured inductively again.

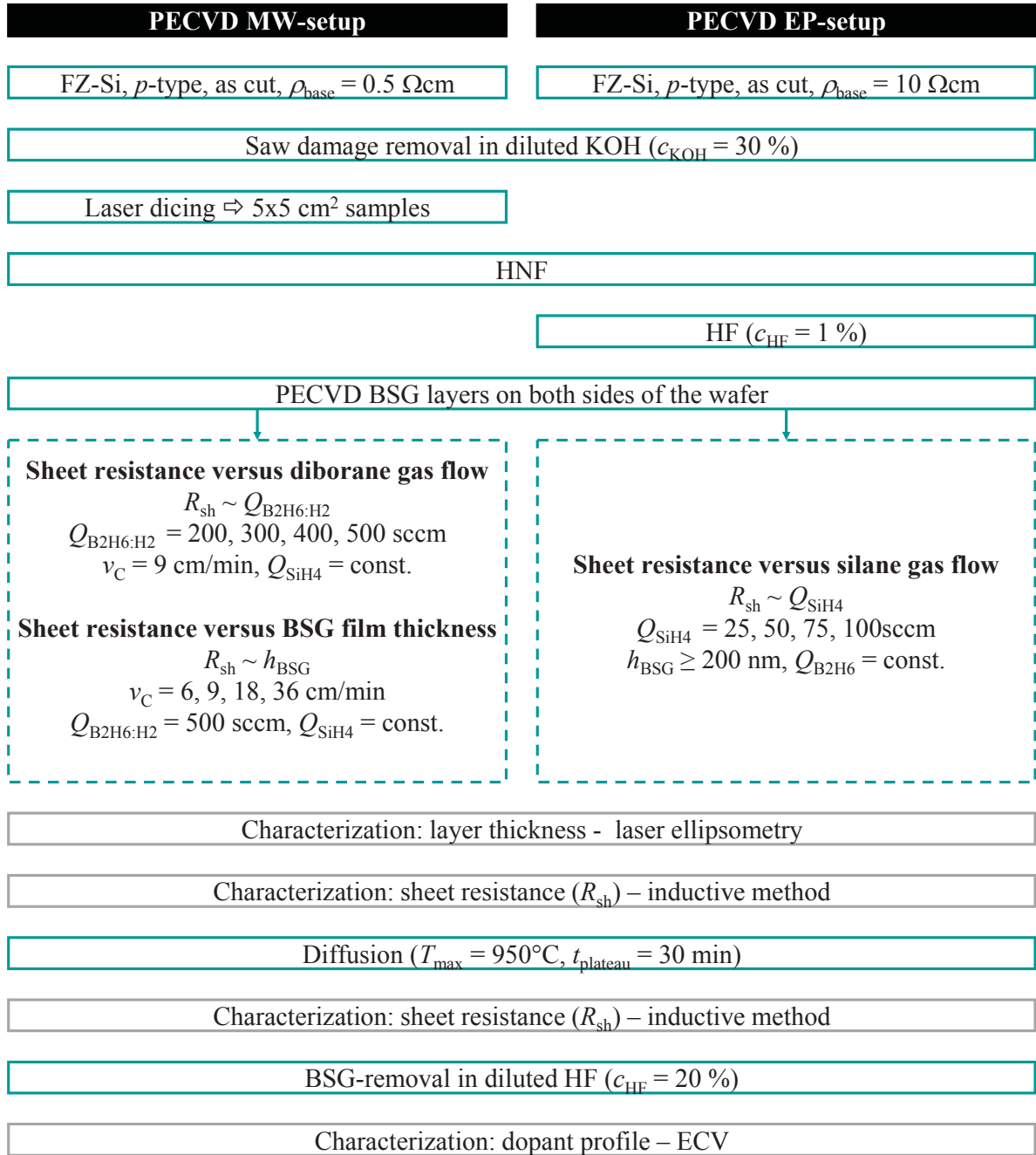


Figure 4.2 Flow chart depicting the process sequences for the preparation of symmetrical $p^+/p/p^+$ -samples. The samples are primarily used for the characterization of the highly doped surfaces. BSG deposition is performed with two different PECVD setups.

With the priory determined sheet resistance of the base $R_{\text{sh,B}}$ and the total sheet resistance $R_{\text{sh,T}}$ after diffusion, the emitter sheet resistance $R_{\text{sh,p}^+}$ was calculated with the following equation.

$$R_{\text{sh,p+}} = 2 \cdot \frac{R_{\text{sh,B}} \cdot R_{\text{sh,T}}}{R_{\text{sh,B}} - R_{\text{sh,T}}} \quad (4-1)$$

Notice that the equation is valid for symmetrically diffused samples featuring highly doped surfaces on both sides of the wafer. Due to the application of FZ-Si wafers instead of Cz-Si wafers, the impact of thermal donors on the specific base resistivity and the bulk sheet resistance, respectively, has not to be considered. With the knowledge of the emitter sheet resistance, the boron doping-level of the highly doped surfaces is quantified.

After diffusion, the BSG layers were removed in diluted hydrofluoric (HF) acid with a concentration of $c_{\text{HF}} = 20\%$. Finally, the dopant concentration profiles of the highly doped surfaces were characterized with an electrochemical capacitance-voltage (ECV) profiler. The measurement uses the dependence of the charge carrier concentration on the electrical properties of the electrochemically generated space charge region at the interface electrolyte-silicon. Detailed information concerning ECV can be derived from [104].

4.2.2 Results and discussion

Figure 4.3 shows the dependence of the sheet resistance $R_{\text{sh,p+}}$ on the diborane gas flow $Q_{\text{B}_2\text{H}_6:\text{H}_2}$ used during PECVD (constant silane gas flow Q_{SiH_4} and carrier velocity v_{C}). Symbols and error bars are the mean value and the standard deviation of measurement data obtained on single wafer samples. The measurement was performed with the inductive method by scanning the wafer along three lines, so called line scans, with five data points per line. As a consequence, error bars describe the homogeneity of B-doping upon single wafer samples. Wafer samples were processed on three different PECVD carrier positions (star, circle, square). For a better comparison of the measurement data in dependence of the carrier position at a constant $Q_{\text{B}_2\text{H}_6:\text{H}_2}$, the data is slightly shifted to each other.

The $R_{\text{sh,p+}}$ decreases with increasing $Q_{\text{B}_2\text{H}_6:\text{H}_2}$. This means that the boron doping-level in silicon increases with increasing $Q_{\text{B}_2\text{H}_6:\text{H}_2}$. It is assumed that the incorporation rate of boron into the growing layer increases with increasing $Q_{\text{B}_2\text{H}_6:\text{H}_2}$. The related increase in the B-concentration of the BSG layer with increasing $Q_{\text{B}_2\text{H}_6:\text{H}_2}$ enables an enhanced diffusion current density from the BSG layer into silicon and, therefore, a decrease in $R_{\text{sh,p+}}$. The active solubility limit and the diffusion length of boron in silicon is limited by the thermal conditions during diffusion. This is the reason why the $R_{\text{sh,p+}}$ saturates for a $Q_{\text{B}_2\text{H}_6:\text{H}_2}$ exceeding 500 sccm.

The homogeneity of B-doping improves with increasing $Q_{B_2H_6:H_2}$. This correlation is assumed to be related to the increase in B-concentration in the BSG layer as well. Samples deposited on carrier positions indicated with a star systematically show a higher $R_{sh,p+}$ than those deposited on other carrier positions. This correlation is caused by a technical property of the machine. Unfortunately, the MW-source and the gas outlet valve are in opposite positions but shifted towards each other. First the carrier passes the MW-source (carrier below) and afterwards the carrier passes the gas outlet valve (carrier on top). Only after having passed the gas outlet valve are stable deposition conditions achievable. The spatial dependence of the $R_{sh,p+}$ could be minimized by arranging the MW-source and the gas outlet valve in opposite positions without spatial shift.

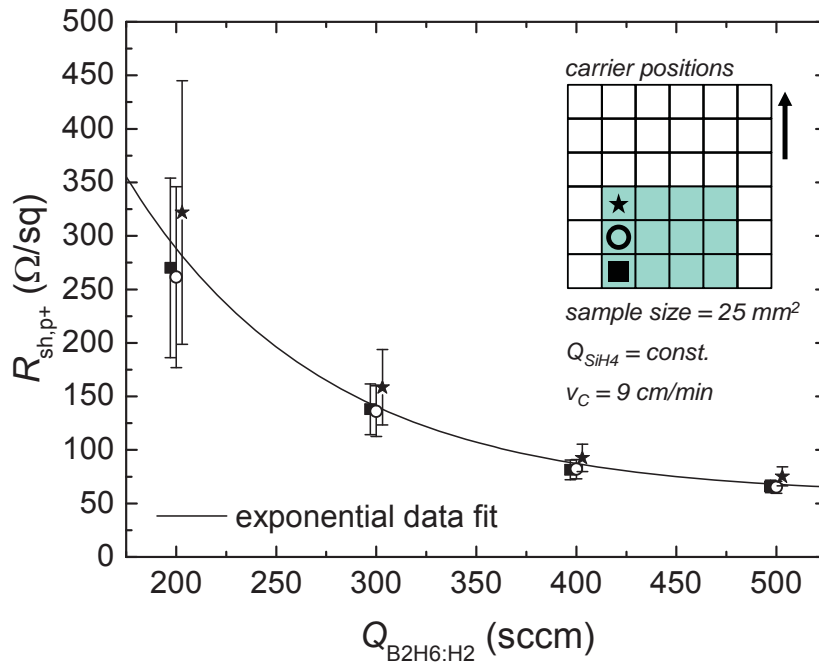


Figure 4.3 Inductively measured sheet resistance $R_{sh,p+}$ of boron-doped surfaces in dependence of the diborane gas flow $Q_{B_2H_6:H_2}$ during BSG deposition for three different carrier positions (MW-setup). Symbols and error bars correspond to the mean value and deviation of the measurement data (15 measurement points) obtained on single wafer samples.

Figure 4.4 depicts the hole concentration p in the diffused samples in dependence of the wafer depth z near the silicon surface for the varied diborane gas flows $Q_{B_2H_6:H_2}$ during PECVD. By assuming that all boron atoms act as active dopants and the diffused B-dopants exceed the base doping by several orders of magnitude, the measured hole concentration equals the B-concentration of the highly doped surface.

The hole concentration profiles correspond to the typical boron shape (compare e.g. [105]). With increasing $Q_{\text{B}_2\text{H}_6:\text{H}_2}$, the area under the p - z curve increases and therefore the $R_{\text{sh},p+}$ decreases. This correlation is induced by an increase in B-concentration and in profile depth. For all the profiles, a boron depletion is detectable near the silicon surface ($z = 0\mu\text{m}$). This depletion zone usually occurs until a depth of 30 nm and is assumed to be an artifact of the ECV measurement. Notice that during ECV the surface gets etched and characterized in cycles. During the first cycles, ECV signals might be influenced by defects at the initial silicon surface, distorting the measurement signal.

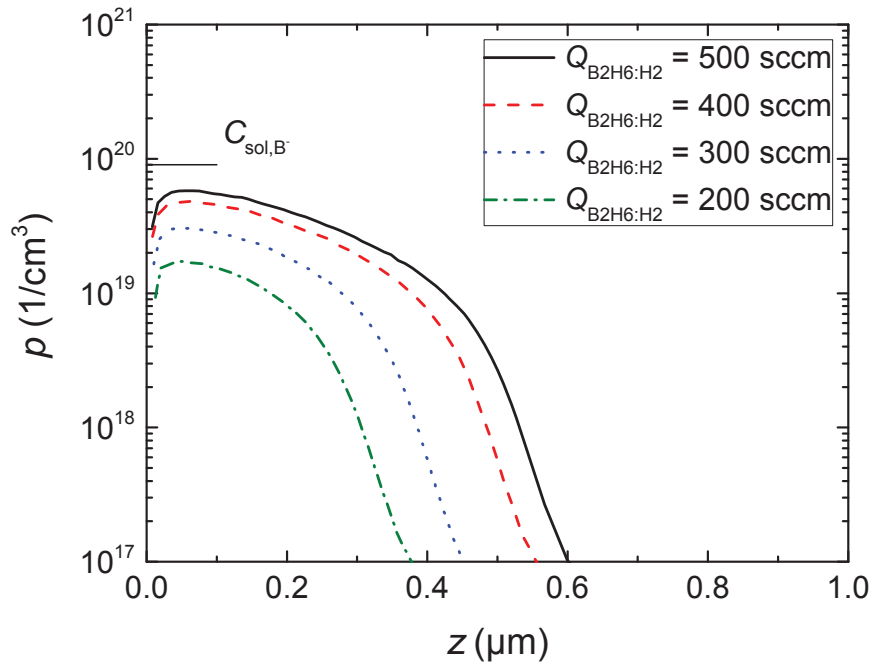


Figure 4.4 Concentration of holes p versus wafer depth z for four different diborane gas flows $Q_{\text{B}_2\text{H}_6:\text{H}_2}$ during BSG deposition (MW-setup). The measurement of the concentration profiles was carried out with ECV.

The layer thickness h_{BSG} versus deposition time t_{dep} (left) and the sheet resistance $R_{\text{sh},p+}$ as a function of h_{BSG} (right) are depicted in Figure 4.5. Notice that the gas flows were kept constant during the single deposition processes. The $Q_{\text{B}_2\text{H}_6:\text{H}_2}$ was set to 500 sccm. The thickness is expressed by the mean value and the standard deviation of a five point measurement upon one BSG coated wafer sample (circle). The measurement was performed with an ellipsometer before the diffusion process. The sheet resistance is expressed as already described above (compare Figure 4.3). The error bars describe the homogeneity of B-doping upon single wafer samples.

The graph on the right hand side can be interpreted in two regimes. The first regime describes the h_{BSG} dependence of $R_{\text{sh},p+}$ in the range of 0 to 175 nm. In this range, the

$R_{sh,p+}$ decreases with increasing h_{BSG} . The B-content of the BSG layer is not sufficient for the layer to act as an infinite dopant source. The second regime describes the h_{BSG} dependence of $R_{sh,p+}$ in the range of 175 to 350 nm. In this range, the $R_{sh,p+}$ is nearly independent from h_{BSG} . Hence, a BSG layer featuring an h_{BSG} in this range acts as an infinite dopant source.

At this point it is important to mention that the critical thickness of a BSG layer to act as either a finite or an infinite dopant source depends on several parameters such as B-concentration in the BSG layer, diffusion temperature, and diffusion time, for example. The homogeneity of B-doping increases with increasing h_{BSG} and is expected to be related to the high B-content of layers featuring a high thickness, as well.

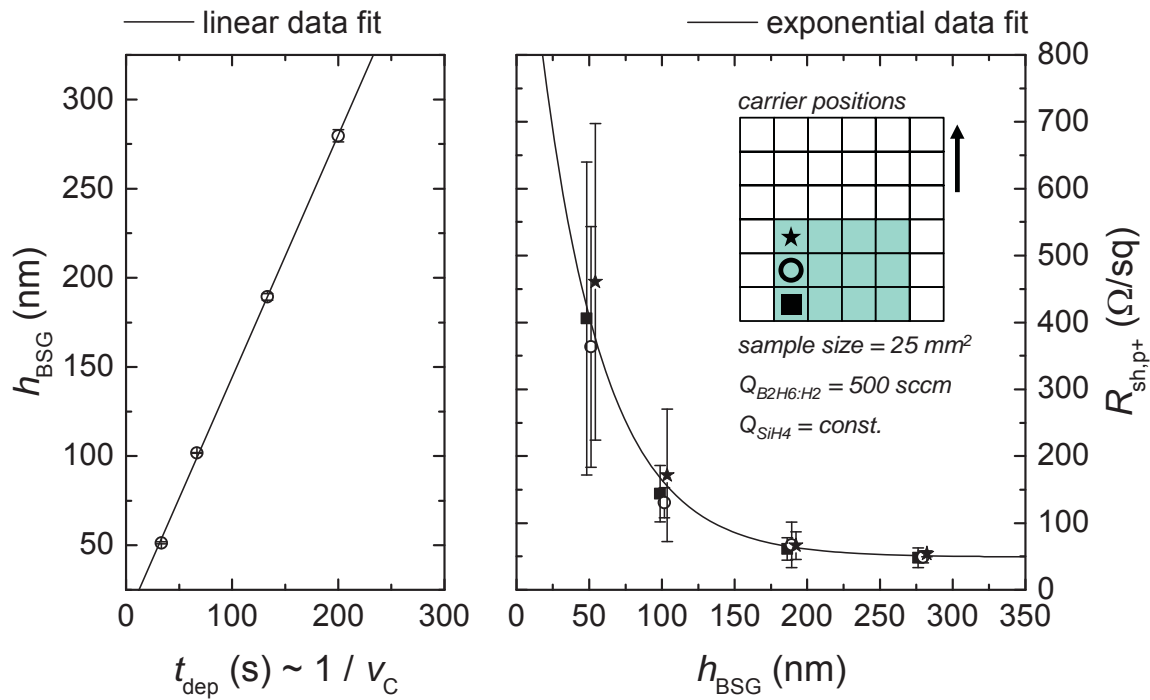


Figure 4.5 BSG film thickness h_{BSG} versus deposition time t_{dep} during PECVD (left) and sheet resistance $R_{sh,p+}$ of boron-doped surfaces diffused from a BSG layer in dependence of the BSG layer thickness (right). The layers were deposited with the MW-setup. Depicted are the mean value (symbol) and the standard deviation (error bar) of measurement points obtained on single wafer samples. The thickness was measured with an ellipsometer (five measurement points per wafer). The sheet resistance was measured according to the inductive method (fifteen measurement points per wafer).

Figure 4.6 depicts the hole concentration p of the diffused samples in dependence of the wafer depth z near the silicon surface for different BSG layer thicknesses h_{BSG} . It is clearly visible that the B-concentration at the silicon surface $p(z = 0 \mu m)$ increases with increasing h_{BSG} . The profile depth saturates if the BSG layer exceeds an h_{BSG} between

102 and 189 nm. The BSG layer with an h_{BSG} of 280 nm indicates a maximum B-concentration of $9 \cdot 10^{19} \text{ cm}^{-3}$, which equals the active solubility limit of boron in silicon at a temperature of 950°C .

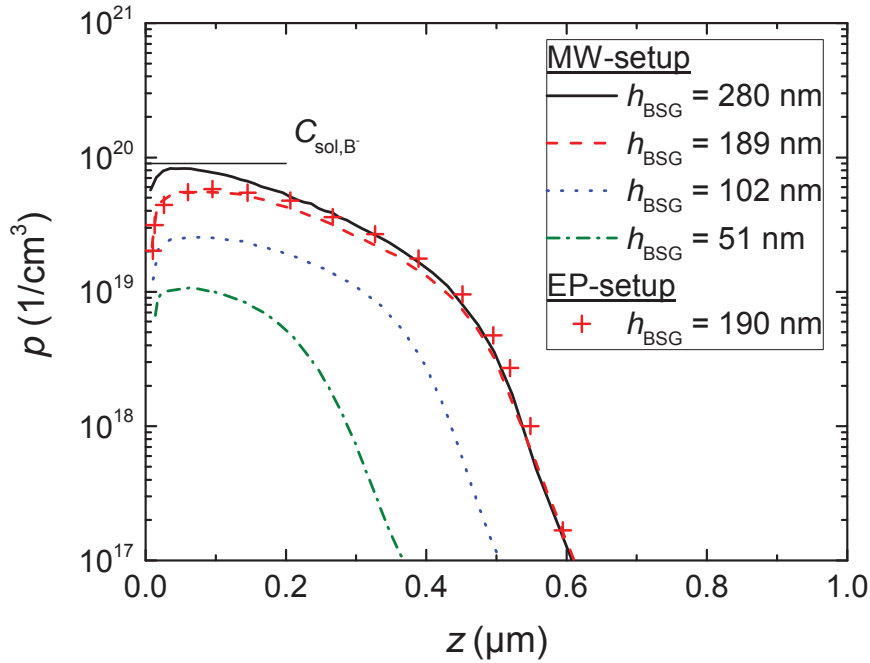


Figure 4.6 Concentration of holes p versus wafer depth z for four BSG layer thicknesses h_{BSG} . The hole concentration profile of a boron-doped surface diffused from a BSG layer deposited with the EP-setup is depicted as well. The measurement of the concentration profiles was carried out with ECV.

In the following, the results obtained by B-diffusion from BSG layers deposited with the EP-setup are presented. The impact of the silane gas flow Q_{SiH_4} on the deposition rate r_{dep} and on the sheet resistance $R_{\text{sh,p}+}$ for a constant diborane gas flow $Q_{\text{B}_2\text{H}_6:\text{H}_2}$ is depicted in Figure 4.7. The deposition rate was determined by calculating the ratio of the layer thickness and the deposition time. The thickness of the layer upon one wafer sample was measured by performing a five point measurement with an ellipsometer. As usual, the sheet resistance is expressed by the mean and the standard deviation of measurement points (inductive method) obtained upon single wafers. Due to the increase in sample area (25 to 156 mm^2), the number of measurement points per line scan was increased from five up to 15 measurement points per line scan. The error bar describes the homogeneity of B-doping upon one wafer.

The $R_{\text{sh,p}+}$ increases exponentially with increasing Q_{SiH_4} . Due to the proportional relation between the boron incorporation rate and the $Q_{\text{B}_2\text{H}_6:\text{H}_2}$ as well as between r_{dep} and the Q_{SiH_4} , the B-concentration of the BSG-layer increases with increasing the ratio

of $Q_{B_2H_6:H_2}/Q_{SiH_4}$ and decreasing Q_{SiH_4} , respectively. By varying the deposition time during PECVD, the BSG layer thickness was always set to a thickness slightly higher than 200 nm to avoid a major impact of the layer thickness. As a consequence, the $R_{sh,p+}$ saturates for a Q_{SiH_4} lower than 50 sccm. The dopant concentration profile of the B-doped surface diffused from a BSG layer deposited with a Q_{SiH_4} of 50 sccm is included in Figure 4.6 and almost matches the one diffused from a BSG layer with an h_{BSG} of 189 nm deposited by the MW-setup.

Remarkable is the homogeneity of B-doping achieved with a Q_{SiH_4} of 50 sccm. The relative standard deviation of the sheet resistance ($\Delta R_{sh,p+}/R_{sh,p+}$) along a wafer with an area of 156 mm² is below 1 %_{rel}, which indicates an excellent homogeneity. For comparison, samples fabricated with the BSG layer of the MW-setup feature a relative standard deviation of approximately 3 %_{rel} on a wafer with an area of 25 mm².

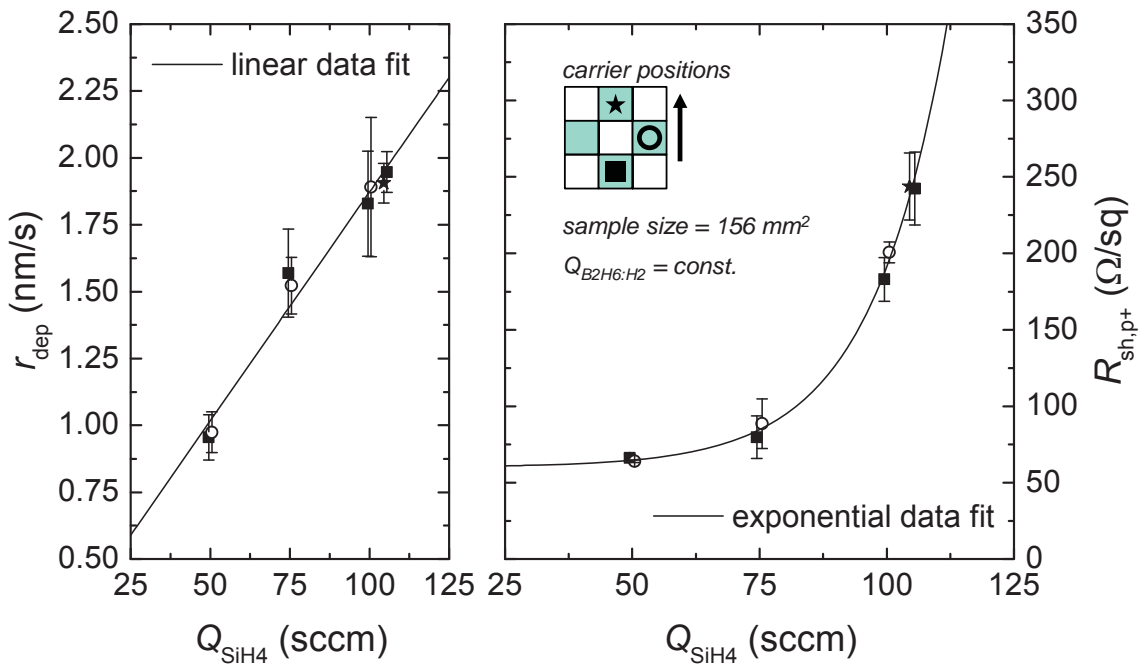


Figure 4.7 Deposition rate r_{dep} and sheet resistance $R_{sh,p+}$ of boron-doped surfaces diffused from a BSG layer in dependence of the silane gas flow Q_{SiH_4} during BSG layer deposition (EP-setup) on wafers located at three different carrier positions. Depicted are the mean value (symbol) and the standard deviation (error bar) of measurement points obtained on single wafer samples. The thickness was measured with an ellipsometer (five measurement points per wafer). The sheet resistance was measured according to the inductive method (fifteen measurement points per wafer).

In this section, several PECVD processes were successfully developed to applicate BSG layers acting as B-dopant sources for emitter formation. The $R_{sh,p+}$ is adjustable in

a wide range ($R_{sh,p+} = 50 - 450 \text{ } \Omega/\text{sq}$) by varying several PECVD process parameters such as the $Q_{B_2H_6:H_2}$ and the carrier velocity (MW-setup) as well as the Q_{SiH_4} (EP-setup). Furthermore, an adjustment of the maximum B-concentration and the profile depth is possible. The realized B-doped surfaces indicate dopant concentration profiles which are assumed to be suitable for emitter formation in terms of a BC-BJ solar cell. The next section deals with the development of PECVD processes in order to applicate PSG/SiO_x stacks acting as P-dopant sources for the formation of the BSF and the FSF.

4.3 Formation of phosphorus-doped surfaces from PSG layers

4.3.1 Sample preparation and characterization

For the formation of the BSF and the FSF, P-diffusion from stacks consisting of phosphorus-doped silicate glass (PSG) and silicon oxide (SiO_x) layers is carried out. The PSG deposition process had been investigated by Arne Fallisch et al. and was published, for instance, in [106]. By considering for the required phosphorus doping-levels in silicon (compare section 4.1), the special process conditions of the base line process and the special thermal requirements of the co-diffusion process, the PSG layer deposition process has to be adapted.

Therefore, samples for the electrical characterization of P-doped silicon surfaces were fabricated. Due to the different requirements of BSF and FSF formation, these samples were divided into BSF and FSF samples. Moreover, the BC-BJ base line process includes additional deposition and cleaning processes after deposition of the PSG/SiO_x stack. The impact of these additional processes on P-diffusion from a PSG/SiO_x stack was investigated as well and is referred to as *cell process impact*.

The flow chart in Figure 4.8 illustrates the process sequence utilized for sample preparation. All samples were processed in a symmetrical manner on FZ-Si material with a base resistivity of 1 Ohmcm. First, the samples were treated in a KOH solution to remove the saw-damage. Afterwards, FSF samples were textured in an alkaline solution. Immediately before PSG deposition, all samples were cleaned with an HNF cleaning procedure to ensure wafer surfaces without contamination and residuals. The silane gas flow Q_{SiH_4} was varied with 40, 50, and 60 sccm. In the case of BSF formation and in order to achieve a high phosphorus doping-level in silicon, PSG deposition was carried out with a silane gas flow of 30, 40, and 50 sccm. In the case of *cell process impact* samples, the PSG layers were deposited with a silane gas flow of 40 sccm. For FSF formation, PSG deposition was carried out with a silane gas flow of

40, 50, and 60 sccm. All PSG layers were deposited with a constant TMPi gasflow $Q_{\text{TMPi:Ar}}$ of 10 sccm.

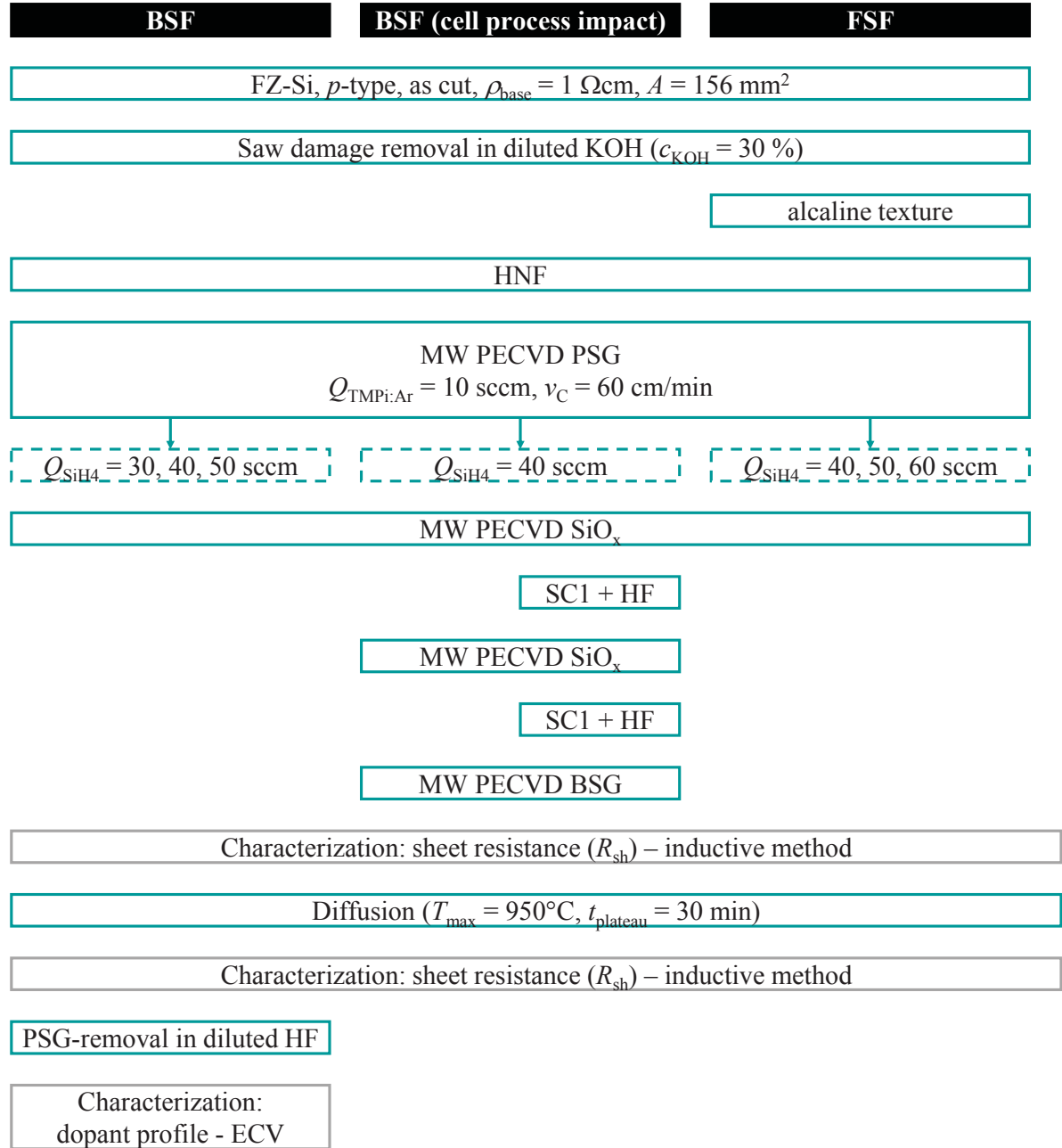


Figure 4.8 Flow chart depicting the process sequences for the preparation of symmetrical $n^+/p/n^+$ -samples. The samples are used for the characterization of the P-doped surfaces (n^+ -Si) diffused from a PSG/SiO_x stack. The samples are divided into BSF and FSF samples. Cell process impact samples consider special process conditions during processing according to the BC-BJ base line process.

After PSG deposition, the PSG layer of every sample was coated with an additional SiO_x layer with a thickness of around 200 nm to prevent interactions of the bare PSG

layer with the ambiance. *Cell process impact* samples were additionally coated with a thick SiO_x layer featuring a thickness of around 400 nm and a BSG layer featuring a thickness of around 200 nm.

In the BC-BJ base line process, the additional SiO_x layer acts as a diffusion barrier against boron. The BSG layer acts as B-dopant source for emitter formation. Thus, the sample configuration allows for a determination of layer stacking on P-diffusion from a PSG/ SiO_x stack, which is relevant for the cell as well. After the deposition of the PSG/ SiO_x stack and before the deposition of the BSG layer, some samples were cleaned with SC1 and HF. Since patterning of the PSG/ SiO_x stack and the SiO_x layer is carried out with printed organics, patterning steps are finished with the latter cleaning procedure. The cell relevant impact of this cleaning procedure on P-diffusion from a PSG/ SiO_x stack can therefore be determined.

After layer deposition, all samples were diffused in a tube furnace. The thermal budget corresponds to the one used for boron-diffusion from BSG layers. To determine the phosphorus doping-level in silicon, inductive measurements of the sheet resistance were carried out before and after diffusion in order to calculate the sheet resistance of the P-doped surface. Finally, the samples were treated in an HF bath ($c_{\text{HF}} = 20\%$) in order to remove the layers. In order to ensure a high validity of the carrier concentration profiles in silicon after diffusion, ECV measurements were only carried out on damage etched (planar) surfaces.

4.3.2 Results and discussion

The dependence of the sheet resistance $R_{\text{sh},n+}$ on the silane gas flow Q_{SiH_4} for planar (left) and textured (right) surfaces is depicted in Figure 4.9. The sheet resistance is expressed by symbols and error bars, whereby symbols correspond to the mean value and error bars to the standard deviation of the measurement data obtained on single wafer samples. The wafers were scanned along three lines featuring 15 measurement points per line scan. Thus, the error bar describes the homogeneity of P-doping on single wafers. After the experiment discussed in this section, several cell experiments were performed including similar samples and the same inductive sheet resistance analysis like discussed in this section. The mean and the standard deviation of the averaged measurement data obtained on these wafers is depicted as hollow symbols and denoted as reproducibility.

Independent from the surface topography, the $R_{\text{sh},n+}$ increases with increasing Q_{SiH_4} . This effect is comparable with the relation between the $R_{\text{sh},p+}$ and the Q_{SiH_4} of B-doped surfaces diffused from a BSG layer (compare Figure 4.7). Thus, the P-concentration in the growing PSG-layer depends on the gas flow ratio of $Q_{\text{TMPi}}/Q_{\text{SiH}_4}$. Therefore, the

P-concentration in the PSG layer decreases and the $R_{sh,n+}$ increases with increasing Q_{SiH_4} . Due to the low layer thickness ($h_{PSG} \approx 90\text{-}120$ nm) of the deposited PSG layers, all PSG layers are assumed to act as finite dopant sources. If the Q_{SiH_4} falls below a critical value, the P-concentration in the PSG layer increases to such an extent that the $R_{sh,n+}$ is independent from the Q_{SiH_4} . In this case, the PSG layer would act as an infinite dopant source. On planar surfaces, PSG layers allow for an adjustment of the $R_{sh,n+}$ between 40 and 250 Ω/sq . On textured surfaces, $R_{sh,n+}$ values between 100 and 500 Ω/sq are adjustable. Compared to planar surfaces, the diffusion from the PSG layer into silicon is slightly retarded on textured surfaces.

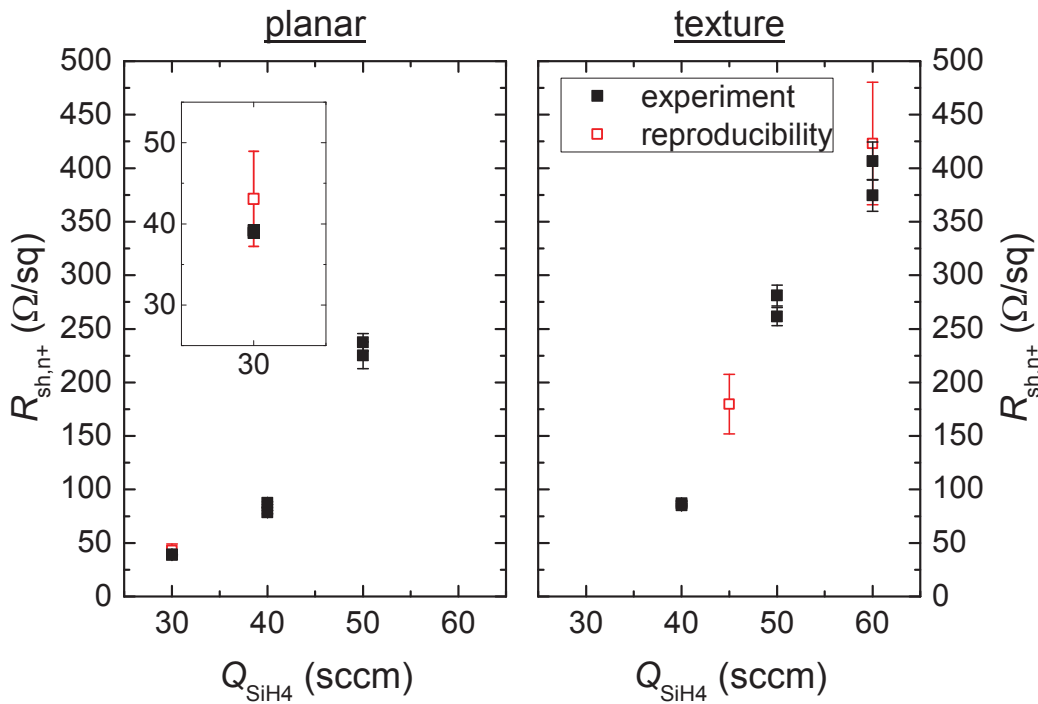


Figure 4.9 Sheet resistance $R_{sh,n+}$ of P-doped surfaces diffused from a PSG/ SiO_x stack versus silane gas flow Q_{SiH_4} during MW PECVD for planar surfaces (left) and textured surfaces (right). Solid symbols and error bars represent the mean value and the standard deviation of measurement points (inductive method, 45 measurement points) obtained on single wafers of one experiment. Hollow symbols and error bars represent the mean and standard deviation of the averaged sheet resistance data obtained by measuring similar samples prepared in succeeding cell experiments and, therefore, describe the process reproducibility.

Figure 4.10 depicts the electron concentration n in dependence of the wafer depth z for different silane gas flows Q_{SiH_4} during PECVD. Since the measured electron concentration is far below the active solubility limit of phosphorus in silicon, the electron concentration is equal to the dopant concentration. The maximum

P-concentration and the profile depth increases with decreasing Q_{SiH_4} . Thus, P-doped surfaces diffused from a PSG layer deposited with a Q_{SiH_4} of 30 sccm feature the highest P-concentration at the silicon surface ($z = 0 \mu\text{m}$) of around $1 \cdot 10^{20} \text{ cm}^{-3}$. In comparison, those diffused from a PSG layer deposited with a Q_{SiH_4} of 50 sccm feature a surface concentration of $1 \cdot 10^{19} \text{ cm}^{-3}$. Moreover, by decreasing the Q_{SiH_4} to lower values, the shape of the concentration profile approximates the typical kink and tail shape of P-doped surfaces. The dependence of the profile depth on the Q_{SiH_4} can be explained by the proportional relation between P-concentration and the P-diffusion coefficient in silicon [107]. PSG deposition with a low Q_{SiH_4} enables the application of a PSG layer with a high P-concentration. These sources provide the highest P-concentration and P-diffusion coefficient, respectively, in silicon during the entire time span of diffusion. Thus, PSG deposition with a low Q_{SiH_4} allows for deep P-diffusion into silicon. A PSG layer deposited with a Q_{SiH_4} of 30 sccm provides a P-doped surface with a depth of around 800 nm. In comparison, a PSG layer deposited with a Q_{SiH_4} of 50 sccm provides a depth of around 400 nm.

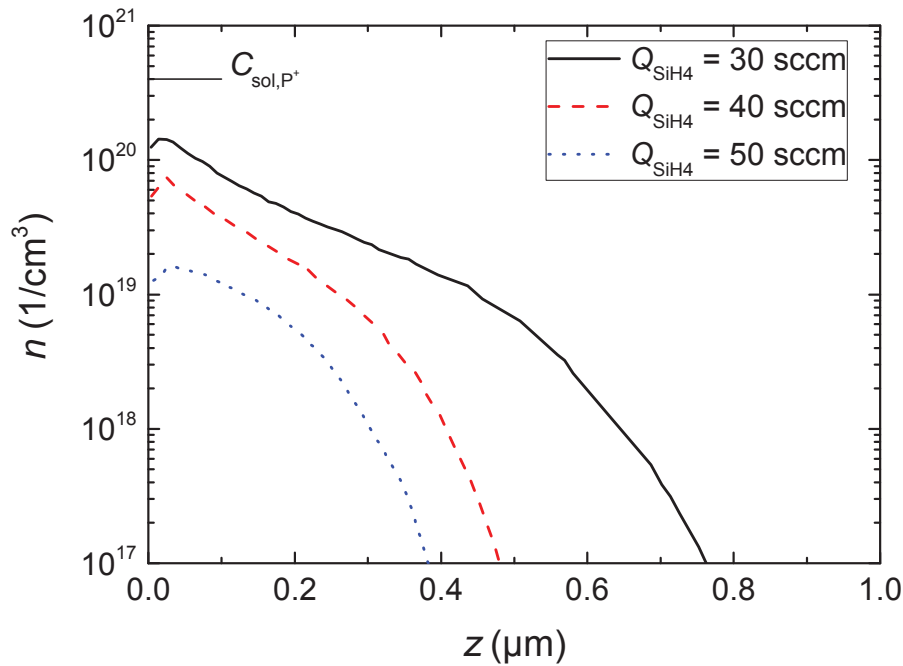
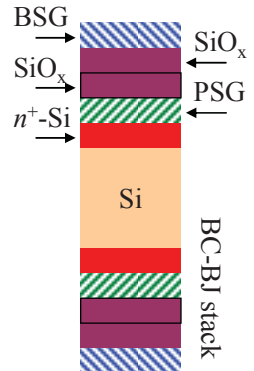
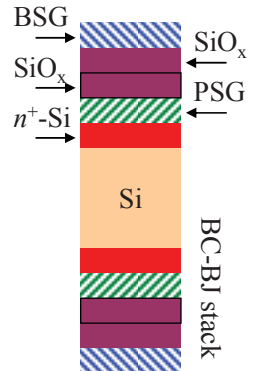


Figure 4.10 Concentration of electrons n versus wafer depth z for four silane gas flows Q_{SiH_4} during PSG deposition. The measurement of the concentration profiles was carried out with ECV.

The so-called *cell process impact* on the P-diffusion from the PSG/SiO_x stack is summarized in Table 4.1. Therefore, the mean value $R_{\text{sh},n+}$ and the standard deviation $\Delta R_{\text{sh},n+}$ of measurement data obtained upon single wafers (A and B) are depicted in

dependence of the sample type. PSG/SiO_x refers to the symmetrical sample type used for the investigations concerning the PSG deposition process. PSG/SiO_x/SiO_x/BSG refers to the stacking situation during co-diffusion of the BC-BJ solar cell. Notice again that the first SiO_x layer serves as a barrier against humidity and protects the PSG layer, whereas the second SiO_x layer is utilized as a diffusion barrier against boron diffusing from the BSG layer. PSG/SiO_x/SiO_x/BSG (clean) includes the cleaning processes which are necessary as long as patterning is performed with organic inks as etching barriers. The most important finding is that stacking and cleaning issues have almost no impact on the $R_{sh,n+}$ and, hence, P-diffusion from a PSG/SiO_x stack. The relative standard deviation for each sample is usually lower than 2 %_{rel} which indicates a homogeneous P-diffusion from the PSG/SiO_x stack.

Table 4.1 Averaged sheet resistance $R_{sh,n+}$ and standard deviation $\Delta R_{sh,n+}$ in dependence of the special process conditions of the BC-BJ solar cell. These are stacking issues and cleaning steps. Inductive sheet resistance measurements (45 measurement points per wafer) were performed on two wafers (A and B) per group. The PSG layer was deposited with a silane gas flow of 40 sccm.

Sample type		$R_{sh,n+}$ (Ω/sq)	$\Delta R_{sh,n+}$ (Ω/sq)	$\Delta R_{sh,n+}$ (% _{rel})	
PSG/SiO _x	A	87.3	1.3	1.5	
	B	78.8	1.5	1.9	
PSG/SiO _x /SiO _x /BSG	A	88.1	1.5	0.9	
	B	86.1	0.7	1.4	
PSG/SiO _x /SiO _x /BSG (clean)	A	85.8	1.3	1.5	
	B	86.1	1.7	2.0	

In this section, MW PECVD deposition processes were successfully developed in order to applicate PSG/SiO_x stacks as P-dopant sources suitable for BSF and FSF formation. Additionally, certain conditions such as the influence of stacking issues and cleaning procedures were found to have no significant impact on P-diffusion. Thus, the investigated dopant sources are suitable for integration in a BC-BJ solar cell. A PSG layer deposited with a Q_{SiH_4} of 30 sccm features a high dopant concentration and profile depth and is assumed to fulfil the requirements of a BSF. The requirements of a FSF are assumed to be fulfilled by a PSG layer deposited with a Q_{SiH_4} higher than 50 sccm.

The next section deals with the formation of P-doped surfaces diffused from POCl_3 as a gaseous dopant source. Therefore, POCl_3 is desired to act as dopant source for FSF formation.

4.4 Formation of phosphorus-doped surfaces with POCl_3

4.4.1 Sample preparation and characterization

In this section, POCl_3 diffusions are utilized in order to form FSF adequate phosphorus doping-levels in silicon.

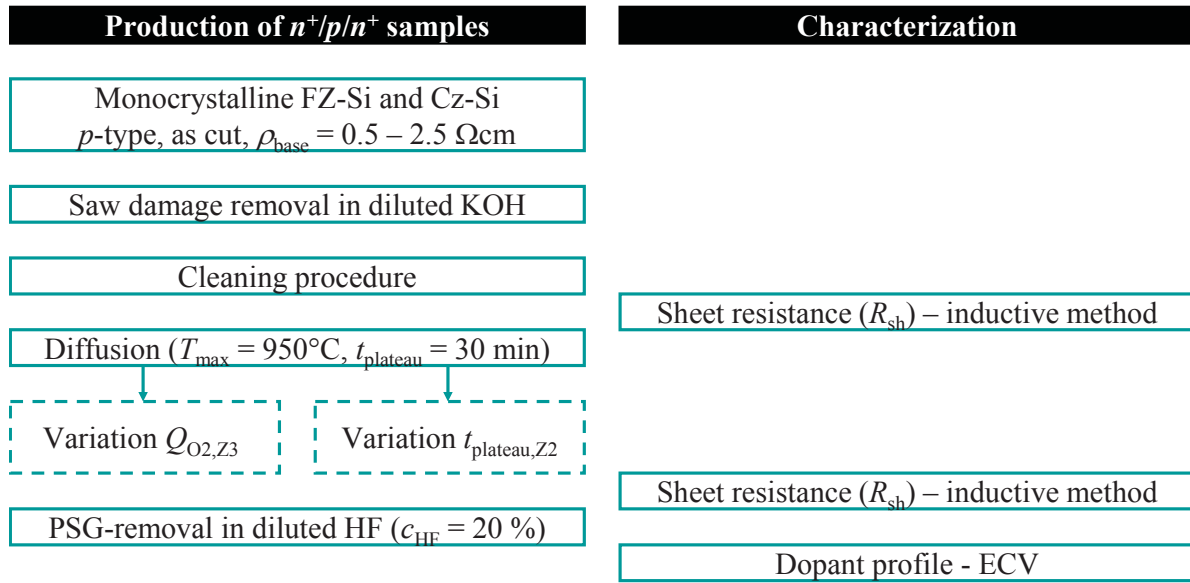


Figure 4.11: Flow chart depicting the process steps used for the production of symmetrical $n^+/p/n^+$ samples utilized for the investigation of P-diffusion from POCl_3 (left). Characterization methods used during the assembly are depicted as well (right).

For the investigations done in this section, symmetrical samples were processed according to the flow chart depicted in Figure 4.11. These samples were based on monocrystalline silicon material featuring a p -type base doping. To remove the saw-damage and to provide clean surfaces without residuals, wafers were treated in diluted KOH and in a following cleaning procedure. The finishing HF dip of the cleaning procedures was performed directly before the thermal treatment, so that interactions of a native oxide with the reactive gases would be negligible. Before and after diffusion, inductively performed sheet resistance measurements were carried out in order to determine the sheet resistance of the highly doped silicon surface. After diffusion, thermally grown PSG layers were etched back with diluted HF. P-doped

surfaces with a high relevance for BC-BJ applications were measured by ECV to obtain the P-concentration profile.

The objective is to evaluate thermal processes including POCl₃ for the diffusion of a BC-BJ adequate FSF. Hence, P-doped surfaces featuring a low surface concentration are of interest. Since the active solubility limit of phosphorus in silicon is approximately $4 \cdot 10^{20} \text{ cm}^{-3}$ at 950°C, the achievement of a low surface concentration is a main challenge. The idea followed in this work is to grow a PSG layer during a short time span and to separate it from the silicon surface before the high temperature of 950°C is reached. Thus, in the first experiments, the PSG layer was grown during the first part of the heating ramp and separated during the second part of the heating ramp by the usage of a high oxygen gas flow. Unfortunately, the realized P-doped surfaces featured relative standard deviations in sheet resistance higher than 15 %_{rel}. These high values are outside of the desired FSF specifications. The problem of non-homogeneously doped surfaces could be solved by integrating a second temperature plateau in the beginning of the temperature profile. In the following, this new temperature profile is introduced in detail.

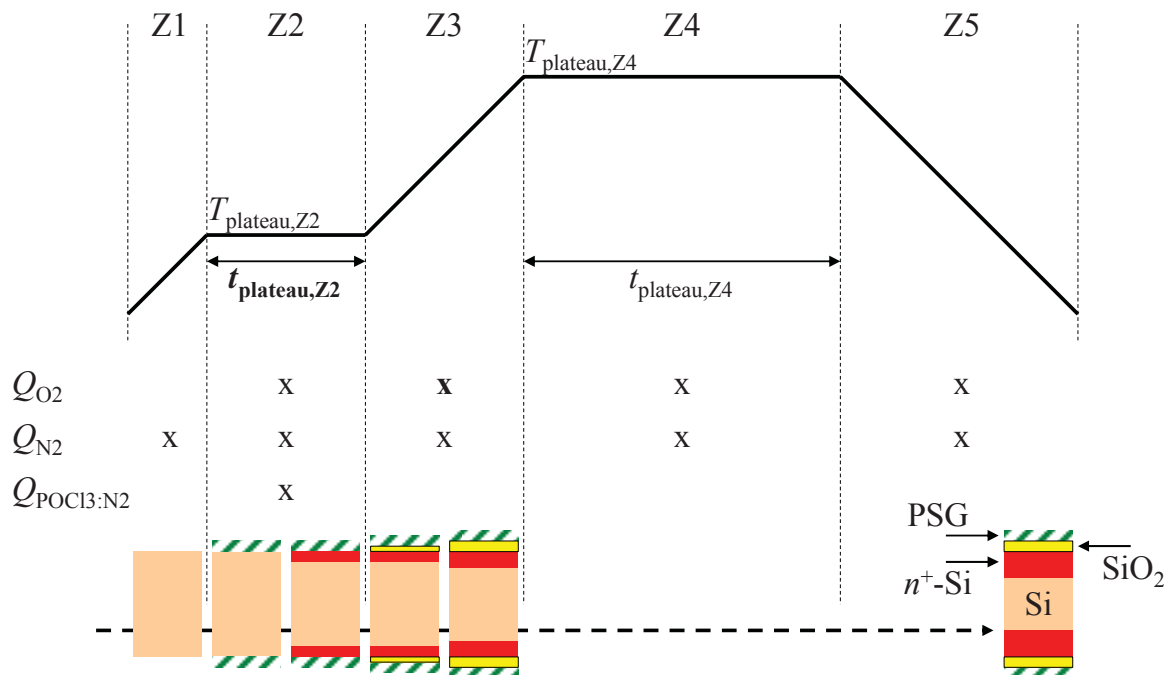


Figure 4.12 Two plateau temperature profile of thermal treatments used for the formation of P-doped surfaces from thermally grown PSG layers. The temperature profile is divided into 5 zones (Z1-5). During Z2 a PSG layer is grown. Z3 allows for a separation of the grown PSG layer by adjusting the oxygen gas flow Q_{O_2} . The high thermal budget of Z3-5 allows for a drive-in of the P-dopants.

The temperature profile of the thermal treatment used for POCl_3 diffusion is depicted in Figure 4.12. This temperature profile is divided into five temperature zones (Z1-5). Z1 is the heating ramp after which the plateau temperature $t_{\text{plateau,Z2}}$ of Z2 is reached. During the heating ramp of Z1, the process chamber gets flooded with nitrogen. The wafers still feature blank surfaces.

Z2 features a constant temperature over a time span of $t_{\text{plateau,Z2}}$. During the plateau of Z2, the reactive gases POCl_3 and oxygen O_2 are coupled into the process chamber, leading to the growth of a crystalline PSG layer. During the growth of the PSG layer in Z2, phosphorus starts to diffuse into silicon, whereby the formation of the n^+ -Si layer is induced as well. Z3 is the second heating ramp after which the temperature $t_{\text{plateau,Z4}}$ of Z4 is reached. During this heating ramp the POCl_3 valve is closed again and the process chamber is only flooded with O_2 and nitrogen N_2 . The availability of oxygen leads to a diffusion of oxygen through the PSG layer. As soon as oxygen reaches the silicon surface, a silicon dioxide (SiO_2) layer is grown between the PSG layer and the silicon surface. The silicon oxide serves as a diffusion barrier and leads to a retardation of P-diffusion from the PSG layer into silicon. In addition, P-dopants in silicon are incorporated by the growing SiO_2 layer. Z4 is the second temperature plateau featuring a plateau time of $t_{\text{plateau,Z4}}$. During this temperature zone, phosphorus is driven into the wafer which is assumed to be related to a significant decrease in dopant concentration at the silicon surface. Z5 is the cooling ramp of the temperature profile. During Z4 and Z5 the process chamber is flooded with oxygen and nitrogen. Compared to Z3, the gas flows of oxygen and nitrogen are strongly reduced.

Except for the first temperature plateau Z2 and the gas flows in Z3, the modified temperature profile corresponds to the temperature profile used for the previous investigations concerning B- and P-diffusion from BSG layers and PSG/ SiO_x stacks deposited by PECVD. Since the thermal budget of the temperature profiles are almost identical, a major impact of the modified temperature profile on P-diffusion from a PSG layer and B-diffusion from a BSG layer is assumed to be negligible.

In this work, many variations concerning the two plateau temperature profile were performed. Significant results were obtained by varying the plateau time during Z2 and the oxygen gas flow during Z3. The plateau time $t_{\text{plateau,Z2}}$ was varied with 15, 20, 25, and 30 minutes at an oxygen gas flow $Q_{\text{O}_2,\text{Z3}}$ of 2.5 slm. The oxygen gas flow $Q_{\text{O}_2,\text{Z3}}$ was varied with 0.0, 1.0, 2.5, 5.0, and 10.0 slm at a plateau time $t_{\text{plateau,Z2}}$ of 15 min. The results of these variations are discussed in the following section. In order to investigate the impact of the special diffusion atmosphere on the diffusion from solid dopant sources, some wafers featuring solid dopant sources on both sides of the wafer were treated in selected diffusion processes as well. Therefore, single BSG layers and

PSG/SiO_x stacks were used as dopant sources. The BSG layers were deposited with the MW-setup, a diborane gas flow of 500 sccm, and a thickness of around 200 nm (Compare section 4.2). The PSG layers of the PSG/SiO_x stacks were deposited with a silane gas flow of 40 sccm and a total thickness of around 300 nm (Compare section 4.3).

4.4.2 Results and discussion

Figure 4.13 depicts the dependence of the sheet resistance $R_{sh,n+}$ and the homogeneity of P-doping upon single wafers, expressed by the relative standard deviation $\Delta R_{sh,n+}$, on the oxygen gas flow $Q_{O_2,Z3}$ in time zone 3.

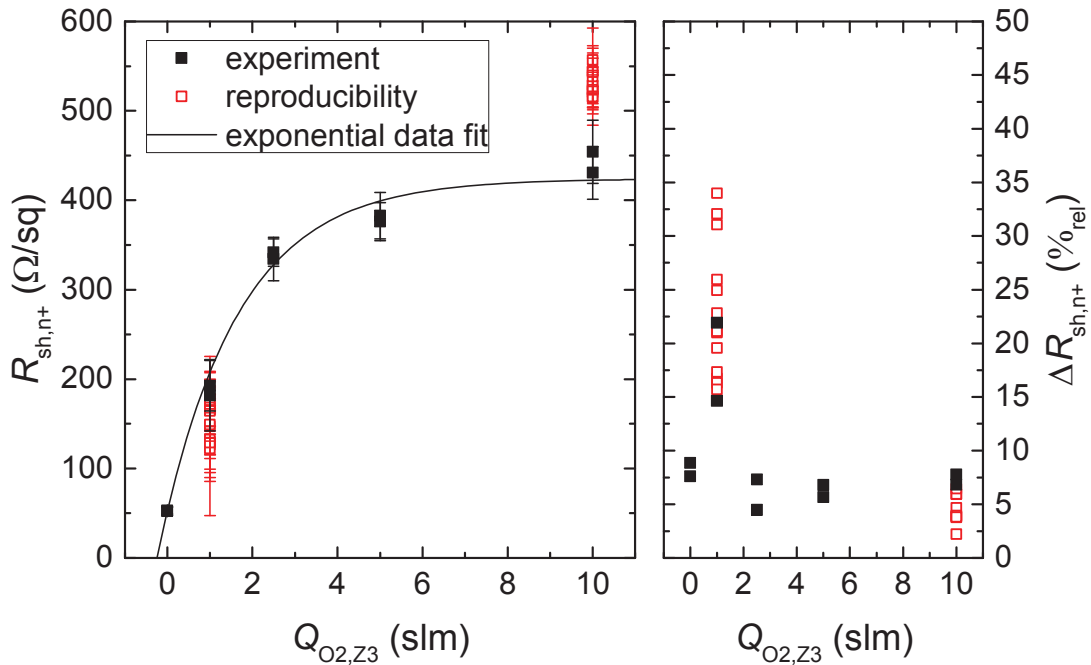


Figure 4.13 Sheet resistance $R_{sh,n+}$ (left) and relative sheet resistance deviation $\Delta R_{sh,n+}$ (right) in dependence of the oxygen gas flow $Q_{O_2,Z3}$ during ramp up. The sheet resistance is expressed by the mean value (symbol) and the standard deviation (error bar) of measurement points obtained on single wafers (45 measurement points). Reproducibility refers to similar samples which were prepared in succeeding experiments and analyzed in the same manner.

The sheet resistance is expressed by the mean value (symbol) and the standard deviation (error bar) of the measurement data obtained on single wafers. As usual, wafers were scanned along three lines featuring 15 measurement points per line scan. Solid symbols are based on measurement data obtained in one experiment. Hollow

symbols are based on measurement data obtained on wafers processed in succeeding experiments and, hence, describe the reproducibility of the experiment.

The $R_{sh,n+}$ increases with increasing Q_{O_2,Z_3} . This correlation is very prominent in the Q_{O_2,Z_3} range from 0 to 2 slm. For values exceeding 2 slm, the $R_{sh,n+}$ is less dependent on the Q_{O_2,Z_3} . Moreover, the relatively high $\Delta R_{sh,n+}$ at a Q_{O_2,Z_3} of 1 slm is remarkable. Except for samples diffused with the latter Q_{O_2,Z_3} of 1 slm, the $\Delta R_{sh,n+}$ is approximately 6 %_{rel.} In comparison, samples diffused with a Q_{O_2,Z_3} of 1 slm feature a $\Delta R_{sh,n+}$ of 15 and 22 %_{rel.} This effect could also be verified in succeeding experiments and is, consequently, significant.

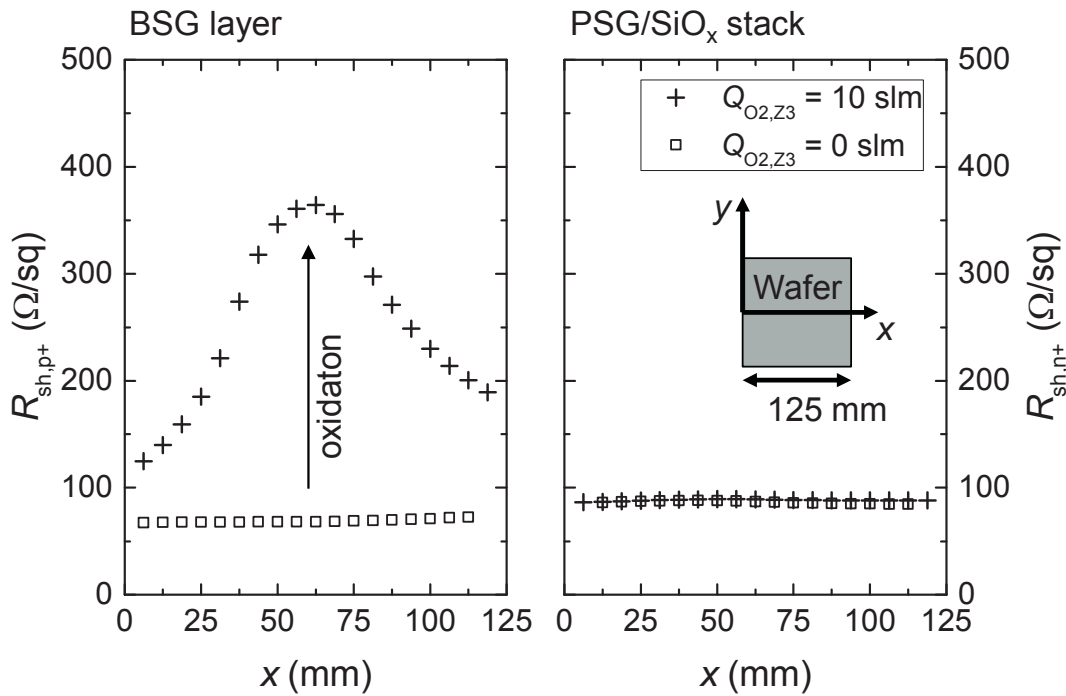


Figure 4.14 Sheet resistance $R_{sh,p+}$ line scan across a wafer featuring B-doped surfaces diffused from a BSG layer (left) and a wafer featuring P-doped surfaces diffused from a PSG/SiO_x stack (right). The diffusion was performed with a low ($Q_{O_2,Z_3} = 0$ slm) and a high oxygen gas flow ($Q_{O_2,Z_3} = 10$ slm) during the heating phase.

The explanation for this effect is the growth of a SiO₂ layer between the PSG layer and the silicon surface, which acts as a diffusion barrier against phosphorus. The growth of a SiO₂ layer between the grown PSG layer and the silicon surface can be simulated according to the oxidation model of Deal-Grove [108]. A high Q_{O_2,Z_3} induces a high oxygen concentration in the process chamber, an enhanced diffusion of oxygen through the grown PSG layer, and a faster separation of the PSG layer from the silicon surface. Thus, the amount of phosphorus diffused into silicon is also low for a high

$Q_{O_2,Z3}$, which leads to a high $R_{sh,n+}$. Samples diffused with a $Q_{O_2,Z3}$ of 1 slm feature an incomplete oxidation process leading to a high $\Delta R_{sh,n+}$. To avoid a high fluctuation of the BC-BJ cell performance, the spatial distribution of the $R_{sh,n+}$ (especially FSF) needs to be as homogeneous as possible. On the other hand, solid dopant sources on the rear side of the cell used for BSF and emitter formation should not be separated from the rear side by the growth of a SiO₂ layer between solid dopant sources and silicon. The impact of a high oxygen gas flow on diffusion from solid dopant sources is discussed in the following.

Figure 4.14 depicts the sheet resistance line scan of a B-doped surface diffused from a single BSG layer (left) and that of a P-doped surface diffused from a PSG/SiO_x stack (right). The sheet resistance of B-doped surfaces is referred to as $R_{sh,p+}$, whereas the sheet resistance of P-doped surfaces is referred to as $R_{sh,n+}$. The line scans were recorded on samples diffused with a $Q_{O_2,Z3}$ of 0 and 10 slm during diffusion. Thus, the line scans allow for discussing the impact of the high $Q_{O_2,Z3}$ during POCl₃ diffusion on B- and P-diffusion from BSG layers and PSG/SiO_x stacks.

BSG coated samples treated in a diffusion process without $Q_{O_2,Z3}$ indicate an $R_{sh,p+}$ of around $69 \pm 2 \Omega/\text{sq}$. The homogeneity of B-doping upon single wafers is very high. If the diffusion is performed with a high $Q_{O_2,Z3}$, the $R_{sh,p+}$ increases drastically up to $254 \pm 76 \Omega/\text{sq}$. In this case, the homogeneity of B-doping suffers. Especially the center of the wafer reveals a strong increase in $R_{sh,p+}$. The prominent increase in $R_{sh,p+}$ is assumed to be caused by undesired interface oxidation between the BSG layer and the silicon surface. In the case of P-diffusion from the PSG/SiO_x stack, no significant dependence of the $R_{sh,n+}$ on the $Q_{O_2,Z3}$ during diffusion is detectable. The P-doped surface realized without $Q_{O_2,Z3}$ during diffusion features an $R_{sh,n+}$ of $86 \pm 1 \Omega/\text{sq}$. The one realized with $Q_{O_2,Z3}$ features an $R_{sh,n+}$ of $88 \pm 1 \Omega/\text{sq}$. It is assumed that the insensitivity of P-diffusion from PSG/SiO_x stacks to the $Q_{O_2,Z3}$ is caused by the SiO_x layer acting as a diffusion barrier against oxygen.

The most important findings of Figure 4.13 and Figure 4.14 are summarized as follows. A low $Q_{O_2,Z3}$ leads to inadequate doping-levels which are not suitable for FSF applications. A $Q_{O_2,Z3}$ of 1 slm is related to an inhomogeneous P-doping. A high $Q_{O_2,Z3}$ features a negative impact on solid dopant sources. In order to achieve a co-diffusion process combining POCl₃ and solid dopant sources, the $Q_{O_2,Z3}$ should be set as low as possible. Due to the latter findings, it is assumed that moderate $Q_{O_2,Z3}$ are suitable for co-diffusion processes. The evaluation of the sheet resistance dependence on the thermal budget during diffusion is, thus, carried out by using a $Q_{O_2,Z3}$ of 2.5 slm.

The sheet resistance of P-doped surfaces $R_{sh,n+}$ diffused from POCl₃ in dependence of the time span $t_{\text{plateau},Z2}$ during the first temperature plateau and the oxygen gas flow

$Q_{O_2,Z3}$ during the heating phase is depicted in Figure 4.15 on the left hand side. The sheet resistance is expressed by the mean and the standard deviation of measurement data obtained on single wafers (three inductive line scans featuring 15 measurements points each). Moreover, the electron concentration n versus depth z of selected samples is depicted on the right hand side.

At a constant $t_{\text{plateau},Z2}$ of 15 min, the $R_{\text{sh},n+}$ increases with increasing $Q_{O_2,Z3}$. This increase in $R_{\text{sh},n+}$ is related to a decrease in P-concentration at the silicon surface ($z = 0 \mu\text{m}$) and a decrease in profile depth. Additionally, at a constant $Q_{O_2,Z3}$ of 2.5 slm, the $R_{\text{sh},n+}$ decreases almost linearly with increasing $t_{\text{plateau},Z2}$. Due to the increase in $t_{\text{plateau},Z2}$, the P-diffusion from the growing PSG layer is prolonged and, consequently, the $R_{\text{sh},n+}$ decreases. The variation in $t_{\text{plateau},Z2}$ allows for a precise adjustment of the $R_{\text{sh},n+}$ in the range of 190 to 350 Ω/sq with a sensitivity of around 10 $\Omega/(\text{sq}\cdot\text{min})$. The $\Delta R_{\text{sh},n+}$ of the samples is usually below 5 %_{rel.} Thus, a POCl_3 diffusion featuring a $Q_{O_2,Z3}$ of 2.5 slm is assumed to provide both a high flexibility in order to achieve FSF adequate doped surfaces and a low impact on solid dopant sources.

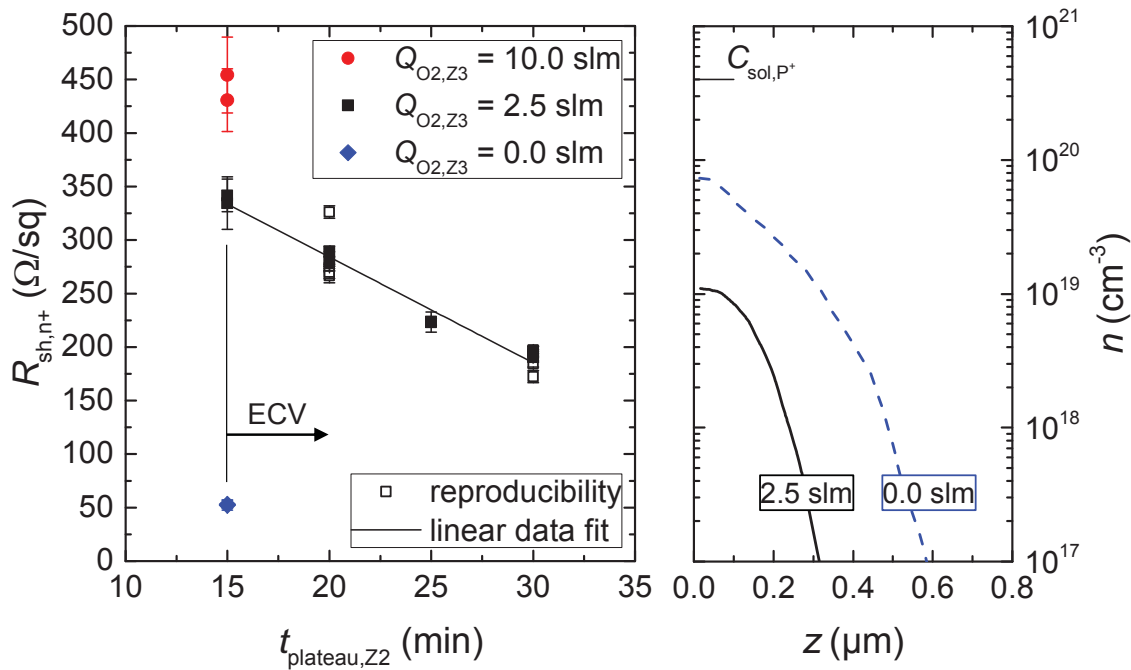


Figure 4.15 Sheet resistance $R_{\text{sh},n+}$ of P-doped surfaces diffused from a thermally grown PSG layer in dependence of the plateau time $t_{\text{plateau},Z2}$ and the oxygen gas flow $Q_{O_2,Z3}$ during the heating phase (left) and dopant concentration profiles (ECV) of selected samples (right). The constant C_{sol,P^+} depicts the active solubility limit of phosphorus in silicon at a temperature of 950°C.

To sum up, P-doped surfaces diffused from POCl₃ were successfully achieved. In order to reduce oxidation rates, the oxygen gas flow during the heating phase $Q_{O_2,Z3}$ of the developed diffusion processes was set as low as possible. In order to achieve doping-levels suitable for FSF applications, the plateau time during the first temperature plateau $t_{\text{plateau},Z2}$ was varied. Thus, P-doped surfaces with a sheet resistance $R_{\text{sh},n+}$ in the range of 190 to 350 Ω/sq were found to be adjustable. In general, the latter investigations appear to support the assumption that the $Q_{O_2,Z3}$ or rather the oxygen concentration in the diffusion ambience has a significant impact on diffusion from solid dopant sources. In order to make BSG layers suitable for co-diffusion processes featuring POCl₃, these layers need to be further modified. This modification is discussed in the following section.

4.5 Emitter formation in POCl₃ based co-diffusion processes

4.5.1 Sample preparation and characterization

In the previous chapter it became clear that the gaseous phase during co-diffusion processes has an undesired impact on B-diffusion from a BSG layer. In fact, the sheet resistance of B-doped surfaces diffused from a BSG layer increases significantly if the oxygen gas flow during diffusion increases. This increase is assumed to be manipulated by oxygen which diffuses through the BSG layer and oxidizes the interface of the BSG layer and the silicon surface. In the case of P-diffusion from a PSG layer, which was additionally covered with a SiO_x layer, this effect was found to be of minor impact. In this section, investigations concerning the performance of a BSG layer covered with an additional SiO_x layer as a diffusion barrier against oxygen are demonstrated. Therefore, the interactions of the BSG layer with the additional SiO_x layer and the corresponding impact of the SiO_x layer on B-diffusion from the BSG layer into silicon is the focus.

Compared to other thin layers such as PECVD SiN_x layer, for instance, a SiO_x layer features similar thermal properties to those of a BSG layer (B-doped SiO_x layer) [109, 110]. Thus, undesired effects such as layer flaking during diffusion caused by different thermal expansion coefficients of the single layers are less probable in the case of the BSG/SiO_x stack.

Symmetrical samples were prepared on monocrystalline *p*-type FZ-Si material according to the flow chart in Figure 4.16. After saw-damage removal and cleaning, the wafers were coated with a BSG layer on both sides of the wafer. To adjust the B-concentration in the BSG layer, a variation of the diborane gas flow $Q_{\text{B}_2\text{H}_6:\text{H}_2}$ was performed. The variation includes the maximum $Q_{\text{B}_2\text{H}_6:\text{H}_2}$ of the setup which is

consisting of a BSG and a SiO_x layer was verified in a diffusion process including POCl₃. The latter diffusion process was chosen to be the one favored for the assembly of the BC-BJ solar cell and features an oxygen gas flow of 2.5 slm during the heating phase from the first to the second temperature plateau (compare Figure 4.12).

4.5.2 Results and discussion

The thickness of the BSG/SiO stack was set to feature nearly the same thickness as the PSG/SiO stack of around 300 nm. No significant dependence of the BSG film thickness on the diborane gas flow was detectable. Figure 4.17 depicts the sheet resistance $R_{sh,p+}$ versus the diborane gas flow $Q_{B_2H_6:H_2}$ used during BSG deposition for a BSG layer and a BSG/SiO_x stack. The sheet resistance is expressed by the mean value and the standard deviation of the inductive measurement data obtained on single wafers. The measurement data was obtained by measuring the wafers along three lines with 15 measurement points per line. Thus, the error bar ($\Delta R_{sh,p+}$) describes the homogeneity of B-doping upon single wafer.

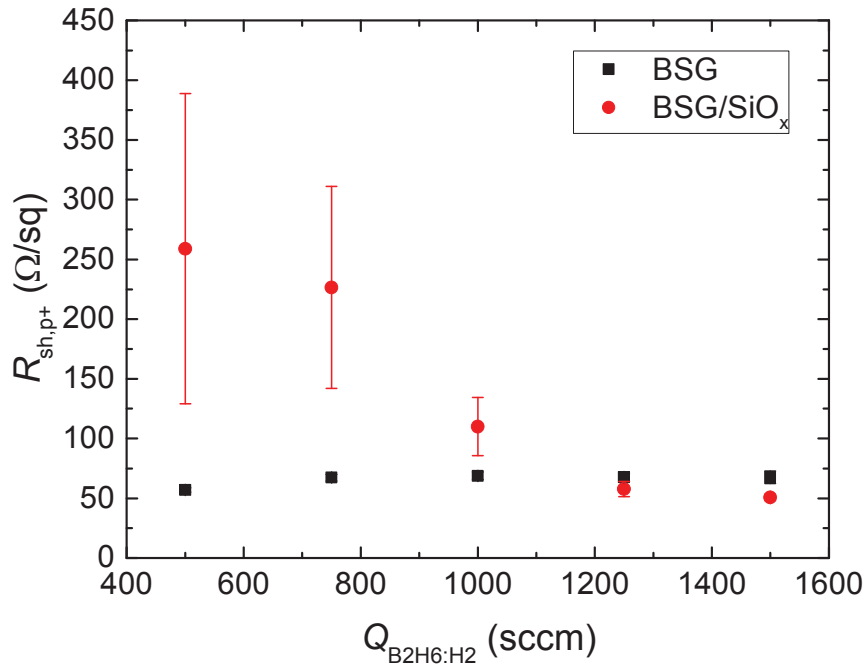


Figure 4.17 Sheet resistance $R_{sh,p+}$ in dependence of the diborane gas flow $Q_{B_2H_6:H_2}$ for B-diffusion from a BSG layer (BSG) and a stack consisting of a BSG and a SiO_x layer (BSG/SiO_x). The sheet resistance is expressed by the mean value and the standard deviation of inductively recorded measurement data (45 measurement points) upon single wafers.

In the case of B-diffusion from a BSG layer without a SiO_x capping, the $R_{\text{sh,p+}}$ is almost independent from the $Q_{\text{B2H6:H2}}$. Only a slight increase in $R_{\text{sh,p+}}$ is detectable if the $Q_{\text{B2H6:H2}}$ increases from 500 up to 750 sccm. A BSG layer deposited with a Q_{B2H6} of 500 sccm induces an $R_{\text{sh,p+}}$ of $57 \pm 1.9 \Omega/\text{sq}$. In comparison, a BSG layer deposited with a Q_{B2H6} of 750 sccm induces an $R_{\text{sh,p+}}$ of $67.3 \pm 2.7 \Omega/\text{sq}$.

Compared to a BSG layer, the $R_{\text{sh,p+}}$ dependence on the $Q_{\text{B2H6:H2}}$ of samples diffused from a BSG/ SiO_x stack differs. Here, a low $Q_{\text{B2H6:H2}}$ is related to a high $R_{\text{sh,p+}}$ and $\Delta R_{\text{sh,p+}}$. This means, B-diffusion is retarded and more inhomogeneous. For example, a stack featuring a BSG layer deposited with a $Q_{\text{B2H6:H2}}$ of 500 sccm induces a B-doped surface with an $R_{\text{sh,p+}}$ of $258.9 \pm 129.9 \Omega/\text{sq}$. With increasing Q_{B2H6} the $R_{\text{sh,p+}}$ as well as the $\Delta R_{\text{sh,p+}}$ decrease significantly. If the BSG layer is deposited with a $Q_{\text{B2H6:H2}}$ of 1250 sccm, no significant difference is detectable between B-diffusion from a single BSG layer and a BSG/ SiO_x stack. In the case of a BSG layer deposited with a $Q_{\text{B2H6:H2}}$ of 1500 sccm, the BSG/ SiO_x stack provides a B-doped surface with an $R_{\text{sh,p+}}$ slightly lower than those diffused from a single BSG layer. Thus, the BSG/ SiO_x stack provides a B-doped surface featuring an $R_{\text{sh,p+}}$ of $50.7 \pm 2.6 \Omega/\text{sq}$. In comparison, the single BSG layer provides a B-doped surface featuring an $R_{\text{sh,p+}}$ of $67.7 \pm 5.2 \Omega/\text{sq}$.

To sum up, two results seem to be significant. First, the BSG/ SiO_x stack deposited with a low $Q_{\text{B2H6:H2}}$ reveals a high $R_{\text{sh,p+}}$ and an inhomogeneous formation of the doped silicon surface. Second, the BSG/ SiO_x stack deposited with a high $Q_{\text{B2H6:H2}}$ provides a low $R_{\text{sh,p+}}$ and a homogeneous formation of the doped silicon surface. Moreover, at a $Q_{\text{B2H6:H2}}$ of 1500 sccm, stacks provide a lower $R_{\text{sh,p+}}$ than the single layers.

In the case of the BSG/ SiO_x stack, the relatively high $R_{\text{sh,p+}}$ at a low $Q_{\text{B2H6:H2}}$ is explained according to the following theory. If a BSG layer on top of the silicon surface is additionally covered with a SiO_x layer, two diffusion interfaces are available: Si-BSG and BSG- SiO_x . Moreover, due to the high segregation coefficient of boron in SiO_x , the SiO_x layer on top of the BSG layer acts as a sink for boron during diffusion [112]. Thus, B-diffusion from the BSG layer is bidirectional and the diffusion interfaces can interact with each other. The interaction is assumed to be caused by the interface specific expansion of boron depletion in the BSG layer during diffusion. In the case of interacting or rather overlapping depletion zones, an impact of the interface BSG- SiO_x on B-diffusion from BSG into silicon is expected. Due to the limited active solubility of boron in silicon at a given temperature, the expansion of B-depletion at the interface Si-BSG gets thinner by increasing the B-concentration in the BSG layer. Thus, there must be a critical B-concentration in the BSG layer where the diffusion processes at both interfaces Si-BSG and BSG- SiO_x switch from interacting to non-interacting. In the case of a BSG layer with a B-concentration lower than the

critical concentration, the depletion zones overlap, the diffusion interfaces interact, and the doping-level of boron in silicon after diffusion is affected. In the case of a BSG layer with a B-concentration higher than the critical B-concentration, depletion zones are separated from each other and B-diffusion from a BSG layer into silicon is not affected by the availability of the SiO_x layer.

To support this theory, the relation between B-concentration in the BSG layer and the $Q_{B_2H_6:H_2}$ during BSG deposition needs to be verified. Therefore, absorbance spectra in dependence of the wave number were measured by FTIR. A number of FTIR studies revealed a B-O vibration mode absorbing at a wavenumber of around 1370 1/cm, e.g. [113]. The absorbance of this vibration mode depends on the number of sensitive B-O bonds and, hence, the concentration of sensitive B-O bonds, the layer thickness, and the aperture size.

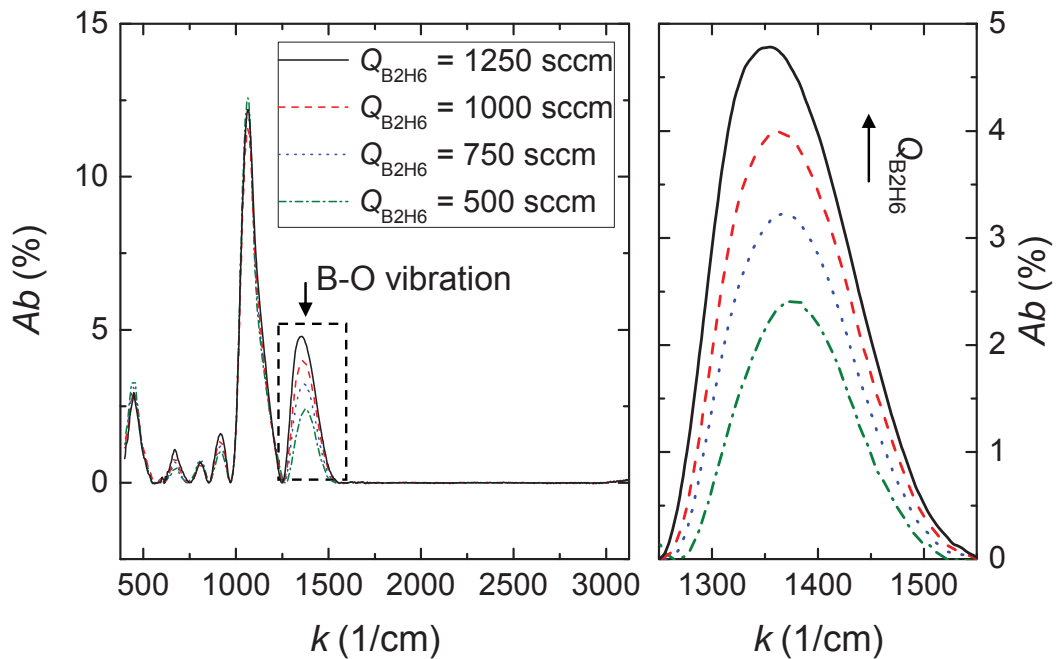


Figure 4.18 Absorbance Ab in dependence of the wave number k of BSG coated wafer samples deposited with four different diborane gas flow $Q_{B_2H_6:H_2}$. The measurements were performed by FTIR spectroscopy.

Figure 4.18 depicts the normalized FTIR measurements performed on samples integrating BSG layers deposited with a $Q_{B_2H_6}$ of 500, 750, 1000, and 1250 sccm. A normalized FTIR measurement means that the absorbance is independent from dimensions such as the layer thickness and the aperture size and therefore only dependent on the concentration of sensitive B-O bonds. The graph shows that there is a steady rise in absorbance if the $Q_{B_2H_6:H_2}$ increases. By assuming that the

B-concentration in the BSG layer has a proportional relation to the concentration of sensitive B-O bonds, the relation found indicates a positive dependence of the B-concentration in the BSG layer on the $Q_{\text{B}_2\text{H}_6:\text{H}_2}$. Thus, the statement that B-diffusion from a BSG/SiO_x stack depends upon the $Q_{\text{B}_2\text{H}_6:\text{H}_2}$ and the B-concentration in the BSG layer, respectively, is valid. A quantitative analysis of boron in the BSG layer can be performed by secondary ion mass spectroscopy (SIMS) as performed by Rothhardt et al. [114], for example. A calibration of the $Q_{\text{B}_2\text{H}_6:\text{H}_2}$ dependent absorbance measured by FTIR with the $Q_{\text{B}_2\text{H}_6:\text{H}_2}$ dependent B-concentration in BSG layers measured by SIMS, for instance, would allow for a calibration of the FTIR setup in order to utilize FTIR for the determination of the B-concentration in BSG layers.

One non-understood effect remains: if the BSG deposition is performed with a $Q_{\text{B}_2\text{H}_6:\text{H}_2}$ of 1500 sccm, B-diffusion from a stack provides a lower $R_{\text{sh,p+}}$ than B-diffusion from a single layer. One possible explanation for the effect is the high affinity of a BSG layer featuring a high B-concentration to absorb humidity from the environment. This absorption might lead to effects hindering boron to diffuse from the BSG layer into silicon. To support this assumption, a so-called water test was performed with two BSG coated silicon wafers. The first wafer featured a BSG layer deposited with a $Q_{\text{B}_2\text{H}_6:\text{H}_2}$ of 500 sccm, whereas the second wafer featured a BSG layer deposited with a high $Q_{\text{B}_2\text{H}_6:\text{H}_2}$. Before diffusion, these wafers were exposed to deionized water and afterwards dried with an air gun. Afterwards the BSG layers were optically characterized by microscopy.

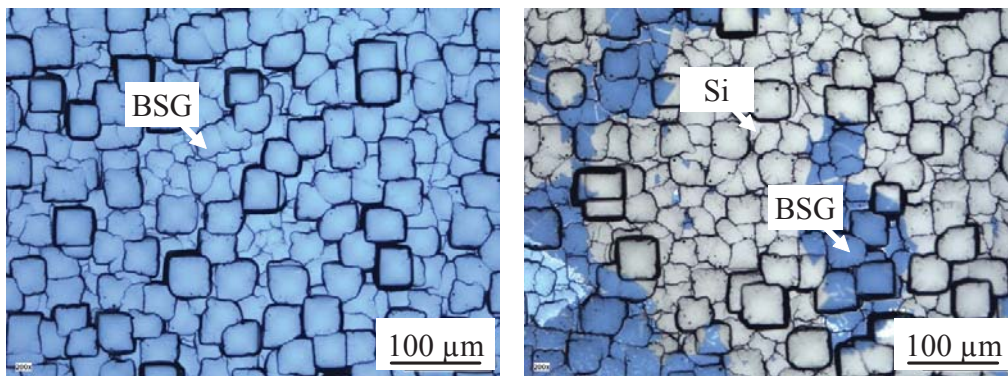


Figure 4.19 Microscopic top view of BSG layers deposited with a diborane gas flow of 500 sccm (left) and a diborane gas flow of 1250 sccm (right) after a water test. In the water-test, BSG coated wafers were exposed to water and afterwards dried by an air pistol.

Figure 4.19 shows the microscopic top view of a wafer featuring a BSG layer deposited with a low (left) and high $Q_{\text{B}_2\text{H}_6:\text{H}_2}$ (right). The images were recorded after the water test. By comparing the images, it is quite obvious that the BSG layer

deposited with a high $Q_{\text{B}_2\text{H}_6:\text{H}_2}$ is strongly affected in the water test. The layer deposited with a low $Q_{\text{B}_2\text{H}_6:\text{H}_2}$ is not affected by the water test. It is assumed that the BSG layer deposited with a high $Q_{\text{B}_2\text{H}_6:\text{H}_2}$ interacts with water. This interaction might be absorption of humidity, swelling of the layer, and, as a consequence, a decrease in layer adhesion upon the silicon surface. The latter loss in adhesion, which might occur due to absorption of humidity available in the natural environment as well, might lead to a decrease in B-diffusion from the BSG layer into silicon and, therefore, to an increase in the $R_{\text{sh,p+}}$ of the B-doped silicon surface. In the case of a BSG/SiO_x stack, it is assumed that the additional SiO_x layer serves as a protection layer preventing the absorption of humidity from the natural environment. Thus, B-diffusion from a BSG/SiO_x should not be affected. As a consequence, the BSG/SiO_x stack deposited with a $Q_{\text{B}_2\text{H}_6:\text{H}_2}$ of 1500 sccm provides a stronger B-diffusion than the single BSG layer deposited with the same $Q_{\text{B}_2\text{H}_6:\text{H}_2}$.

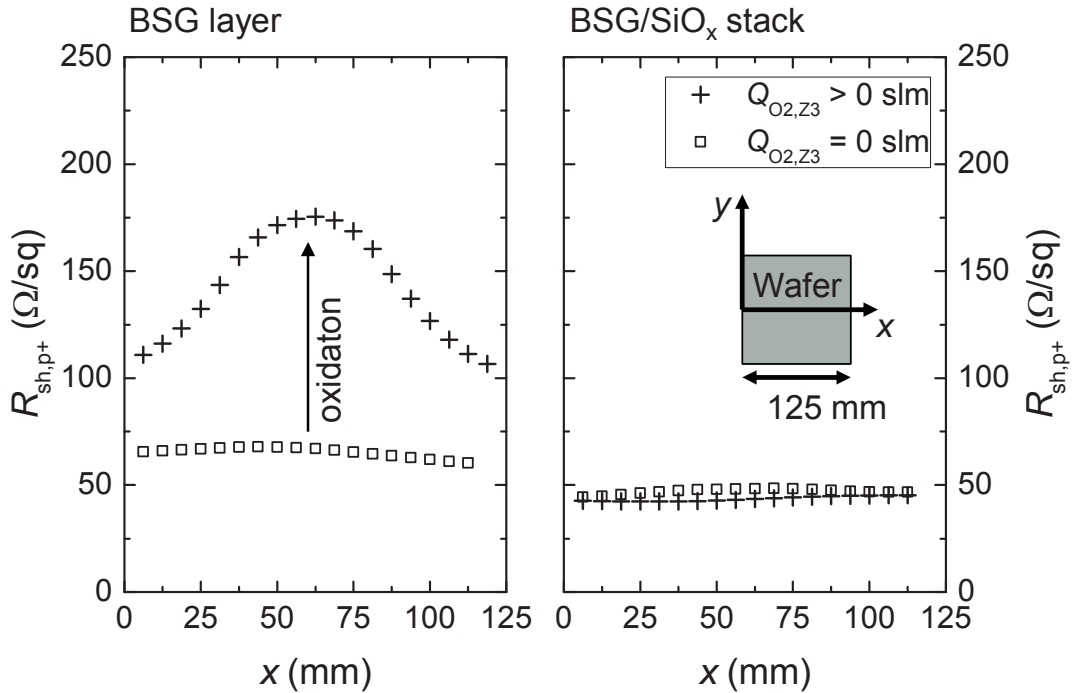


Figure 4.20 Sheet resistance line scan (R_{sh} versus x) across a wafer featuring B-doped surfaces diffused from a BSG layer (left) and a BSG/SiO_x stack (right). Both layers were deposited with a diborane gas flow of 1500 sccm. The diffusion was performed with a low ($Q_{\text{O}_2,\text{Z}_3} = 0$ slm) and a high oxygen gas flow ($Q_{\text{O}_2,\text{Z}_3} > 0$ slm) during the heating phase. The results are valid for every oxygen gas flow between 0 and 10 slm.

As a result of this important experiment, it is possible to cover the BSG layer with an additional SiO_x layer acting both as humidity protection prior to and an oxygen

diffusion barrier during the diffusion step. Therefore, the BSG layer needs to be deposited with a high $Q_{\text{B}_{2\text{H}_6:\text{H}_2}}$ to avoid a huge depletion in BSG at the interface Si-BSG.

Figure 4.20 depicts the sheet resistance line scan of a B-doped surface diffused from a single BSG layer (left) and a BSG/SiO_x stack (right) for two different oxygen gas flows during the heating ramp of the two plateau temperature profile $Q_{\text{O}_2,\text{Z3}}$.

In the case of B-diffusion from a single BSG layer, the oxygen gas flow during diffusion has a significant impact on the $R_{\text{sh,p+}}$. Without oxygen gas flow during heating, the $R_{\text{sh,p+}}$ measured upon the silicon surface is $69 \pm 2 \text{ } \Omega/\text{sq}$, whereas with an increased oxygen gas flow the $R_{\text{sh,p+}}$ is $143 \pm 24 \text{ } \Omega/\text{sq}$. As already revealed in the previous section, the increase in oxygen gas flow leads to an increase in $R_{\text{sh,p+}}$ and $\Delta R_{\text{sh,p+}}$. Hence, the utilized single BSG layers are not suitable for co-diffusion processes featuring high oxygen gas flows. In the case of B-diffusion from a BSG/SiO_x stack, the $R_{\text{sh,p+}}$ is independent from the oxygen gas flow. Without oxygen gas flow, the $R_{\text{sh,p+}}$ measured upon the B-doped surface is $47 \pm 1 \text{ } \Omega/\text{sq}$, whereas with oxygen gas flow the $R_{\text{sh,p+}}$ is $44 \pm 1 \text{ } \Omega/\text{sq}$. The difference between the $R_{\text{sh,p+}}$ values is negligible and probably induced by an effect which is independent from the oxygen gas flow. It can be concluded that a BSG/SiO_x stack is not or at least less sensitive to a high oxygen gas flow and can, hence, be used in the favored co-diffusion processes featuring POCl₃ and a high oxygen gas flow.

4.6 Chapter summary

The chapter was divided into four major sections focusing on the development of diffusion processes. Therefore, the PECVD of a BSG layer as boron-dopant source, a PSG/SiO_x stack as phosphorus-dopant source, POCl₃ as gaseous dopant source, and a modification of the BSG layer in order to be stable in POCl₃ based co-diffusion processes were analyzed. Since a co-diffusion process was the focus, all the diffusion processes were optimized with an almost constant thermal budget. This means that all the diffusion processes were developed with a constant temperature of 950°C and a plateau time of 30 minutes. Thermal processes with POCl₃ feature a second temperature plateau with a negligible thermal budget.

Within the scope of emitter formation with a BSG layer, two BSG deposition processes were considered. It was found that the deposition of a BSG layer is a flexible choice in order to adjust the boron doping-level in silicon by varying the B-concentration incorporated in the BSG layer and the layer thickness. Thus, an adjustment of the sheet resistance $R_{\text{sh,p+}}$ between 50 and 450 Ω/sq was found to be possible.

The BSF and FSF formation were enabled by using PSG/SiO_x stacks as dopant sources. Thus, the PSG deposition processes were optimized on planar and textured surfaces. The sheet resistance $R_{sh,n+}$ on planar surfaces was found to be adjustable between 40 and 250 Ω/sq , whereas the $R_{sh,n+}$ on textured surfaces was found to be adjustable between 100 and 500 Ω/sq . The latter adjustments were based on a variation of the P-concentration in the PSG layer. In order to integrate a PSG layer as dopant source for BSF formation, several boundary conditions were considered as well. An impact of layer stacking and wet chemical treatments on P-diffusion from a PSG/SiO_x stack could not be detected.

For the formation of phosphorus doped surfaces with POCl₃, a two plateau temperature profile was introduced. These POCl₃ based diffusion processes feature an increase in oxygen gas flow in order to obtain FSF adequate doping-levels. To limit the impact of the special atmosphere during diffusion on solid dopant sources, the oxygen gas flow during diffusion was kept as low as possible. Finally, an adjustment of the $R_{sh,n+}$ between 175 and 400 Ω/sq was possible by varying the plateau time during the first temperature plateau at an adequate oxygen gas flow.

In the case of POCl₃ based co-diffusion processes with an increased oxygen gas flow, the BSG layer used as the B-dopant source for emitter formation needed to be modified. This modification includes a protection of the BSG layer with an additional SiO_x layer on top and an increase in B-concentration in the BSG layer. Thus, interface oxidation between the BSG layer and the silicon surface as well as a negative impact of the SiO_x layer on B-diffusion from the BSG-layer into silicon could be avoided.

According to the knowledge gained in this chapter, two co-diffusion modules are performable. The first co-diffusion module is based on three solid dopant sources. The second co-diffusion module utilizes two solid dopant sources and a gaseous dopant source. Both co-diffusion modules fulfill the BC-BJ cell related requirements. The next step is the application of the investigated co-diffusion modules in the base line process of the favored BC-BJ solar cell. Due to the lower process risk, the first generation solar cells were processed by utilizing the co-diffusion module featuring only solid diffusion sources. The corresponding cell experiment is discussed in the next chapter along with an intensive discussion of recombination effects, among other things.

5 Co-diffused back-contact back-junction solar cells

The first cell batch, here denoted as co-diffused back-contact back-junction solar cells, enabled the production of highly efficient solar cells which were intensively characterized. The most important results are published within this chapter but were also partly published in the proceedings of the 28th European Photovoltaic Solar Energy Conference and Exhibition (Paris, France, 2013). The publication was accompanied by an oral presentation of the author of this thesis at the same conference. A refereed journal paper focusing on the findings in section 5.6 (influence of cell structure on cell performance) was published in the IEEE journal of Photovoltaics (volume 3, 2013). A sophisticated plating step, developed by Mathias Kamp et al., enabled further characterization of cell specific series resistance losses. Parts of the plating related findings in section 5.7 were published in Solar Energy Materials and Solar Cells (volume 120, 2014) as a referred journal paper and in the proceedings of the 4th international conference on Crystalline Silicon Photovoltaics (s'-Hertogenbosch, Netherlands, 2014).

5.1 Challenge

According to the introduced base line process (section Figure 3.5) and the investigated co-diffusion process featuring solid dopant sources (section 4.2 and 4.3), BC-BJ solar cells were prepared. In this preparation, several process variations were performed to improve the performance of the BC-BJ solar cell step by step. These variations include a variation of the base material, the passivation layers, the B-dopant source for emitter formation, and the cell structure (doping structure). The influence of the metal finger height on the cell performance is discussed in the last section. The chapter starts with a characterization of the base line process.

5.2 Characterization of the base line process

In this section, the characterization of critical process modules is performed. The process modules are the patterning modules (BSF definition, gap definition, contact opening, and contact separation) and the co-diffusion module. Since the resolution and the accuracy of the utilized patterning technology is of utmost importance, all the accomplished patterning modules are characterized by light microscopy. Notice that inaccurately performed patterning steps can lead to a prominent decrease in shunt

resistance. Due to the high defect concentration in passivation layers [115, 116], a metal finger overlapping the space charge region might short circuit the cell and, consequently, would strongly decrease the conversion efficiency of the cell. The surface passivation quality and the series resistance of the cell depend strongly on the dopant concentration profile of every single doped surface. Thus, the co-diffused dopant concentration profile of the FSF, the BSF, and the emitter, measured by ECV, are discussed.

The *BSF definition* is the pattern transfer of the ink to the PSG/SiO_x stack (total thickness of around 300 nm) carried out in a buffered etching solution containing HF. The etch rate of the PSG layer and the SiO_x layer was found to be around 358 nm/min [117]. Figure 5.1 depicts the state of the BSF definition after printing and pattern transfer on damage etched and polished surfaces. After printing, the ink lines feature a width of 360 μm . After etching and stripping, the realized PSG/SiO_x lines feature a width of 330 μm on saw-damage etched surfaces and 310 μm on polished surfaces. The difference in width of printed lines and PSG/SiO_x lines arises from under etching effects which are assumed to depend, among other things, on ink adhesion, the etch rate, and the layer thickness.

The color gradient at the edges of the PSG/SiO_x structures reveals a continuous increase of the layer thickness from the silicon surface up to the highest point of the PSG/SiO_x structure. The width of regions with color gradient is approximately 20 μm per edge. The thickness of the PSG/SiO_x stack was chosen to be around 300 nm. Assuming a linear increase of the stack thickness from the silicon surface up to the highest point of the PSG/SiO_x line, the gradient of the edges is approximately 0.9°.

The *gap definition* is the pattern transfer of the ink into a thick SiO_x layer (layer thickness of around 500 nm). Like the BSF definition, the pattern transfer is accomplished by utilizing a buffered etching solution containing HF. Figure 5.2 depicts the state of the gap definition after printing and after the pattern transfer on damage etched and polished surfaces. After printing, the ink lines feature a width of around 550 μm . After etching, the realized SiO_x lines, covering the PSG/SiO_x lines fabricated in the BSF definition, feature a width of around 510 μm . This corresponds to an under etching of 20 μm per edge. Compared to the PSG/SiO lines realized during BSF definition, the edges of the SiO_x lines reveal a wider region with color gradient than the PSG/SiO_x lines. This increase is probably caused by the increased etching time used to etch through the relatively thick SiO_x layer. According to the dimensions shown, the gap regions would ideally feature a width of around 100 μm . Since the alignment accuracy of the printer was found to be $\pm 10 \mu\text{m}$ (compare section 3.3.4), the width of the gap region can vary between 80 to 120 μm . The gap regions of the

example with the saw-damage etched surface feature almost similar dimensions. In the case of the polished surface, the dimensions of the gap regions are around 85 and 115 μm . Nevertheless, since the SiO_x fingers cover the PSG/ SiO_x fingers completely, the regarded variations should not prominently affect the cell performance.

BSF-definition

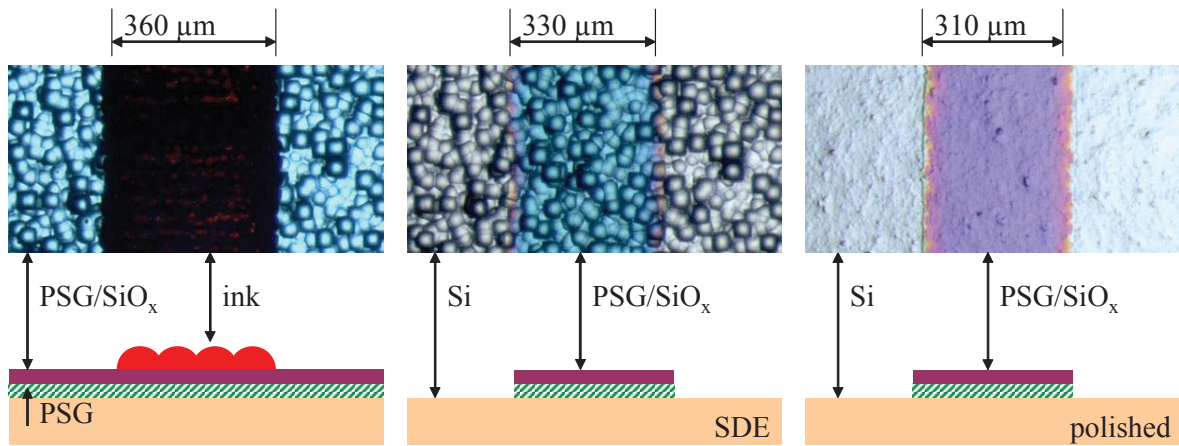


Figure 5.1 Microscopic top view and schematic cross section of structures defined in the patterning module BSF definition. Depicted are line structures after printing (left) and patterning (middle) on a saw-damage etched (SDE) surface and patterning on a polished surface (right).

gap definition

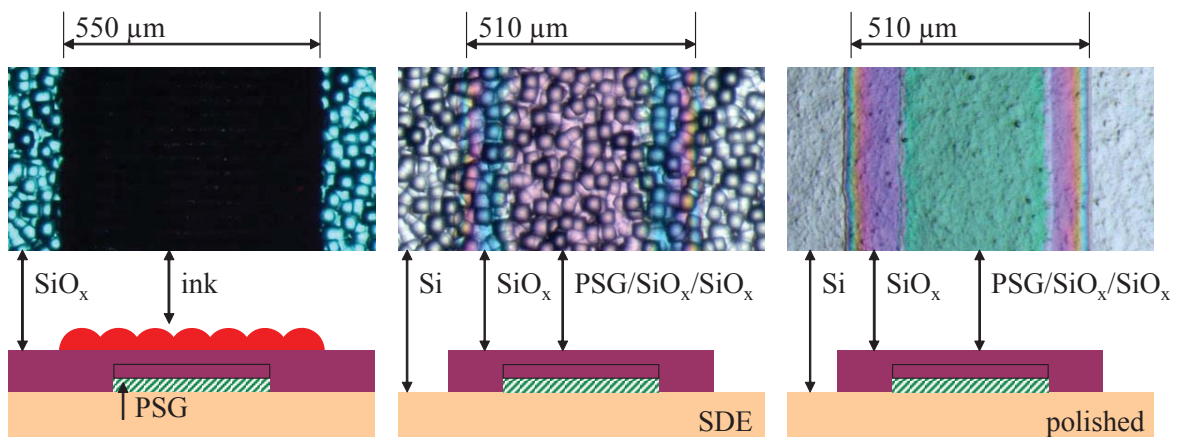


Figure 5.2 Microscopic top view and schematic cross section of structures defined in the patterning module gap-definition. Depicted are line structures after printing (left) and patterning (middle) on a saw-damage etched (SDE) surface and patterning on a polished surface (right).

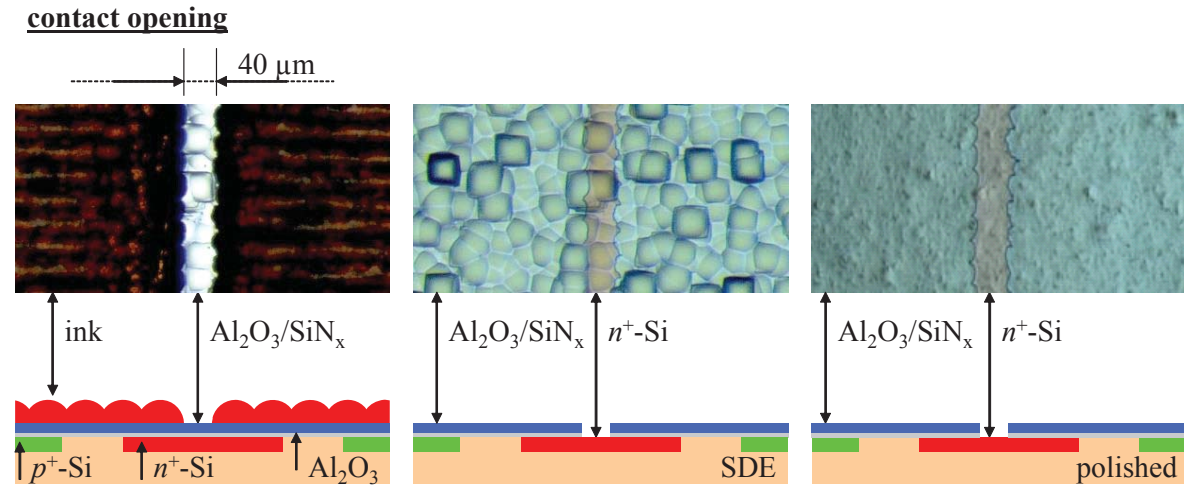


Figure 5.3 Microscopic top view and schematic cross section upon structures defined in the patterning module contact opening. Depicted are line structures after printing (left) and patterning (middle) on a saw-damage etched (SDE) surface and patterning on a polished surface (right).

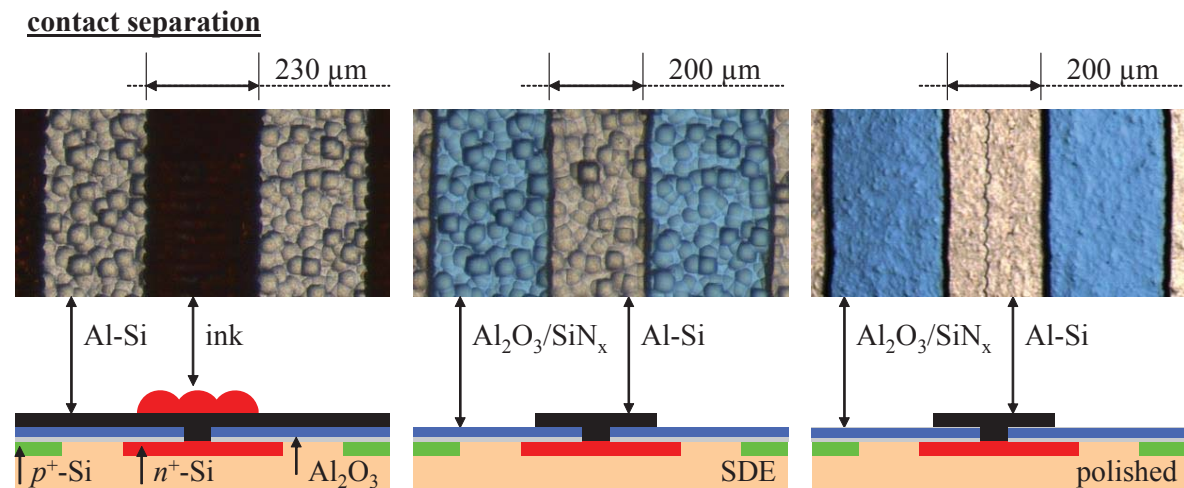


Figure 5.4 Microscopic top view and schematic cross section upon structures defined in the patterning module contact separation. Depicted are line structures after printing (left) and patterning (middle) on saw-damage etched (SDE) surfaces. The picture on the right hand side shows the patterning transfer on polished surfaces.

The *contact opening* is the pattern transfer of the ink into the $\text{Al}_2\text{O}_3/\text{AR-SiN}_x$ stack used as rear side passivation layer. Like the BSF and the gap definition, the pattern transfer is performed in a buffered etching solution containing HF. The etch rate of the dominating AR-SiN_x was found to be 5 nm/min [117]. Figure 5.3 depicts the state of the contact opening after printing and after the pattern transfer on damage etched and polished surfaces. After printing, the open ink lines featured a width of around 40 μm .

Independent from the surface topography (SDE or polished surface), the realized open lines in the rear side passivation stack feature a comparable width. Hence, the pattern transfer of the ink mask in $\text{Al}_2\text{O}_3/\text{SiN}_x$ can be performed without significant under etching effects. By taking a closer look at the edges of the open line in $\text{Al}_2\text{O}_3/\text{SiN}_x$, the shape of the ink droplets is recognizable. This observation underlines the strong adhesion of the ink on silicon nitride coated substrates and the corresponding less pronounced under etching.

The *contact separation* is the pattern transfer of the ink into the Al-Si layer. The pattern transfer of the ink into Al-Si was carried out by using a chemical solution consisting of phosphoric, hydrochloric, and acetic acid diluted in water. The etch rate of Al-Si in this etchant depends exponentially on the temperature. Unfortunately, the adhesion of the ink correlates negatively with temperature so that adequate etching results were obtained at room temperature (298 K, room temperature). At this temperature, the etch rate of Al-Si compound was found to be around 430 nm/min. The adhesion time of the ink in the etching solution is longer than 20 minutes. These properties are sufficient to etch Al-Si layers up to a thickness of 3 μm .

Figure 5.4 depicts the state of the contact separation after printing and after the pattern transfer on damage etched and polished surfaces. After printing, the ink lines have a width of 230 μm . After etching, the linear electrodes reveal a width of around 200 μm on saw-damage etched and polished surfaces. These dimensions correspond to an under etching of 15 μm per edge. The gap between electrodes contacting BSF and emitter is around 250 μm .

The carrier concentration profiles measured by ECV are depicted in Figure 5.5. The graph on the left hand side shows the concentration of holes in the emitter and electrons in the BSF in dependence of the depth relative to the rear surface z_{rear} . The graph on the right hand side depicts the concentration of electrons in the FSF in dependence of the depth relative to the front surface z_{front} .

In the following, the depth of the carrier profiles is extracted at the intersection of an exponential regression fitting the ECV-measured data and a constant carrier concentration of $1 \cdot 10^{17} \text{ cm}^{-3}$. The hole concentration profile of the emitter features a maximum boron concentration of $7.4 \cdot 10^{19} \text{ cm}^{-3}$ at a depth of around 50 nm. The profile depth is around 600 nm. The electron concentration profile of the BSF has a maximum electron concentration of $1.2 \cdot 10^{20} \text{ cm}^{-3}$ which is reached at a depth of around 14 nm. The profile depth is approximately 800 nm. The shape of the profile slightly corresponds to a so-called kink and tail profile induced by different diffusion mechanisms of phosphorus in silicon (compare 3.4). The electron concentration profile of the FSF exhibits a maximum phosphorus concentration of $6.8 \cdot 10^{18} \text{ cm}^{-3}$ at a depth of

around 15 nm and a profile depth of around 380 nm. Since the FSF provides a P-doped surface with a lower electron concentration than the BSF, the shape of the FSF does not correspond to kink and tail.

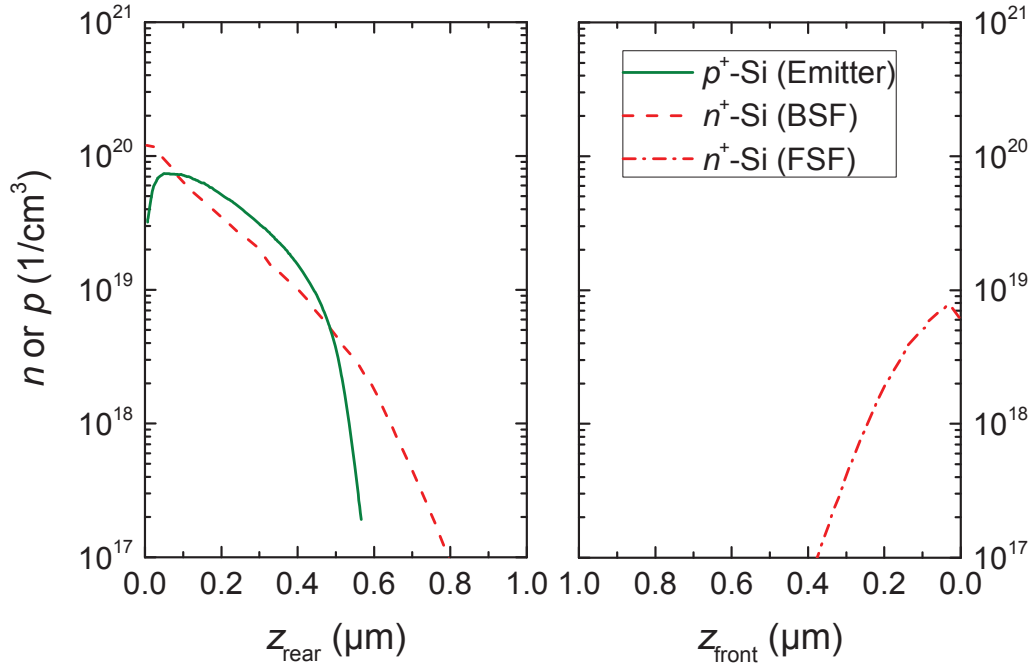


Figure 5.5 Electron concentration n or hole concentration p in dependence of the wafer depth. The left graph shows the electron and hole concentration of the BSF and the emitter in dependence of the depth relative to the rear surface z_{rear} . The right graph depicts the electron concentration profile of the FSF in dependence of the depth relative to the front surface z_{front} .

According to the high dopant concentration, the emitter and the BSF region should be easily contactable by PVD-coated aluminum-silicon compounds. Since the maximum carrier concentration is in both cases below the active solubility limit of boron ($9 \cdot 10^{19} \text{ cm}^{-3}$) and phosphorus ($4 \cdot 10^{20} \text{ cm}^{-3}$), harmful precipitation which might induce a remarkable decrease in cell conversion efficiency is not assumed to be an issue. The FSF features a sheet resistance of around $350 \Omega/\text{sq}$ and a very low surface concentration of less than $1 \cdot 10^{19} \text{ cm}^{-3}$. This is a promising trade-off which probably allows for low resistive losses in silicon on the one hand and a high surface passivation quality on the other.

5.3 Influence of material on cell performance

5.3.1 Motivation

One major objective of this study is to assemble BC-BJ solar cells on industrially relevant Cz-Si material. The aim of the following experiment is to clarify if either Cz-Si material is applicable for BC-BJ solar cells or not. Therefore, cells based on Cz-Si material featuring a damage etched and a shiny etched rear surface are compared to those using cost-intensive FZ-Si material.

The performance of a BC-BJ solar cell depends strongly on the bulk specifications. Since excess carriers are mainly generated at the front side of the solar cell, the minorities have to diffuse from the front to the rear side of the solar cell to be collected by the emitter. Minorities generated between FSF and BSF have to overcome a long lateral path length to reach the emitter. Thus, material with a high bulk quality is recommended. Compared to FZ-Si material, Cz-Si material usually contains a higher amount of oxygen. Interactions of oxygen with silicon can induce bulk defects acting as recombination centers which are harmful for the bulk carrier lifetime. Especially the short circuit current density is sensitive to the bulk carrier lifetime.

Unsure is the influence of the rear surface topography on the solar cell performance. Compared to smooth surfaces, rough surfaces like damage etched surfaces might lead to an improved reflection due to scattering effects at the rear side [118]. This effect would lead to higher quantum efficiency in the long wavelength range. Compared to rough surfaces, smooth surfaces might enable an increase in passivation quality due to a more homogeneous deposition of passivation layers [119]. The increase in passivation quality might lead to an increase in the open circuit voltage. Technological aspects like under etching are dependent on the surface topography of the rear side as well (compare section 5.2).

The dependence of the material and surface topography on the cell performance is investigated in this section.

5.3.2 Cell preparation and characterization

BC-BJ solar cells were processed according to the base line process described in section 3.5.1. As base material, damage etched (rough) FZ- and Cz-Si material as well as shiny etched (smooth) Cz-Si material were utilized.

The cell dimensions of the characterized cells are depicted in Table 5.1. The width of the n -type region ($x_{BSF} + 2 \cdot x_{gap}$) was chosen to be 500 μm . The pitch distance x_{pitch} was set to 1500 μm . By considering the width of the n -type region and the x_{pitch} , the emitter coverage EC is calculated according to the following equation:

$$EC = 1 - \frac{x_{BSF} + 2 \cdot x_{gap}}{x_{pitch}} \quad (5-1)$$

Thus, the cells in question were chosen to feature an EC of 67 %. The line openings in the rear side passivation layer were chosen to feature a width x_{CO} of 40 μm . The metal fingers contacting the BSF were set to feature a width $x_{met,n}$ of 200, whereas the width of the metal fingers contacting the emitter $x_{met,p}$ was selected to be 800 μm . The wafer thickness W depends on the applied material. The dimensions of choice are assumed to feature a trade-off between industrial feasibility [120] and conversion efficiency of the solar cell. Granek et al. processed a BC-BJ solar cell with almost similar dimensions featuring an efficiency of 20.9 % [39].

Table 5.1 Cell dimensions. These are the active cell area A , the wafer thickness W , the pitch distance x_{pitch} , the BSF width x_{BSF} , the width of the gap x_{gap} between emitter and BSF, the emitter coverage EC , the width of the contact openings in the rear side passivation layer, and the width of the BSF electrodes $x_{met,n}$ as well as the one of the emitter electrodes $x_{met,p}$.

A (cm^2)	W (μm)	x_{pitch} (μm)	x_{BSF} (μm)	x_{gap} (μm)	EC (%)	x_{CO} (μm)	$x_{met,n}$ (μm)	$x_{met,p}$ (μm)
4	160-210	1500	300	100	67	40	200	800

In order to estimate the bulk lifetime of the favored saw-damage etched Cz-Si material, the wafers were passivated on both sides with thermally grown SiO_2 layers after a saw-damage etch and a cleaning step had been applied. The thermally grown SiO_2 layers provide a very high surface passivation quality on n -type material [121]. To characterize the bulk resistivity, the wafers were inductively analyzed before and after oxidation. After passivation and low temperature annealing, the wafers were characterized by quasi steady state photo conductance (QSSPC) [122]. Based on the obtained data, the bulk carrier lifetime was determined by employing the slope method introduced by Kane and Swanson [123]. Due to the very high purity of FZ-Si material, the bulk carrier lifetime of the FZ-Si material was assumed to be only limited by

intrinsic Auger recombination $\tau_{\text{bulk,int}}$. In this case, the charge carrier dependent bulk carrier lifetime is calculated according to the model of Kerr et al. [124].

The cells were characterized by J - V measurements, Suns V_{OC} measurements, quantum efficiency (QE) measurements, and local QE measurements performed by the spectrally resolved light beam induced current (SR-LBIC) method. The SR-LBIC method allows for a spatially resolved measurement of the quantum efficiency [125].

5.3.3 Results and discussion

The properties of the varied materials are depicted in Table 5.2. These are the wafer thickness after texturing W , the specific base resistivity before ρ_{bulk} and after co-diffusion $\rho_{\text{bulk,T}}$, the intrinsic dopant concentration after co-diffusion $N_{\text{dop,T}}$, the QSSPC measured bulk carrier lifetime τ_{bulk} , and the bulk carrier lifetime limited by extrinsic Auger recombination $\tau_{\text{Aug,ex}}$.

Table 5.2 Material properties. These are the wafer thickness after texturing W , specific base resistivity before ρ_{bulk} and after co-diffusion $\rho_{\text{bulk,T}}$, dopant concentration after co-diffusion $N_{\text{dop,T}}$, the QSSPC measured bulk carrier lifetime τ_{bulk} , and the Auger limitation of the bulk carrier lifetime according to Kerr et al. $\tau_{\text{Aug,ex}}$ for an excess carrier density Δn of $1 \cdot 10^{15} \text{ cm}^{-3}$ in dependence of the varied materials.

Material	W (μm)	ρ_{bulk} (Ωcm)	$\rho_{\text{bulk,T}}$ (Ωcm)	$N_{\text{dop,T}}$ ($1/\text{cm}^3$)	τ_{bulk} (ms)	$\tau_{\text{Aug,ex}}$ (ms)
1 – n , Cz	160	4.3	4.9	$9.4 \cdot 10^{14}$	1.8-2.5	23.2
2 – n , Cz, smooth	190					
3 – n , FZ	210	4.3	4.3	$1.1 \cdot 10^{15}$	/	21.8

The wafer thickness W of the investigated materials varied due to the different initial thickness of the supplied wafers and the different wet chemical processes used to adjust the surface topography. Compared to FZ-Si material, Cz-material features a different base resistivity before ρ_{bulk} and after diffusion $\rho_{\text{bulk,T}}$. During diffusion, the base resistivity of the Cz-Si material increases by $0.6 \Omega\text{cm}$ up to $4.9 \Omega\text{cm}$. The FZ-Si material indicates a constant base resistivity of $4.3 \Omega\text{cm}$. This effect is caused by the high amount of oxygen and related Si-O defects in the Cz-Si material. Some Si-O related defects are known to act as thermal electron donors which are annealed and deactivated during a high temperature step (compare section 3.1). In the case of n -type material, the high temperature step leads to an increase in base resistivity.

According to the following equation, the diffusion length L_p of holes (minority charge carriers) in n -type silicon is calculated as a function of the Boltzmann constant k , the

temperature T , the elementary charge q , the carrier dependent mobility of holes $\mu_p(N_{\text{dop}})$, and the lifetime of holes τ_p .

$$L_p = \sqrt{\frac{kT}{q} \cdot \mu_p(N_{\text{dop}}) \cdot \tau_p} \quad (5-2)$$

Notice that the equation is only valid for low level injection conditions. By inserting τ_{bulk} from Table 5.2 for τ_p , L_p is between 1470 μm ($\tau_p = \tau_{\text{bulk}} = 1.8$ ms) and 1730 μm ($\tau_p = \tau_{\text{bulk}} = 2.5$ ms). Hence, the L_p of the Cz-Si material of choice is much higher than half of the BSF width ($L_p > 4.5 x_{\text{BSF}}$) and the wafer thickness ($L_p > 9 W$). As a rule of thumb, a minimum minority diffusion path length of 4 W was assumed by Granek et al. [39]. If the additional processes of the base line process do not negatively affect the bulk carrier lifetime, the cell performance should not be limited by the material.

According to the varied material properties, in the following, cells are denoted as *saw-damage etched Cz- and FZ-cell* as well as *smooth Cz-cell*.

Table 5.3 J-V characteristics of solar cells (best cell per group) fabricated on Cz- (1) and FZ-Si material with a saw-damage etched (3) as well as on Cz-Si material featuring a smooth rear surface (2). The measurements were performed under one sun conditions. The pseudo fill factor pFF and the ideal fill factor FF_0 are extracted from the J-V curve measured by $\text{Suns}V_{\text{OC}}$.

Material	V_{OC} (mV)	J_{SC} (mA/cm ²)	FF (%)	pFF-FF (% _{abs})	FF_0 -pFF (% _{abs})	η (%)
1 – n, Cz	642.4	38.5	73.0	5.6	5.1	18.1
2 – n, Cz, smooth	641.3	38.7	73.7	5.4	4.6	18.3
3 – n, FZ	641.8	38.7	74.3	4.3	5.1	18.4

The results of the J - V and $\text{Suns}V_{\text{OC}}$ measurements are summarized in Table 5.3. The open circuit voltage V_{OC} , the short circuit current density J_{SC} , the fill factor FF and the conversion efficiency η were extracted from the J - V measurements. The pFF was extracted from the J - V curve measured by $\text{Suns}V_{\text{OC}}$. The ideal fill factor FF_0 was calculated in dependence of the V_{OC} measured by $\text{Suns}V_{\text{OC}}$. All these parameters are depicted in dependence of the selected wafer materials. Notice that only the best cell per group is depicted. In the proceedings of this work the spatially resolved standard deviation in efficiency of identically processed small-size cells along a wafer area of 243mm² will be found to be below 0.2 %_{abs}.

Independent from the wafer material, the cells feature comparable solar cell parameters with efficiencies between 18.1 and 18.4 %. The V_{OC} of 641 to 643 and the J_{SC} of 38.5 to 38.7 mA/cm² are on a comparable level. Notice that the measurement accuracy of the J - V measurement setup is ± 0.2 mA/cm². Thus, the measured difference in J_{SC} cannot be significantly attributed to the difference in material properties.

Significant differences in cell performance are observable by regarding the fill factor FF and the fill factor losses. Fill factor losses are qualified by regarding the difference between ideal fill factor and fill factor $FF_0 - FF$. The measurement of the pseudo fill factor allows for a separation of fill factor losses arising from the series resistance $pFF - FF$ and the leakage current $FF_0 - pFF$. Compared to the damage etched Cz-cell, the damage etched FZ-cell indicates a decrease in $pFF - FF$ of around 1.3 %_{abs}. The corresponding decrease in series resistance of the FZ-cell is assumed to be partly related to the lower bulk resistivity of the FZ-Si material ($\rho_{bulk,T} = 4.3$ Ωcm) compared to the Cz-Si material ($\rho_{bulk,T} = 4.9$ Ωcm) after co-diffusion. Compared to the other cells, the shiny etched Cz-cell exhibits a decrease $FF_0 - pFF$ of 0.5 %_{abs} which originates from a decrease in leakage current. A possible reason for this effect is the enhanced homogeneity of emitter formation including an enhanced homogeneity of the emitter depth and expansion of the space charge region.

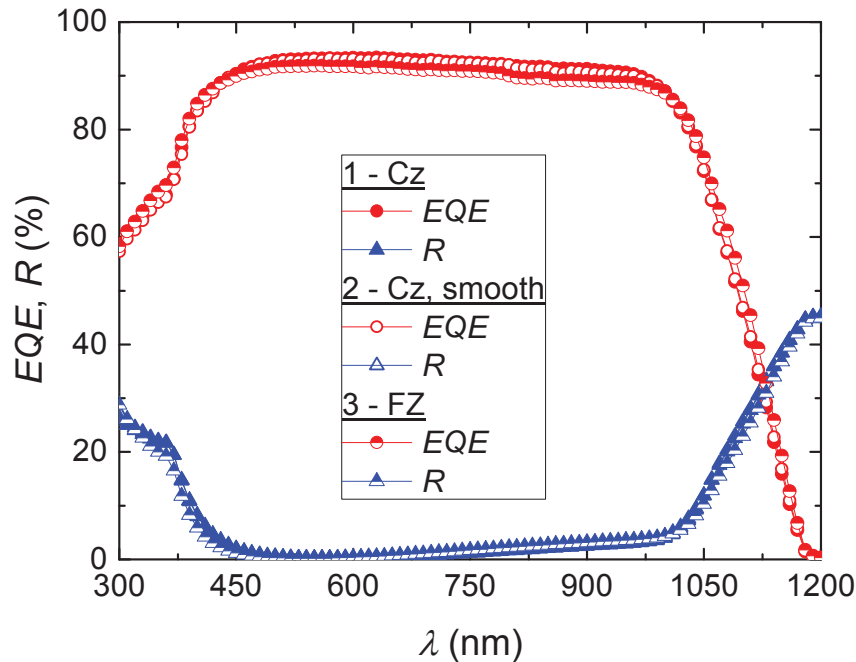


Figure 5.6 External quantum efficiency EQE and reflection R in dependence of the wavelength λ for solar cells manufactured on Cz-Si wafers, Cz-Si wafers with a smooth surface and FZ-Si wafers.

The external quantum efficiency EQE and the reflection R in dependence of the wavelength λ for the different materials are shown in Figure 5.6. The EQE indicates no significant dependence on the material properties. The EQE - λ curves correspond to a J_{SC} of 39.1 mA/cm² for the damage etched Cz-cell, 39.0 mA/cm² for the shiny etched Cz-cell, and 38.8 mA/cm² for the damage etched FZ-cell. Thus, the J_{SC} values obtained by the J - V measurements and the QE measurements slightly differ. Possible reasons for the difference are the measurement tolerance of the used setups, on the one hand, and inaccurate positioning of the cell samples underneath the aperture during measurement, on the other hand.

The R - λ curves are independent from the material properties as well. For example, the R - λ curve of the saw-damage etched Cz-cell has the following progression. With increasing wavelength, the R decreases from 27.9% at 300 nm down to 0.2 % at 570 nm, slightly increases to 3.5 % at 980 nm, and, afterwards, increases sharply up to 45.2 % at 1200 nm. The R - λ curve corresponds to a loss in J_{SC} of around 2.6 mA/cm². These losses occur because of interface reflection at the front side of the cell and escape light. The wavelength dependent difference between $(1-R)$ and EQE corresponds to a loss in J_{SC} of around 4.7 mA/cm². These losses might originate from parasitic absorption at free carriers, recombination and transmission losses.

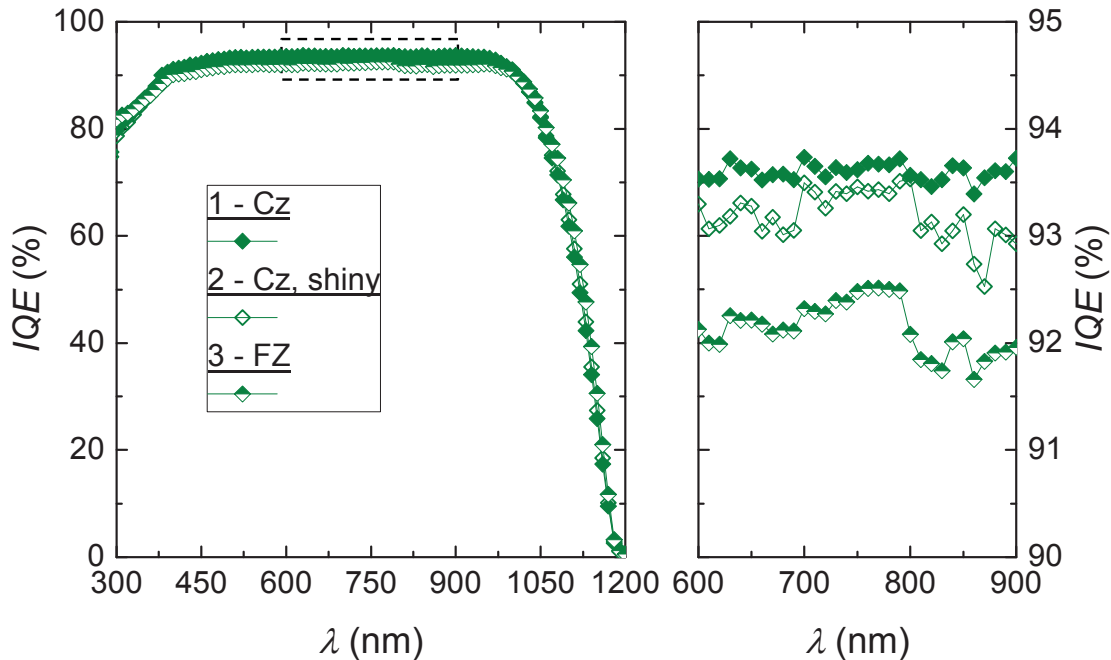


Figure 5.7 Internal quantum efficiency IQE versus wavelength λ for the varied cell material on the left and a detailed view on the IQE in the middle wavelength range on the right.

Figure 5.7 shows the internal quantum efficiency IQE in dependence of the wavelength λ for the varied cell materials, on the left, and a magnified graph depicting the IQE of the cells in the middle wavelength range, on the right hand side.

Compared to the EQE , the IQE is mainly affected by recombination losses. Thus, the IQE in the middle wavelength range ($600 \text{ nm} \leq \lambda < 900 \text{ nm}$) is very sensitive to bulk recombination. As expected by considering the progression of the $EQE-\lambda$ and $R-\lambda$ curves, the $IQE-\lambda$ curves are almost independent from the regarded material properties as well. However, two findings are observed. First, the IQE does not reach 1 in the middle wavelength range. Second, the $IQE-\lambda$ curve indicates a significant drop in the short wavelength range ($\lambda < 600 \text{ nm}$). The IQE in the small wavelength range is especially sensitive to recombination at the front side. Thus, it is assumed that the cells suffer from bulk and, additionally, from front side recombination. Bulk recombination can occur due to electrical shading which means the recombination of holes upon the BSF region.

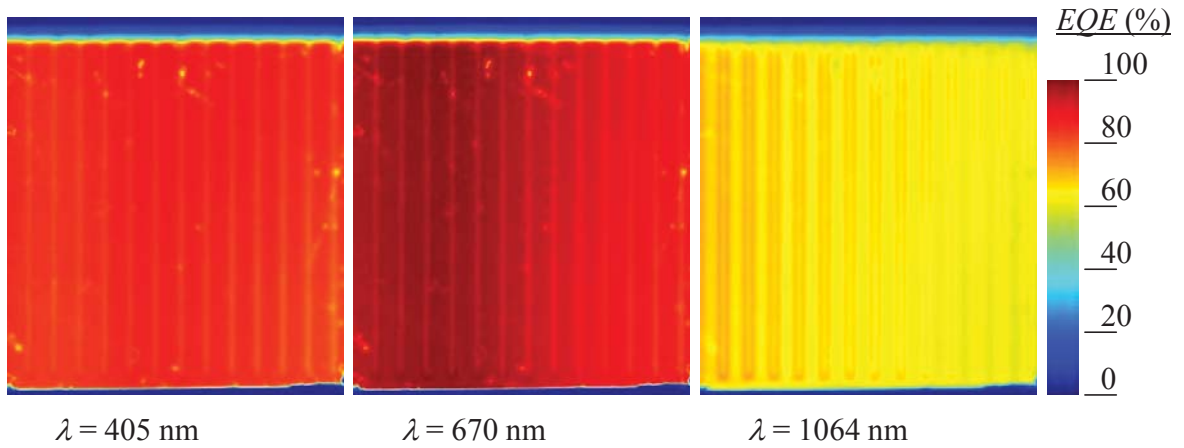


Figure 5.8 Spatially resolved quantum efficiency EQE of the BC-BJ cell fabricated from damage etched Cz-Si material. The measurements were performed with an SR-LBIC setup at three different wavelengths λ .

In order to further characterize electrical shading, a spatially resolved QE measurement was performed at a wavelength of 405 nm, 670 nm, and 1064 nm. The measurement results obtained by characterizing the saw-damage etched Cz-cell is depicted in Figure 5.8.

The EQE mean measured at a wavelength of 670 nm is approximately 93 % and therefore in accordance with the value obtained by the global QE measurements. At 405 and 670 nm, the BSF regions feature a lower EQE than the surrounding emitter areas. This difference in EQE is caused by electrical shading. At 1064 nm, the metal

electrodes and the non-metallized fractions are recognizable. Compared to the metallized fraction, the *EQE* signal of the non-metallized fraction is higher. This increase in *EQE* might be accomplished by an improved light trapping due to a higher interface reflection as well as less parasitic layer absorption in the range of the non-metallized area.

The main finding of the material variation is that the solar cell performance is rather independent from the varied materials. BC-BJ cells based on saw-damage etched Cz-Si material indicate similar characteristics like those processed on cost-intensive FZ-Si material. In turn, Si-O related defects are assumed to be not limiting the Cz-cell performance at this stage. The utilization of shiny etched (smooth) surfaces indicates a slight advantage in *pFF*. However, the solar cell performance is assumed to be mainly limited by process related issues. At this point, it is expected that the cell is mainly limited by the following loss mechanisms.

The J_{SC} suffers from front recombination and a process dependent decrease in bulk carrier lifetime. The V_{OC} is limited by the passivation quality of the solar cell. The leakage current negatively influences the *FF*. Possible origins of the latter effect might be recombination in the space charge region and metal spiking. Besides intrinsic series resistance losses in silicon, the *FF* might also suffer from series resistance losses originating from the design of the metallization grid.

Based on the latter assumptions, the following sections in this chapter deal with a modification of the base line process in order to increase the efficiency step by step.

5.4 Influence of passivation scheme on cell performance

5.4.1 Motivation

The main objective of the following experiment is to improve the passivation quality of the solar cell. An improvement of the FSF passivation in particular could lead to an increase in short circuit current density as well as in open circuit voltage. A simple way to interchange the passivation scheme is to thermally grow a silicon dioxide (SiO_2) as passivation layer on the front and on the rear side. Thermally grown SiO_2 layers are known to feature a very high passivation quality on P-doped surfaces and therefore feature a high potential to increase the overall passivation quality of the cell [121]. From a technological point of view, two deposition steps, in fact the PECVD of the SiON_x layer and the ALD of the Al_2O_3 layer, are substituted by the thermal oxidation process. Hence, the process complexity of the base line process decreases slightly as well.

5.4.2 Cell preparation and characterization

In order to investigate the impact of thermally grown passivation layers on the cell performance, symmetrically passivated BC-BJ cells featuring a stack consisting of a SiO_2 layer and a PECVD silicon nitride (SiN_x) layer on both sides (*SiO passivation scheme*) were fabricated and compared to cells with an unsymmetrical passivation scheme. This unsymmetrical passivation scheme corresponds to the one already introduced in the base line process (compare section Figure 3.5) and includes a stack consisting of a PECVD silicon oxynitride (SiON_x) and a SiN_x layer on the front and of an ALD aluminum oxide (Al_2O_3) layer and PECVD SiN_x layer on the rear side (*SiON-AlO passivation scheme*). In the following and in terms of an easier differentiation of the differently passivated cells, cells are additionally denoted according to the front passivation layer as *SiO₂* and *SiON_x* passivated cells.

Table 5.4 Cell dimensions. These are the active cell area A , the wafer thickness W , the pitch distance x_{pitch} , the BSF width x_{BSF} , the width of the gap x_{gap} between emitter and BSF, the emitter coverage EC , the width of the contact openings in the rear side passivation layer, and the width of the BSF electrodes $x_{\text{met},n}$ as well as the one of the emitter electrodes $x_{\text{met},p}$.

A (cm ²)	W (μm)	x_{pitch} (μm)	x_{BSF} (μm)	x_{gap} (μm)	EC (%)	x_{CO} (μm)	$x_{\text{met},n}$ (μm)	$x_{\text{met},p}$ (μm)
4	160	1500	300	100	67	40	200	800
4	160	2500	300	100	80	40	200	1800

The diagram illustrates the cross-section of a solar cell with the following layers and dimensions:

- Layers (from top to bottom):**
 - $x_{\text{CO},n}$: Contact opening in the rear passivation layer.
 - $x_{\text{met},n}$: Width of the rear metal contact.
 - x_{BSF} : Width of the Back Surface Field (BSF) region.
 - x_{gap} : Gap between the emitter and BSF.
 - $x_{\text{CO},p}$: Contact opening in the front passivation layer.
 - $x_{\text{met},p}$: Width of the front metal contact.
 - x_{pitch} : Total pitch distance between metal contacts.
 - x_{emitter} : Width of the emitter region.
- Legend:**
 - Orange: n -type Si
 - Green: p^+ -Si (emitter)
 - Red: n^+ -Si (BSF)
 - Black: electrodes
 - Blue: passivation

Solar cells with the dimensions listed in Table 5.4 are compared. The varied dimension is the pitch distance x_{pitch} . Since the width of the BSF x_{BSF} and of the gap regions x_{gap} are kept constant, the emitter coverage EC increases with increasing x_{pitch} . The width of the metal fingers contacting the emitter $x_{\text{met},p}$ was chosen to increase with the x_{pitch} as well.

The manufactured solar cells were characterized by J - V , $\text{Suns}V_{\text{OC}}$, and QE measurements.

In order to qualify the potential of the passivation schemes, symmetrically doped and passivated samples were fabricated. In turn, damage etched wafers (n -type, FZ, $\rho_{\text{bulk}} = 9 \Omega\text{cm}$, $N_{\text{dop}} = 5 \cdot 10^{14} \text{ cm}^{-3}$, $W = 214 \mu\text{m}$) without doped surfaces (gap), with P-doped surfaces (BSF), and B-doped surfaces (emitter) were passivated with the rear passivation stack. Textured wafers with P-doped surfaces (FSF) were passivated with the front passivation stack. The dark saturation current density of every single cell surface was obtained by QSSPC measurements at room temperature and data analysis according to the slope method in high injection ($\Delta n > 10 N_{\text{dop}} = 5 \cdot 10^{15} \text{ cm}^{-3}$) with an intrinsic carrier concentration of n_i of $8.4 \cdot 10^9 \text{ cm}^{-3}$. By summing up the area weighted dark saturation current density J_0 of every single cell surface, an effective dark saturation current density $J_{0,\text{eff}}$ can be calculated. In dependence of the dark saturation current density $J_{0,i}$ of the cell surfaces i and the corresponding area fraction n_i , the $J_{0,\text{eff}}$ is calculated according to the following equation.

$$J_{0,\text{eff}} = J_{0,\text{FSF}} + n_{\text{E}} J_{0,\text{E}} + n_{\text{BSF}} J_{0,\text{BSF}} + n_{\text{GAP}} J_{0,\text{GAP}} \quad (5-3)$$

Notice that the depicted equation is only valid for a cell without bulk recombination and recombination underneath the metal contacts. Moreover, a homogeneous carrier generation rate being independent from the wafer depth is assumed. By inserting $J_{0,\text{eff}}$ in the one-diode equation allows for a calculation of the open circuit voltage limit $V_{\text{OC,limit}}$,

$$V_{\text{OC,limit}} = \frac{kT}{q} \ln\left(\frac{J_{\text{SC}}}{J_{0,\text{eff}}} + 1\right) \quad (5-4)$$

with the Boltzmann constant k , the temperature T , the elementary charge q , and the short circuit current density J_{SC} . In the following, the estimation of the $V_{\text{OC,limit}}$ is called voltage analysis.

5.4.3 Results and discussion

The results of the J - V and the Suns V_{OC} measurements of the solar cells featuring the different passivation schemes and pitch distances x_{pitch} are depicted in Table 5.5. From the table it is apparent that the thermal oxidation allows for an increase in conversion efficiency η up to 18.9 %. Compared to SiON_x passivated cells featuring a J_{SC} of 38.5 mA/cm^2 ($x_{\text{pitch}} = 1500 \mu\text{m}$), SiO_2 passivated cells indicate an increase in J_{SC} of 1.2 mA/cm^2 up to 39.7 mA/cm^2 . The SiO_2 passivated cell with a x_{pitch} of $2500 \mu\text{m}$ and

a related emitter coverage of 80 % exhibits a J_{SC} of 40 mA/cm² which underlines a high minority collection probability of the cell.

Independent from the passivation scheme, the cells exhibit a drop in open circuit voltage V_{OC} with increasing x_{pitch} . This drop is more prominent in the case of SiO₂ passivated cells. The origin of this drop is analyzed in the following voltage analysis.

Independent from the passivation scheme, the fill factor FF decreases with increasing x_{pitch} . This decrease is mainly caused by an increase in series resistance $pFF-FF$. For example, increasing the x_{pitch} of SiON_x passivated cells by 1000 μ m leads to an increase in $pFF-FF$ of 2.9 %_{abs}. Consequently, advantages of a large x_{pitch} , for example the high minority collection probability, can only be fully exploited if additional series resistance losses are kept at a minimum. Therefore, the overall conductivity of the cell needs to be modified. An improvement of the series resistance could be obtained by a decrease in bulk resistivity, in the sheet resistance of the FSF, and an adaption of the metal grid [37].

Table 5.5 J-V characteristics (one sun conditions) of the best solar cells per group fabricated with and without thermal oxidation for a pitch distance x_{pitch} of 1500 μ m and 2500 μ m. The pseudo fill factor pFF and the ideal fill factor FF_0 are extracted from the J-V curve measured by Suns V_{OC} .

Passivation (front/back)	x_{pitch} (μ m)	V_{OC} (mV)	J_{SC} (mA/cm ²)	FF (%)	$pFF-FF$ (% _{abs})	FF_0-pFF (% _{abs})	η (%)
SiON _x /Al ₂ O ₃	1500	642.4	38.5	73.0	5.6	5.1	18.1
	2500	640.1	38.7	69.9	8.5	5.3	17.3
SiO ₂ /SiO ₂	1500	642.0	39.7	74.1	4.5	5.1	18.9
	2500	633.6	40.0	71.3	8.6	3.7	18.1

Compared to the SiON_x passivated cell with a x_{pitch} of 2500 μ m, the SiO₂ passivated cell with the same x_{pitch} exhibits a decrease in FF_0-pFF of 1.4 %_{abs} and, consequently, a significantly lower leakage current. The origin of this decrease in leakage current is unclear. Electron accumulation and depletion in the range of the gap region influenced by positive charges in SiO₂ and by negative charges in Al₂O₃ [126, 127], respectively, are, due to the low charge densities in the layers, not assumed to feature a great impact on the pFF . A more probable reason for the high pFF is a wafer position dependent benefit.

The voltage analysis of SiON_x cells passivated according to the SiON-AlO passivation scheme is depicted in Figure 5.9. The analysis is divided into a table on the left and a graph on the right hand side. The table contains the $J_{0,i}$ determined from the

QSSPC measurements in dependence of the cell region (i). These are the FSF, the GAP, the emitter (E) and the BSF region. The $J_{0,\text{eff}}$ and the open circuit voltage limit $V_{\text{OC},\text{limit}}$ of the pitch distances in question (x_{pitch} of 1500 and 2500 μm) are depicted as well. The graph on the right hand side shows the area weighted J_0 of every cell region as a function of the x_{pitch} .

SiON-AlO passivation scheme

$J_{0,i}$	Value (fA/cm ²)
$J_{0,\text{FSF}}$	66.0 ± 2.5
$J_{0,\text{GAP}}$	5.6 ± 0.4
$J_{0,\text{E}}$	91.9 ± 6.4
$J_{0,\text{BSF}}$	126.9 ± 1.2
x_{pitch} (μm)	$J_{0,\text{eff}}$ (fA/cm ²)
1500	149.0
2500	152.6
x_{pitch} (μm)	$V_{\text{OC},\text{limit}}$ (mV)
1500	675.8
2500	675.1

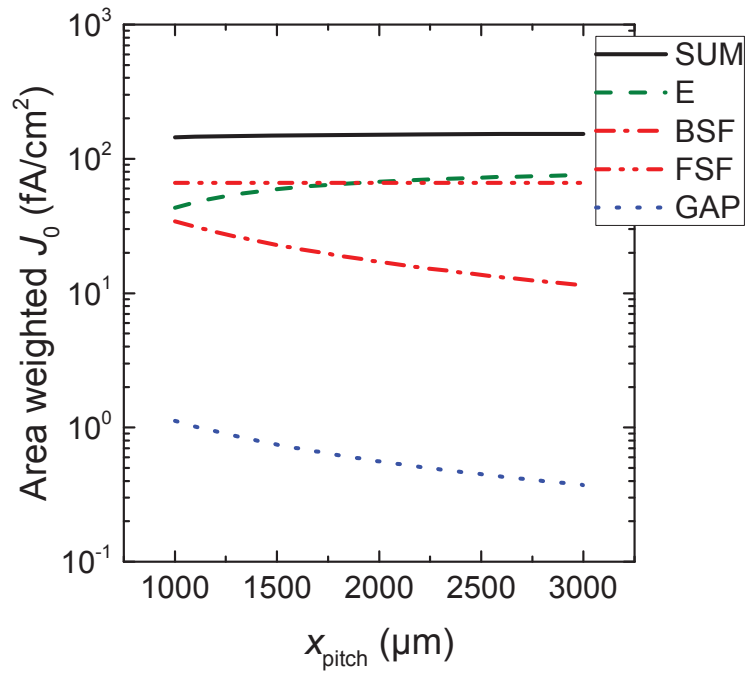


Figure 5.9 Voltage analysis of cells passivated according to the SiON-AlO passivation scheme. The analysis is based on dark saturation current densities J_0 extracted from QSSPC measurements performed on adequate samples corresponding to the different regions of a BC-BJ solar cell. The error bar of $J_{0,i}$ corresponds to the standard deviation of a five point measurement upon a wafer featuring an area of 156 mm².

The $J_{0,\text{eff}}$ of cells featuring the SiON/AlO-passivation scheme is mainly limited by FSF and emitter recombination. The impact of BSF recombination increases with decreasing x_{pitch} . Recombination in the gap region is negligible. At a x_{pitch} of 1500 μm , the $V_{\text{OC},\text{limit}}$ of the SiON_x passivated cell is 675 mV. Increasing the x_{pitch} up to 2500 μm leads to a minor decrease in $V_{\text{OC},\text{limit}}$. This decrease is insignificant and, hence, the $V_{\text{OC},\text{limit}}$ is almost independent from the x_{pitch} in the regarded range.

The voltage analysis of the SiO passivation scheme is depicted in Figure 5.10. The $J_{0,\text{BSF}}$ of around 52 fA/cm² and the $J_{0,\text{FSF}}$ of below 15 fA/cm² were found to be very

low and, in addition, underline the high passivation ability of the P-doped surfaces diffused from the investigated PSG/SiO_x stacks. In comparison, the FSF passivated with the SiON_x/AR-SiN_x stack induces a $J_{0,FSF}$ of 66 fA/cm². Hence, SiO₂ layers are a high-quality choice for FSF passivation. Unfortunately, the SiO₂ passivated cells suffer from the $J_{0,E}$ of around 578 fA/cm². This suffering causes a low $V_{OC,limit}$ of around 651 mV at a x_{pitch} of 1500 μ m and a significant drop in $V_{OC,limit}$ with increasing x_{pitch} . Independent from the passivation scheme, the passivation related limit in voltage decreases with increasing pitch distance. This effect originates from the low emitter and FSF passivation quality. A decrease in $J_{0,E}$ and $J_{0,FSF}$ would lead to a stronger correlation between $V_{OC,limit}$ and the area weighted $J_{0,BSF}$ and, thus, to an increasing $V_{OC,limit}$ with increasing x_{pitch} .

SiO passivation scheme

$J_{0,i}$	Value (fA/cm ²)
$J_{0,FSF}$	14.8 ± 0.2
$J_{0,GAP}$	6.8 ± 0.5
$J_{0,E}$	577.5 ± 23.3
$J_{0,BSF}$	52.0 ± 0.9
x_{pitch} (μ m)	$J_{0,eff}$ (fA/cm ²)
1500	398.5
2500	476.0
x_{pitch} (μ m)	$V_{OC,limit}$ (mV)
1500	650.6
2500	645.9

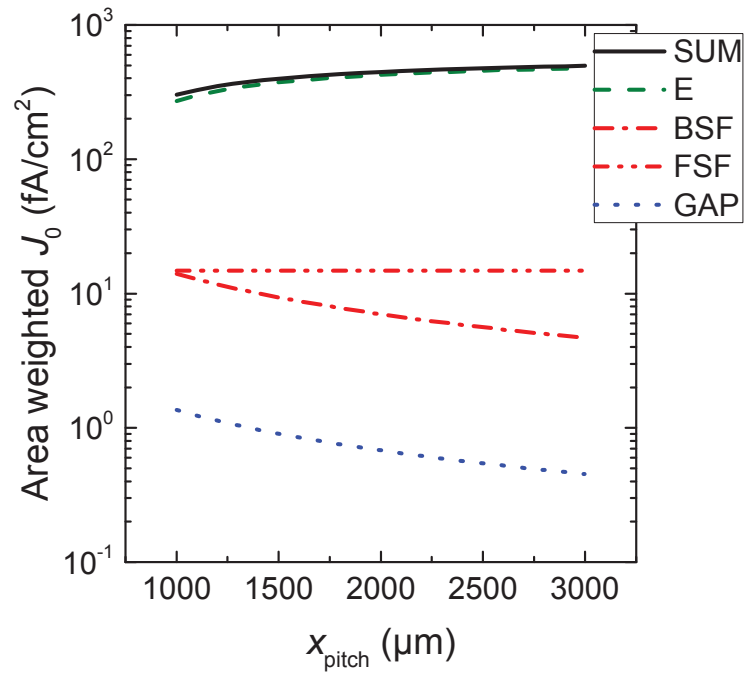


Figure 5.10 Voltage analysis of cells passivated according to the SiO passivation scheme. The analysis is based on dark saturation current densities J_0 extracted from QSSPC measurements performed on adequate samples corresponding to the different regions of a BC-BJ solar cell. The error bar of $J_{0,i}$ corresponds to the standard deviation of a five point measurement upon a wafer featuring an area of 156 mm².

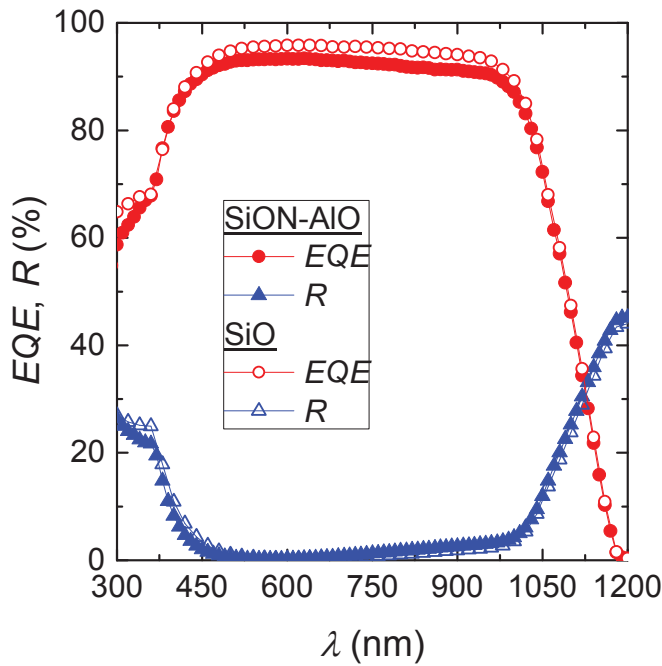
The tendency of a decrease in $V_{OC,limit}$ with an increasing x_{pitch} of cells featuring both passivation schemes was also visible by regarding the J - V measured V_{OC} .

Unfortunately, especially in the case of the SiON-AlO passivation scheme, the difference between $V_{OC,limit}$ and J - V measured V_{OC} is approximately 30 mV. This great difference might be caused by recombination effects which are not considered in the voltage analysis: bulk recombination and recombination underneath the metal contacts. Both recombination effects can have a strong impact on the V_{OC} . By assuming low level injection, the dark saturation current density caused by the bulk $J_{0,bulk}$ is calculated according to the following equation [128],

$$J_{0,bulk} = \frac{qWn_i^2}{N_{dop}t_p} \quad (5-5)$$

with the intrinsic carrier concentration n_i , the base dopant concentration N_{dop} , and the life time of holes (minority charge carriers) t_p . By inserting the data from Table 5.2, the $J_{0,bulk}$ is 78 fA/cm². The J_0 underneath the metal contacts can reach values up to 2000 fA/cm² [129, 130] and might have a strong impact on V_{OC} as well, especially for high contact opening coverages. The cells integrate line openings with a width of 40 μ m. Thus, the contact opening coverage of a cell featuring a x_{pitch} of 1500 μ m is 4 % per polarity. This corresponds to an area weighted J_0 underneath the metal contacts of 80 fA/cm². If these values are considered in the voltage analysis, the $V_{OC,limit}$ of the SiON_x passivated cell with a x_{pitch} of 1500 μ m drops drastically from 675.8 mV to 655.3 mV. Compared with the J - V measured V_{OC} , the modified $V_{OC,limit}$ still reveals an offset of 12.9 mV. By considering the latter recombination effects in the SiO₂ passivated cell with the same pitch distance, the $V_{OC,limit}$ drops from 650.6 mV down to 640.9 mV and is, in consequence, in a good agreement with the J - V measured V_{OC} of 642.0 mV. The remaining difference in J - V measured V_{OC} and $V_{OC,limit}$ of the SiON_x passivated cell can be explained by the realistic generation profile of the cell device. Thus, the generation rate of excess carriers at the front is higher than at the rear side of the cell and, in consequence, the impact of the $J_{0,FSF}$ on the V_{OC} is higher than expected. Since the voltage analysis assumes a carrier generation rate independent from the wafer depth, cells featuring a high $J_{0,FSF}$ are comparably overestimated to those featuring a low $J_{0,FSF}$. Accordingly, the voltage analysis presented in this chapter is only representative in the case of low recombination at the cell's front side.

In the following, the influence of the passivation schemes on J_{SC} is discussed by taking a closer view on the quantum efficiency of the cells. The external quantum efficiency EQE and reflection R in dependence of the wavelength λ for cells with the SiON-AlO and SiO passivation scheme featuring a constant x_{pitch} of 1500 μ m are depicted in Figure 5.11.



SiON-AIO	
λ range (nm)	J_{SC} gain (mA/cm ²)
300-600	12.4
601-900	18.8
901-1200	7.9

SiO	
λ range (nm)	J_{SC} gain (mA/cm ²)
300-600	13.3
601-900	19.1
901-1200	7.8

Figure 5.11 External quantum efficiency EQE and reflection R in dependence of the wavelength λ for solar cells manufactured with the unsymmetrical SiON-AIO passivation and those manufactured with the symmetrical SiO passivation scheme. The table on the right hand side depicts components of J_{SC} gained in defined spectral ranges.

Compared with the SiON_x passivated cell, the SiO₂ passivated cell provides a significantly higher J_{SC} gain in the short and the middle wavelength range. Since the propagation of the R - λ curves appears to be independent from the passivation scheme, the J_{SC} gain of the SiO₂ passivated cell is assumed to be mainly caused by a decrease in recombination losses.

By regarding the internal quantum efficiency IQE in dependence of λ for both passivation schemes in Figure 5.12, a discussion of recombination losses caused by the different passivation schemes is possible. For a better visualization, the graph on the right hand side shows the rescaled IQE of the regarded solar cells in the short wavelength range.

Compared to the SiON_x passivated cell, the SiO₂ passivated cell exhibits a higher IQE in the complete wavelength range between 300 nm and 900 nm. This means that recombination losses are strongly decreased by utilizing the SiO passivation scheme for cell production. Thus, it is confirmed that the very low $J_{0,FSF}$ of the SiO₂ passivated cell leads to a strong decrease in recombination losses at the front side and, as a consequence, to the strong increase in J_{SC} .

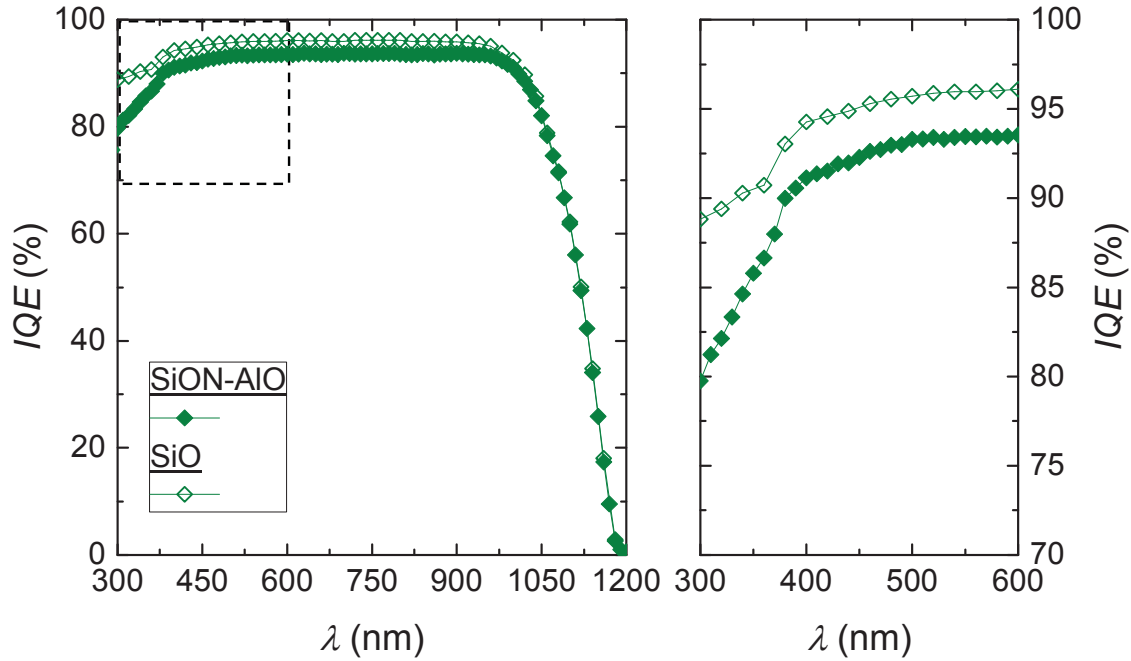


Figure 5.12 Internal quantum efficiency IQE versus wavelength λ for the varied passivation schemes on the left and a detailed view on the IQE in the short wavelength range on the right hand side.

The main conclusion of this section is that an improvement of the BC-BJ solar cell is possible, by integrating thermally grown SiO_2 layers as passivation layers. The integration of a SiO_2 layer at the front side enables a strong decrease in $J_{0,FSF}$ down to 15 fA/cm^2 and, therefore, enables a strong increase in J_{SC} . Unfortunately, the quality of emitter passivation by thermally grown SiO_2 is very low ($J_{0,E} = 577.5 \text{ fA/cm}^2$) and limits the V_{OC} up to around 650 mV . Thus, the high potential of the very low $J_{0,FSF}$ to increase the conversion efficiency of the cell could not be fully exploited.

According to the findings made in this section, the fabrication of a solar cell featuring a thermally grown SiO_2 layer as front and an Al_2O_3 layer as rear side passivation layer would be a promising choice in order to achieve a major increase in conversion efficiency. According to the J_0 demonstrated in the voltage analysis, such cells would feature a passivation limit in V_{OC} of 686.7 mV . By considering for bulk recombination and recombination underneath the metal contacts, the limitation in open circuit voltage drops down to 659.6 mV . By increasing the emitter passivation quality, an increase in V_{OC} might be achievable. The latter issue is one of the key objectives in the following chapter.

5.5 Influence of B-dopant source on cell performance

5.5.1 Motivation

In this section, the impact of two different PECVD processes utilized to deposit a BSG-layer as B-dopant source on the cell performance is discussed.

The solar cell performance of BC-BJ cells strongly depends on the emitter formation. First, the emitter covers a major area of the cell's rear side. Thus, the dark saturation current density of the passivated emitter $J_{0,E}$ has a high impact on the open circuit voltage V_{OC} . Second, impurities incorporated in the BSG-layer might diffuse into the space charge region which is adjacent to the emitter. This would lead to an increase in recombination within the space charge region and, consequently, to a decrease in pseudo fill factor pFF . Third, since the desired emitter regions are uncovered before PECVD, destructive PECVD conditions like, for example, contamination and powerful microwave radiation can result in a decrease in lifetime, minority diffusion length, and therefore short circuit current density J_{SC} .

5.5.2 Cell preparation and characterization

The solar cells were processed according to the base line process (compare section 5.2). As mentioned in the motivation, two different PECVD processes were utilized to deposit a BSG layer. The first PECVD process uses microwave generators for plasma activation. This process is referred to as MW-setup. The second one uses electrical power for plasma activation. This process is referred to as EP-setup. Both processes were investigated in this work. Detailed information concerning the process parameter dependence of the sheet resistance can be found in section 4.2.

The dimensions of the characterized solar cells are depicted in Table 5.6. Compared are solar cells featuring two different pitch distances. Since the width of the BSF x_{BSF} and the width of the gap x_{gap} are constant, the emitter coverage EC increases with increasing pitch distance x_{pitch} .

The fabricated solar cells were characterized by J - V , $SunV_{OC}$, and QE measurements.

To evaluate the impact of the PECVD on the $J_{0,E}$ and the bulk life time, QSSPC measurements were performed. Therefore, symmetrical samples (n -type, FZ, $\rho_{bulk} = 9 \Omega\text{cm}$, $N_{dop} = 5 \cdot 10^{14} \text{ cm}^{-3}$, $W = 214 \mu\text{m}$) were prepared according to the processes used in the base line process. B-diffusion was carried out by using BSG-layers deposited with the two different PECVD processes mentioned above. These layers were deposited on both sides of the wafer. After diffusion and removal of the BSG-layers, the front and the rear side of the wafer were passivated with a stack

consisting of Al_2O_3 and AR-SiN_x . The latter stack corresponds to the one used as rear passivation stack of the cell. The passivation was activated by performing a thermal anneal which was also applied for the solar cells. In order to evaluate the impact of the PECVD process and emitter formation on the bulk carrier lifetime and the $J_{0,E}$, symmetrical samples without emitter were processed as well. Except for the PECVD process used for deposition of BSG-layers, these samples were processed according to the same process sequence.

Table 5.6 Cell dimensions. These are the active cell area A , the wafer thickness W , the pitch distance x_{pitch} , the BSF width x_{BSF} , the width of the gap x_{gap} between emitter and BSF, the emitter coverage EC , the width of the contact openings in the rear side passivation layer, and the width of the BSF electrodes $x_{\text{met},n}$ as well as the one of the emitter electrodes $x_{\text{met},p}$.

A (cm^2)	W (μm)	x_{pitch} (μm)	x_{BSF} (μm)	x_{gap} (μm)	EC (%)	x_{CO} (μm)	$x_{\text{met},n}$ (μm)	$x_{\text{met},p}$ (μm)
4	160	1500	300	100	67	40	200	800
4	160	2500	300	100	80	40	200	1800

The lifetime data obtained by the QSSPC measurements at room temperature was analyzed by using the slope method in high injection ($\Delta n > 10 N_{\text{dop}} = 5 \cdot 10^{15} \text{ cm}^{-3}$). Thus, an extraction of the dark saturation current density J_0 and the bulk carrier lifetime τ_{bulk} was possible.

In the following, cells utilizing a BSG layer deposited with the MW- or the EP-setup are denoted as *MW-cells* or *EP-cells*.

5.5.3 Results and discussion

Table 5.7 depicts the cell parameters extracted from J - V and $\text{Suns } V_{\text{OC}}$ measurements in dependence of the PECVD setup used for deposition of a BSG layer during cell processing for two different pitch distances x_{pitch} of the cell.

Compared to MW-cells, EP-Cells feature a significant increase in conversion efficiency η . By comparing cells with a pitch distance of $1500 \mu\text{m}$, the efficiency increases from 18.1 % (MW-setup) up to 19.4 % (EP-setup). This η gain is caused by

an increase in V_{OC} of 7.4 mV, an increase in J_{SC} of 1.6 mA/cm², and an increase in fill factor FF of 1.3 %_{abs} of the EP-cell compared to the MW-cell.

The increase in FF is explained by regarding the FF losses due to the series resistance expressed by the difference between pseudo fill factor and fill factor $pFF-FF$ and the fill factor losses due to leakage current expressed by the difference between ideal fill factor and pseudo fill factor FF_0-pFF . Independent from the PECVD setup, both cells feature a $pFF-FF$ loss of 5.6 %_{abs} at a x_{pitch} of 1500 μ m. Hence, series resistance losses are similar and the difference in FF originates from FF_0-pFF . The MW-cell features an FF_0-pFF of 5.1 %_{abs}. In comparison, the EP-cell exhibits an FF_0-pFF of 3.9 %_{abs}. Thus, the increase in FF of the EP-cell is the result of a decrease in leakage current.

Table 5.7 J-V characteristics (one sun conditions) of cells in dependence of the PECVD setup utilized for deposition of BSG layers for a pitch distance x_{pitch} of 1500 μ m and 2500 μ m. Demonstrated are the best cells out of every group. The pseudo fill factor pFF and the ideal fill factor are extracted from the J-V curve measured by $SunsV_{OC}$.

PECVD setup (BSG)	x_{pitch} (μ m)	V_{OC} (mV)	J_{SC} (mA/cm ²)	FF (%)	$pFF-FF$ (% _{abs})	FF_0-pFF (% _{abs})	η (%)
MW-setup	1500	642.4	38.5	73.0	5.6	5.1	18.1
	2500	640.1	38.7	69.9	8.5	5.3	17.3
EP-setup	1500	650.0	40.1	74.3	5.6	3.9	19.4
	2500	648.2	40.2	71.1	8.7	4.0	18.5

Independent from the utilized PECVD setup, the efficiency decreases with increasing x_{pitch} . This decrease is caused by an increase in $pFF-FF$ and, consequently, higher series resistance losses. A striking finding is the strong increase in V_{OC} and J_{SC} of EP-cells compared to MW-cells. In the following, these gains are further characterized by regarding the QSSPC and the QE measurements.

Figure 5.13 shows the Auger corrected inverse effective lifetime ($1/\tau_{eff}-1/\tau_{Aug,int}$) versus the carrier injection level Δn for a lifetime sample featuring B-doped surfaces diffused from a BSG layer deposited with the MW-setup (MW-setup), with the EP-setup (EP-setup), and for a lifetime sample without B-doped surfaces (no B-diffusion). The J_0 is extracted by the slope of the linear regression. The intercept of the linear regression is related to the bulk carrier lifetime τ_{bulk} .

The undiffused sample features a very low J_0 of 5.7 fA/cm² and a high τ_{bulk} of around 3.4 ms. By integrating B-doped surfaces in the lifetime samples, the J_0 increases, whereas the τ_{bulk} decreases. Thus, the integration of highly doped surfaces has a

negative impact on J_0 and τ_{bulk} . The negative impact on the J_0 might be caused by Auger recombination and surface recombination which are both in a positive correlation with the dopant concentration. The negative impact on τ_{bulk} might be caused by crystalline damage in the silicon wafer originating from Si-B precipitates on the one and by a destructive impact of the utilized PECVD process on the other hand. By comparing the lifetime samples featuring highly doped surfaces, the lifetime sample processed with the EP-setup features a lower J_0 and a higher τ_{bulk} than the lifetime sample processed with the MW-setup. These results suggest that emitter formation from a BSG-layer deposited with the EP-Setup is less destructive and provides emitters with a higher passivation quality.

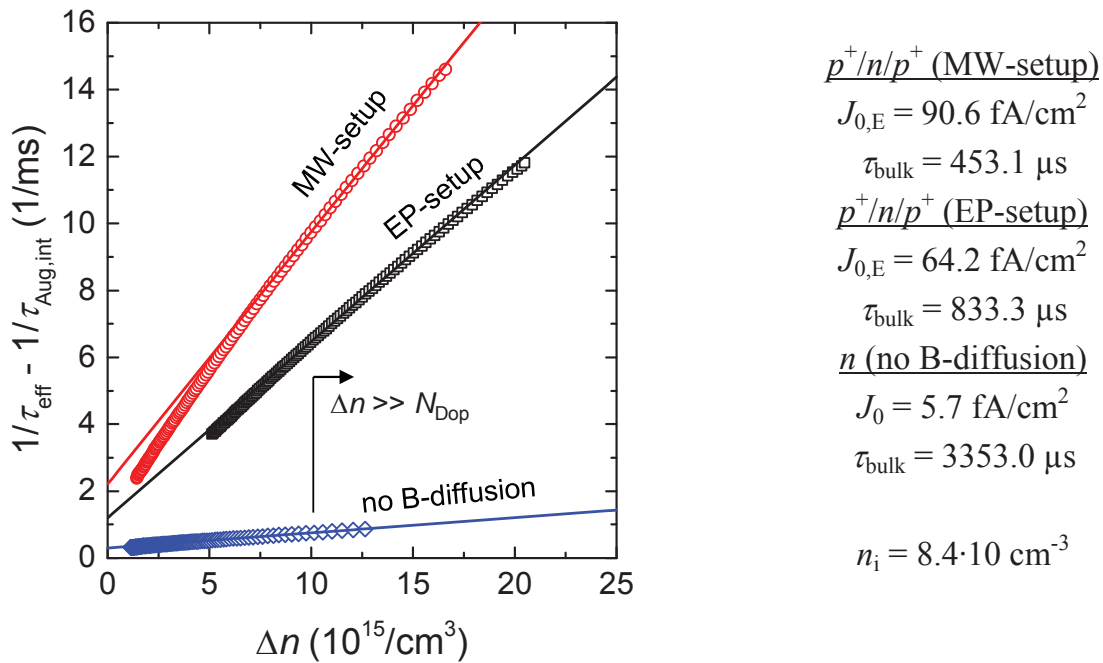
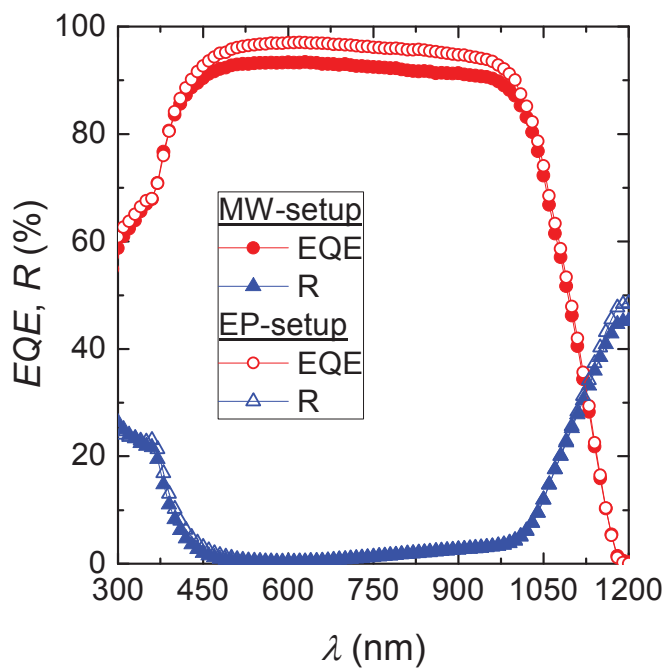


Figure 5.13 Inverse lifetime measured by QSSPC at room temperature in dependence of the injection level. Dark saturation current density J_0 and bulk carrier lifetime τ_{bulk} of the processes are calculated according the slope method in high injection ($\Delta n \gg N_{\text{Dop}}$). The intrinsic carrier concentration n_i used for calculations is depicted as well.

The external quantum efficiency EQE and the reflection R in dependence of the wavelength λ for cells fabricated with the compared PECVD processes are depicted in Figure 5.14. The measurements were performed with cells featuring a x_{pitch} of $1500 \text{ } \mu\text{m}$.

The EQE - λ curve of the EP-cell corresponds to a J_{SC} of 40.4 mA/cm². The one of the MW-cell corresponds to a J_{SC} of 39.1 mA/cm². Again, the J_{SC} values extracted from J - V and QE measurements slightly differ to each other. Nevertheless, these differences are assumed to be caused by measurement uncertainties. Especially in the middle wavelength range, the EP-cell provides a prominent increase in J_{SC} by 0.8 mA/cm² up to 19.6 mA/cm². The EQE in the middle wave length range is very sensitive to the bulk life time. In the following, recombination effects are further discussed by regarding the IQE of both cells.



MW-setup	
λ range (nm)	J_{SC} gain (mA/cm ²)
300-600	12.4
601-900	18.8
901-1200	7.9

EP-setup	
λ range (nm)	J_{SC} gain (mA/cm ²)
300-600	12.7
601-900	19.6
901-1200	8.1

Figure 5.14 External quantum efficiency EQE and reflection R in dependence of the wavelength λ for solar cells manufactured with BSG deposited with two different PECVD techniques. The table on the right hand side depicts components of J_{SC} gained in defined spectral ranges.

The internal quantum efficiency IQE of the cells in dependence of the wavelength λ is depicted in Figure 5.15. The graph on the right hand side indicates a magnified section of the IQE in the middle wavelength range. Notice again that the IQE mainly depends on recombination losses.

Compared to the MW-cell, the EP-cell indicates a significant increase in IQE in the middle wavelength range. The IQE of the EP-cell approximates an IQE of 98 %. In comparison, the MW-cell features an IQE below 94 %. Thus, the EP-cell indicates significantly lower recombination in the middle wavelength range which finally leads

to the regarded increase in J_{SC} . The $IQE-\lambda$ curves in the short and long wave length range only differ marginally from each other.

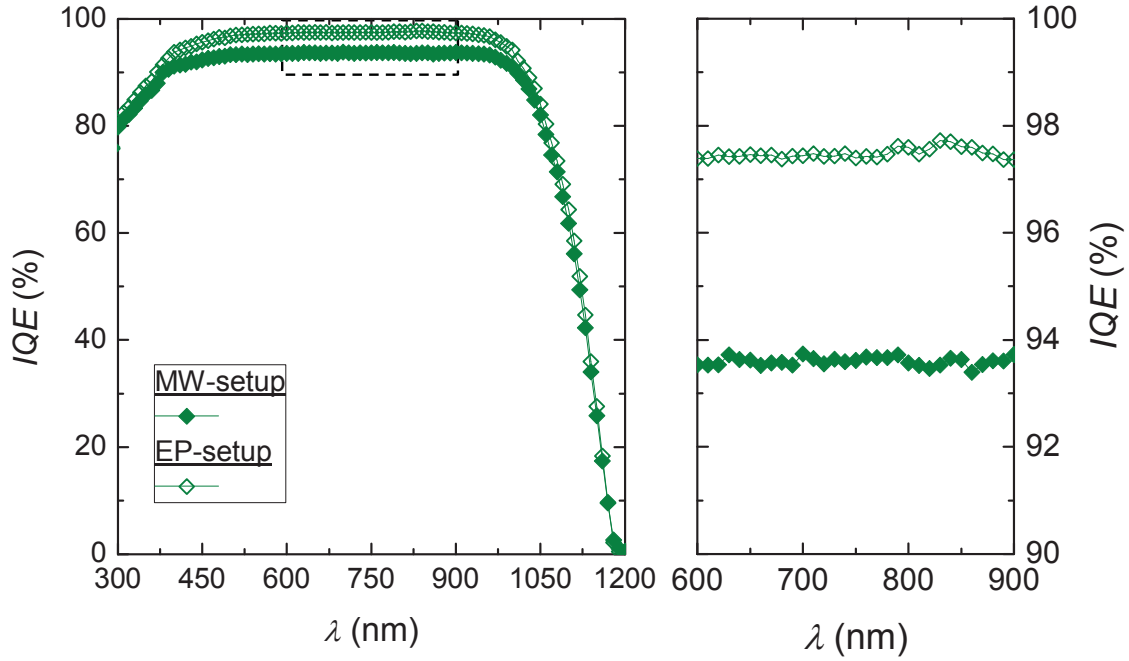


Figure 5.15 Internal quantum efficiency IQE versus wavelength λ for solar cells manufactured with a BSG layer deposited with two different PECVD techniques.

To conclude, the integration of a BSG layer used as dopant source for emitter formation based on an electrical power source (EP-setup) for plasma activation has several advantages compared to the setup using microwaves for plasma generation (MW-source). The gain in efficiency is based on a low $J_{0,E}$, a low negative impact on the bulk carrier lifetime, and a decrease in leakage current detectable in the improved pseudo fill factor pFF . A solar cell featuring thermally grown SiO_2 as front side passivation layer ($J_{0,FSF} = 14.8 \text{ mA/cm}^2$, compare section 5.4) and an emitter diffused from a BSG-layer deposited with the EP-setup ($J_{0,E} = 64.2 \text{ mA/cm}^2$) would provide a passivation limit in V_{OC} of around 691.9 mV. Moreover, the integration of a SiO_2 layer as front side passivation layer and a BSG layer deposited with the EP-setup were found to prominently increase the J_{SC} . Thus, a major increase in efficiency is expected as both modifications of the base line process are combined. Unfortunately, the limitation in V_{OC} drops down to 661.3 mV as bulk recombination and contact recombination are considered.

Since the FF and the pFF are still limiting the efficiency, the next section deals with a modification of the cell structure. This modification aims at a decrease in leakage

current by manipulating the highly doped surfaces, on the one hand, and a decrease in process complexity by omitting the gap region, on the other hand side.

5.6 Influence of cell structure on cell performance

5.6.1 Motivation

In this section, the cell structure of the BC-BJ cells is varied. Therefore, cells with and without gap region featuring shallowly and deeply diffused doped surfaces are investigated. Cells without gap exhibit several advantages. By assuming a constant dimension for the pitch distance and the BSF, the emitter coverage of the cell increases. This increase is assumed to be connected to an increase in minority collection probability and, hence, to an increase in J_{SC} . However, adjacent emitter and BSF regions might generate an increase in leakage current due to trap assisted tunneling and, in consequence, to an increase in the dark saturation current density J_{02} and/or a decrease in the shunt resistance [131, 132]. A technological advantage of cells without gap is that the process sequence omits a complete patterning module, in fact the gap-definition.

Compared to shallowly diffused doped surfaces, deeply diffused doped surfaces have the following advantages. Up to now, the demonstrated BC-BJ cells have a low pseudo fill factor ($pFF < 80\%$) indicating a high leakage current. As discussed, one possible cause of the high leakage current is assumed to be caused by aluminum spiking. Aluminum spiking means the penetration of aluminum through the space charge region. The undesired process is caused by the high solubility of silicon in aluminum at high temperatures [133] and was already reported by several researchers, e.g. Kathkouda et al. [134]. The integration of deep dopant profiles might be a possibility to increase the so-called spiking resistance, decrease the leakage current, and to increase the pFF . In this work, deep dopant profiles were realized by performing a second thermal process after the removal of the dopant sources.

5.6.2 Cell preparation and characterization

In order to realize solar cell structures without gap and with deeply diffused doped surfaces, the BC-BJ base line process was changed according to the following modifications (see also Figure 5.16).

The realization of gap free BC-BJ solar cells was performed by leaving out the PECVD of the SiO_x layer (b-3) and the following patterning module referred to as the gap-definition (b-4). Hence, the deposition of the BSG layer was carried out directly after patterning the PSG/ SiO_x stack on the rear side of the solar cell. The described

process modification leads to an increase in the interface area between BSG and silicon and, thus, to an increase in emitter coverage EC if the dimensions of the pitch distance x_{pitch} and the BSF width x_{BSF} are kept constant, as done in this work.

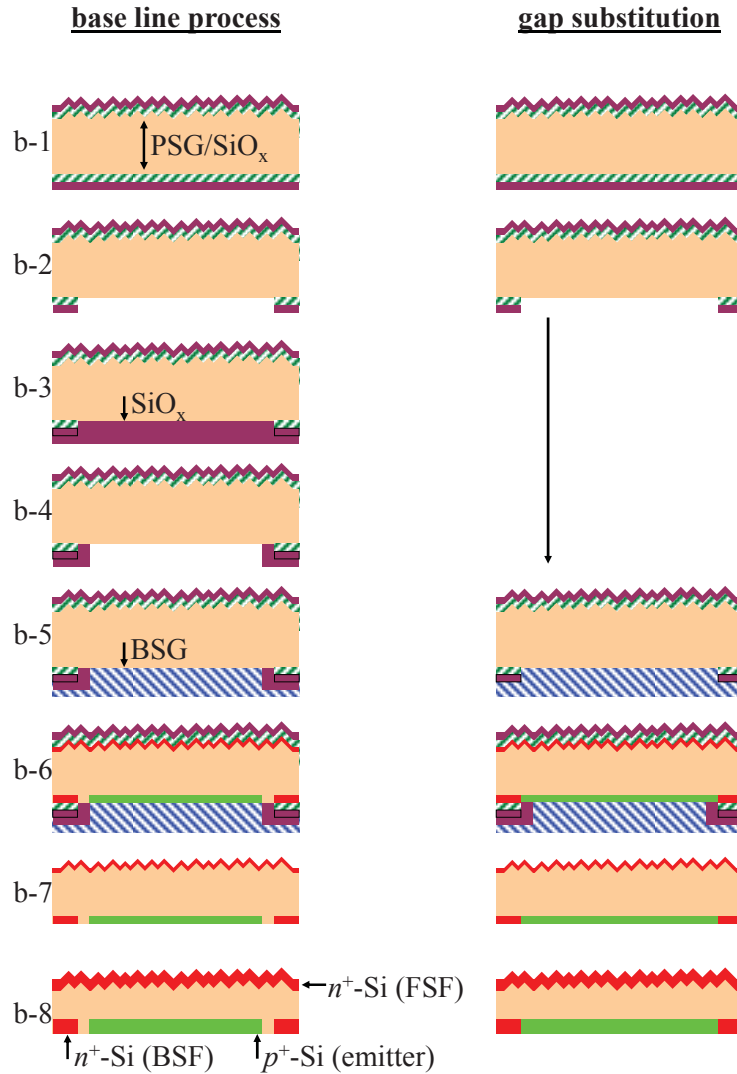


Figure 5.16 Base line process (left) used for the assembly of BC-BJ solar cells and gap substitution (right hand side) as evaluated in this section. For the assembly of a device without gap region between BSF and emitter, one deposition process (b-3) and a patterning module (b-4) are omitted. For the realization of deeply diffused areas, a so-called drive-in process is performed after the removal of dopant sources (b-8).

The integration of deeply diffused surfaces was realized by utilizing a second thermal treatment, the so-called drive-in process (b-8), after removal of the solid dopant sources (b-7). The drive-in process was performed in a quartz tube furnace. The temperature profile of choice features one temperature plateau with a maximum temperature of 1000°C and a plateau time of 60 minutes. In order to avoid the thermal

growth of a silicon dioxide layer on both sides of the wafer, the process chamber was flushed with nitrogen as inert gas. Due to boron segregation, the growth of silicon dioxide on B-doped surfaces might lead to a prominent depletion of boron at the silicon surface as Benick et al demonstrated on cell level [135]. The denudation might be related to an excess carrier dependent life time and a prominent increase in contact resistance. By flushing the process chamber with an inert gas, the latter risks are assumed to be preventable.

Table 5.8 Cell dimensions. These are the active cell area A , the wafer thickness W , the pitch distance x_{pitch} , the BSF width x_{BSF} , the width of the gap x_{gap} between emitter and BSF, the emitter coverage EC , the width of the contact openings in the rear side passivation layer, and the width of the BSF electrodes $x_{met,n}$ as well as the one of the emitter electrodes $x_{met,p}$.

A (cm ²)	W (μ m)	x_{pitch} (μ m)	x_{BSF} (μ m)	x_{gap} (μ m)	EC (%)	x_{CO} (μ m)	$x_{met,n}$ (μ m)	$x_{met,p}$ (μ m)
4	160	1500	300	100	67	40	200	800
4	160	1500	300	0	80	40	200	800

In the following section, the performance of BC-BJ solar cells with and without gap and with and without drive-in is discussed. Cells with a x_{pitch} of 1500 μ m and a x_{BSF} of 300 μ m are compared. For a complete presentation of the cell dimensions see Table 5.8. Cells with gap ($x_{gap} = 100$ μ m) feature an emitter coverage of 67 %. In comparison, cells without gap ($x_{gap} = 0$ μ m) feature an emitter coverage of 80 %.

To characterize the impact of the drive-in process on the dopant concentration profile of the BSF, the FSF, and the emitter, the realized doped surfaces were characterized by ECV measurements. The fabricated solar cells were characterized by J - V measurements, $SunsV_{OC}$ measurements, and QE measurements. Cross sections were fabricated to estimate the penetration depth of spikes. These cross sections were analyzed with the help of a scanning electron microscope (SEM). In the following, cells processed without drive-in are referred to as *initial cells*, whereas cells with drive in are denoted as *drive-in cells*.

5.6.3 Results and discussion

Figure 5.17 depicts the carrier concentration profiles of the emitter, the BSF, and the FSF without (thin lines, see also Figure 5.5) and with drive in (thick lines).

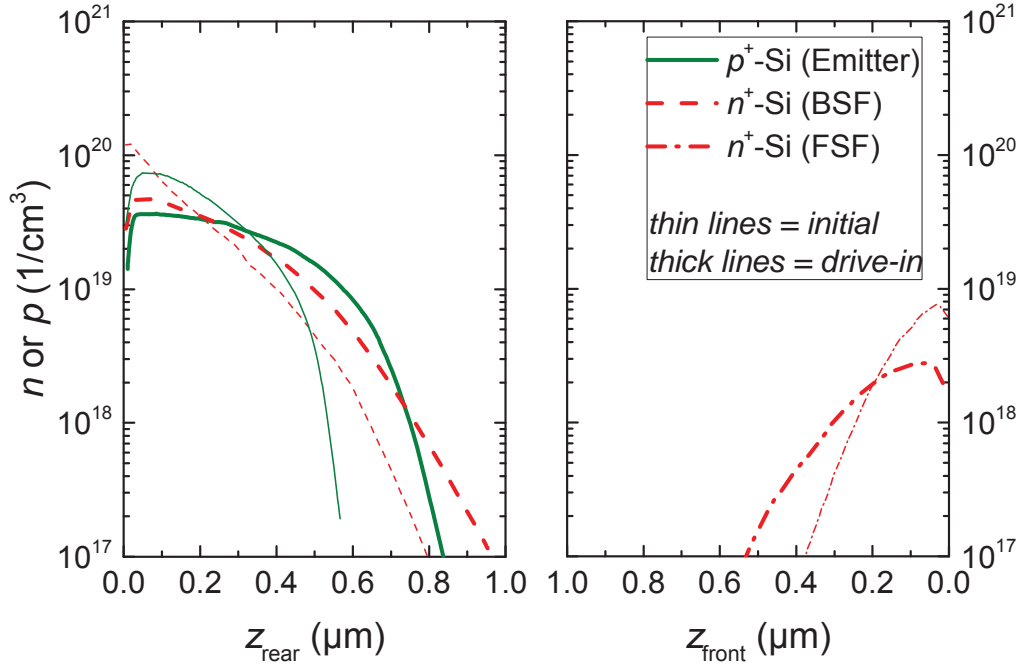


Figure 5.17 Electron concentration (n) or hole concentration (p) in dependence of the wafer depth. The left graph shows the electron and hole concentration of the BSF and the emitter in dependence of the depth relative to the rear surface (z_{rear}). The right graph depicts the electron concentration profile of the FSF in dependence of the depth relative to the front surface (z_{front}). Carrier concentration profiles of doped surfaces without drive-in are shown as thinner lines, whereas doped surfaces with drive-in are highlighted as thicker lines.

The impact of the drive-in process on the initial carrier concentration profiles of the highly doped surfaces (emitter, BSF, and FSF) after co-diffusion is the following. Due to the drive-in process and the absence of dopant sources during the second thermal treatment, the dopant concentration profiles were manipulated. This manipulation is related to a decrease in dopant concentration and an increase in profile depth. The sheet resistance of the doped surfaces was found to be independent from the drive-in process. In the case of the emitter, the maximum hole concentration decreases from $7.4 \cdot 10^{19} \text{ cm}^{-3}$ (initial) down to $3.6 \cdot 10^{19} \text{ cm}^{-3}$ (drive-in). The depth of the hole concentration profile increases from around 600 μm (initial) up to around 839 nm (drive-in). Notice again that the depth of the carrier profiles is extracted at the intersection of an exponential regression fitting the ECV measured data and a constant carrier concentration of $1 \cdot 10^{17} \text{ cm}^{-3}$. In the case of the BSF, the maximum electron

concentration decreases from $1.2 \cdot 10^{20} \text{ cm}^{-3}$ (initial) down to $4.8 \cdot 10^{19} \text{ cm}^{-3}$ (drive-in). The profile depth increases from 796 nm (initial) up to 966 nm (drive-in). The FSF exhibits a decrease in maximum electron concentration from $6.8 \cdot 10^{18} \text{ cm}^{-3}$ (initial) down to $2.8 \cdot 10^{18} \text{ cm}^{-3}$ (drive-in), whereas the profile depth increases from 376 nm (initial) up to 531 nm (drive-in).

Table 5.9 depicts the J - V characteristics of cells with and without gap and with and without drive-in. The most striking result to emerge from the data is that a conversion efficiency η of 20 % was obtained by cells without gap and with drive-in. In the following, the influences of the cell structure on the cell performance are discussed.

Table 5.9 J - V characteristics (one sun conditions) of solar cells in dependence of the cell structure. The pseudo fill factor (pFF) and the ideal fill factor (FF_0) are extracted from the J - V curve measured by Suns V_{OC} . Compared are cells with and without gap and with and without drive-in. Depicted are the best cells out of every group.

Cell structure		V_{OC}	J_{SC}	FF	pFF - FF	FF_0 - pFF	η
Gap	Drive-in	(mV)	(mA/cm ²)	(%)	(% _{abs})	(% _{abs})	(%)
no	no	639.3	38.7	74.3	3.6	5.9	18.4
yes	no	642.4	38.6	73.0	5.6	5.1	18.1
no	yes	656.9	40.6	75.2	4.9	3.9	20.0
yes	yes	652.7	40.0	73.7	6.2	4.0	19.2

By comparing the initial cells (no drive-in) with and without gap region, the omission of the gap enables a slight increase in efficiency. This efficiency gain mainly results from an increase in fill factor FF of 1.3 %_{abs}. The increase in FF is accompanied by a minor increase in FF_0 - pFF of 0.8 %_{abs} and a major decrease in pFF - FF of 2.0 %_{abs}. Thus, the omission of the gap leads to a slight increase in leakage current and a strong decrease in series resistance. The open circuit voltage V_{OC} and the short circuit current density J_{SC} of both cell structures are independent from the presence of a gap region.

It is expected that the decrease in series resistance is partly provided by an increase in lateral conductivity in silicon in the range of the substituted gap regions. The slight increase in FF_0 - pFF losses of the cells without gap might be caused by an amplification of trap assisted recombination current in the space charge region, for example. However, by comparing the mean and standard deviation of four cells of each group (no drive-in, with and without gap), the difference in FF_0 - pFF is rather insignificant. Compared to cells without gap featuring an FF_0 - pFF in the range of 6.1 ± 0.2 %, cells with gap indicate an FF_0 - pFF in the range of 6.8 ± 1.5 %.

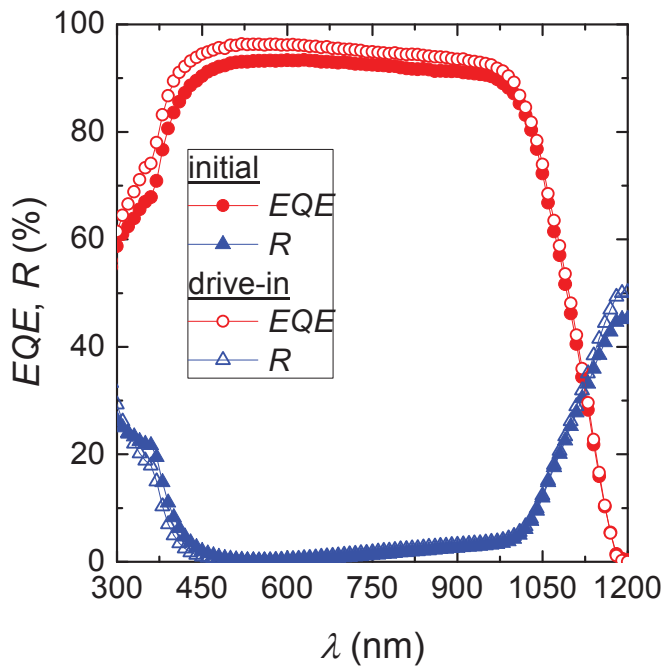
By comparing the cells integrating gap regions with and without drive-in, a striking increase in J_{SC} and V_{OC} is detectable for cells fabricated with the drive-in process. Drive-in cells exhibit an increase in J_{SC} of 1.4 mA/cm^2 and an increase in V_{OC} of 10.3 mV . It is expected that the decrease in dopant concentration of the deeply diffused profiles leads to a decrease in recombination caused by a decrease in surface and Auger recombination. The connected improvement of the solar cell passivation quality, especially the improvement of the front side passivation quality, causes the observed increase in V_{OC} and J_{SC} . Moreover, the drive-in cell shows a higher FF than the initial cell. This FF gain is the result of a minor decrease in pFF - FF of $0.6 \%_{abs}$ and a major decrease in FF_0 - pFF of $2.1 \%_{abs}$. Consequently, drive-in cells have a higher series resistance, whereas the leakage current is lower. The increase in series resistance of the drive-in cell might be caused by an increase in the specific contact resistivity. The electrical contact resistivity of Al-Si electrodes on B- and P-doped surfaces is known to increase with decreasing dopant surface concentration. Since the drive-in process is related to a decrease in dopant concentration at the silicon surface, an increase in contact resistivity and, hence, series resistance is possible. The major decrease in leakage current of drive-in cells is assumed to be caused by a major increase in spiking resistance which originates from the high depth of the emitter.

The achieved increase in efficiency caused by substituting the gap region is valid for drive-in cells as well. The cell with gap region indicates an efficiency of 19.2% . In comparison, the cell without gap region indicates a gain in efficiency of $0.8 \%_{abs}$ up to 20.0% . This increase is caused by an increase in V_{OC} of 4.2 mV , in J_{SC} of 0.6 mA/cm^2 and an increase in FF of $1.5 \%_{abs}$. The increase in V_{OC} and J_{SC} of cells without gap is assumed to be caused by the increase in emitter coverage leading to an increase in minority collection probability. The increase in FF is caused by a significant decrease in series resistance which was also observed for the initial cells. Moreover, the comparable leakage current of the drive-in cells leads to the assumption that the substitution of the gap region is not related to an increase in trap assisted recombination currents in the space charge region.

Major observations are that the substitution of the gap region and the execution of the drive-in process have a positive impact on the cell performance. In order to further evaluate the gain in J_{SC} of cells fabricated with the drive-in process, QE measurements of cells with and without drive-in are compared. To verify that spiking is an issue limiting the FF , the penetration depth of spikes is evaluated.

The external quantum efficiency EQE and reflection R versus wavelength λ for a cell without drive-in (initial) and with drive-in are depicted in Figure 5.18. Compared to initial cells, drive-in cells feature a significant increase in EQE over the complete

wavelength range. By calculating from the EQE , the drive in cell features a J_{SC} of 40.3 mA/cm^2 , whereas the initial cell features a J_{SC} of 39.1 mA/cm^2 . The total increase in J_{SC} of the drive-in cell is mainly caused by an increase in J_{SC} gain of 0.5 mA/cm^2 in the low and middle wave length range. Moreover, the drive-in cell features a simultaneous increase in EQE and R in the long wavelength range. This effect is probably caused by the drive-in related decrease in dopant concentration at the rear side and the related decrease in free carrier absorption.



initial	
λ range (nm)	J_{SC} gain (mA/cm^2)
300-600	12.4
601-900	18.8
901-1200	7.9

drive-in	
λ range (nm)	J_{SC} gain (mA/cm^2)
300-600	12.9
601-900	19.3
901-1200	8.1

Figure 5.18 External quantum efficiency EQE and reflection R in dependence of the wavelength λ for solar cells manufactured with and without drive-in. Cells without drive-in are labeled as initial. The table on the right hand side depicts components of J_{SC} gained in defined spectral ranges.

The internal quantum efficiency IQE versus wavelength λ of the cells in question is depicted in Figure 5.19. The graph on the right hand side indicates a magnified section of the IQE in the short wavelength range.

Compared to the initial cell, the drive-in cell features an increase in IQE over the complete wavelength range. This increase is very prominent in the low and the middle wavelength range. Both cells feature a drop in IQE in the short wavelength range. In the case of the initial cell, the IQE features a value of 79.8 % at a wavelength of 300 nm increasing up to the maximum value of 93.7 % at a wavelength 700 nm. In comparison, the drive-in cell features an IQE of 87.0 % at 300 nm increasing up to a maximum value of 96.4 % at 520 nm. Thus, the drive-in cell exhibits a significant

decrease in front and bulk recombination. The decrease in front recombination is assumed to be related to the decrease in dopant concentration in the FSF. Moreover, it is assumed that the decrease in front recombination leads to an increase in the minority diffusion length. Thus, the *IQE* in the middle wavelength range, which is very sensitive to the minority diffusion length, increases as well [136].

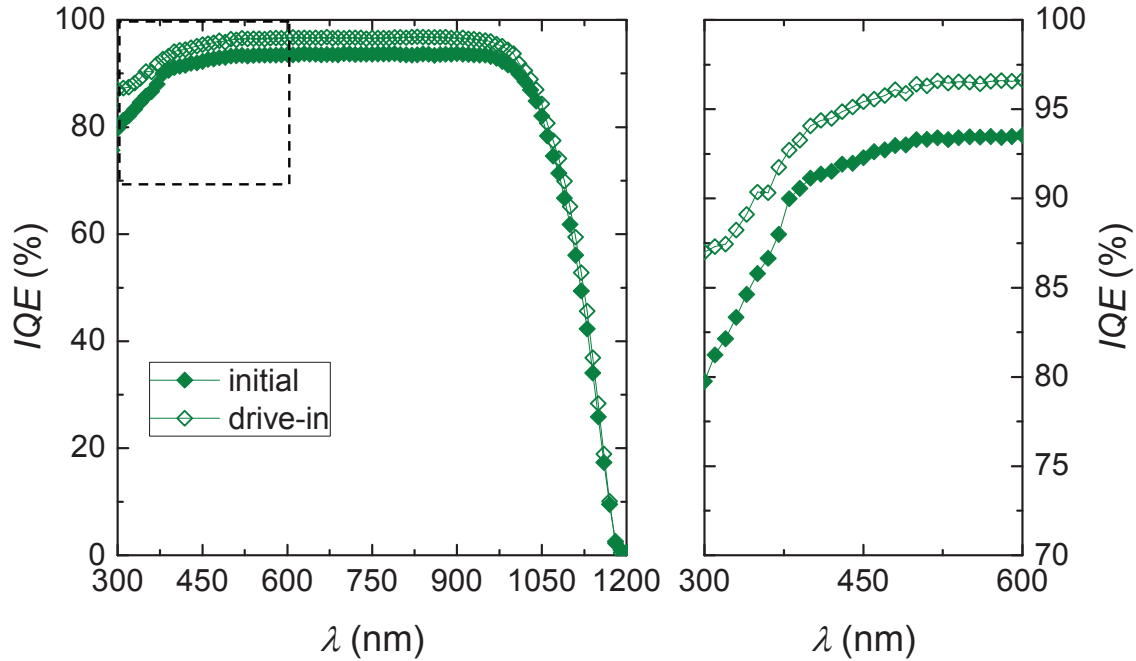


Figure 5.19 Internal quantum efficiency *IQE* versus wavelength λ for solar cells manufactured with and without drive-in. Cells without drive-in are labeled as initial. The graph on the right hand side shows the *IQE* of the compared cells in the short wavelength range.

As already mentioned, the initial cells suffer from a high leakage current. Especially by using Al or Al-Si alloys as electrode material, spiking issues can feature a strong impact on the leakage current and, consequently, on the efficiency. Figure 5.20 presents a magnified cross section of a BC-BJ solar cell, depicting the electrical contact between a selected Al-Si metal finger and the BSF (n^+ -Si). Notice that the growth of spikes is assumed to be independent from the doping-type and to feature a major destructive impact on the cell performance if they penetrate through the emitter (p^+ -Si) and the surrounding space charge region. Clearly visible is the formation of a metal spike penetrating the silicon bulk until a depth of approximately 580 nm. In the case of drive-in cells featuring an emitter depth of around 510 μm , this penetration depth of the spike is sufficient to short circuit the space charge region. In the case of drive-in cells featuring an emitter depth of around 839 μm , cells are assumed to be less

prone to spiking. Thus, the latter assumption is a possible explanation for the increase in leakage current of the initial cells featuring a pFF limitation between 77.9 % to 78.6 %.

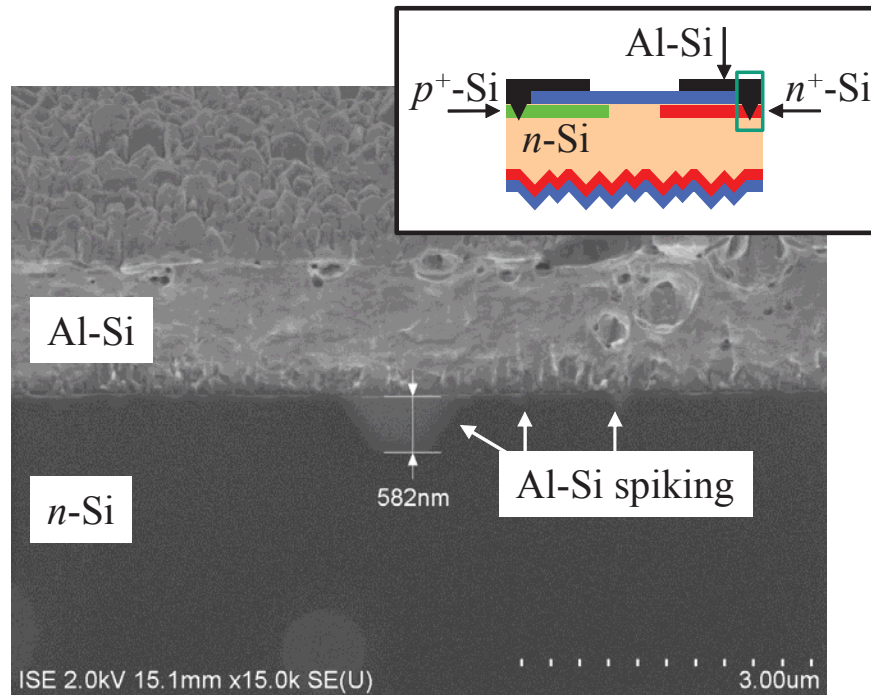


Figure 5.20 Cross section of a BC-BJ solar cell in the range of the interface Al-Si/ n^+-Si (BSF) recorded by SEM. Spikes feature a penetration depth up to 582 nm and are therefore deep enough to penetrate through the emitter (p^+-Si) and the surrounding space charge region.

The present section exhibits important findings guiding the way for further solar cell improvements. One major finding is that gap free solar cells do not significantly suffer from an additional leakage current arising from enhanced recombination in the space charge region between emitter and BSF. On the contrary, the efficiency increases significantly due to an increase in FF and J_{SC} . The FF was assumed to increase due to an increase in intrinsic conductivity of the solar cell. The J_{SC} was expected to increase due to an increase in emitter coverage and the corresponding increase in minority collection probability. For upcoming solar cell improvements, the gap free solar cell without gap region is of high interest, because the process sequence features a drastic reduction in process steps. Thus, one PECVD process and a complete patterning module including inkjet printing, etching, ink removal, and cleaning can be omitted.

The second major finding is that the drive-in process, utilized to manipulate the doped surfaces, allows for a strong increase in efficiency. Thus, a solar cell with an efficiency of 20.0 % could be processed. The increase in efficiency was found to be mainly caused by an increase in J_{SC} and FF . The J_{SC} was assumed to increase due to an

increase in front side passivation quality which has a positive impact on the IQE in the low and the middle wave length range. A quite similar impact on the J_{SC} was already found by integrating silicon dioxide layers as front and rear side passivation (compare section 5.4). The increase in FF was found to be related to an increase in spiking resistance. Unfortunately, since the drive-in solar cell is fabricated according to a process sequence featuring an additional cost-intensive thermal treatment, the solar cell is not of high interest for industrial application. However, the cell results reveal that a major increase in efficiency is possible by increasing the front side passivation quality and the spiking resistance.

After regarding the impact of metal thickening in the next section, further solar cell improvements focus on the gap free solar cell without drive-in.

5.7 Influence of metal thickening on cell performance

5.7.1 Motivation

In the last section, BC-BJ solar cells with conversion efficiencies up to 20.0 % were demonstrated. Since these solar cells still clearly suffer from fill factor losses, this section deals with an improvement of the fill factor FF .

The best cell features an FF of 75.7 %, a pseudo fill factor pFF of 80.1 %, and an ideal fill factor FF_0 of 84.0 %. The difference in ideal fill factor and pseudo fill factor $FF_0 - pFF$ of 3.6 %_{abs} is caused by leakage current. Al spiking was found to be one major mechanism inducing these losses. The difference between pseudo fill factor and fill factor $pFF - FF$ of 4.4 %_{abs} is caused by the series resistance. Since the cells are in a readily processed state, the FF losses caused by shunting are inherent and cannot be resolved anymore. The FF losses due to series resistance are dividable into intrinsic and extrinsic series resistance losses. Intrinsic series resistance losses arise from the series resistance components of the wafer. These are the series resistance of the highly doped surfaces (FSF, BSF, and emitter) and the bulk. Extrinsic series resistance losses originate from the series resistance components of the metallization. These are the contact resistance and the resistance of the metal fingers. Intrinsic series resistance losses and extrinsic losses due to the contact resistance are not resolvable anymore. However, the extrinsic series resistance losses caused by the metal fingers might be improvable. The latter improvement is the objective of this section and is performed by thickening the metal fingers with a plating process.

5.7.2 Cell modification and characterization

The thickening of the Al-Si metal fingers was performed by using a zincate process followed by electrically driven Ag-plating. The zincate process is a wet chemical dipping process in an alkaline solution consisting of zinc oxide (ZnO), sodium hydroxide (NaOH), and potassium sodium tartarate ($\text{KNaC}_4\text{H}_4\text{O}_6$). The chemical components allow for a simultaneous removal of aluminum oxide upon the Al-Si surface and the deposition of zinc. Thus, dielectric aluminum oxide is substituted by zinc which is known to be compatible with plating processes [137].

Table 5.10 Cell dimensions. These are the active cell area A , the wafer thickness W , the pitch distance x_{pitch} , the BSF width x_{BSF} , the width of the gap x_{gap} between emitter and BSF, the emitter coverage EC , the width of the contact openings in the rear side passivation layer, and the width of the BSF electrodes $x_{\text{met},n}$ as well as the one of the emitter electrodes $x_{\text{met},p}$.

A (cm^2)	W (μm)	x_{pitch} (μm)	x_{BSF} (μm)	x_{gap} (μm)	EC (%)	x_{CO} (μm)	$x_{\text{met},n}$ (μm)	$x_{\text{met},p}$ (μm)
4	160	1500	300	0	80	40	200	800
4	160	2000	300	0	85	40	200	1300

The diagram illustrates the cross-section of a BC-BJ cell. It shows the following layers and dimensions from top to bottom: a passivation layer (blue) with contact openings of width $x_{\text{CO},n}$ and $x_{\text{CO},p}$; an n^+ -Si (BSF) layer (red) with width x_{BSF} ; a p^+ -Si (emitter) layer (green) with width x_{emitter} ; and an n -type Si substrate (orange). Metal electrodes (black) are deposited on the BSF and emitter layers, with widths $x_{\text{met},n}$ and $x_{\text{met},p}$ respectively. The pitch distance x_{pitch} is the total width of one cycle of emitter and BSF regions. A gap x_{gap} is shown between the emitter and BSF regions.

In order to investigate the pitch distance dependent impact of metal thickening on the cell performance, cells with two different pitch distances were modified. The dimensions of the BC-BJ cells are depicted in Table 5.10. In order to get an insight in the dimensions of the modified metal fingers, the cells were analyzed with the help of a light microscope before and after plating. To investigate the thickness and the composition of the single layers, cross sectional samples were prepared and analyzed with SEM and energy dispersive X-ray (EDX) measurements. In order to evaluate the impact of the plating process on the cell performance, cells were characterized by J - V and $\text{Suns } V_{\text{OC}}$ measurements before and after plating.

5.7.3 Results and discussion

The microscopic top view on the rear side of a selected BC-BJ cell before and after plating is depicted in Figure 5.21. In order to point out the position of the

microscopically recorded images upon the rear side of the cell, the plated rear side of the complete small-size cell is depicted as well (right hand side). The microscopic images show the n -metal finger at the center. The outer borders of the p -metal fingers are visible at the left and the right hand side of every microscopic picture. In between the n -metal and p -metal fingers non-metalized areas are visible. These areas feature a width of approximately $250\text{ }\mu\text{m}$.

Topview on rear side

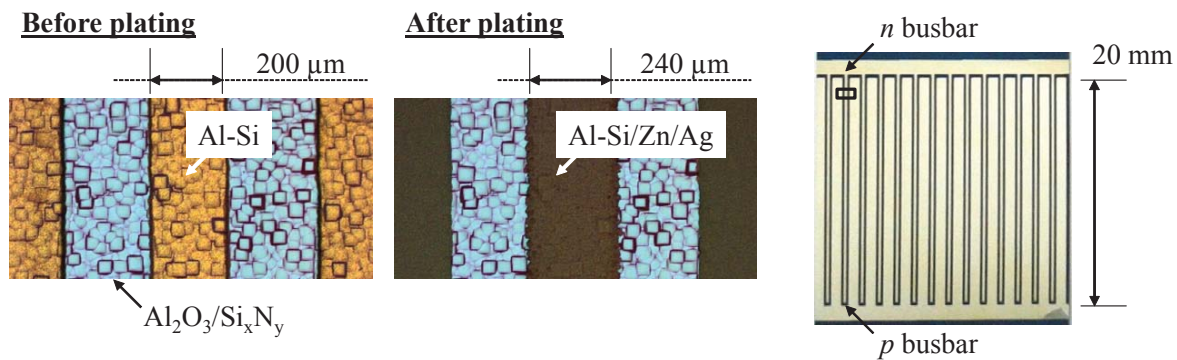


Figure 5.21 Microscopic top view on BC-BJ cells before (left) and after plating (middle). The picture on the right hand side depicts the top view on the complete rear side of the small-size BC-BJ cell after plating. The magnified area is highlighted by a small black frame.

By comparing the microscopic images before and after plating, a lateral growth of the fingers is recognizable. This lateral growth has an expansion of around $20\text{ }\mu\text{m}$ per edge. By comparing the distance of certain pillows on the silicon surface with the outer edges of the n -fingers before and after plating, the lateral growth is detectable as well. Due to the alignment accuracy of the inkjet printer of $\pm 10\text{ }\mu\text{m}$, the width of the n -metal fingers after plating ($250\text{ }\mu\text{m}$) and the BSF fingers ($300\text{ }\mu\text{m}$), the lateral growth is not assumed to be critical for the cell performance. As long as metal fingers do not overlap the space charge region between BSF and emitter, an increase in leakage current is expected to be negligible. Else, plating is assumed to increase the leakage current due to defects like pinholes in the passivation layers.

The cross-section of the plated n -metal finger is depicted in Figure 5.22. Therefore, a magnified picture recorded by SEM is depicted on the left and the same including the composition analysis characterized by EDX is depicted on the right hand side. The Al-Si layer indicates a layer thickness of around $3\text{ }\mu\text{m}$. The plated Ag layer features a layer thickness of around $3\text{ }\mu\text{m}$ as well. In between the Al-Si layer and the Ag-layer, the thin Zn layer is visible. Usually, plating leads to an isotropic finger growth. This

means that the lateral and vertical finger growth should be the same. Since a lateral finger growth of 20 μm per edge was detected, here, this is not the case. One possible reason for this might be that aluminum residuals are available at the edges of the fingers before plating, which are not visible by microscopy. These residuals might be plated as well.

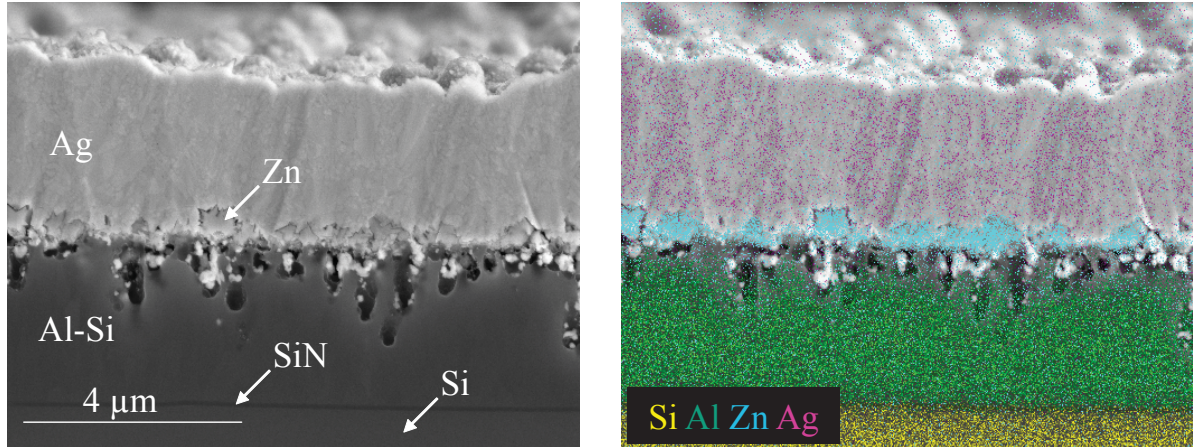


Figure 5.22 SEM picture (left) and EDX measurement (right) recorded with the help of a cross-section sample. The different colors of the EDX measurement represent the different materials of the metal stack consisting of an Al-Si layer, a Zn layer and a plated Ag layer.

The SEM picture including the EDX analysis allows for an analysis of the composition of the plated metal finger. The most important finding was that the Ag layer does not seem to include an aluminum contamination due to Al-out diffusion. Thus, the Ag layer should provide adequate conditions for contacting those fingers with cell connectors. The contacting behavior of cell integrated electrodes with cell connectors is of importance in order to integrate large-size cells in modules.

The cell characteristic parameters of the modified cells are depicted in Table 5.11. Therefore, the parameters are listed in dependence of the execution of a plating step for two different pitch distances x_{pitch} . A calibrated measurement of the best cell is depicted as well.

Independent from the x_{pitch} , the FF increases after plating. The cell featuring a x_{pitch} of 1500 μm exhibits an FF of 75.2 % before plating and an FF of 75.9 % after plating. The FF gain of 0.7 %_{abs} is caused by a decrease in series resistance. The conversion efficiency η of the cell increases by 0.2 %_{abs} up to 20.2 %. In the case of the cell featuring a x_{pitch} of 2000 μm , the fill factor gain of 1.0 %_{abs} is more prominent and enables an increase in efficiency from 19.9 % up to 20.2 % by 0.3 %_{abs}.

The grid series resistance $R_{S,\text{grid}}$ is expressed by the following equation.

$$R_{S,grid} = \frac{1}{3} \frac{\rho_{met} y_{met}^2}{h_{met}} \left(\frac{x_{pitch}}{x_{met,n}} + \frac{x_{pitch}}{x_{met,p}} \right) \quad (5-6)$$

Thus, the grid series resistance is a function of the specific resistivity ρ_{met} , the finger length y_{met} , the finger height h_{met} , the width of the n -metal $x_{met,n}$ and the p -metal finger $x_{met,p}$, and the pitch distance x_{pitch} . The equation reveals a linear dependence of $R_{S,grid}$ on x_{pitch} . Solar cells with a high x_{pitch} feature a high $R_{S,grid}$ and, consequently, a high potential in decreasing the series resistance by plating. This explains the more prominent increase in FF of cells featuring a x_{pitch} of 2000 μm compared to that featuring a x_{pitch} of 1500 μm . The cell featuring a pitch distance of 2000 μm was independently measured by the Fraunhofer ISE CalLab PV cells laboratory. The cell features an efficiency of 20.5 % and, finally, the highest conversion efficiency of cells demonstrated in this chapter.

Table 5.11 J-V characteristics measured under one sun conditions of solar cells fabricated with different pitches x_{pitch} with and without plating process.

x_{pitch} (μm)	Plating	V_{OC} (mV)	J_{SC} (mA/cm ²)	FF (%)	p FF (%)	FF_0 (%)	η (%)
1500	No	656.9	40.6	75.2	80.1	83.9	20.0
	Yes	653.8	40.6	75.9	80.5	83.9	20.2
	Yes	657.2	40.7	75.6			20.2*
2000	No	656.1	40.6	74.7	80.8	84.0	19.9
	Yes	655.0	40.7	75.7	80.6	84.0	20.2
	Yes	658.7	40.9	76.0			20.5*

*Independently confirmed by the Fraunhofer ISE CalLab PV cells laboratory

5.8 Chapter summary

In this chapter a base line process for industrially scalable BC-BJ solar cells was introduced. Based on this process sequence, several modifications were performed in order to increase the conversion efficiency η step by step. These modifications include a variation of the material, the passivation scheme, the boron-dopant source, and the cell structure (including dopant profiles) as well as a metal thickening process performed by plating.

In the variation of the material, the main objective was to compare the performance of BC-BJ solar cells processed on industrially convertible Cz-Si material and those based on cost-intensive FZ-Si material. Also the necessity of a cost-intensive etching step in order to provide ultra-smooth surfaces was analyzed. It was found that the performance of the cells is independent from the investigated materials on the observed efficiency level. Thus, the limitation of the cells was assumed to be caused by the utilized processes. The solar cell fabricated with the favored Cz-Si material without shiny etched rear surface was found to achieve an efficiency of 18.1 %.

In the variation of the passivation scheme, two passivation schemes were compared. The first passivation scheme was $\text{SiON}_x/\text{AR-SiN}_x$ as front passivation stack and $\text{Al}_2\text{O}_3/\text{AR-SiN}_x$ as rear passivation stack. The second passivation scheme was a thermally grown SiO_2 covered with AR-SiN_x on both sides of the wafer. Due to the very high surface passivation quality of thermally grown SiO_2 upon the phosphorus-doped FSF ($J_{0,\text{FSF}} = 14.8 \text{ fA/cm}^2$), the J_{SC} could be increased. This finally led to an improvement in efficiency up to 18.9 %. Unfortunately, it was found that thermally grown SiO_2 has a low passivation quality upon the boron-doped emitter ($J_{0,\text{E}} = 577.5 \text{ fA/cm}^2$). A combination of the passivation stacks $\text{SiO}_2/\text{AR-SiN}_x$ as front and $\text{Al}_2\text{O}_3/\text{AR-Si}_2\text{N}_3$ as rear passivation stack was determined to be a promising passivation scheme allowing for a passivation limit in open circuit voltage V_{OC} of up to 687 mV.

Within the variation of BSG layers used for emitter formation, two BSG deposition processes were compared which are based on two different PECVD setups. Compared to the BSG process based on the so-called MW-setup (plasma generation with micro waves), the BSG process based on the so-called EP-setup (plasma generation with electrical power) was found to provide an emitter with a lower dark saturation current density ($J_{0,\text{E}} = 64.2 \text{ fA/cm}^2$) and a less destructive impact on the silicon bulk and carrier lifetime, respectively. Thus, the introduction of the BSG process based on the EP-setup enabled an increase in efficiency up to 19.4 %. This efficiency gain was found to be mainly driven by an increase in short circuit current density J_{SC} and fill factor FF . By integrating the modified emitter (EP-setup) in the BC-BJ cell, the above mentioned passivation limit in V_{OC} would increase up to 692 mV.

In the variation of the cell structure, BC-BJ solar cells were processed with and without gap and with and without an additional thermal process, the so-called drive-in process. Cells without gap between emitter and BSF and without drive-in process could be processed without additional leakage current. These solar cells featured an efficiency of up to 18.4 %. Due to the avoidance of the gap region, a strong decrease in process complexity could be achieved, whereas the efficiency level could be slightly

increased compared to cells featuring a gap region. The drive-in process was found to lead to a decrease in dopant surface concentration of all the integrated doped surfaces and, therefore, to a significant increase in surface passivation quality. Thus, cells with drive-in enabled an increase in efficiency of up to 20.0 %. The latter increase in efficiency was found to be mainly caused by an increase in J_{SC} and FF . Moreover, Al spiking was detected and expected to cause a significant limitation in FF .

Finally, the metallization of the BC-BJ cells was further regarded in the last part of this chapter. The lateral resistance of metal fingers could be improved by performing a silver plating process. The compatibility of aluminum metal fingers with the plating process was provided by a zincate process. Due to plating, the series resistance could be increased and, as a consequence, the maximum efficiency of 20.5 % was achieved.

It is important to mention that all these variations were performed based on the suggested base line process. In order to determine the impact of these variations on the cell performance, only one variation was performed, whereas all the other processes were kept constant. To further increase the efficiency, the following investigation includes a careful combination of the variations performed in this chapter. The cell with the highest industrial relevance and, therefore, the one of interest is the cell without gap region and without drive-in process. A process simplification and an efficiency improvement of the selected cell structure are carried out. In the context of the process simplification, the co-diffusion process is executed by integrating the *co-diffusion module featuring $POCl_3$ and two solid dopant sources*. Within the efficiency improvement, processes which have a positive impact on the cell performance are joined in a new base line process in order to further increase the efficiency. To increase the spiking resistance of the cell, a solution which is not connected to an increase in process complexity is demonstrated. Concerning the efficiency improvement, the co-diffusion process is carried out by using the proved *co-diffusion module featuring solid dopant sources*.

6 Process simplification and efficiency improvement

Succeeding cell experiments, here denoted as process simplification and efficiency improvement, led to the fabrication of highly efficient solar cells. Processes and cells were intensively characterized. The main findings are characterized in this chapter and were already published in the proceedings of the 29th European Photovoltaic Solar Energy Conference and Exhibition (Amsterdam, Netherlands, 2019). The publication was accompanied by an oral presentation of the author at the same conference.

6.1 Challenge

This chapter deals with a process simplification and an efficiency improvement. Therefore, a new base line process is introduced.

Figure 6.1 depicts the process sequences of the old base line process, the new base line process, and a further simplification of the new base line process. The product of the old base line process is a BC-BJ cell with gap (compare section 3.5, Figure 3.5). The highest conversion efficiency of 20.5 % could be achieved by carrying out a cost-intensive thermal process (drive-in). The product of the new base line process is a gap free solar cell which is fabricated without drive-in process. In this case, the PECVD of a SiO_x layer after BSF definition on the rear side can be omitted. Additionally, a complete patterning module including inkjet printing, etching, ink removal, and cleaning is avoided.

In the *process simplification*, the new base line process is further simplified by introducing a co-diffusion process with POCl_3 as gaseous dopant source for FSF formation. As a consequence, PECVD processes utilized to deposit the PSG/ SiO_x stack on the front side can be skipped. In the *efficiency improvement*, gap-free solar cells without drive-in process are processed according to the new base line process. Processes which were found to have a strong impact on the conversion efficiency are joined in order to fully exploit the potential in conversion efficiency of the simplified cell structure.

The cost-saving potential of a co-diffusion module compared to a diffusion module utilizing sequentially performed diffusion steps in order to process a BC-BJ solar cell with gap was already introduced in section 3.5.2. In this section, the cost saving potential of a gap-free solar cell based on the same co-diffusion module and that of a gap-free solar cell based on a co-diffusion module featuring POCl_3 are analyzed. Notice that the co-diffusion module only covers the processes between the process

modules *texturing* as well as *passivation and metallization* (Compare Figure 3.5). The results of the cost-calculation are depicted in Table 6.1.

Old base line with gap (optional D-in)	New base line without gap and D-in	Simplification without gap (POCl_3)
	Single side texturing	
PECVD PSG/ SiO_x (front)		
PECVD PSG/ SiO_x (rear)		
Patterning (BSF-definition)		
PECVD SiO_x (rear)		
Patterning		
PECVD BSG (rear)		PECVD BSG/ SiO_x (rear)
Co-diffusion		Co-diffusion (POCl_3)
Wet chemical processing		
Drive-in (D-in)		
Passivation		
Patterning (Contact opening)		
Metallization		
Patterning (Contact separation)		

The figure shows three cross-sectional diagrams of solar cells. The left diagram (Old base line) shows a cell with a gap, featuring n^+ -Si (BSF) and p^+ -Si (emitter) layers, with an arrow indicating 'etching + drive-in'. The middle diagram (New base line) shows a cell without a gap, featuring n^+ -Si (FSF) and p^+ -Si (emitter) layers, with an arrow indicating 'BSG'. The right diagram (Simplification) shows a cell without a gap, featuring n^+ -Si (FSF) and p^+ -Si (emitter) layers, with an arrow indicating 'PSG/ SiO_x '.

Figure 6.1 Process sequences used for the assembly of solar cells with gap and drive-in (left), without gap and drive-in (middle) and without gap and drive-in with a POCl_3 based co-diffusion (right).

A co-diffusion module utilizing only PECVD layers as dopant sources in order to produce a cell with gap is related to process costs of 64.8 eurocent/wafer. A co-diffusion module utilizing only PECVD layers as dopant sources, as well, in order to fabricate a cell without gap provides a decrease in process costs of 28 %_{rel} down to

46.7 eurocent/wafer. And finally, a co-diffusion module utilizing PECVD layers and a gas as dopant sources in order to manufacture a cell without gap allows for a further decrease in process costs of 15 %_{rel} down to 39.8 eurocent/wafer. Moreover, the process sequence of the cell based on the latter co-diffusion module features the lowest number of process steps and, hence, a decrease in process sequence complexity and effort, respectively. The fabrication of a cell using a co-diffusion setup combining solid and gaseous dopant sources in order to realize the doped structure of a BC-BJ cell without gap is, indeed, related to a strong process simplification.

Table 6.1 Process sum and process costs of co-diffused BC-BJ cells in dependence of the doping structure (gap or no gap) and of the dopant source utilized for FSF formation (PSG or POCl₃). The doping-structure with gap is referred to as old, whereas the doping-structure without gap is referred to as new base line process.

Process Type	Old base line (gap + PSG)		New base line (no gap + PSG)		New base line (no gap + POCl ₃)	
	steps	costs	steps	costs	steps	costs
	(€ct/Wafer)		(€ct/Wafer)		(€ct/Wafer)	
PECVD	6	27.9	5	23.1	4	20.1
Inkjet	4	19.4	2	9.7	1	3.5
Wet chemistry	7	11.9	4	8.3	4	8.3
Diffusion	1	5.6	1	5.6	1	7.9
Sum	18	64.8	12	46.7	10	39.8

6.2 Process simplification by co-diffusion with POCl₃

6.2.1 Motivation

Up to now, the highest conversion efficiency of 20.5 % was achieved with a gap-free solar cell fabricated with a process sequence featuring a cost-intensive drive-in process. Due to the drive-in process, the doped surfaces of the cell could be manipulated. On the one hand, the manipulation of the doped surfaces led to an increase in external quantum efficiency in the low and the middle wavelength range which is strongly related to recombination at the front side of the cell. On the other hand, the cells indicated a high series resistance leading to a loss in fill factor of around 4.9 %_{abs}. Thus, in order to maintain the efficiency and to fully exploit the potential of a decrease in process steps and costs, the integration of a highly conductive FSF featuring a low dark saturation current density is preferred.

6.2.2 Cell preparation and characterization

The cell preparation was performed according to the simplified base line process depicted in Figure 6.1 labeled as *Simplification*. Thus, a gap-free solar cell was processed according to a process sequence using POCl_3 as gaseous dopant source for FSF-formation. The cells were processed on industrial-size Cz-Si material.

In order to perform a co-diffusion process which allows for the simultaneous diffusion of the FSF at the front and of the BSF and the emitter at the rear side, the following co-diffusion configuration was realized (compare also section 4.4 and 4.5).

Table 6.2 Cell dimensions. These are the active cell area A , the wafer thickness W , the pitch distance x_{pitch} , the BSF width x_{BSF} , the width of the gap x_{gap} between emitter and BSF, the emitter coverage EC , the width of the contact openings in the rear side passivation layer, and the width of the BSF electrodes $x_{\text{met},n}$ as well as the one of the emitter electrodes $x_{\text{met},p}$.

A (cm^2)	W (μm)	x_{pitch} (μm)	x_{BSF} (μm)	x_{gap} (μm)	EC (%)	x_{CO} (μm)	$x_{\text{met},n}$ (μm)	$x_{\text{met},p}$ (μm)
4	160	1500	300	0	80	40	200	800
4	160	1750	300	0	83	40	200	1050

The BSF was diffused from a pre-patterned PSG/ SiO_x stack. The emitter was diffused from a BSG/ SiO_x stack. The additional SiO_x layer is necessary to avoid a SiO_2 growth between the BSG layer and silicon during the diffusion process featuring an increase in oxygen gas flow compared to co-diffusion processes with only solid dopant sources. To avoid an impact of the additional SiO_x layer on B-diffusion from the BSG layer into silicon, the B-concentration in BSG was increased. Thus, the BSG-layer was deposited with a diborane gas flow $Q_{\text{B}_2\text{H}_6:\text{H}_2}$ of 1500 sccm. The co-diffusion process with POCl_3 was carried out with a temperature profile featuring two temperature plateaus. The plateau time of the first temperature plateau $t_{\text{plateau},Z2}$ was set to 25 minutes. The oxygen gas flow of the heating phase $Q_{\text{O}_2,Z3}$ during the first and the second temperature plateau was chosen to be 2.5 slm. In order to verify the investigations made in section 4.4 and 4.5 on cell-level, a reference BC-BJ solar cell was processed in a POCl_3 based co-diffusion process featuring a high $Q_{\text{O}_2,Z3}$ of 10 slm during the heating phase.

Furthermore, the BSG layer was not protected with a SiO_x layer. Thus, the emitter formation is assumed to be strongly hindered by the growth of a SiO₂ layer between the BSG layer and silicon during diffusion.

The dimensions of the solar cells are summarized in Table 6.2. Cells were chosen to feature two pitch distances x_{pitch} of 1500 and 1750 μm resulting in two emitter coverages EC of 80 and 83 %.

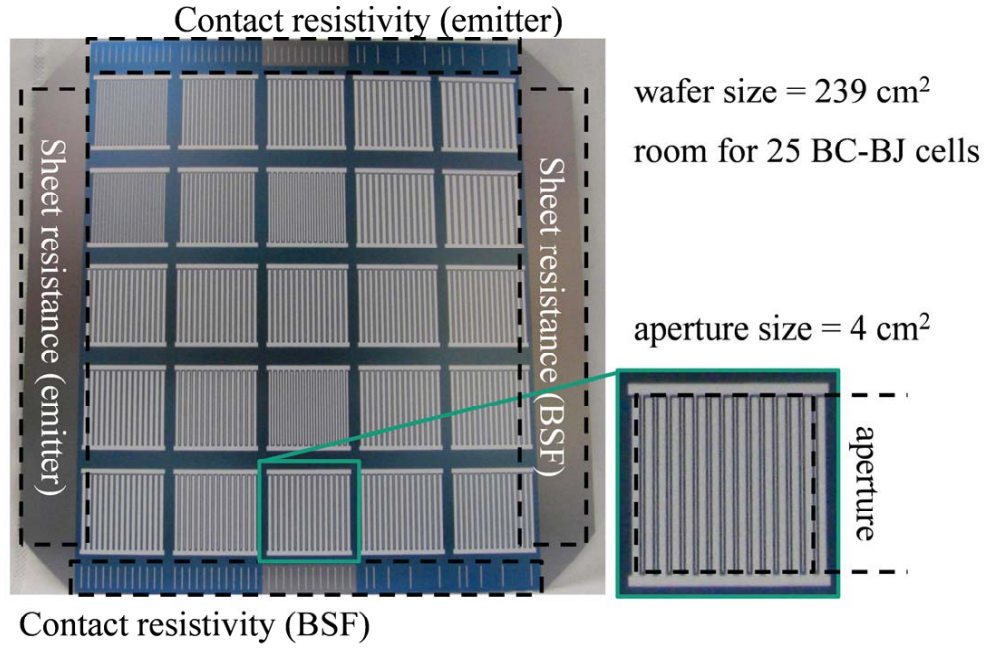


Figure 6.2 Topview of the rear side of a large-scale wafer featuring 25 BC-BJ solar cells. The areas in the range of the wafer edges integrate test structures for the measurement of the specific contact resistivity and the sheet resistance upon emitter and BSF.

The FSF was characterized by the sheet resistance $R_{\text{sh},n+}$, the dopant concentration profile and the dark saturation current density $J_{0,\text{FSF}}$. In turn, samples featuring the cell characteristic front side on both sides of the wafer were prepared on n -type Cz-Si material ($\rho_{\text{bulk}} = 3.6 \Omega\text{cm}$, $N_{\text{dop}} = 1.3 \cdot 10^{15} \text{ cm}^{-3}$, $W = 158 \mu\text{m}$). The cell characteristic front side consists of an alkaline textured surface, the FSF realized in the POCl₃ diffusion process, and the front side passivation stack (PECVD SiON_x/Ar-SiN_x). The $R_{\text{sh},n+}$ of the FSF was measured inductively. The $J_{0,\text{FSF}}$ was determined by QSSPC measurements at room temperature and life time analysis according to the slope method ($n_i = 8.5 \cdot 10^9 \text{ cm}^{-3}$). The dopant concentration profile of the FSF was measured by ECV. Therefore, the front side passivation stack of a selected BC-BJ cell was

etched back and characterized. As references, samples diffused from PSG/SiO_x stacks (with and without drive-in) instead of POCl₃ were processed and characterized as well. The sheet resistance of the emitter $R_{sh,p+}$ was measured. Therefore, test areas integrated onto the rear design of the industrial-size wafer were characterized by four point measurements (compare Figure 6.2). Especially the emitter formation from a BSG layer during co-diffusion processes with POCl₃ was found to be critical.

In order to estimate the material properties, wafers were passivated on both sides with the rear passivation stack. Before, these wafers were saw-damage etched, PECVD coated with SiO_x layers on both sides of the wafer, exposed to the thermal treatment used for co-diffusion, and treated in an etch solution containing HF in order to remove the SiO_x layers again. Before and after diffusion, the bulk resistivity was inductively measured. The bulk carrier lifetime was measured by QSSPC at room temperature and analyzed according to the slope method.

The cells were characterized by $J-V$, Suns V_{OC} measurements, and QE measurements. The gap free solar cell implementing a cost-intensive drive-in process in the process sequence was regarded as a reference cell ($x_{pitch} = 1500 \mu m$). This solar cell was found to feature an efficiency of 20.2 % (compare section 5.7).

6.2.3 Results and discussion

The analysis of the FSF according to the ECV and QSSPC measurement is depicted in Figure 6.3. Therefore, the ECV measured electron concentration profile of the FSF diffused in a POCl₃ containing diffusion step as used for cell preparation in this section is compared to those diffused from pre-deposited PECVD PSG/SiO_x stacks with and without drive-in process as already applied for cell preparation in chapter 5. The FSF diffused from POCl₃ indicates a maximum electron concentration of $1.7 \cdot 10^{19} \text{ cm}^{-3}$ and a profile depth of 397 nm (extracted at an electron concentration of $1.0 \cdot 10^{17} \text{ cm}^{-3}$). By integrating the concentration profile, the $R_{sh,n+}$ of the FSF diffused from POCl₃ was calculated to be 235 Ω/sq and is in a good agreement with the inductively measured $R_{sh,n+}$ of $236 \pm 8 \Omega/\text{sq}$. The relative standard deviation of the sheet resistance is below 3.5 %_{rel} which indicates a homogeneous P-diffusion. The $J_{0,FSF}$ was found to be 46 fA/cm^2 . Compared to the FSF diffused from the PSG/SiO_x stack without drive-in ($R_{sh,n+} = 354 \Omega/\text{sq}$, $J_{0,FSF} = 66 \text{ fA}/\text{cm}^2$), the $R_{sh,n+}$ and the $J_{0,FSF}$ could be decreased. Thus, the realized FSF diffused from POCl₃ as gaseous dopant source provides both an increase in electrical conductivity and a decrease in front side recombination. Moreover, the surface passivation quality of the FSF diffused in the POCl₃ containing diffusion process achieves almost the quality of the FSF diffused from the PSG/SiO_x stack with additional drive-in process ($R_{sh,n+} = 390 \Omega/\text{sq}$, $J_{0,FSF} = 40 \text{ fA}/\text{cm}^2$). Possible

explanations for the relatively high surface passivation quality of the FSF diffused in the POCl₃ containing diffusion step might be the affinity of chlorine to capture metal impurities from the silicon surface [78] as well as the cleaning effect of the SiO₂ growth between PSG and silicon during diffusion in the time span of the second temperature plateau (compare section 4.4.1). As motivated in the beginning of this section, the improved properties of the FSF diffused from POCl₃ should lead to a significant increase in conversion efficiency.

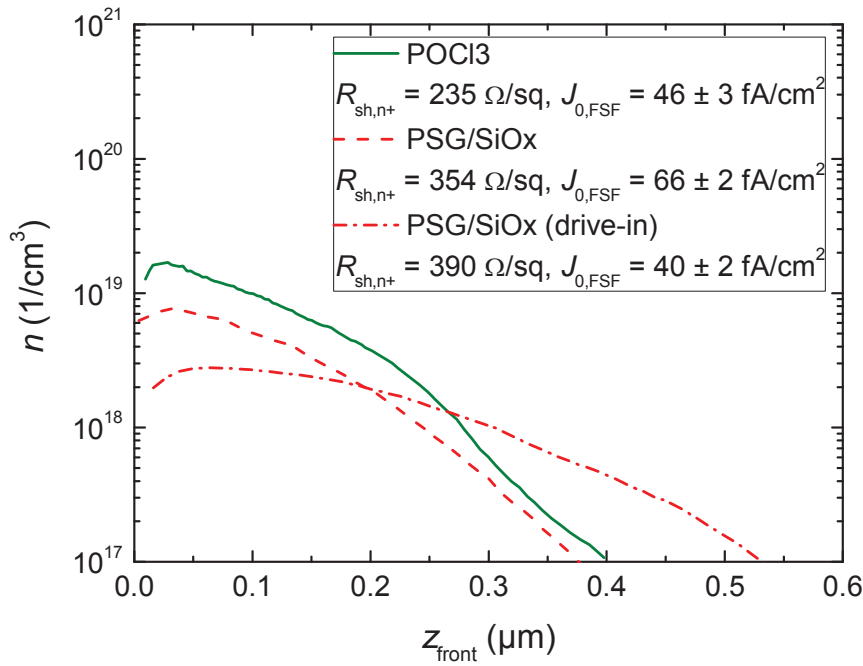


Figure 6.3 Electron concentration n versus wafer depth z_{front} measured by ECV of an FSF diffused in a POCl₃ containing diffusion step and those diffused by utilizing pre-deposited PECVD PSG/SiO_x stacks as diffusion sources. The graph includes the sheet resistance $R_{\text{sh},n+}$ calculated from the profile and the dark saturation current density ($J_{0,\text{FSF}}$) determined from QSSPC measurements (slope method). The $J_{0,\text{FSF}}$ is expressed by the mean and the standard deviation of a five point measurement upon a large-scale wafer ($A = 239 \text{ cm}^2$).

The sheet resistance of the emitter was found to feature a value of $54.3 \pm 0.5 \text{ } \Omega/\text{sq}$. Thus, the relative standard deviation of the $R_{\text{sh},p+}$ is below $1.0 \text{ } \%$ _{rel} and corresponds to an homogeneously performed B-diffusion from the BSG/SiO_x stack. Moreover, interface oxidation between silicon and the BSG-layer during the co-diffusion process featuring an $Q_{\text{O}_2,\text{Z3}}$ of 2.5 slm is neglected.

The material properties of the cell wafers are depicted in Table 6.3. During diffusion, the bulk resistivity of the material increases by $0.5 \text{ } \Omega\text{cm}$ up to $3.1 \text{ } \Omega\text{cm}$. The bulk carrier lifetime was measured to be between 2.6 and 3.2 ms. Hence, the minority

diffusion length L_p in the Cz-Si material of choice is between 1760 and 2050 μm and, therefore, assumed to be compatible with the requirements of a BC-BJ cell.

The J - V and $\text{Suns}V_{\text{OC}}$ measured cell parameters are depicted in Table 6.4. The cell parameters are presented in dependence of the P-dopant source (P-source) and in dependence of the pitch distance (x_{pitch}). The P-source referred to as $\text{POCl}_3, \text{O}_2\downarrow$ means a thermally grown PSG-layer as a result of a co-diffusion process with a low oxygen gas flow. The P-source referred to as $\text{POCl}_3, \text{O}_2\uparrow$ denotes the equivalent with a high oxygen gas flow. The P-source denoted as PSG/SiO_x was deposited by PECVD and treated with a negligibly low oxygen gas flow during co-diffusion. Cells based on a co-diffusion module utilizing POCl_3 is denoted as *POCl₃ cells*, whereas those based on PECVD processes are referred to as *PECVD cells*.

Table 6.3 Material properties. These are the wafer thickness after texturing W , specific base resistivity before ρ_{bulk} and after co-diffusion $\rho_{\text{bulk},T}$, dopant concentration after co-diffusion $N_{\text{dop},T}$, the QSSPC measured bulk carrier lifetime (τ_{bulk}).

Material	W (μm)	ρ_{bulk} (Ωcm)	$\rho_{\text{bulk},T}$ (Ωcm)	$N_{\text{dop},T}$ ($1/\text{cm}^3$)	τ_{bulk} (ms)
1 – n, Cz	160-170	2.7	3.2	$1.5 \cdot 10^{15}$	2.6-3.5

Table 6.4 J-V and $\text{Suns}V_{\text{OC}}$ characteristics of BC-BJ cells in dependence of the P-source utilized for FSF formation and pitch distance x_{pitch} . The pseudo fill factor pFF and the ideal fill factor FF_0 were extracted from the $\text{Suns}V_{\text{OC}}$ data. The compared P-sources are thermally grown PSG layers featuring different oxygen gas flows during co-diffusion ($\text{POCl}_3, \text{O}_2$) and a PECVD PSG/SiO_x stack (PSG/SiO_x). Depicted are the best cells out of every group.

P-Source (front)	x_{pitch} (μm)	V_{OC} (mV)	J_{SC} (mA/cm^2)	FF (%)	pFF-FF (% _{abs})	FF_0 -pFF (% _{abs})	η (%)
$\text{POCl}_3, \text{O}_2\uparrow$	1500	598.5	38.5	62.1	8.4	12.4	14.3
PSG/SiO_x	1500	657.2	40.7	75.6	4.9	3.4	20.2*
$\text{POCl}_3, \text{O}_2\downarrow$	1500	654.2	40.4	76.9	2.9	4.1	20.3*
$\text{POCl}_3, \text{O}_2\downarrow$	1750	655.7	40.5	77.2	3.0	3.7	20.5*

*Independently confirmed by the Fraunhofer ISE CalLab PV cells laboratory

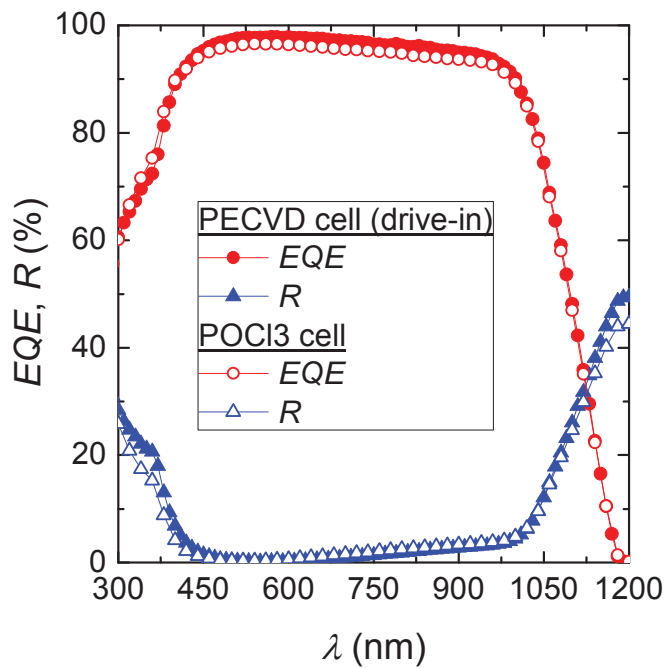
By comparing POCl_3 cells fabricated with a low ($\text{POCl}_3, \text{O}_2\downarrow$) and a high oxygen gas flow ($\text{POCl}_3, \text{O}_2\uparrow$), the evaluated co-diffusion module enables a significant increase in efficiency η from 14.3 % up to 20.3 %. This increase in efficiency is related to an

increase in open circuit voltage V_{OC} of around 56 mV, in short circuit current density J_{SC} of 1.9 mA/cm², and in fill factor FF of 14.8 %_{abs}. The increase in FF is caused by a decrease in $pFF-FF$ of 5.5 %_{abs} related to the series resistance and in FF_0-pFF of 8.3 %_{abs} related to the leakage current.

It is assumed that the cells based on a high oxygen gas flow suffer from interface oxidation between silicon and the solid B-dopant source. The interface oxidation induces a retardation of B-diffusion and therefore an emitter with a low doping-level. In consequence, the contact resistance of the Al-Si/ p^+ -Si interface increases, whereas the spiking resistance decreases. The V_{OC} of the cell featuring a high oxygen gas flow is assumed to suffer from a low passivation quality at the rear side of the solar cell. Due to the low sensitivity of the J_{SC} to the rear side passivation quality, the J_{SC} of 38.5 mA/cm² achieved by the cell fabricated with a high oxygen gas flow is still on a relatively high level. The findings made by the latter cell comparison verify the findings made during the process development (compare section 4.4 and 4.5) on cell-level.

By comparing the POCl₃ cell fabricated with a low oxygen gas flow (POCl₃, O₂↓) and the PECVD cell (PSG/SiO_x) with a x_{pitch} of 1500 μm, the efficiency of the POCl₃ cell is similar. The PECVD cell tends to feature a slightly higher V_{OC} and J_{SC} but, however, the POCl₃ cell features a significantly higher FF . This gain in FF is related to a minor increase in FF_0-pFF by 0.7 %_{abs} and a major decrease in $pFF-FF$ by 2.0 %_{abs}. The FF_0-pFF advantage of the PECVD cell is connected to the drive in process and the deep dopant profiles, respectively. Thus, the spiking resistance of the PECVD cell is higher. The dominating $pFF-FF$ advantage of the POCl₃ cell is caused by the relatively low bulk resistivity ($\rho_{bulk}[POCl_3] = 3.2 \Omega\text{cm}$ vs. $\rho_{bulk}[PECVD] = 4.9 \Omega\text{cm}$) and the improved sheet resistance of the FSF ($R_{sh,n+}[POCl_3] = 235 \Omega/\text{sq}$ vs. $R_{sh,n+}[PECVD] = 354 \Omega/\text{sq}$). Moreover, the increase in lateral conductivity of POCl₃ cells enables an insignificant correlation between $pFF-FF$ and x_{pitch} . As a consequence, the maximum efficiency of 20.5 % is achieved with a x_{pitch} of 1750 μm. The efficiency gain of the cell featuring a high x_{pitch} is attributable to a slight increase in all characteristic cell parameters. The increase in J_{SC} and V_{OC} is caused by an improved minority collection probability and passivation quality, whereas both increases are related to the slight increase in EC with increasing x_{pitch} . The increase in FF is caused by a decrease in FF_0-pFF by 0.4 %_{abs} indicating a decrease in leakage current. The width of line openings x_{CO} in the rear passivation layer was chosen to be independent from the pitch distance x_{pitch} . Thus, with increasing x_{pitch} the contact opening coverage COC decreases, whereas the spiking resistance increases. This might be an explanation for the effect of decreasing leakage current with increasing x_{pitch} .

In order to further compare the front side passivation quality of cells fabricated with thermally grown PSG (POCl_3) and the PECVD PSG/ SiO_x stack (drive-in), in the following, the QE measurements performed with a POCl_3 and a PECVD cell are discussed. Figure 6.4 depicts the wavelength λ dependent external quantum efficiency EQE and reflection R of the compared cell types.



PECVD cell (D-in)

λ range (nm)	J_{SC} gain (mA/cm ²)
300-600	13.0
601-900	19.6
901-1200	8.2

POCl₃ cell

λ range (nm)	J_{SC} gain (mA/cm ²)
300-600	13.6
601-900	19.1
901-1200	7.8

Figure 6.4 External quantum efficiency EQE and reflection R versus wavelength λ of solar cells manufactured with two different P-dopant sources for FSF-formation. These are a PECVD PSG/ SiO_x stack (PECVD cell) and a thermally grown PSG layer (POCl_3 cell). The FSF diffused from the stack was additionally treated in a drive-in process. Cells without drive-in are labeled as initial. The table on the right hand side depicts components of J_{SC} gained in defined spectral ranges.

By comparing the EQE - λ curves of both cell types, the EQE of the POCl_3 cell is higher in the short and lower in the middle and long wave length range. The PECVD cell features a total J_{SC} gain of 40.8 mA/cm², whereas the POCl_3 cell features 40.5 mA/cm². Since the R of the POCl_3 cell is lower in the short wave length range, the increase in EQE is probably partly caused by a decrease in interface reflection at the front side of the cell. In the long wave length range, the simultaneous decrease in EQE and R of the POCl_3 cell is probably caused by an increase in free carrier absorption at the rear side of the cell. This effect could already be observed by comparing cells with and without drive-in process in section 5.6.

Figure 6.5 depicts the wavelength λ dependent internal quantum efficiency IQE of the compared cells. Due to the low $J_{0,FSF}$ related to the front side of the cells in question (e.g. $J_{0,FSF}[POCl_3] = 46 \text{ fA/cm}^2$), the IQE - λ curve and related recombination effects of both cells are quite similar. Thus, the PECVD cell features an IQE of 84.6 % at a wavelength of 300 nm and of 98.3 % at 830 nm. In comparison, the POCl₃ cell indicates an IQE of 81.1 % at a wavelength 300 nm and of 97.2 % at 780 nm. The IQE - λ curves of the compared cells proof that a cell integrating an FSF diffused from a thermally grown PSG layer allows for nearly the same recombination losses like a cell integrating an FSF diffused from a PSG/SiO_x stack which was additionally treated in a cost-intensive drive-in process. Moreover, the remaining difference in IQE of the regarded cells can be balanced completely by increasing the x_{pitch} of the POCl₃ cell up to 1750 μm .

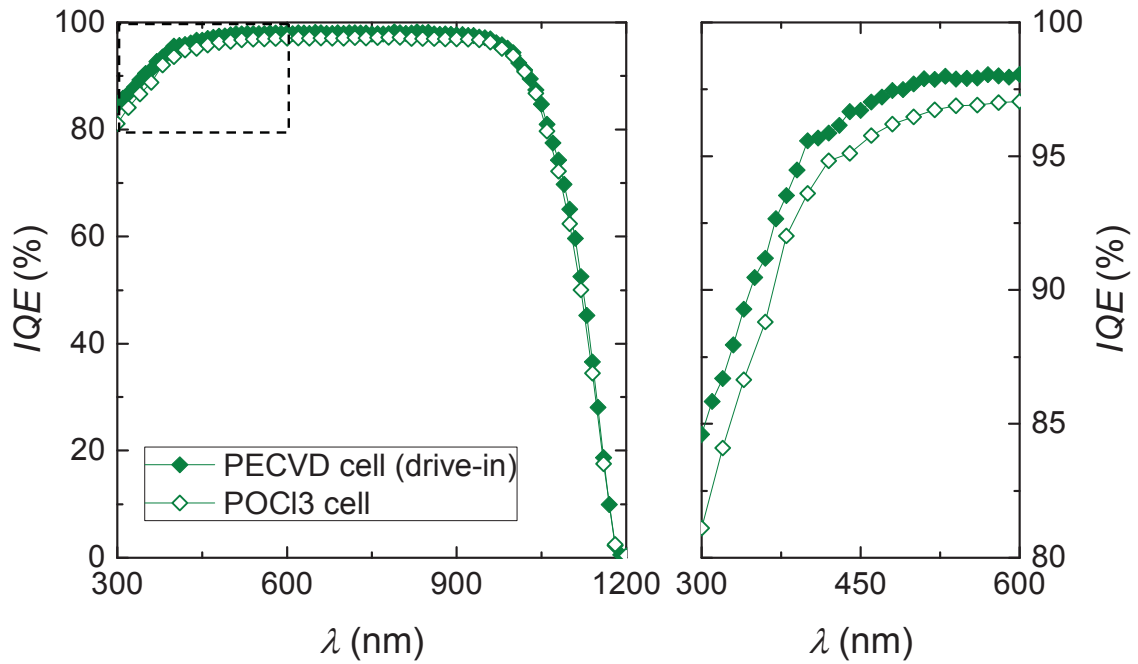


Figure 6.5 Internal quantum efficiency IQE versus wavelength λ of solar cells manufactured with two different P-dopant sources for FSF formation. These are a PECVD PSG/SiO_x stack (PECVD cell) and a thermally grown PSG layer (POCl₃ cell). The FSF diffused from the stack was additionally treated in a drive-in process.

To conclude this section, the up to now highest conversion efficiency of 20.5 % of a gap-free cell featuring a drive-in process could be maintained by making use of a co-diffusion module which drastically decreases the process steps and costs. The co-diffusion module is based on a co-diffusion setup making use of PSG/SiO_x and BSG/SiO_x stacks as rear dopant sources and a thermally grown PSG layer as front

dopant source as investigated in the sections 4.4 and 4.5. Compared to the cell featuring an FSF diffused from a PSG/SiO_x stack which was not treated in a drive-in process, the sheet resistance and the $J_{0,FSF}$ diffused from the thermally grown PSG-layer could be simultaneously improved. Thus, the FSF diffused from the thermally grown PSG layer was found to feature a sheet resistance $R_{sh,n+}$ of 236 Ω/sq (PSG/SiO_x; $R_{sh} = 354 \Omega/\text{sq}$) and a $J_{0,FSF}$ as passivated with a SiON_x/AR-SiN_x stack of 46 fA/cm² (PSG/SiO_x; $J_0 = 66 \text{ fA/cm}^2$). The decrease in $R_{sh,n+}$ of the FSF in combination with a decrease in bulk resistivity was found to lead to a major decrease in series resistance losses and, consequently, in FF . In addition, the decrease in $J_{0,FSF}$ was found to enable a V_{OC} and a J_{SC} very similar to a cell fabricated with a PSG/SiO_x stack as dopant source and an additional drive-in process.

6.3 Efficiency improvement

6.3.1 Motivation

The improvement of the cell conversion efficiency is based on the findings of the previous chapter. Besides the passivation scheme of the base line process featuring a SiON_x/SiN_x stack on the front and an Al₂O₃/SiN_x stack on the rear side, a SiO₂/SiN_x stack on the front is combined with an Al₂O₃/SiN_x stack on the rear side in order to fully exploit the potential of low surface recombination losses. For emitter formation, BSG layers are used allowing for a very high surface passivation quality and a lowly destructive impact on the bulk carrier lifetime. Since Al-spiking is regarded as an issue decreasing the shunt resistance and therefore the fill factor, a modification of the contact opening coverage is performed in order to increase the so-called spiking resistance. All the mentioned modifications of the base line process and the cell design are expected to lead to a significant increase in cell efficiency.

6.3.2 Cell preparation and characterization

The solar cells were fabricated according to the new base line process (compare Figure 6.1, middle). Thus, the gap free solar cells were fabricated with a co-diffusion setup applying only solid dopant sources. A cost-intensive drive-in process was omitted. Cz-Si material with an n -type base doping was utilized. In order to qualify the process homogeneity upon industrial-size wafers ($A = 15.6 \times 15.6 \text{ cm}^2$), the wafers integrated Twenty five BC-BJ solar cells featuring the same dimensions. The dimensions of the processed BC-BJ solar cells are listed in Table 6.5.

The wafer thickness W was measured to be around 170 μm . The pitch distance x_{pitch} was set to be 1500 μm , the width of the BSF x_{BSF} was set to be 300 μm , and hence the emitter coverage EC was set to be 80 %.

Since the diffusion was carried out without a mentionable oxygen gas flow, the emitter was diffused from an uncoated BSG layer. The BSG layer was deposited by means of PECVD with the EP-setup. Compared to the MW-setup, the emitter diffused from a BSG layer deposited with the EP-setup was found to feature lower recombination losses. As passivated with aluminum oxide, dark saturation current densities $J_{0,E}$ of 64 fA/cm^2 were determined. Moreover, the deposition process was found to provide a less destructive impact on the bulk carrier lifetime which is crucial for a highly efficient BC-BJ solar cell performance (compare section 5.5).

According to the base line process, a $\text{SiON}_x/\text{SiN}_x$ stack was used as front and an $\text{Al}_2\text{O}_3/\text{SiN}_x$ stack as rear side passivation. A significant decrease in dark saturation current density related to the front side $J_{0,\text{FSF}}$ down to 15 fA/cm^2 was obtained, by passivating the FSF with a $\text{SiO}_2/\text{SiN}_x$ stack (compare section 5.4). Since the thermally grown SiO_2 layer was found to indicate a low emitter passivation quality, the $\text{Al}_2\text{O}_3/\text{SiN}_x$ stack at the rear side needs to be maintained. To integrate a passivation scheme featuring a $\text{SiO}_2/\text{SiN}_x$ stack as front and an $\text{Al}_2\text{O}_3/\text{SiN}_x$ stack as rear passivation, the base line process was modified as follows.

Table 6.5 Cell dimensions. These are the active cell area A , the wafer thickness W , the pitch distance x_{pitch} , the BSF width x_{BSF} , the width of the gap x_{gap} between emitter and BSF, the emitter coverage EC , the contact opening coverage COC in the rear side passivation layer, and the width of the BSF electrodes $x_{\text{met},n}$ as well as the one of the emitter electrodes $x_{\text{met},p}$.

A (cm^2)	W (μm)	x_{pitch} (μm)	x_{BSF} (μm)	x_{gap} (μm)	EC (%)	COC (%)	$x_{\text{met},n}$ (μm)	$x_{\text{met},p}$ (μm)
4	167	1500	300	0	80	2	200	800

n -type Si
 p^+ -Si (emitter)
 n^+ -Si (BSF)

electrodes
 passivation

After co-diffusion, the doped glasses were etched back. Afterwards, thin SiO_2 layers were thermally grown (dry oxidation) on both sides of the wafer. Subsequently, the SiO_2 layer at the front side was coated with a PECVD AR- SiN_x . To remove the SiO_2

layer at the rear side, the wafers were treated in a short HF-Dip. During this HF-dip, the SiO_2 layer at the front side is wet chemically protected by the SiN_x layer, whereas the uncovered SiO_2 layer at the rear side is removed. Finally, the $\text{Al}_2\text{O}_3/\text{SiN}_x$ stack was deposited on the rear side.

In order to increase the spiking resistivity of the cells, squarely shaped contact openings were introduced. These contact openings feature a contact opening coverage *COC* of 2 %. Up to now, linearly shaped line openings with a *COC* of 8 % were utilized (see also Figure 6.2). To estimate a pseudo fill factor independent from spiking, solar cells were processed without contact openings in the active area of the cell. The contact openings underneath the metal busbars were maintained.

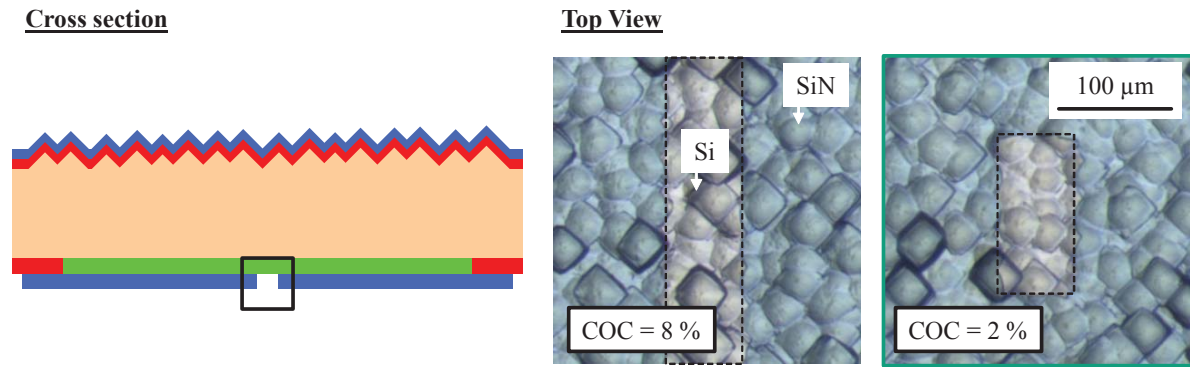


Figure 6.6 Cross section of a BC-BJ cell (left) and top view on the rear side of the BC-BJ cell after contact opening (right). To obtain low contact opening coverages *COC*, squarely shaped contact opening are introduced.

The wafer related material properties were characterized according to the sample configuration and characterization methods already described in section 6.2. The cells were characterized by J - V , $\text{Suns } V_{\text{OC}}$ measurements, and QE measurements.

6.3.3 Results and discussion

The material properties of the cell wafers are depicted in Table 6.6. During diffusion, the bulk resistivity ρ_{bulk} of the material increases by 0.5 Ωcm up to 3.3 Ωcm . The bulk carrier lifetime was measured to be higher than 3.0 ms which corresponds to a minority diffusion length L_p of at least 1900 μm and, thus, the material of choice is assumed to fulfil the requirements of a BC-BJ solar cell.

The characteristic cell parameters in dependence of the passivation scheme (Passivation) and the *COC* are depicted in Table 6.7. In the following, cells featuring a SiO_2 passivation layer are referred to as *SiO₂ cells*, whereas those featuring a SiON_x passivation layer are denoted as *SiON_x cells*. Indeed, the processes joined in the new

base line process and the modification of the contact opening pattern in the rear side passivation stack allow for the fabrication of a cell featuring a remarkably high conversion efficiency η of 21.1 % independently confirmed by the Fraunhofer ISE CalLab PV cells.

Table 6.6 Material properties. These are the wafer thickness after texturing W , specific base resistivity before ρ_{bulk} and after co-diffusion $\rho_{\text{bulk,T}}$, dopant concentration after co-diffusion $N_{\text{dop,T}}$, the QSSPC measured bulk carrier lifetime τ_{bulk} .

Material	W (μm)	ρ_{bulk} (Ωcm)	$\rho_{\text{bulk,T}}$ (Ωcm)	$N_{\text{dop,T}}$ ($1/\text{cm}^3$)	τ_{bulk} (ms)
1 – n, Cz	167	2.8	3.3	$1.4 \cdot 10^{15}$	≈ 3

Table 6.7 Results of J-V and Suns V_{OC} (pFF, FF_0) measurements performed with the best solar cell per group in dependence of the front passivation layer and the contact opening coverage COC. The parameters of the reference cell without contact openings (COC = 0 %) are depicted as well.

Passivation	COC (%)	V_{OC} (mV)	J_{SC} (mA/cm^2)	FF (%)	pFF-FF (% _{abs})	FF_0 -pFF (% _{abs})	η (%)
SiO ₂	2	666.0	41.1	75.6	4.9	3.6	20.7
SiON _x	2	663.8	40.8	78.0	4.1	1.9	21.1*
	0	649.1	21.2	28.5	53.5	1.9	3.9

*Independently confirmed by the Fraunhofer ISE CalLab PV cells

Both cell types feature a relatively high open circuit voltage V_{OC} and short circuit current density J_{SC} , whereas both values are slightly higher in the case of the SiO₂ cell. The observed benefit in V_{OC} and J_{SC} is related to the very high surface passivation quality of the SiO₂ layer on the FSF. This issue is further discussed by regarding the results of the QE measurements. Unfortunately, the high passivation quality of the SiO₂ cell could not be fully exploited due to the relatively low fill factor FF of 75.6 %. In comparison, the SiON_x cell indicates a significantly higher FF of 78.0 %. This increase in FF is the result of a simultaneous decrease in pFF-FF of 0.8 %_{abs} and in FF_0 -pFF of 1.7 %_{abs}. Thus, the SiO₂ cell features a higher series resistance and leakage current than the SiON_x cell. The increase in series resistance of the SiO₂ cell is assumed to be connected to an increase in contact resistance. The increase in contact resistance might be the result of boron depletion at the silicon rear surface (emitter) caused by segregation of boron in the growing SiO₂ layer during oxidation. Moreover,

the segregation induced boron depletion at the silicon surface might lead to an injection dependence of the life time in low level injection [138] and, consequently, to the observed decrease in pFF of the SiO_2 compared to the SiON_x cell.

Table 6.8 J-V characteristics of 25 BC-BJ solar cells processed with PECVD passivation layers in dependence of the wafer position Pos. The solar cells were processed identically on one wafer featuring a size of 239 cm^2 .

Pos	V_{OC} (mV)	J_{SC} (mA/cm^2)	FF (%)	η (%)
1	663.6	41.3	77.3	21.2
2*	663.8	40.8	78.0	21.1
3	663.4	41.3	76.1	20.9
4	663.4	41.3	76.4	20.9
5	660.3	41.3	76.7	20.9
6	658.6	41.1	77.7	21.0
7	662.0	41.1	77.9	21.2
8	660.2	40.9	77.8	21.0
9*	661.9	40.6	78.3	21.1
10	660.5	41.2	77.0	20.9
11	656.3	40.7	78.1	20.9
12	658.1	41.1	77.4	20.9
13	658.1	40.6	77.7	20.7
14	656.5	40.8	78.0	20.9
15	661.6	41.0	77.8	21.1
16	659.6	40.8	78.1	21.0
17	656.1	41.0	78.2	21.0
18	658.3	40.5	78.3	20.9
19	660.7	40.9	78.1	21.1
20	663.1	41.3	77.5	21.2
21	649.7	41.0	77.9	20.8
22	653.3	41.0	77.9	20.9
23	654.5	41.1	76.4	20.6
24	652.9	40.7	77.8	20.7
25	654.7	41.2	77.3	20.9
x_{av}	658.8	41.0	77.6	21.0
Δx	3.8	0.2	0.6	0.2
Δx (%)	0.6	0.6	0.8	0.7

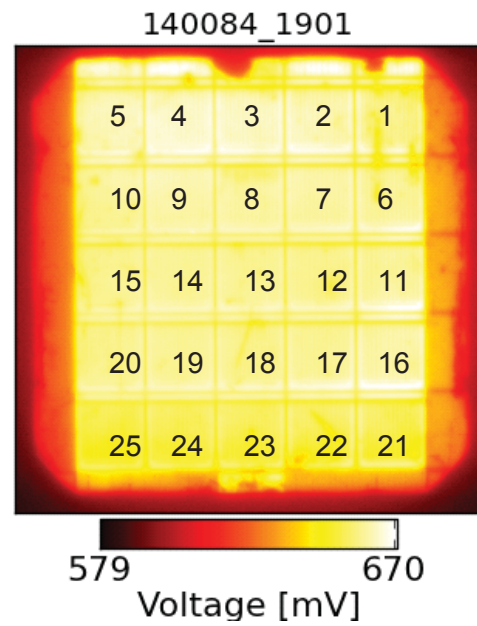


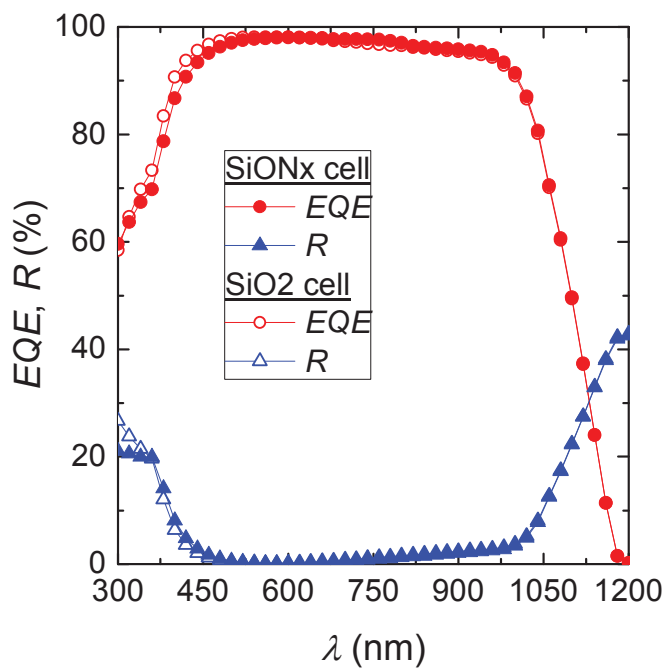
Photo luminescence (PL) image of the wafer integrating the solar cells in question after patterning the rear side passivation layer (no metal electrodes). The rear side of the cell was irradiated, the PL emission of the cell was detected, and translated in a voltage. Passivated areas are indicated by low recombination losses and feature high voltage signals, whereas non-passivated areas suffer from high recombination losses and feature a relatively low voltage signal.

** Calibrated measurement
(Fraunhofer ISE CalLab PV Cells)*

However, the SiON_x cell features a remarkably high pseudo fill factor pFF of 82.1 % and a very low $\text{FF}_0\text{-pFF}$ of 1.9 %_{abs}. In comparison, the reference cell without contact openings in the active cell area ($\text{COC} = 0\%$) features the same value. The observed similarity leads to the assumption that the leakage current is not amplified by spiking anymore. The remaining leakage current might be caused by recombination in the space charge region and other parasitic effects.

Twenty five solar cells fabricated with the SiON_x front passivation layer feature a standard deviation in efficiency of below 0.2 %_{abs} (compare Table 6.8). Solar cells fabricated with the SiO_2 front passivation layer feature a deviation in efficiency of around 0.3 %_{abs}. Independent from the passivation scheme, both deviations are low and demonstrate the high homogeneity of the applied processes over an industrial-size wafer.

The external quantum efficiency EQE and reflection R versus wavelength λ of cells fabricated with a SiON_x and a SiO_2 front passivation layer are depicted in Figure 6.7.



SiON	
λ range nm	J_{SC} gain mA/cm ²
300-600	13.6
601-900	19.5
901-1200	8.0

SiO	
λ range nm	J_{SC} gain mA/cm ²
300-600	13.8
601-900	19.5
901-1200	8.0

Figure 6.7 External quantum efficiency EQE and reflection R versus wavelength λ for solar cells with PECVD SiON_x and thermally grown SiO_2 as front side passivation layer.

The SiON_x cell indicates a maximum EQE of 98.6 % at a wavelength of 760 nm. The SiO_2 cell features a maximum EQE of 98.3 % at 520 nm. Except for the short wavelength range, the $\text{EQE}-\lambda$ and the $R-\lambda$ curve of both cells are completely comparable. Thus, both cells feature a J_{SC} gain of 19.5 mA/cm² in the middle and of

8.0 mA/cm² in the long wavelength range. In the short wavelength range, the SiON_x cell provides a J_{SC} gain of 13.6 mA/cm². In comparison, the SiO₂ cell exhibits an increase in J_{SC} gain of 0.2 mA/cm² up to 13.8 mA/cm². The decrease in reflection of the SiON_x cell in the low wave length range is assumed to be caused by additional absorption losses in the SiON_x layer compared to the SiO₂ layer.

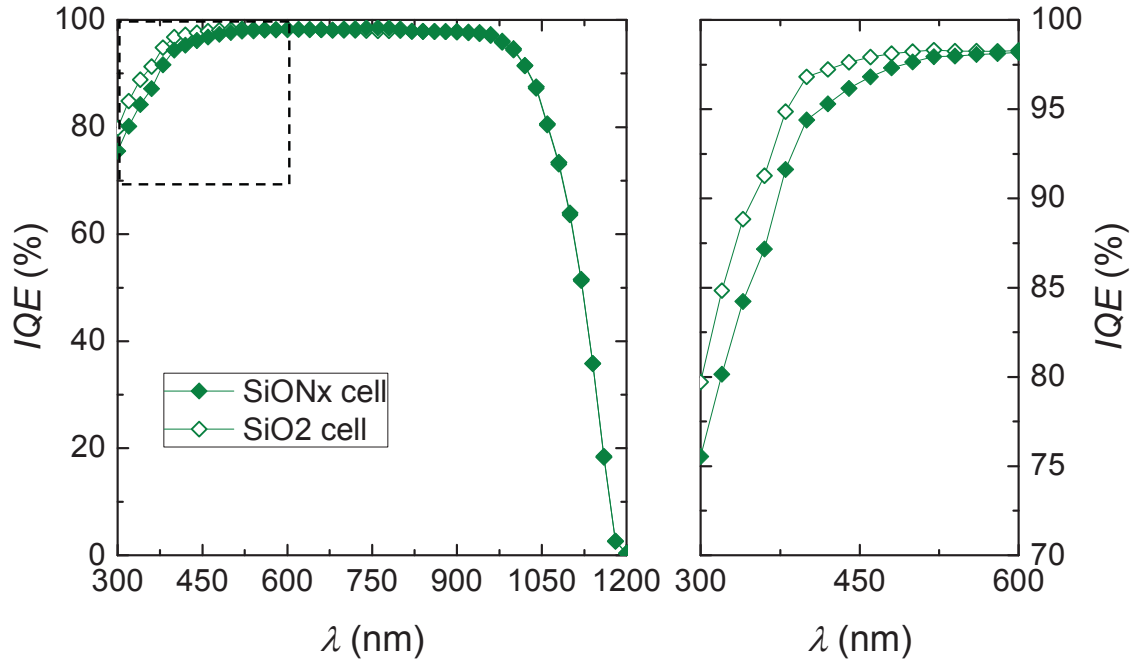


Figure 6.8 Internal quantum efficiency (IQE) in dependence of the wavelength (λ) for solar cells with PECVD SiON_x and thermally grown SiO₂ as front side passivation layer.

The internal quantum efficiency IQE versus wavelength λ of cells fabricated with a SiON_x (SiON) and a SiO₂ (SiO) front passivation layer is depicted in Figure 6.8.

Compared to the SiON_x cell, the SiO₂ cell indicates an increase in IQE in the short wavelength range. SiO₂ cells feature a maximum IQE of 98.3 % at a wavelength of 520 nm. SiON_x cells indicate a maximum IQE of 98.6 % at a wavelength of 760 nm. The increase in IQE of the cell fabricated with the SiO₂ passivation layer is caused by the higher passivation quality of these layers at the front side of the cell. The remaining loss in IQE is expected to be mainly caused by the design of the BSF and the corresponding electrical shading.

The investigations made in this section demonstrate that an efficiency improvement of BC-BJ solar cells processed according to the new base line process up to 21.1 % is possible. These cells feature no gap region and are processed without a cost-intensive drive-in process underlining the industrial relevance of these cells. By integrating a

passivation scheme featuring a SiO_2 layer at the front and an Al_2O_3 layer at the rear side, a high V_{OC} of 666.0 mV and J_{SC} of 41.1 mA/cm² could be achieved. Furthermore, by integrating a modified contact opening pattern with a COC of only 2 %, the spiking resistivity and the related pFF could be increased up to 82.1 %.

6.4 Chapter summary

Industrially relevant BC-BJ cells without gap region based on a new base line process featuring only one single thermal treatment were introduced in this chapter.

In the *process simplification*, the new base line process was further simplified by a co-diffusion module utilizing PECVD layers and a gas, in fact POCl_3 , as dopant sources. Compared with a co-diffusion module utilizing only solid dopant sources at least one deposition process can be skipped. Thus, cells based on the simplified new base line process feature the lowest number of process steps and costs.

Compared to the front surface field (FSF) diffused from a PSG/ SiO_x stack featuring a dark saturation current density $J_{0,\text{FSF}}$ of 66.0 fA/cm² and a sheet resistance $R_{\text{sh},\text{n}+}$ of 354.3 Ω/sq , the FSF diffused from POCl_3 was found to feature a $J_{0,\text{FSF}}$ of 46 fA/cm² and an $R_{\text{sh},\text{n}+}$ of 253.2 Ω/sq . Thus, the FSF formed with POCl_3 features a potential to simultaneously decrease recombination and series resistance losses. The best BC-BJ solar cell processed according to the simplified new base line process was found to feature a conversion efficiency η of 20.5 % ($V_{\text{OC}} = 655.7$ mV, $J_{\text{SC}} = 40.5$ mA/cm², $\text{FF} = 77.2$ %). Before, such a high efficiency was only achieved by a cell fabricated according to a cost-intensive process sequence featuring an additional thermal treatment. Thus, the simplified new base line process offers a strong decrease in process complexity, whereas the efficiency level is maintainable.

In the *efficiency improvement*, cells were prepared according to the new base line process featuring the co-diffusion module utilizing only solid dopant sources. Therefore, the integration of a BSG layer deposited with the promising EP-setup and a passivation scheme featuring a thermally grown SiO_2 layer as front and an Al_2O_3 layer as rear passivation layer were applied. In order to increase the spiking resistance, a new contact opening pattern was realized in the rear passivation stack. The highest efficiency achieved was found to be 21.1 % ($V_{\text{OC}} = 663.6$ mV, $J_{\text{SC}} = 40.8$ mA/cm², $\text{FF} = 78.0$ %). Twenty five BC-BJ cells of this type exhibited an absolute standard deviation in efficiency of below 0.2 %_{abs} which underlines the high homogeneity of the developed processes on industrial-size wafers. By making use of the new passivation scheme, the open circuit voltage V_{OC} and the short circuit current density J_{SC} could be further increased up to 666.0 mV and 41.1 mA/cm², respectively. Unfortunately, the cells suffer additionally from an increase in fill factor losses arising from both series

resistance and leakage current. By comparing the pseudo fill factor pFF of the best cell of 82.1 % with the one of a reference cell without contact openings in the active cell area of 82.0 %, it could be concluded that Al spiking is not limiting the conversion efficiency of the cell anymore.

One possibility to further improve the conversion efficiency would be to combine the knowledge obtained in the process simplification and the efficiency improvement. In fact, by fabricating BC-BJ cells with a co-diffusion module utilizing the BSG layer deposited by the EP-setup for emitter and the regarded $POCl_3$ co diffusion process for FSF formation. The higher front side passivation quality and the lower $R_{sh,n+}$ of the FSF would probably lead to an increase in J_{SC} and to a decrease in series resistance and, as a consequence, to an increase in FF . Therefore, further investigations need to be done to improve the compatibility of a BSG layer deposited by the EP-setup with the $POCl_3$ co-diffusion process.

In order to evaluate the main loss mechanisms and the pitch distance dependent conversion efficiency limit of the best BC-BJ solar cell fabricated in this work, the next chapter deals with a loss analysis of this cell. The properties of a BC-BJ solar cell processed according to the above mentioned co-diffusion module featuring a BSG-layer deposited with the EP-setup and the regarded $POCl_3$ co-diffusion process are implemented in the simulation as well. Besides the front side passivation stack consisting of a PECVD $SiON_x$ layer and an AR- SiN_x layer, the stack featuring a thermally grown SiO_2 layer is applied within the simulation.

7 Loss analysis of the best cell

In order to guide the way for future efficiency improvements of the solar cell evaluated in this thesis, a loss analysis of the best performing solar cell was carried out. The results of this loss analysis are exclusively published in this thesis.

7.1 Motivation

The solar cell manufactured in this work was found to feature a limitation in open circuit voltage and fill factor. This limitation is caused by recombination and resistance losses. QUOKKA is a 3D-simulation program enabling the simulation of resistance and recombination losses in the silicon bulk [139]. The program numerically solves the charge carrier transport in a quasi-neutral silicon device. Highly doped regions like the FSF, the BSF, and the emitter are taken into account as so-called conductive boundaries [140]. The conductive boundary is defined by the sheet resistance and the dark saturation current density of the highly doped region.

The following chapter deals with an analysis, based on the QUOKKA simulation, of the loss mechanisms of the best cell. This cell features a conversion efficiency of 21.1 % and was discussed in the last chapter. The cell is free of a gap region. The doping structure of the cell was diffused in a co-diffusion module which utilizes PECVD PSG/SiO_x stacks for FSF and BSF formation and a PECVD BSG layer (EP-setup) for emitter formation. Since the BSG layer of the EP-setup has not been optimized for POCl₃ co-diffusion processes, the improved properties of an FSF formed in a POCl₃ co-diffusion process (as discussed in the process simplification) and of an emitter diffused from a BSG layer deposited by utilizing the EP-setup (as discussed in the efficiency improvement) could not be combined up to now. In order to derive the gain in conversion efficiency of a cell based on the latter co-diffusion module, a simulation implementing the improved properties of an FSF diffused in a POCl₃ co-diffusion process are discussed as well. The dark saturation current density of the FSF is varied by utilizing two passivation layers, these are thermally grown silicon dioxide (SiO₂) and PECVD silicon oxynitride (SiON_x). Based on the varied cell properties, the dependence of the conversion efficiency on the pitch distance is regarded. In the last part of this chapter, an efficiency estimation is done which is based on the simulation results and the performance of a sophisticated BC-BJ solar cell featuring a modified cell design.

7.2 Simulation parameters

The properties of the best cell which are required as input parameters for the simulation are listed in Table 7.1. These are the cell dimensions, the properties of the conductive boundaries (FSF, BSF, and emitter), and the properties of the electrodes.

The cell dimensions include the wafer thickness W , the pitch distance x_{pitch} , the width of the BSF x_{BSF} , the width of the emitter x_{E} , the emitter coverage EC , and the contact opening coverage COC . Notice that the EC is a function of x_{pitch} and x_{E} . The COC is a function of the x_{pitch} , the width of the contact openings upon the emitter $x_{\text{CO,p}}$, and the BSF $x_{\text{CO,n}}$.

The required properties of the conductive boundaries are the dark saturation current density J_0 and the sheet resistance R_{sh} . The J_0 was measured by QSSPC, the R_{sh} was determined from the ECV measured carrier concentration profile.

Table 7.1 Dimensions, properties of the conductive boundaries (FSF, BSF, and emitter), and properties of the electrodes of the solar cell implemented in the simulation tool QUOKKA. Except for the dark saturation current density underneath the metal contacts $J_{0,\text{met,BSF}}$ and $J_{0,\text{met,E}}$, the properties were evaluated by measurements. The simulation was performed by assuming a wafer with a bulk resistivity of $3.3 \, \Omega\text{cm}$ and a high life time of $5 \, \text{ms}$.

Dimensions					
W (μm)	x_{pitch} (μm)	x_{BSF} (μm)	x_{E} (μm)	EC (%)	COC (%)
160	1500	300	1200	80	2
Conductive boundaries					
$R_{\text{sh,FSF}}$ (Ω/sq)	$J_{0,\text{FSF}}$ (fA/cm^2)	$R_{\text{sh,BSF}}$ (Ω/sq)	$J_{0,\text{BSF}}$ (fA/cm^2)	$R_{\text{sh,E}}$ (Ω/sq)	$J_{0,\text{E}}$ (fA/cm^2)
354	$66 \cdot 10^{-15}$	38	$127 \cdot 10^{-15}$	55	$64 \cdot 10^{-15}$
Electrodes					
$R_{\text{S,grid}}$ (Ωcm^2)	$\rho_{\text{C,BSF}}$ ($\text{m}\Omega\text{cm}^2$)	$\rho_{\text{C,E}}$ ($\text{m}\Omega\text{cm}^2$)	$J_{0,\text{met,BSF}}$ (fA/cm^2)	$J_{0,\text{met,E}}$ (fA/cm^2)	
0.13	1.0	2.3	315	665	

The properties of the electrodes are the series resistance of the grid $R_{S,grid}$, the specific contact resistance at the interface electrode/BSF $\rho_{C,BSF}$ and electrode/emitter $\rho_{C,E}$, and the dark saturation current density underneath the metallized BSF $J_{0,met,BSF}$ and emitter $J_{0,met,E}$. The series resistance of the grid was calculated according to equation (5-6). The specific contact resistivity was evaluated by 4 point measurements according to the transmission line method [141, 142]. Electrodes featured a contact area of around $200 \mu m \times 5 mm$ and a 2 mm distance from each other. $J_{0,met,BSF}$ and $J_{0,met,E}$ were calculated by considering the carrier concentration profile and by setting the silicon surface recombination velocity to the limit [130]. Therefore, a simulation tool called EDNA was utilized [143].

In this chapter, the conversion efficiency of the cell is shown as a function of the x_{pitch} . In order to consider for an increase in p -metal finger width $x_{met,p}$ with increasing x_{pitch} , the $R_{S,grid}$ was adapted. In order to consider for a COC independent from the x_{pitch} , the width of $x_{CO,n}$ and $x_{CO,p}$ was adapted as well.

7.3 Results and discussion

The cell parameters of the measured and the simulated BC-BJ cell are depicted in Table 7.2. The difference in cell parameters is depicted as well.

Table 7.2 Cell parameters of the best cell measured by the Fraunhofer ISE CalLab PV cells laboratory (Measured), of the best cell simulated with the chosen simulation tool (Simulated) and the calculated difference in cell parameters of the measured and the simulated cell (Difference).

Comment	V_{OC} (mV)	J_{SC} (mA/cm ²)	FF (%)	p FF (%)	FF_0 (%)	η (%)
Measured	663.8	40.8	78.0	82.1	84.0	21.1
Simulated	677.3	41.3	79.7			22.3
Difference	13.5	0.5	1.7			1.2

The simulated cell features a conversion efficiency η of 22.3 %. Hence, the efficiency of the simulated cell is higher than the one of the measured or rather real cell. The increase in the efficiency is mainly caused by an increase in fill factor FF of 1.7 %_{abs}. It is assumed that the elimination of leakage current in the simulation leads to the regarded increase in FF . In reality, the best cell features an FF loss (difference between ideal and pseudo fill factor; $FF_0 - pFF$) of 1.9 %_{abs} arising from the leakage current. The increase in open circuit voltage V_{OC} is assumed to be caused by the

elimination of bulk recombination. Inadequate simulation parameters under estimating the dark saturation current density underneath the metal contacts might influence the regarded difference in V_{OC} as well. The difference in short circuit current density J_{SC} of the measured and the simulated cell is expected to be caused by an insufficient description of optical losses in the passivation stacks. In general, the simulation is expected to provide a realistic estimation of the cell specific electrical losses – these are resistance and recombination losses - without taking into account losses arising from parasitic effects like leakage current.

The loss analysis based on the properties of the best solar cell fabricated in this work is depicted in Figure 7.1. Therefore, a pie chart is depicted indicating the distribution of resistance and recombination losses. The resistance losses are divided into internal, contact and external resistance losses. The recombination losses are further divided into losses arising from recombination in the BSF, the emitter, the FSF, and the bulk.

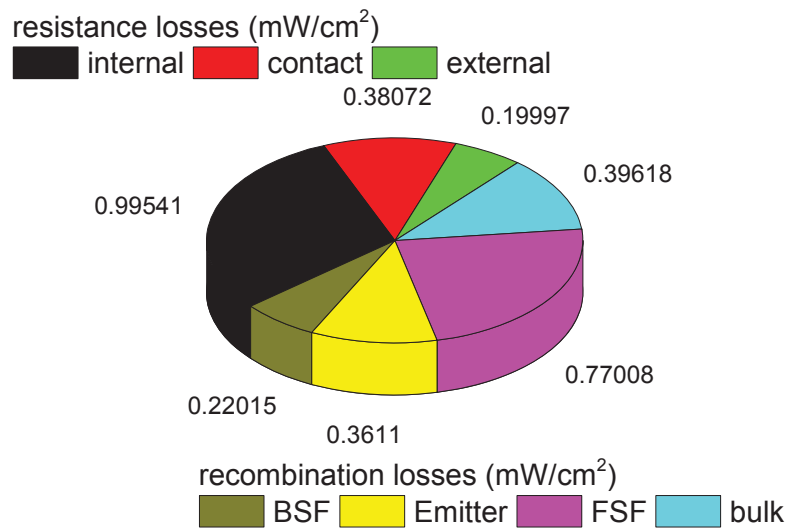


Figure 7.1 Distribution of cell loss mechanisms divided into resistance and recombination losses. The losses are depicted as power losses which directly correspond to the loss in efficiency of the regarded solar cell.

Resistance losses lead to a decrease in the efficiency of 1.6 %_{abs}. A percentage of around 63 % of these resistance losses are internal, 24 % are contact, and 13 % are external resistance losses. Thus, the efficiency of the simulated solar cell is strongly affected by internal resistance losses.

Recombination losses lead to a decrease in the efficiency of 1.7 %_{abs}. A percentage of around 49 % of these recombination losses are caused by FSF recombination, 25 % by bulk recombination, 23 % by emitter recombination, and 14 % by BSF recombination,

whereby emitter and BSF recombination include the recombination losses underneath the metal contacts. Notice that the dark saturation current density at the front side $J_{0,\text{FSF}}$ has an impact on both the V_{OC} and the J_{SC} and, as a consequence, a major impact on the efficiency.

Possible options to decrease the internal resistance losses are to decrease the sheet resistance of the FSF $R_{\text{sh},n+}$ and to decrease the x_{pitch} . By decreasing the $J_{0,\text{FSF}}$, recombination losses at the front side of the cell decrease. Both can be provided by an FSF diffused in a POCl_3 co-diffusion process featuring an $R_{\text{sh},n+}$ of 235 Ω/sq and a $J_{0,\text{FSF}}$ of 46 fA/cm^2 . By making use of the high passivation quality of thermally grown SiO_2 ($J_{0,\text{FSF}} < 15 \text{ fA}/\text{cm}^2$), a further decrease in recombination losses at the front side of the cell is achievable. In order to estimate a realistic efficiency limit based on the measured FSF properties, a variation of the pitch distance is performed, whereby the FSF properties listed in the following table are implemented.

Table 7.3 FSF properties, these are the sheet resistance $R_{\text{sh},n+}$ and the dark saturation current density $J_{0,\text{FSF}}$, in dependence of the applied diffusion source (P-Source) and the front side passivation layer (FS-Pass) as implemented in the simulation.

Label	P-Source	FS-Pass	$R_{\text{sh},n+}$ (Ω/sq)	$J_{0,\text{FSF}}$ (fA/cm^2)
PSG-SiON _x	PSG/SiO _x	PECVD SiON _x	354	66
POCl_3 -SiON _x	POCl_3	PECVD SiON _x	235	46
POCl_3 -SiO ₂	POCl_3	thermal SiO ₂	235	15

Figure 7.2 depicts the dependence of the simulated conversion efficiency η of the cell as a function of the pitch distance x_{pitch} for the varied front side constellations. The measured efficiency of the real cell featuring an FSF diffused from the PECVD PSG/SiO_x stack passivated with a PECVD stack consisting of a SiON_x and an AR-SiN_x layer is highlighted as well. Independent from the constellation, the efficiency decreases with increasing x_{pitch} . This decrease in efficiency is mainly caused by an increase in internal resistance losses. Independent from x_{pitch} , the cell efficiency increases by applying POCl_3 as P-diffusion source and by exploiting the high passivation quality of a thermally grown SiO₂ layer. The corresponding efficiency gain is listed in Table 7.4.

By regarding the cell parameters in dependence of the P-source for cells featuring a constant x_{pitch} of 1500 μm and SiON_x as front side passivation layer, the integration of the POCl_3 co-diffusion process leads to an increase in efficiency of 0.2 %_{abs} up to 22.5 %. Due to the higher front side passivation quality of a cell fabricated with the

POCl_3 co-diffusion process, the V_{OC} and J_{SC} increase by 3.4 mV and 0.1 mA/cm^2 , respectively. Moreover, due to the lower sheet resistance of the FSF and the corresponding decrease in series resistance, the FF increases slightly by 0.2 %_{abs}. This increase in FF would be more prominent for a cell featuring an x_{pitch} exceeding 1500 μm .

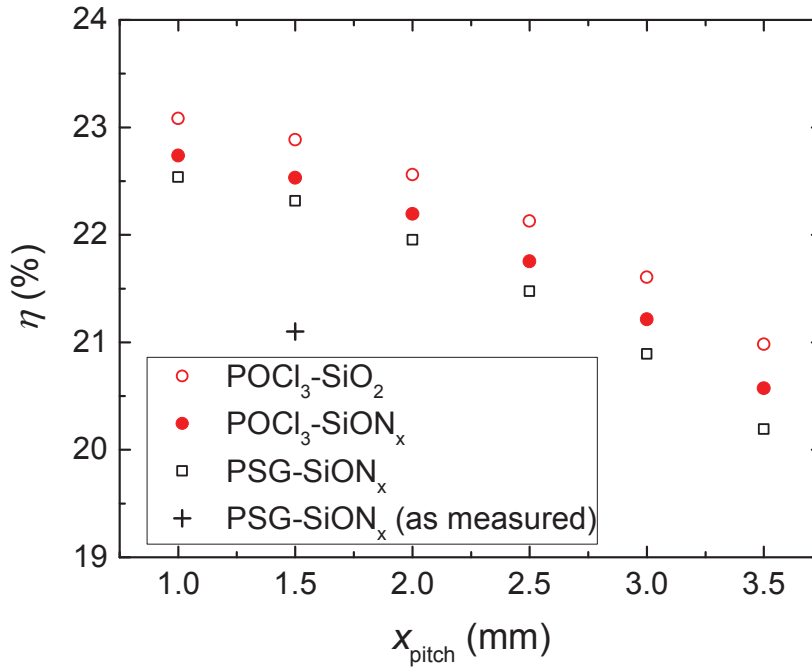


Figure 7.2 Simulated efficiency η versus the pitch distance x_{pitch} of solar cells featuring three different front side constellations. These are an FSF diffused from a PECVD PSG/ SiO_x stack passivated with a PECVD SiON_x /AR- SiN_x (PSG- SiON_x) stack as well as an FSF diffused in POCl_3 containing diffusion steps passivated with the latter PECVD stack ($\text{POCl}_3\text{-SiON}_x$) and a stack consisting of a thermally grown SiO_2 layer and a PECVD coated AR- SiN_x layer ($\text{POCl}_3\text{-SiO}_2$). The efficiency of the measured cell is depicted as well.

By regarding the cell parameters in dependence of the x_{pitch} for cells fabricated with the POCl_3 co-diffusion process (P-source = POCl_3) passivated with a SiON_x layer, the decrease in x_{pitch} from 1500 down to 1000 μm leads to an increase in efficiency of 0.2 %_{abs} up to 22.7 %. This increase in efficiency is mainly caused by a prominent increase in FF from 79.9 % ($x_{\text{pitch}} = 1500 \mu\text{m}$) up to 81.0 % ($x_{\text{pitch}} = 1000 \mu\text{m}$). The increase in FF is the result of a decrease in series resistance or, rephrased, a decrease in resistance losses. Due to the design rules made, the EC decreases with decreasing x_{pitch} . As a consequence, recombination losses enhance with decreasing x_{pitch} . These additional recombination losses arise due to a decrease in rear side passivation quality ($J_{0,\text{BSF}} > J_{0,\text{E}}$) and due to an increase in the electrical shading effect. The decrease in

rear side passivation quality of a cell featuring a x_{pitch} of 1000 μm leads to the decrease in V_{OC} of around 1.2 . The slightly more prominent electrical shading results in the slight decrease in J_{SC} of 0.1 mA/cm^2 .

By comparing the cell parameters in dependence of the front side passivation for cells fabricated with the POCl_3 co-diffusion process and a x_{pitch} of 1000 μm , the integration of a thermally grown SiO_2 layer is related to an increase in efficiency of 0.4 %_{abs} up to 23.1 %. This efficiency gain originates from the higher surface passivation quality which is connected to an increase in V_{OC} of 6.1 mV and in J_{SC} of 0.2 mA/cm^2 .

Table 7.4 Cell parameters of measured and simulated cells in dependence of the utilized P-source for FSF formation, front side passivation layer (referred to as FS-Pass), and the pitch distance x_{pitch} . The dependence of the simulated cell parameters on the diffusion source and the passivation layer is based on the different electrical properties of the FSF like sheet resistance and dark saturation current density.

Comment	P-source	FS-Pass	x_{pitch} (μm)	V_{OC} (mV)	J_{SC} (mA/cm^2)	FF (%)	η (%)
Measured	PSG/ SiO_x	SiON_x	1500	663.8	40.8	78.0	21.1
Simulated	PSG/ SiO_x	SiON_x	1500	677.3	41.1	79.7	22.3
Simulated	POCl_3	SiON_x	1500	680.7	41.4	79.9	22.5
Simulated	POCl_3	SiON_x	1000	679.5	41.3	81.0	22.7
Simulated	POCl_3	SiO_2	1000	685.6	41.5	81.1	23.1

In conclusion: compared to the best cell up to now, an improvement in efficiency of around 0.8 %_{abs} is achievable by exploiting the properties of an FSF diffused in a POCl_3 co-diffusion process, decreasing the x_{pitch} down to 1000 μm , and integrating thermally grown SiO_2 as front side passivation layer.

7.4 Conversion efficiency estimation

In this section, a loss analysis of the best solar cell was performed by utilizing the simulation tool QUOKKA. QUOKKA enables a determination of power losses arising from resistance and recombination losses. The main loss mechanisms limiting the conversion efficiency of the cell were found to be internal resistance and FSF recombination losses. A realistic approach based on available processes was suggested in order to decrease these loss mechanisms. An increase in efficiency of 0.2 %_{abs} is possible by forming the FSF with a POCl_3 co-diffusion process. An additional increase in efficiency of 0.2 %_{abs} is achievable by modifying the pitch distance x_{pitch} of the cell.

By passivating the front side with a thermally grown SiO_2 layer, an increase in efficiency of 0.4 %_{abs} is expected. By neglecting losses arising due to leakage current, an efficiency improvement up to 23.1 % should be achievable. This cell was found to feature a simulated **fill factor of 81.1 %** at a pitch distance of 1000 μm .

Due to the actual design rules of the BC-BJ solar cell, the decrease in x_{pitch} would be connected to a decrease in emitter coverage EC and, as a consequence, to a decrease in open circuit voltage V_{OC} and in short circuit current density J_{SC} . One promising possibility to provide both a low x_{pitch} and a high EC is the substitution of the BSF fingers by local BSF isles as proposed in e.g. [115]. The requirement of a cell design featuring BSF isles is the integration of electrically insulating rear passivation layers which allow for a so-called decoupling of the doped pattern from the metallization pattern. In this work, insulation stacks were investigated by making use of metal insulator semiconductor structures. The investigations were published in [144]. An insulation stack which was found to feature a very high shunt resistance is a stack consisting of ALD Al_2O_3 with a thickness of 20 nm, PECVD SiO_x featuring a thickness of 1500 μm , and PECVD SiN_x with a thickness of around 80 nm.

By processing according to the new base line process and by performing an additional PECVD step in order to deposit a thick SiO_x layer on the rear side of the solar cell, BC-BJ cells featuring a x_{pitch} of 1000 μm and an EC of 91 % were prepared. The cell parameters of such a cell are depicted in Table 7.5. The pseudo fill factor pFF and the ideal fill factor FF_0 were determined by $\text{Suns}V_{\text{OC}}$ measurements. The cell features a remarkably high J_{SC} of **42.4 mA/cm²**. This clearly indicates the high potential of such a solar cell featuring an insulation stack as rear side passivation. Due to the relatively low V_{OC} of 652.5 mV and fill factor FF of 76.4 %, the drastic gain in J_{SC} could not be fully exploited. The pFF of 81.0 % indicates an inconspicuous increase in leakage current ($FF_0 - pFF = 2.9$ %_{abs}). Thus, the insulation stack deposited on the rear side of the cell is assumed to mainly avoid additional short circuits but needs to be improved further.

By utilizing the voltage analysis of a cell featuring the above mentioned structure and dimensions, the limitation in V_{OC} is **701.9 mV**. Therefore, the impact of the bulk and the recombination underneath the metal contact was neglected. The dark saturation current density of the FSF was set to 15 fA/cm² (as measured), of the BSF to 127 fA/cm² (as measured), and of the emitter to 30 fA/cm² (as measured in [145]). This underlines the high potential of the solar cell to achieve a high V_{OC} with the available processes. A possibility to fully exploit this potential would be the introduction of passivated contacts like published by Feldmann et al. in [146].

Table 7.5 Cell parameters measured by J-V and Suns V_{OC} measurements of a cell integrating an insulation stack as rear passivation layer. The insulation stack enables a cell design featuring a low pitch distance x_{pitch} and a high emitter coverage EC.

x_{pitch} (μm)	EC (%)	V_{OC} (mV)	J_{SC} (mA/cm ²)	FF (%)	pFF (%)	FF ₀ (%)	η (%)
1000	91	652.5	42.4*	76.4	81.0	83.9	21.1

*Confirmed by a measurement of the quantum efficiency

To conclude, the integration of a co-diffusion module utilizing POCl_3 as gaseous dopant source for FSF formation and a BSG layer deposited by the EP-setup for emitter formation would allow for the fabrication of cells with a conversion efficiency exceeding 22 %. By applying thermally grown SiO_2 as front side passivation layer, the efficiency would increase further and exceed 23 %. The integration of insulation stacks would enable the fabrication of cells featuring a low x_{pitch} and a high EC and therefore a decrease in resistance and recombination losses. A process sequence which utilizes the modified co-diffusion module, the thermal growth of a SiO_2 layer as front side passivation, and the deposition of an insulation stack as rear side passivation is assumed to enable a major increase in conversion efficiency **exceeding 24 %**. In order to approach the latter high efficiency level, further investigation and experimentation towards industrially convertible insulating thin films and passivated metal contacts is strongly recommended.

8 Summary

In this thesis, highly efficient small-size back-contact back-junction (BC-BJ) silicon solar cells were fabricated by utilizing co-diffusion processes which enable a remarkable decrease in process steps and costs. The BC-BJ solar cells were processed on large-size monocrystalline n -type Cz-Si wafers in an industrial pilot-line environment. Patterning techniques, diffusion processes, and the combination of processes to working BC-BJ process sequences were exclusively developed in this work.

The BC-BJ solar cell features three differently doped surfaces. These are the front surface field (FSF, n^+ -Si), the back surface field (BSF, n^+ -Si), and the emitter (p^+ -Si). The introduction of these doped surfaces by sequentially performed cost-intensive thermal processes, denoted as sequential diffusion, is related to process costs of 85 eurocent per wafer. Co-diffusion processes enable the simultaneous diffusion of all required doped surfaces in only one thermal process and, consequently, a reduction in process costs by 24 %_{rel} down to 64.8 eurocent per wafer.

In order to exploit the innovation of a co-diffusion process and the related decrease in process costs, **the first part** of this work was dedicated to the evaluation of co-diffusion processes fulfilling the special requirements of BC-BJ solar cells. As dopant sources, solid dopant sources, in fact boron- (BSG) and phosphorus-doped silicate glass (PSG) layers deposited by means of plasma enhanced chemical vapor deposition (PECVD), and a gaseous dopant source, in fact POCl_3 , were utilized.

BSG layers, deposited by two different PECVD setups, enabled an adjustment of the doping-level expressed by the sheet resistance R_{sh} in a wide range ($R_{\text{sh}} = 50\text{-}500 \text{ } \Omega/\text{sq}$) by varying process parameters like the diborane gas flow and the film thickness. Surfaces with a maximum boron-concentration of $9 \cdot 10^{19} \text{ cm}^{-3}$ and a depth of 600 nm could be fabricated, which are suitable for the emitter of a BC-BJ cell. The deposition of stacks consisting of a PSG and a silicon oxide (SiO_x) layer acting as solid P-dopant sources were adapted to the special requirements of the BSF and the FSF as well as to the special boundary conditions of the BC-BJ related process sequences. BSF adequate surfaces featuring a phosphorus-concentration of $1\text{-}2 \cdot 10^{20} \text{ cm}^{-3}$ and a depth of around 800 nm could be achieved. Additionally, P-diffusion from a PSG/ SiO_x stack was determined to be independent of cleaning processes as well as layer stacking and, as a consequence, compatible to the BC-BJ process sequence. FSF adequate surfaces with a maximum P-concentration of $7 \cdot 10^{18} \text{ cm}^{-3}$ and a depth of around 380 nm could be achieved on textured surfaces. The successful development of BSG layers and

PSG/SiO_x stacks in order to achieve BC-BJ adequate doping-levels resulted in the first BC-BJ adequate co-diffusion module featuring solid dopant sources.

The second co-diffusion module includes the combination of two solid dopant sources for emitter and BSF-formation on the rear and POCl₃ as a gaseous dopant source for FSF-formation on the front side of the cell. First, diffusion processes featuring POCl₃ were evaluated in order to achieve FSF adequate doping-levels. Within the scope of these evaluations, a strong correlation between the sheet resistance and the oxygen gas flow during diffusion processes featuring POCl₃ could be determined. It was found that a minimum oxygen gas flow is required in order to achieve a homogenous P-diffusion. At a minimum oxygen gas flow, a linear adjustment of the sheet resistance ($R_{sh} = 190\text{--}350 \Omega/\text{sq}$) was possible by varying the plateau time during the thermal growth of the PSG layer. FSF adequate surfaces with a maximum P-concentration slightly higher than $1 \cdot 10^{19} \text{ cm}^{-3}$ and a depth of around 400 nm could be achieved on textured surfaces. The compatibility of BSG layers to diffusion processes featuring POCl₃ was achieved by setting the oxygen gas flow during diffusion as low as possible and by protecting the BSG layer with an additional SiO_x layer. Out-diffusion of boron from the BSG layer into the SiO_x layer during diffusion could be prevented by increasing the boron-concentration in the BSG layer. The successful development of POCl₃ processes in order to achieve FSF adequate doping-levels and the modification of the BSG layer to the BSG/SiO_x stack resulted in the second co-diffusion module featuring solid and gaseous dopant sources.

The second part of this work focused on the production of BC-BJ solar cells with a gap region according to the co-diffusion module featuring solid dopant sources. A stack consisting of a PECVD silicon oxynitride (SiON_x) layer and an anti-reflection silicon nitride (AR-SiN_x) layer was utilized as a front side passivation, whereas a stack consisting of an atomic layer deposition (ALD) aluminum oxide (Al₂O₃) layer and an AR-SiN_x layer was deposited as the rear side passivation. Based on several modifications of the initial base line process, the conversion efficiency η was improved step by step. Solar cells with industrially convertible dimensions like a BSF width x_{BSF} of 300 μm and a pitch distance x_{pitch} of 1500 μm were fabricated.

A first observation was that BC-BJ solar cells feature an efficiency between 18.1 to 18.4 % independent of the applied material. Thus, the solar cells were assumed to be limited by the process techniques. In this state, the BC-BJ solar cell based on *n*-type Cz-Si material featured an efficiency of 18.1 %, an open circuit voltage V_{OC} of 641.8 mV, a short circuit current density J_{SC} of 38.7 mA/cm², and a fill factor FF of 73.0 %.

By integrating a thermal silicon dioxide (SiO_2) as passivation layer on both sides of the solar cell, the efficiency could be increased by 0.8 %_{abs} up to 18.9 % ($V_{\text{OC}} = 642.0$ mV, $J_{\text{SC}} = 39.7$ mA/cm², $FF = 74.1$ %). The gain in efficiency was significantly caused by a very low front side recombination expressed by the dark saturation current density of the FSF $J_{0,\text{FSF}}$ below 15 fA/cm². A voltage analysis based on the dark saturation current densities of every single passivated doped surface enabled an estimation of the passivation limit in open circuit voltage $V_{\text{OC,limit}}$, whereby bulk and contact recombination were neglected. Thus, the passivation scheme of the base line process was determined to allow for a $V_{\text{OC,limit}}$ of 676 mV. Due to the very low emitter passivation quality, the passivation scheme with SiO_2 layers on both sides of the wafer featured a $V_{\text{OC,limit}}$ of 651 mV. A combination of a thermal SiO_2 layer on the front and an Al_2O_3 layer on the rear side of the solar cell was assumed to enable both a high J_{SC} due to the high passivation quality of the front side and a relatively high $V_{\text{OC,limit}}$ of 687 mV.

The next gain in efficiency could be achieved by implementing an improved BSG layer for emitter formation. Thus, the efficiency could be increased by 1.3 %_{abs} up to 19.4 % ($V_{\text{OC}} = 650.0$ mV, $J_{\text{SC}} = 40.1$ mA/cm², $FF = 74.0$ %). The gain in efficiency was achieved by a decrease in the dark saturation current density of the emitter $J_{0,\text{E}}$ from 91 down to 64 fA/cm² and a less destructive impact of the improved PECVD process and/or diffusion process on the bulk life time.

A variation in doping-structure was performed for two major reasons: cost-reduction by omission of the gap-region and defect observation. The defect observation was carried out by performing an additional thermal process (drive-in) which allows for the formation of very deep doped surfaces. The first important finding was that the omission of the gap region has no negative impact on the cell performance and is rather related to an increase in FF . The second important finding was that deep profiles and a corresponding increase in passivation quality and spiking resistivity enable an increase in efficiency up to 20.0 % ($V_{\text{OC}} = 656.9$ mV, $J_{\text{SC}} = 40.6$ mA/cm², $FF = 75.2$ %). The penetration depth of spikes could be determined to be around 600 nm by cross-section samples regarded with the help of scanning electron microscope (SEM) imaging.

The second part was completed by thickening the electrodes of the best cells with the help of a plating step. Thus, an efficiency of 20.5 % ($V_{\text{OC}} = 658.7$ mV, $J_{\text{SC}} = 40.9$ mA/cm², $FF = 75.7$ %) could be achieved which was independently confirmed by the Fraunhofer ISE CalLab PV cells laboratory.

Based on the fundamental knowledge of the second part of this thesis, a modified base line process was introduced allowing for the assembly of gap-free solar cells without

drive-in. Due to the omission of the gap region, process costs related to the co-diffusion module could be further decreased by 28 %_{rel} down to 46.7 eurocent per wafer. The co-diffusion module with POCl₃ in the diffusion atmosphere was found to feature the lowest process costs of 39.8 eurocent per wafer.

The third part of this work was, consequently, dedicated to the exploitation of the high cost saving and efficiency potential of the gap-free BC-BJ solar cell based on co-diffusion. By utilizing the co-diffusion module with POCl₃, the potential in cost saving was exploited by maintaining the conversion efficiency of a cell featuring two temperature steps (co-diffusion and drive-in). The efficiency of 20.5 % ($V_{OC} = 655.7$ mV, $J_{SC} = 40.5$ mA/cm², $FF = 77.2$ %) was independently confirmed by the Fraunhofer ISE CalLab PV cells laboratory and is the result of an improved FSF featuring an increase in passivation quality as passivated with PECVD SiON_x ($J_{0,FSF} = 46$ fA/cm²) and an increase in lateral conductivity due to a decrease in the sheet resistance of the FSF ($R_{sh,n+} = 235$ Ω/sq) and the specific resistivity of the wafer. In comparison, the FSF diffused from the PSG/SiO_x stack without drive-in was found to feature a $J_{0,FSF}$ of 66 fA/cm² and an $R_{sh,n+}$ of 354 Ω/sq.

The exploitation of the efficiency potential was carried out with the proven co-diffusion module utilizing solid dopant sources. In order to increase the passivation quality and the bulk life time, the improved BSG layer was utilized for emitter formation. An increase in spiking resistivity was achieved by decreasing the contact opening coverage *COC* from 8 % down to 2 %. Consequently, the highest efficiency of 21.1 % ($V_{OC} = 663.8$ mV, $J_{SC} = 40.8$ mA/cm², $FF = 78.0$ %) could be achieved which was independently confirmed by the Fraunhofer ISE CalLab PV cells laboratory. Moreover, the standard deviation in efficiency of 25 identically processed small-size (4cm²) BC-BJ cells on one industrial-size (239 cm²) wafer was below 0.2 %_{abs} and underlines the compatibility of the investigated processes to fabricate industrial-size BC-BJ solar cells. The highest V_{OC} of 666.0 mV and J_{SC} of 41.1 mA/cm² was achieved with a BC-BJ solar cell featuring a SiO₂/AR-SiN_x front and an Al₂O₃/AR-SiN_x passivation stack.

The last part of this work included a loss analysis (QUOKKA) and a guideline towards increasing efficiencies of the gap-free and co-diffused BC-BJ solar cell. It was found that the best cell mainly suffers due to internal resistance and recombination losses at the front side. Co-diffusion modules combining POCl₃ for FSF and BSG layers deposited with the EP-setup for emitter formation, thermally grown silicon dioxide as a front side passivation layer, insulating thin films, and passivated contacts were found to be key technologies for increasing the efficiency up to 24 %.

9 Outlook

The best cell, which features a FSF diffused from a PSG/SiO_x stack and a PECVD SiON_x/AR-SiN_x front side passivation stack, is mainly limited by lateral resistance losses and front side recombination losses. A short term improvement in conversion efficiency η is assumed to be possible by combining the improved BSG layer (EP-setup) and a diffusion process featuring POCl₃ in a new co-diffusion module. The electrical properties of the corresponding FSF and the emitter as well as a decrease in pitch distance towards 1000 μm would lead to a gain in efficiency exceeding 22 %. The findings of this thesis showed that the compatibility of a solid dopant source to a diffusion process featuring POCl₃ is not trivial and rather needs to be improved carefully by protecting the solid dopant source with an additional layer and by adjusting the gaseous mixture during the diffusion process in order to achieve low oxidation rates, for example.

A long term improvement in efficiency approaching 24 % is assumed to be achievable by exploiting the potential of passivated contacts and insulating thin films. Insulating thin films enable the integration of innovative doping-structures, like BSF isles, featuring relatively high emitter coverages at low pitch distances. As a consequence, a simultaneous increase in all cell parameters and, hence, a major increase in efficiency is possible. The high potential in short circuit current density J_{SC} of cells featuring an insulation stack could already be demonstrated within this thesis. By integrating an additional PECVD process in the base line process of a gap-free and co-diffused BC-BJ solar cell, a solar cell with an emitter coverage of 91 % and a pitch distance of 1000 μm was fabricated. The solar cell featured a remarkably high J_{SC} of 42.4 mA/cm² (not confirmed by the Fraunhofer ISE CalLab PV cells laboratory) which certainly underlines the efficiency potential of BC-BJ cells with insulation layers.

Since all the processes within the base line process were developed on industrial-size wafers, the maximum conversion efficiency of 21.1 % is already on a high level, and the efficiency deviation along an industrial-size wafer of below 0.2 %_{abs} is very low, the BC-BJ cells developed within this work are suitable for a so-called upscaling of the cell format from small-size (4 cm²) to industrial-size (239 cm²). An industrially convertible upscaling with low metal consumption is assumed to be achievable by a so-called three dimensional busbar design. First generation solar cells utilizing the base line process developed in this work and a three dimensional busbar design were already published by Hendrichs et al. in [147]. An industrial-size BC-BJ solar cell with an efficiency of 18.1 % could already be achieved. The corresponding J - V curve is depicted in Figure 2.5 at the beginning of this thesis.

10 Deutsche Zusammenfassung

In dieser Arbeit wurden hocheffiziente Rückseitenkontakt (RSK) Solarzellen hergestellt. Die Prozessreihe basierte dabei auf einem Diffusionsprozess, welcher die simultane Dotierung aller obligatorischen Hochdotierungen per Diffusion (simultane Diffusion) in einem einzigen Hochtemperaturschritt ermöglicht. Durch die Umgehung vieler einzeln durchgeführter, kostenintensiver Diffusionsschritte, erlaubt die simultane Diffusion eine außerordentliche Reduktion der Prozesskosten. Die Solarzellen wurden auf großformatigem, monokristallinem n -Typ Cz-Si Material in einer industrienahen Pilot-Linie entwickelt. Strukturierungsschritte, Diffusionsprozesse, und die Zusammenstellung der zellrelevanten Prozesslinien wurden exklusiv in dieser Arbeit entwickelt.

RSK Solarzellen integrieren drei Hochdotierungen, u.z. das FSF (n^+ -Si), das BSF (n^+ -Si) und den Emitter (p^+ -Si). Die Herstellung dieser Dotierungen in einer seriellen Abfolge mehrerer Diffusionsschritte (sequentielle Diffusion) ist mit einem Kostenaufwand von 85.0 Eurocent pro Wafer verbunden. Dem gegenüber steht die simultane Diffusion mit einem Kostenaufwand von 64.8 Eurocent pro Wafer, was einem Kostenvorteil von 24 %_{rel} entspricht.

Um das Einsparpotenzial einer simultanen Diffusion ausschöpfen zu können, wurden **im ersten Teil** dieser Arbeit simultane Diffusionsprozesse entwickelt welche den besonderen Anforderungen einer RSK Solarzelle entsprechen. Als feste Dotierstoffquellen wurden Bor- (BSG) und Phosphor-dotierte Silikatglas (PSG) Schichten eingesetzt, welche mit der plasmaunterstützten Gasphasenabscheidung (PECVD) hergestellt wurden. Als gasförmige Dotierstoffquelle wurde POCl_3 eingesetzt.

Durch Anpassung der Prozessparameter während der BSG Abscheidung, wie bspw. Diborangasfluss und BSG-Schichtdicke, wurde eine flexible Einstellung des Dotierstoff-Levels in Silicium, ausgedrückt mit dem Schichtwiderstand R_{sh} , in einem weiten Bereich ($R_{\text{sh}} = 50\text{-}500 \text{ } \Omega/\text{sq}$) erreicht. Emitter adäquate Bor-Dotierungen mit einer maximalen Bor-Konzentration von $9 \cdot 10^{19} \text{ cm}^{-3}$ und einer Tiefe von 600 nm konnten realisiert werden. Für die Integration von Phosphor-Dotierungen (BSF und FSF) wurden Schichtstapel bestehend aus einer PSG Schicht und einer Siliciumoxid (SiO_x) Schicht als Phosphor-Dotierstoffquellen eingesetzt. Bei der Integration der Dotierungen wurden zudem die besonderen RSK Anforderungen und Einflussfaktoren der angestrebten Prozessreihe berücksichtigt. BSF relevante Phosphor-Dotierungen mit einer Phosphor-Konzentration von $1\text{-}2 \cdot 10^{20} \text{ cm}^{-3}$ und einer Tiefe von 800 nm konnten

produziert werden. Der Einfluss der RSK Prozessreihe auf die Phosphor-Diffusion von den eingesetzten Schichtstapeln wurde als unauffällig eingestuft. Untersucht wurden der Einfluss von Reinigungsprozessen und die Auswirkung der speziellen Stapelsituation während der simultanen Diffusion. Schließlich wurden FSF relevante Phosphor-Dotierungen mit einer Phosphor-Konzentration von $7 \cdot 10^{18} \text{ cm}^{-3}$ und einer Tiefe von 380 nm auf texturierten Oberflächen realisiert. Die erfolgreiche Evaluierung von BSG Schichten und PSG/SiO_x Stapeln hinsichtlich ihrer Kompatibilität zu RSK Solarzellen hatte schließlich die Entwicklung des ersten simultanen Diffusionsmoduls als Folge, welches nur auf festen Dotierstoffquellen basiert.

Im Rahmen des zweiten simultanen Diffusionsmoduls wurde der gleichzeitige Einsatz von zwei festen (Herstellung Emitter und BSF) auf der Zellrückseite und POCl₃ als gasförmige Dotierstoffquelle (Herstellung FSF) auf der Zellvorderseite angestrebt. Zunächst wurden Diffusionsprozesse mit POCl₃ hinsichtlich FSF kompatibler Dotierstoff-Level untersucht. Dabei stellte sich eine starke Abhängigkeit des Dotierstoff-Levels von dem Sauerstoffgasfluss während der Diffusion heraus. Homogen ausgeprägte Dotierungen konnten dementsprechend nur mit einem minimalen Sauerstoffgasfluss realisiert werden. Eine lineare Einstellung des Schichtwiderstands ($R_{sh} = 190\text{-}350 \text{ } \Omega/\text{sq}$) wurde durch eine Variation der PSG Belegungszeit bei einem minimalen Sauerstoffgasfluss erreicht. Die generierten Phosphordotierungen zeichneten sich durch eine Phosphor-Konzentration von $1 \cdot 10^{19} \text{ cm}^{-3}$ und einer Tiefe von 400 nm auf texturierten Oberflächen aus und sind daher ideal geeignet für die FSF Applikation. Die Kompatibilität von BSG Schichten zu den Diffusionsprozessen mit POCl₃ wurde durch eine Reduzierung des Sauerstoff Gasflusses während der Diffusion und die Abscheidung einer zusätzlichen SiO_x Schutzschicht auf der BSG Schicht vor der Diffusion erreicht. Der negative Einfluss von Bor-Ausdiffusion aus der BSG Schicht in die aufliegende SiO_x Schicht auf die Bor-Diffusion aus der BSG Schicht in Silicium konnte verhindert werden, indem die Bor Konzentration in der BSG Schicht erhöht wurde. Die erfolgreiche Entwicklung von Diffusionsprozessen mit POCl₃ hinsichtlich ihrer Kompatibilität zu FSF Dotierungen und die Modifikation von BSG Schichten zu BSG/SiO_x Stapeln hatte schließlich die Entwicklung des zweiten simultanen Diffusionsmoduls als Folge, welches auf eine Kombination von festen und gasförmigen Dotierstoffquellen zurückgreift.

Der zweite Teil dieser Arbeit strebte die Produktion von RSK Solarzellen mit Gap (engl. Lücke) mit dem simultanen Diffusionsmodul an, welches auf feste Dotierstoffquellen zurückgreift. Als Vorderseitenpassivierung wurde ein Stapel bestehend aus einer PECVD Siliciumoxynitrid (SiON_x) Schicht und einer Antireflex

Siliciumnitrid (AR-SiN_x) Schicht eingesetzt. Die Rückseitenpassivierung wurde durch Applikation eines Schichtstapels bestehend aus einer Aluminiumoxid (Al₂O₃) Schicht und einer AR-SiN_x Schicht realisiert. Die Al₂O₃ Schicht wurde dabei mittels Atomlagenabscheidung (ALD) hergestellt. Um eine schrittweise Verbesserung des Solarzellenwirkungsgrads zu erreichen, wurde die initiale Prozesslinie stellenweise modifiziert und die hergestellten Solarzellen ausgewertet. Die hergestellten Solarzellen wurden entsprechend industriell umsetzbarer Maßstäbe mit einer BSF Fingerbreite von 300 µm und einer Pitch-Distanz von 1500 µm produziert.

Zunächst stellte sich heraus, dass die RSK Solarzellen nicht von dem Ausgangsmaterial, sondern von den Prozessen limitiert werden. So wurde auf dem favorisierten *n*-Typ Cz-Si Material ein Wirkungsgrad η von 18.1 % erreicht. Die Zelle zeichnete sich durch eine offene Klemmenspannung V_{OC} von 641.8 mV, einer Kurzschlussstromdichte J_{SC} von 38.7 mA/cm² und einem Füllfaktor FF von 73.0 % aus.

Durch den Einsatz von thermisch oxidierten Siliciumdioxid (SiO₂) Schichten als Vorderseiten- und Rückseitenpassivierung konnte eine erste Wirkungsgradsteigerung um 0.8 %_{abs} auf einen Wirkungsgrad von 18.9 % ($V_{OC} = 642.0$ mV, $J_{SC} = 39.7$ mA/cm², $FF = 74.1$ %) erreicht werden. Die Steigerung des Wirkungsgrads wurde primär durch eine sehr hohe Qualität der Vorderseitenpassivierung erreicht, welche durch die Dunkelstromdichte des FSF $J_{0,FSF}$ ausgedrückt wird. So wurde ein $J_{0,FSF}$ kleiner als 15 fA/cm² ermittelt. Eine Spannungsanalyse, welche auf den einzelnen Dunkelströmen der zellspezifischen, passivierten Oberflächen basiert, erlaubte eine Abschätzung der durch die passivierten Oberflächen limitierten offenen Klemmenspannung $V_{OC,limit}$. So ermöglichen die Passivierungen der initialen Prozesslinie ein $V_{OC,limit}$ von 676 mV. Demgegenüber erlauben die SiO₂ Passivierungen der modifizierten Prozesslinie lediglich ein $V_{OC,limit}$ von 651 mV, was besonders durch die geringe Passivierqualität von SiO₂ auf dem Emitter verursacht wird. Die Kombination von einer SiO₂ Schicht als Vorderseiten- und eine Al₂O₃ Schicht als Rückseitenpassivierung wurde als eine interessante Option eingeschätzt, welche durch ein sehr hohes J_{SC} Potenzial und ein $V_{OC,limit}$ von 687 mV ausgezeichnet ist.

Die folgende, signifikante Effizienzoptimierung wurde durch den Einsatz einer optimierten BSG Schicht für die Emitter Formation erreicht. So konnte der Wirkungsgrad um 1.3 %_{abs} auf 19.4 % ($V_{OC} = 650.0$ mV, $J_{SC} = 40.1$ mA/cm², $FF = 74.0$ %) erhöht werden. Die Zelloptimierung wurde durch eine Reduzierung der Emitter Dunkelstromdichte $J_{0,E}$ von 91 auf 64 fA/cm² und einem verringerten,

negativen Einfluss des PECVD Prozesses und/oder der Emitter Formation auf die Volumenlebensdauer erreicht.

Eine Variation der Dotierungsstruktur wurde aus zwei wesentlichen Gründen durchgeführt: Kostenreduktion durch die Substitution des Gap-Bereichs und Identifikation von Defekten durch die Integration von tiefen Dotierungen, welche in einem zweiten Temperaturschritt (Eintreiben) realisiert wurden. Die erste wichtige Entdeckung war, dass die Substitution des Gap-Bereichs keinen negativen, sondern einen positiven Einfluss auf den Füllfaktor und damit den Wirkungsgrad der Zelle hat. Die zweite wesentliche Entdeckung war, dass der zweite Temperaturschritt eine Erhöhung der Passivierungsqualität und der Robustheit gegenüber Legierungsprozessen an der Schnittstelle Aluminium-Silicium, sogenannte Aluminium Spikes, als Folge hatte. So wurde ein neuer Höchstwirkungsgrad von 20.0 % erreicht ($V_{OC} = 656.9 \text{ mV}$, $J_{SC} = 40.6 \text{ mA/cm}^2$, $FF = 75.2 \%$). Anhand von Querschnittsproben, welche in einem Rasterelektronenmikroskop (REM) betrachtet wurden, konnte zudem die Eindringtiefe von Spikes bestimmt werden.

Der zweite Teil der Arbeit wurde mit einer galvanischen Elektrodenaufdickung der besten Solarzellen und einer damit verbundenen weiteren Wirkungsgradsteigerung abgeschlossen. Die Zelle mit dem höchsten Wirkungsgrad von 20.5 % ($V_{OC} = 658.7 \text{ mV}$, $J_{SC} = 40.9 \text{ mA/cm}^2$, $FF = 75.7 \%$) wurde durch eine unabhängig durchgeführte Messung des Fraunhofer ISE Kalibrationslabors bestätigt. Die Wirkungsgradsteigerung war dabei das Resultat einer Verringerung des Serienwiderstands der Solarzelle.

Basierend auf den entscheidenden Ergebnissen aus dem zweiten Teil wurde eine modifizierte Prozesslinie eingeführt, welche die Herstellung von RSK Zellen ohne Gap-Bereich und ohne zweiten Temperaturschritt ermöglicht. Durch die Substitution des Gap-Bereichs können die Prozesskosten des simultanen Diffusionsmoduls um 28 %_{rel} auf 46.7 Eurocent pro wafer reduziert werden. Noch geringere Prozesskosten in Höhe von 39.8 Eurocent pro wafer werden durch das simultane Diffusionsmodul mit POCl_3 erreicht.

Der dritte Teil der Arbeit widmete sich der Ausschöpfung des Einspar- und des Wirkungsgradpotenzials der RSK Solarzelle ohne Gap-Bereich, welche auf der simultanen Diffusion basiert. Die Ausschöpfung des Einsparpotenzials wurde durch die Herstellung einer RSK Solarzelle demonstriert, welche auf Basis des simultanen Diffusionsmoduls mit POCl_3 in nur einem einzigen Temperaturschritt gefertigt wurde. Diese Zelle weist einen Wirkungsgrad von 20.5 % ($V_{OC} = 655.7 \text{ mV}$, $J_{SC} = 40.5 \text{ mA/cm}^2$, $FF = 77.2 \%$) auf, welcher durch eine unabhängig durchgeführte Messung des Fraunhofer ISE Kalibrationslabors bestätigt wurde, und hat somit den

gleichen Wirkungsgrad wie die bis dahin effektivste Zelle, welche jedoch in zwei Temperaturschritten gefertigt wurde und somit deutlich höhere Prozesskosten verursacht. Die Wirkungsgradsteigerung ist das Resultat einer Verringerung von Rekombinationsströmen an der PECVD SiON_x passivierten Vorderseite ($J_{0,\text{FSF}} = 46 \text{ fA/cm}^2$) und einer Erhöhung der lateralen Leitfähigkeit. Die laterale Leitfähigkeit wurde dabei durch eine Reduzierung des FSF Schichtwiderstands ($R_{\text{sh}} = 235 \text{ } \Omega/\text{sq}$) und des spezifischen Widerstands des Substrats erhöht. Zum Vergleich, ein FSF basierend auf der Phosphor-Diffusion von PSG/ SiO_x Stapeln impliziert ein $J_{0,\text{FSF}}$ von 66 fA/cm^2 und einen R_{sh} von $354 \text{ } \Omega/\text{sq}$.

Die Ausschöpfung des Effizienzpotenzials der Zelle ohne Gap-Bereich wurde mit dem bewährten, simultanen Diffusionsmodul, welches ausschließlich auf feste Dotierstoffquellen zurückgreift, durchgeführt. Um die Passivierungsqualität und die Volumenlebensdauer zu erhöhen, wurde die optimierte BSG Schicht erneut zum Einsatz gebracht. Eine Erhöhung der Robustheit gegen Aluminium-Spikes wurde durch eine Verringerung der Kontaktöffnungsfläche von 8 % auf 2 % erreicht. RSK Solarzellen, welche auf den genannten Modifikationen basieren, zeigten den höchsten Wirkungsgrad von 21.1 % ($V_{\text{OC}} = 663.8 \text{ mV}$, $J_{\text{SC}} = 40.8 \text{ mA/cm}^2$, $FF = 78.0 \%$), was durch eine unabhängig durchgeführte Messung des Fraunhofer ISE Kalibrationslabors bestätigt wurde. Zudem implizierten 25 kleinformatige (4 cm^2), identisch hergestellte RSK Solarzellen auf einem großformatigen Wafer (239 cm^3) eine sehr geringe Standardabweichung kleiner als 0.2 %_{abs}, was die Kompatibilität der untersuchten Prozesse für die Herstellung von großformatigen RSK Solarzellen unterstreicht. Das höchste V_{OC} von 666.0 mV und J_{SC} von 41.1 mA/cm^2 wurde mit einer RSK Zelle erreicht, welche einen $\text{SiO}_2/\text{AR-SiN}_x$ Stapel als Vorderseiten und einen $\text{Al}_2\text{O}_3/\text{AR-SiN}_x$ Stapel als Rückseitenpassivierung integriert.

Im letzten Teil der Thesis wurde eine Verlustanalyse (QUOKKA) durchgeführt, welche einen Wegweiser für zukünftige Wirkungsgradsteigerungen der simultan diffundierten RSK Solarzelle ohne Gap-Bereich darstellt. Interne Widerstandsverluste und Rekombinationsverluste an der Zell Vorderseite wurden als bedeutende Verlustmechanismen identifiziert, welche den Wirkungsgrad der Solarzelle limitieren. Die Kombination der optimierten BSG Schicht mit POCl_3 als Diffusionsquellen in einem neuen simultanen Diffusionsmodul, thermisch aufgewachsenes Siliciumdioxid als Vorderseitenpassivierung, sowie elektrisch isolierende Schichten und passivierte Kontakte wurden als Schlüsseltechnologien eingestuft, welche eine Wirkungsgradsteigerung bis über 24 % als Folge haben könnten.

Bibliography

- [1] M. Anschütz, *Weltbevölkerung im 21. Jahrhundert*, Monsenstein und Vannerdat, 2014.
- [2] F. Cocks, *Energy demand and climate change, issues and resolutions*, Wiley-VCH Verlag GmbH & Co. KGaA, 2009.
- [3] BMWi, *Verfügbarkeit und Versorgung mit Energierohstoffen*, Bundesministerium für Wirtschaft und Technologie, 2006.
- [4] Hesketh and Abraham, *Reaction engineering for pollution prevention*, Elsevier, vol. 1, 2000.
- [5] IPCC, *Special report on renewable energy sources and climate change mitigation*, Intergovernmental Panel on Climate Change, 2008.
- [6] IAEA, *The great east japan earthquake expert mission*, International Atomic Energy Agency, 2011.
- [7] R. C. Ewing et al., *Radiation effects in nuclear waste forms for high-level radioactive waste*, Progress in Nuclear Energy, vol. 29, pp. 63-127, 1995.
- [8] P. Würfel, *Physics of solar cells*, Spektrum Akademischer Verlag, Heidelberg, Germany, 2005.
- [9] IEA, *Key world energy statistics*, International Energy Agency, 2011.
- [10] J. Emsley, *The elements (Oxford chemistry guides)*, Oxford University Press, vol. 3, 1998.
- [11] B. Lojek, *History of semiconductor engineering*, Springer-Verlag GmbH, 2006.
- [12] W. Sinke et al., *1 € per watt-peak advanced crystalline silicon modules: the crystalclear integrated project*, in Proceeding of the 23rd European Photovoltaic Solar Energy Conference, Valencia, Spain, pp. 1-6, 2008.
- [13] A. Goetzberger et al., *Crystalline silicon solar cells*, John Wiley & Sons Ltd, Chichester, UK, 1998.
- [14] S. M. Sze, *Physics of semiconductor devices*, John Wiley & Sons, New York, vol. 2, 1981.
- [15] H. Göbel, *Einführung in die Halbleiter-Schaltungstechnik*, Springer-Verlag, Heidelberg, vol. 2, 2006.
- [16] M. A. Green, *Silicon solar cells: advanced principles and practice*, Sydney, Australia, Centre for Photovoltaic Devices and Systems UNSW, 1995.
- [17] D. B. M. Klaassen, *A unified mobility model for device simulation*, IEEE Electron Devices Meeting, pp. 357-60, 1990.
- [18] A. B. Sproul and M. A. Green, *Intrinsic carrier concentration and minority-carrier mobility of silicon from 77 to 300 K*, Journal of Applied Physics, vol. 73, pp. 1214-1225, 1993.

- [19] P. P. Altermatt et al., *Reassessment of the intrinsic carrier density in crystalline silicon in view of band-gap narrowing*, Journal of Applied Physics, vol. 93, pp. 1598-1604, 2003.
- [20] M. A. Green, *Intrinsic concentration, effective densities of states, and effective mass in silicon*, Journal of Applied Physics, vol. 67, pp. 2944-2954, 1990.
- [21] A. Schenk, *Finite-temperature full random-phase approximation model of band gap narrowing for silicon device simulation*, Journal of Applied Physics, vol. 84, pp. 3684-3695, 1998.
- [22] S. Goßner, *Grundlagen der Elektronik. Halbleiter, Bauelemente und Schaltungen*, vol. 8, p. 518, 2011.
- [23] J. Beier and B. Voss, *Humps in dark I-V-curves-analysis and explanation*, in Proceedings of the 23rd IEEE Photovoltaic Specialists Conference, Louisville, Kentucky, USA, 1993, pp. 321-326.
- [24] R. J. Schwartz and M. D. Lammert, *Silicon solar cells for high concentration applications*, in Technical Digest of the International Electron Devices Meeting, Washington DC, pp. 350-2, 1975.
- [25] R. Woehl et al., *19.7% efficient all-screen-printed back-contact back-junction silicon solar cell with aluminum-alloyed emitter*, IEEE Electron Device Letters, vol. 32, pp. 345-347, 2011.
- [26] I. Cesar et al., *Mercury: a back junction back contact front floating emitter cell with novel design for high efficiency and simplified processing*, Energy Procedia, vol. 55, pp. 633-42, 2014.
- [27] M. A. Green and M. J. Keevers, *Optical properties of intrinsic silicon at 300 K*, Progress in Photovoltaics: Research and Applications, vol. 3, pp. 189-192, 1995.
- [28] A. G. Aberle, *Surface passivation of crystalline silicon solar cells: a review*, Progress in Photovoltaics: Research and Applications, vol. 8, pp. 473-87, 2000.
- [29] F. Granek et al., *Front surface passivation of n-type high-efficiency back-junction silicon solar cells using front surface field*, Proceedings of the 22nd European Photovoltaic Solar Energy Conference, pp. 1454-1457, 2007.
- [30] A. Cuevas et al., *Extraction of the surface recombination velocity of passivated phosphorus-doped silicon emitters*, in Proceedings of the 1st World Conference on Photovoltaic Energy Conversion, Waikoloa, USA, pp. 1446-1449, 1994.
- [31] D. B. Laks et al., *Theory of interband Auger recombination in n-type silicon*, Physical Review Letters, vol. 61, pp. 1229-32, 1988.
- [32] P. P. Altermatt et al., *Assessment and parameterisation of coulomb-enhanced auger recombination coefficients in lowly injected crystalline silicon*, Journal of Applied Physics, vol. 82, pp. 4938-44, 1997.
- [33] J. Knobloch et al., *Key-factors influencing diffusion length*, in Proceedings of the 7th European Photovoltaic Solar Energy Conference, Sevilla, Spain, 1986.
- [34] C. Reichel et al., *Investigation of electrical shading effects in back-contacted back-junction silicon solar cells using the two-dimensional charge collection*

- probability and the reciprocity theorem*, Journal of Applied Physics, vol. 109, 2011.
- [35] F. Dross et al., *Minimization of the shadow-like losses for inter-digitated back-junction solar cells*, in Proceedings of the 15th International Photovoltaic Science & Engineering Conference, Shanghai, China, pp. 971-2, 2005.
- [36] D. De Ceuster and P. J. Cousins, *Solar cell with reduced base diffusion area*, WO 2008/013604 A2, 2007.
- [37] S. Kluska et al., *Modeling and optimization study of industrial n-type high-efficiency back-contact back-junction silicon solar cells*, Solar Energy Materials and Solar Cells, vol. 94, pp. 568-77, 2010.
- [38] M. Späth et al., *A novel module assembly line using back contact solar cells*, in Proceedings of the 16th IEEE Photovoltaic Specialists Conference, San Diego, CA, USA, pp. 1-6, 2008.
- [39] F. Granek, *High efficiency back-contact back-junction silicon solar cells*, Technical Faculty, Albert-Ludwigs-University Freiburg, Freiburg, 2009.
- [40] K. Masuko et al., *Achievement of more than 25% conversion efficiency with crystalline silicon heterojunction solar cell*, IEEE Journal of photovoltaics, vol. 4, 2014.
- [41] Bosch and ISFH, 09/2013, *ISFH produce 22.1% efficient c-Si solar PV cell*, <http://www.solarserver.com/solar-magazine/solar-news/archive-2013/2013/kw33/bosch-isfh-produce-221-efficient-c-si-solar-pv-cell.html>
- [42] D. Smith et al., *Toward the practical limits of silicon solar cells*, IEEE Journal of photovoltaics, vol. 4, 2014.
- [43] D. De Ceuster et al., *Low cost, high volume production of >22% efficiency silicon solar cells*, in Proceedings of the 22nd European Photovoltaic Solar Energy Conference, Milan, Italy, pp. 816-9, 2007.
- [44] P. J. Cousins et al., *Generation 3: improved performance at lower cost*, in Proceedings of the 35th IEEE Photovoltaic Specialists Conference, Honolulu, Hawaii USA, 2010.
- [45] ASTM, *Standard for terrestrial solar spectral irradiance tables at air mass 1.5 for a 37° tilted surface*, in ASTM G173-03, ASTM, 2008.
- [46] V. D. Mihailetchi et al., *High efficiency IBC solar cells fabricated on large area n-type silicon using industrial available techniques*, in Proceedings of the 21st Photovoltaic Solar Energy Conference, Fukuoka, Japan.
- [47] G. Galbiati et al., *Large-area back-contact back-junction solar cell with efficiency exceeding 21%*, IEEE Journal of Photovoltaics, pp. 1-6, 2012.
- [48] M. A. Green et al., *Solar cell efficiency tables (version 37)*, Progress in photovoltaics: research and applications, pp. 84-92, 2011.
- [49] R. A. Sinton and A. Cuevas, *A quasi-steady-state open-circuit voltage method for solar cell characterization*, in Proceedings of the 16th European Photovoltaic Solar Energy Conference, Glasgow, UK, pp. 1152-1155, 2000.

- [50] A. Kaminski et al., *Non ideal dark I-V curves behavior of silicon solar cells*, Solar Energy Materials and Solar Cells, vol. 51, pp. 221-31, 1998.
- [51] N. Mingirulli et al., *Hot-melt inkjet as masking technology for back-contacted cells*, in Proceedings of the 34th IEEE Photovoltaic Specialists Conference, Philadelphia, pp. 1064-8, 2009.
- [52] A. Fallisch, *Fabrication, analysis and modelling of emitter wrap-through silicon solar cells*, Dissertation, Technische Fakultät, Albert-Ludwigs-Universität Freiburg im Breisgau, Freiburg im Breisgau, 2012.
- [53] B. Mack et al., *Simulation of the tunnelling current in heavily doped pn-junctions*, in Proceedings of the 21st European Photovoltaic Solar Energy Conference, Dresden, Germany, pp. 493-6, 2006.
- [54] D. Macdonald and A. Cuevas, *Reduced fill factors in multicrystalline silicon solar cells due to injection-level dependent bulk recombination lifetimes*, Progress in Photovoltaics: Research and Applications, vol. 8, pp. 363-75, 2000.
- [55] W. Kern, *Handbook of semiconductor wafer cleaning technology*, Park Ridge, New Jersey, Noyes, 1993.
- [56] K. A. Reinhardt and R. F. Reidy, *Handbook of cleaning for semiconductor manufacturing*, John Wiley & Sons, 2011.
- [57] M. Ohring, *Materials science of thin films. Deposition and structure*, Academic Press, vol. 2, 2001.
- [58] H. Lüth, *Solid surfaces, interfaces and thin films*, Springer-Verlag, Berlin, Germany, vol.4, 2001.
- [59] J. Crank, *The mathematics of diffusion*, Clarendon Press, Oxford, UK, vol. 2 1975.
- [60] D. J. Fisher, *Diffusion in silicon - 10 years of research*, Trans Tech Publications, 1997.
- [61] K. Nakajima and N. Usami, *Crystal growth of silicon for solar cells*, Springer Verlag, Berlin, 2012.
- [62] P. Wagner and J. Hage, *Thermal double donors in silicon*, Applied Physics A, vol. 49, pp. 123-138, 1989.
- [63] N. Meilwes et al., *On the nature and structures of different heat treatment centres in n- and p-type silicon*, Semiconductor Science and Technology, vol. 9, p. 1346, 1994.
- [64] H. Föll, *Formation and nature of swirl defects in silicon*, Applied Physics A, vol. 8, pp. 319-31, 1975.
- [65] A. J. R. de Kock et al., *On the relation between growth striations and resistivity variations in silicon crystals*, physica status solidi (a), vol. 22, pp. 163-166, 1974.
- [66] R. Falster and V. V. Voronkov, *Intrinsic point defects in silicon and their control in crystal growth and wafer processing*, in 11th Workshop on Crystalline Silicon Solar Cell Materials and Processes, East Park, Colorado, USA, 2001.

- [67] J. Haunschild et al., *Cz-Si wafers in solar cell production: efficiency-limiting defects and material quality control*, Photovoltaics International, pp. 40-6, 2012.
- [68] K. Bothe and J. Schmidt, *Electronically activated boron-oxygen-related recombination centers in crystalline silicon*, Journal of Applied Physics, vol. 99, 2006.
- [69] D. Macdonald and L. J. Geerligs, *Recombination activity of interstitial iron and other transition metal point defects in p- and n-type crystalline silicon*, Applied Physics Letters, vol. 85, pp. 4061-3, 2004.
- [70] M. A. Lieberman and A. J. Lichtenberg, *Principles of plasma discharges and materials processing*, John Wiley & Sons, New York, USA, 1994.
- [71] S. B. S. Heil et al., *Reaction mechanisms during plasma-assisted atomic layer deposition of metal oxides: a case study for Al_2O_3* , Journal of Applied Physics, vol. 103, 2008.
- [72] J. A. Thornton, *High rate thick film growth*, Annual Review of Materials Science, vol. 7, pp. 239-60, 1977.
- [73] D. Biro et al., *Inkjet printing for high definition industrial masking processes for solar cell production*, in Proceedings of the 17th International Photovoltaic Science and Engineering Conference, Fukuoka, Japan, 2007.
- [74] J. Specht et al., *Using hotmelt-inkjet as a structuring method for higher efficiency industrial silicon solar cells*, in Proceedings of the International Conference on Digital Printing Technologies and Digital Fabrication, Pittsburgh, USA, pp. 912-7, 2008.
- [75] To be published by D. Stüwe, *Inkjet Printing Processes for Crystalline Silicon Solar Cells*, Dissertation, Technische Fakultät, Albert-Ludwigs-Universität Freiburg im Breisgau, Freiburg im Breisgau, 2015.
- [76] A. Ural et al., *Silicon self-diffusion under extrinsic conditions*, Applied Physics Letters, vol. 79, pp. 4328-30, 2001.
- [77] A. Bentzen, *Phosphorus diffusion and gettering in silicon solar cells*, Dissertation, Department of Physics, University of Oslo, Oslo, 2006.
- [78] R. S. Ronen and P. H. Robinson, *Hydrogen chloride and chlorine gettering: an effective technique for improving performance of silicon devices*, Journal of the Electrochemical Society, pp. 742-752, 1972.
- [79] R. Chen et al., *A model for phosphosilicate glass deposition via $POCl_3$ for control of phosphorus dose in Si*, Journal of Applied Physics, 2012.
- [80] S. Solmi et al., *Dopant and carrier concentration in Si in equilibrium with monoclinic SiP precipitates*, Physical Review B, vol. 53, pp. 7836-41, 1996.
- [81] R. Hull, *Properties of crystalline silicon*, Institution of Engineering and Technology, 1999.
- [82] E. Arai et al., *Interface reactions of B_2O_3 -Si system and boron diffusion into silicon*, Journal of the Electrochemical Society: Solid-State Science and Technology, vol. 120, pp. 980-7, 1973.

- [83] M. A. Kessler et al., *Charge carrier lifetime degradation in Cz silicon through the formation of a boron-rich layer during BBr₃ diffusion processes*, Semiconductor Science and Technology, vol. 25, 2010.
- [84] T. L. Aselage, *The coexistence of silicon borides with boron-saturated silicon: Metastability of SiB₃*, Journal of Materials Research, pp. 1786-1794, 1998.
- [85] C. G. Beck and R. Stickler, *Crystallography of SiP and SiAs Single Crystals and of SiP Precipitates in Si*, Journal of Applied Physics, vol. 37, pp. 4683-4687, 1966.
- [86] R. A. Sinton et al., *Comparing lifetime and photoluminescence imaging pattern recognition methodologies for predicting solar cell results based on as-cut wafer properties*, Progress in Photovoltaics: Research and Applications, pp. 1-6, 2012.
- [87] P. J. Cousins and J. E. Cotter, *The influence of diffusion-induced dislocations on high efficiency silicon solar cells*, IEEE Transactions on Electron Devices, vol. 53, pp. 457-64, 2006.
- [88] B. Bazer-Bachi et al., *Co-diffusion from boron doped oxide and POCl₃*, in Proceedings of the 26th European Photovoltaic Solar Energy Conference and Exhibition, Hamburg, Germany, pp. 1155-9, 2011.
- [89] J. Seiffe et al., *Surface passivation of crystalline silicon by plasma-enhanced chemical vapor deposition double layers of silicon-rich silicon oxynitride and silicon nitride*, Journal of Applied Physics, vol. 109, p. 034105, 2011.
- [90] C. Schwab et al., *Front surface passivation for industrial-type solar cells by silicon oxynitride - silicon nitride stacks*, Proceedings of the 25th European Photovoltaic Solar Energy Conference and Exhibition, pp. 2307-10, 2010.
- [91] A. Richter et al., *Boron emitter passivation with Al₂O₃ and Al₂O₃/SiN_x stacks using ALD Al₂O₃*, IEEE Journal of Photovoltaics, vol. 3, pp. 236-45, 2013.
- [92] P. Engelhart et al., *Laser processing of 22% efficient back-contacted silicon solar cells*, in Proceedings of the 21st European Photovoltaic Solar Energy Conference, Dresden, Germany, pp. 773-6, 2006.
- [93] F. Granek and C. Reichel, *Back-contact back-junction silicon solar cells under UV illumination*, Solar Energy Materials and Solar Cells, vol. 94, pp. 1734-40, 2010.
- [94] V. Mertens et al., *The buried emitter solar cell concept: interdigitated back-junction structure with virtually 100% emitter coverage of the cell area*, in Proceedings of the 24th European Photovoltaic Solar Energy Conference, Hamburg, Germany, pp. 934-6, 2009.
- [95] S. Nold et al., *Cost modelling of silicon solar cell production innovation along the PV value chain*, in Proceedings of the 27th European Photovoltaic Solar Energy Conference and Exhibition, Frankfurt, Germany, pp. 1084-90, 2012.
- [96] P. Rothhardt et al., *Codiffused bifacial n-type solar cells (CoBiN)*, Energy Procedia, vol. 55, pp. 287-94, 2014.

- [97] D. C. Walter et al., *Understanding lifetime degradation in czochralski-grown n-type silicon after high-temperature processing*, in Proceedings of the 28th European Photovoltaic Solar Energy Conference and Exhibition, Paris, France, pp. 1-4, 2013.
- [98] J. Schön et al., *Analysis of simultaneous boron and phosphorus diffusion gettering in silicon*, Physica Status Solidi A, vol. 207, pp. 2589–92, 2010.
- [99] C. Roters, *Abscheidung und Charakterisierung von dotierten dielektrischen Schichten mittels PECVD-Verfahren*, B.Eng. Thesis, Wissenschaftsbereich 2, Technische Fachhochschule Agricola Bochum, Bochum, 2012.
- [100] N. bin Tanvir, *Diffusion sources and barriers for the assembly of back-contact back-junction solar cells*, M.Sc. Thesis, Technische Fakultät, Albert-Ludwigs-Universität Freiburg im Breisgau, Freiburg im Breisgau, 2013.
- [101] D. K. Schroder and D. L. Meier, *Solar cell contact resistance - a review*, IEEE Transactions on Electron Devices, vol. 31, pp. 637-47, 1984.
- [102] M. Spitz et al., *Fast inductive inline measurement of the emitter sheet resistance in industrial solar cell fabrication*, in Proceedings of the 22nd European Photovoltaic Solar Energy Conference, Milan, Italy, pp. 47-50, 2007.
- [103] H. Fujiwara, *Spectroscopic ellipsometry: Principles and applications*, John Wiley & Sons, Chichester, West Sussex, England, 2007.
- [104] E. Peiner et al., *Doping profile analysis in Si by electrochemical capacitance-voltage measurements*, Journal of the Electrochemical Society, vol. 142, pp. 576-80, 1995.
- [105] R. Fair, *Boron diffusion in silicon - concentration and orientation dependence, background effects, and profile estimation*, Journal of the Electrochemical Society, vol. 161, 2014.
- [106] A. Fallisch et al., *Analysis of phosphorus-doped silicon oxide layers deposited by means of PECVD as a dopant source in diffusion processes*, IEEE Journal of Photovoltaics, vol. 2, pp. 450-6, 2012.
- [107] S. Solmi and D. Nobili, *High concentration diffusivity and clustering of arsenic and phosphorus in silicon*, Journal of Applied Physics, vol. 83, pp. 2484-2490, 1998.
- [108] B. E. Deal and A. S. Grove, *General relationship for the thermal oxidation of silicon*, Journal of Applied Physics, vol. 36, pp. 3770-8, 1965.
- [109] K. Bean et al., *Some properties of vapor deposited silicon nitride films using the SiH₄-NH₃-H₂ system*, Journal of the Electrochemical Society, vol. 114, pp. 733-737, 1967.
- [110] A. K. Sinha et al., *Thermal stresses and cracking resistance of dielectric films (SiN, Si₃N₄, and SiO₂) on Si substrates*, Journal of Applied Physics, vol. 49, pp. 2423-2426, 1978.
- [111] W. S. Lau, *Infrared characterization for microelectronics*, World Scientific Publishing Company, Singapore, 1999.

- [112] J. Colby and L. Katz, *Boron segregation at Si-SiO₂ interface as a function of temperature and orientation*, Journal of the Electrochemical Society, vol. 161, 2014.
- [113] R. Horng et al., *Refractive index behavior of boron-doped silica films by plasma-enhanced chemical vapor deposition*, Elsevier - Applied Surface Science, vol. 92, pp. 387-390, 1996.
- [114] P. Rothhardt et al., *19.9 % efficient bifacial n-type solar cell produced by co-diffusion - COBIN*, in Proceedings of the 29th European Photovoltaic Solar Energy Conference and Exhibition, Amsterdam, Netherlands, 2014.
- [115] C. Reichel et al., *Back-contacted back-junction n-type silicon solar cells featuring an insulating thin film for decoupling charge carrier collection and metallization geometry*, Progress in Photovoltaics: Research and Applications, pp. 1-14, 2012.
- [116] P. Saint-Cast et al., *Relevant pinhole characterisation methods for dielectric layers for silicon solar cells*, in Proceedings of the 24th European Photovoltaic Solar Energy Conference, Hamburg, Germany, pp. 2084-7, 2009.
- [117] D. Hahn, *Strukturierung von dielektrischen Schichten mittels Inkjet-Verfahren, Bachelorarbeit, Druck- und Medientechnologie, Hochschule der Medien, Stuttgart, Freiburg im Breisgau*, 2013.
- [118] D. Kray et al., *Theory and experiment on the back side reflectance of silicon wafer solar cells*, Progress in Photovoltaics: Research and Applications, vol. 16, pp. 1-15, 2008.
- [119] C. Schwab et al., *Recombination and optical properties of wet chemically polished thermal oxide passivated Si surfaces*, IEEE Journal of Photovoltaics, vol. 3, pp. 613-20, 2013.
- [120] K. R. McIntosh et al., *The choice of silicon wafer for the production of low-cost rear-contact solar cells*, in Proceedings of the 3rd World Conference on Photovoltaic Energy Conversion, Osaka, Japan, pp. 971-4, 2003.
- [121] S. Mack et al., *Silicon surface passivation by thin thermal oxide/PECVD layer stack systems*, IEEE Journal of Photovoltaics, vol. 1, pp. 135-45, 2011.
- [122] R. A. Sinton et al., *Quasi-steady-state photoconductance, a new method for solar cell material and device characterization*, in Proceedings of the 25th IEEE Photovoltaic Specialists Conference, Washington DC, USA, pp. 457-60, 1996.
- [123] D. E. Kane and R. M. Swanson, *Effect of electron-hole scattering on the current flow in semiconductors*, Journal of Applied Physics, vol. 72, pp. 5294-304, 1992.
- [124] M. J. Kerr et al., *Lifetime and efficiency limits of crystalline silicon solar cells*, in Proceedings of the 29th IEEE Photovoltaics Specialists Conference, New Orleans, Louisiana, USA, pp. 438-41, 2002.
- [125] P. A. Basore, *Extended spectral analysis of internal quantum efficiency*, in Proceedings of the 23rd IEEE Photovoltaic Specialists Conference, Louisville, Kentucky, USA, pp. 147-52, 1993.

- [126] A. G. Aberle et al., *High-efficiency silicon solar cells: fill factor limitations and non-ideal diode behaviour due to voltage-dependent rear surface recombination velocity*, Progress in Photovoltaics: Research and Applications, vol. 1, pp. 133-43, 1993.
- [127] B. Hoex et al., *On the c-Si surface passivation mechanism by the negative-charge-dielectric Al_2O_3* , Journal of Applied Physics, vol. 104, 2008.
- [128] R. M. Swanson and R. A. Sinton, *High-efficiency silicon solar cells*, Advances in Solar Energy, Plenum Press, vol. 6, New York, pp. 427-84, 1990.
- [129] A. Cuevas et al., *Surface recombination velocity of highly doped n-type silicon*, Journal of Applied Physics, vol. 80, pp. 3370-5, 1996.
- [130] R. R. King et al., *Studies of diffused phosphorus emitters: saturation current, surface recombination velocity, and quantum efficiency*, IEEE Transactions on Electron Devices, vol. 37, pp. 365-71, 1990.
- [131] G. A. M. Hurkx et al., *A new recombination model for device simulation including tunneling*, IEEE Transactions on Electron Devices, vol. 39, pp. 331-8, 1992.
- [132] W. Shockley and W. T. J. Read, *Statistics of the recombinations of holes and electrons*, Physical Review, vol. 87, pp. 835-42, 1952.
- [133] R. Woehl et al., *Evaluating the aluminum-alloyed p^+ -layer of silicon solar cells by emitter saturation current density and optical microspectroscopy measurements*, IEEE Transactions on Electron Devices, vol. 58, pp. 441-7, 2011.
- [134] K. Katkhouda et al., *Aluminum-based rear-side PVD metallization for nPERT silicon solar cells*, IEEE Journal of Photovoltaics, vol. 4, pp. 160-167, 2014.
- [135] J. Benick et al., *Surface passivation of boron diffused emitters for high efficiency solar cells*, in Proceedings of the 33rd IEEE Photovoltaic Specialists Conference, San Diego, USA, 2008.
- [136] M. Hermle et al., *Analyzing the effects of front-surface fields on back-junction silicon solar cells using the charge-collection probability and the reciprocity theorem*, Journal of Applied Physics, vol. 103, 2008.
- [137] M. Kamp et al., *Zincate processes for silicon solar cell metallization*, Solar Energy Materials and Solar Cells, vol. 120, pp. 332-8, 2014.
- [138] M. Bivour et al., *Doped layer optimization for silicon heterojunctions by injection-level-dependent open-circuit voltage measurements*, IEEE Journal of Photovoltaics, vol. 4, pp. 566-74, 2014.
- [139] A. Fell et al., *3-D simulation of interdigitated-back-contact silicon solar cells with Quokka including perimeter losses*, IEEE Journal of Photovoltaics, vol. 4, pp. 1040-5, 2014.
- [140] R. Brendel, *Modeling solar cells with the dopant-diffused layers treated as conductive boundaries*, Progress in Photovoltaics: Research and Applications, vol. 20, pp. 31-43, 2012.

- [141] G. K. Reeves and H. B. Harrison, *Obtaining the specific contact resistance from transmission line model measurements*, IEEE Electron Device Letters, vol. 3, pp. 111-3, 1982.
- [142] H. Murrmann and D. Widmann, *Current crowding on metal contacts to planar devices*, IEEE Transactions on Electron Devices, vol. 16, pp. 1022-4, 1969.
- [143] K. R. McIntosh and P. P. Altermatt, *A freeware 1d emitter model for silicon solar cells*, in Proceedings of the 35th IEEE Photovoltaic Specialists Conference, Honolulu, Hawaii, USA, pp. 1-6, 2010.
- [144] R. Keding et al., *Study of the electrical insulation of dielectric passivation layers and stacks for back-contact back-junction silicon solar cells*, in Proceedings of the 28th European Photovoltaic Solar Energy Conference and Exhibition, Paris, France, pp. 1321-6, 2013.
- [145] R. Keding et al., *Silicon doping performed by different diffusion sources aiming co-diffusion*, in Proceedings of the 27th European Photovoltaic Solar Energy Conference and Exhibition, Frankfurt, Germany, pp. 1906-11, 2012.
- [146] F. Feldmann et al., *A passivated rear contact for high-efficiency n-type silicon solar cells enabling high $V_{oc}S$ and $FF > 82\%$* , in Proceedings of the 28th European Photovoltaic Solar Energy Conference and Exhibition, Paris, France, pp. 988-92, 2013.
- [147] M. Hendrichs et al., *Optimization of multi-layer metallization for large-area back-contact back-junction solar cells*, in Proceedings of the 29th European Photovoltaic Solar Energy Conference and Exhibition, Amsterdam, Netherlands, 2014.

List of Constants, Symbols and Acronyms

Constant	Description	Value
c	speed of light	$299792458 \text{ m s}^{-1}$
h	Planck constant	$6.62607 \times 10^{-34} \text{ J s}$
k	Boltzmann constant	$1.3806 \times 10^{-23} \text{ J K}^{-1}$
q	elementary charge	$1.602 \times 10^{-19} \text{ C}$
ϵ_0	dielectric constant in vacuum	1

Symbol	Description	Unit
A	area	m^2
Ab	absorbance	-
C	concentration	m^{-3}
C_{Aug}	Auger recombination coefficient	$\text{m}^{-3} \text{s}^{-1}$
c_{HF}	HF concentration in diluted HF	-
c_{KOH}	KOH concentration in diluted KOH	-
C_{rad}	radiative recombination coefficient	$\text{m}^{-3} \text{s}^{-1}$
C_{S}	surface dopant concentration	m^{-3}
C_{sol}	active solubility limit	m^{-3}
$C_{\text{sol,B-}}$	active solubility limit of boron	m^{-3}
$C_{\text{sol,P+}}$	active solubility limit of phosphorus	m^{-3}
C_{trap}	trap recombination coefficient (SRH)	$\text{m}^{-3} \text{s}^{-1}$
D	diffusion coefficient	$\text{m}^2 \text{s}^{-1}$
D_0	diffusivity	$\text{m}^2 \text{s}^{-1}$
DA	dopant assignment	m^{-2}
D_{n}	diffusion coefficient of electrons	$\text{m}^2 \text{s}^{-1}$
Δn	excess carrier concentration of electrons	m^{-3}
D_{p}	diffusion coefficient of holes	$\text{m}^2 \text{s}^{-1}$
Δp	excess carrier concentration of holes	m^{-3}
E	energy	J
E_{A}	acceptor energy level	J
E_{a}	activation energy	J
E_{C}	lower conductive energy band edge	J
E_{D}	donor energy level	J
E_{F}	Fermi energy level	J
$E_{\text{F,n}}$	quasi Fermi level of electrons	J

Symbol	Description	Unit
$E_{F,p}$	quasi Fermi level of holes	J
E_g	band gap energy	J
EQE	external quantum efficiency	-
E_t	trap energy	J
E_V	upper valence energy band edge	J
$F(E)$	energy state dependent occupation probability	-
FF	fill factor	-
FF_0	ideal fill factor	-
G	generation rate	$m^{-3}s^{-1}$
h_{BSG}	BSG layer thickness	m
h_{met}	metal layer thickness	m
h_{PSG}	PSG layer thickness	m
IQE	internal quantum efficiency	-
J	electrical current density	Am^{-2}
J_0	dark saturation current density	Am^{-2}
$J_{0,BSF}$	J_0 of the passivated BSF	Am^{-2}
$J_{0,bulk}$	J_0 of the bulk	Am^{-2}
$J_{0,E}$	J_0 of the passivated emitter	Am^{-2}
$J_{0,eff}$	effective J_0	Am^{-2}
$J_{0,FSF}$	J_0 of the passivated FSF	Am^{-2}
$J_{0,GAP}$	J_0 of the passivated gap	Am^{-2}
$J_{0,met,BSF}$	J_0 of the metallized BSF	Am^{-2}
$J_{0,met,E}$	J_0 of the metallized emitter	Am^{-2}
J_{01}	dark saturation current density of diode 1 (D1)	Am^{-2}
J_{02}	dark saturation current density of diode 2 (D2)	Am^{-2}
$J_{diff,n}$	diffusion current density of electrons	Am^{-2}
$J_{diff,p}$	diffusion current density of holes	Am^{-2}
$J_{drift,n}$	drift current density of electrons	Am^{-2}
$J_{drift,p}$	drift current density of holes	Am^{-2}
J_{Mpp}	current density at maximum power point	Am^{-2}
J_n	current density of electrons	Am^{-2}
J_p	current density of holes	Am^{-2}
J_{ph}	photo current density	Am^{-2}
J_{SC}	short circuit current density	Am^{-2}
K	ratio of capture cross sections	-
k	wave number	m^{-1}

Symbol	Description	Unit
L_n	diffusion length of electrons	m
L_p	diffusion length of holes	m
n	carrier concentration of electrons	m ⁻³
$N(E)$	energy state dependent density of states	cm ⁻³ J ⁻¹
n_1	diode ideality factor of diode 1 (D1)	-
n_2	diode ideality factor of diode 2 (D2)	-
N_A	acceptor concentration	m ⁻³
n_{BSF}	area fraction of the BSF	-
N_C	density of energy states in the conduction band	m ⁻³
N_D	donor concentration	m ⁻³
N_{dop}	dopant concentration	m ⁻³
$N_{dop,T}$	dopant concentration after co-diffusion	m ⁻³
n_E	area fraction of the emitter (EC)	-
n_{GAP}	area fraction of the gap	-
n_i	intrinsic carrier concentration	m ⁻³
n_{id}	diode ideality factor	-
N_t	trap density	m ⁻³
N_V	density of energy states in the valence band	m ⁻³
p	carrier concentration of holes	m ⁻³
P_0	irradiated power	W
pFF	pseudo fill factor	-
P_{Mpp}	power at maximum power point	W
$Q_{B2H6:H2}$	diborane gas flow	m ³ s ⁻¹
$Q_{O2,Z3}$	oxygen gas flow during temperature zone 3	m ³ s ⁻¹
Q_{SiH4}	silane gas flow	m ³ s ⁻¹
Q_{TMPi}	trimethylphosphit gas flow	m ³ s ⁻¹
R	reflection	-
R_S	series resistance	Ωm ²
$R_{S,grid}$	grid series resistance	Ωm ²
R_{Sh}	shunt resistance	Ωm ²
R_{sh}	sheet resistance	Ω
$R_{sh,B}$	base sheet resistance	Ω
$R_{sh,n+}$	sheet resistance of the BSF and FSF	Ω
$R_{sh,p+}$	sheet resistance of the emitter	Ω
$R_{sh,T}$	total sheet resistance	Ω
T	temperature	K

Symbol	Description	Unit
t	time	s
T_{\max}	maximum temperature	K
t_{plateau}	plateau time	s
$t_{\text{plateau,Z2}}$	plateau time during temperature zone 2	s
$t_{\text{plateau,Z4}}$	plateau time during temperature zone 4	s
U	recombination rate	$\text{m}^{-3}\text{s}^{-1}$
U_{Aug}	Auger recombination rate	$\text{m}^{-3}\text{s}^{-1}$
U_{rad}	radiative recombination rate	$\text{m}^{-3}\text{s}^{-1}$
U_{trap}	trap recombination rate	$\text{m}^{-3}\text{s}^{-1}$
V	electrical voltage	Volt
v_{C}	carrier velocity	ms^{-1}
V_{D}	diffusion voltage	Volt
V_{I}	impressed voltage	Volt
V_{Mpp}	voltage at the maximum power point	Volt
V_{OC}	open circuit voltage	Volt
v_{th}	thermal velocity	ms^{-1}
W	wafer thickness	m
x_{BSF}	width of BSF region	m
x_{CO}	width of contact opening	m
$x_{\text{CO,n}}$	width of contact opening upon BSF	m
$x_{\text{CO,p}}$	width of contact opening upon emitter	m
x_{emitter}	width of emitter region	m
x_{gap}	width of gap region	m
$x_{\text{met,n}}$	width of n-metal finger	m
$x_{\text{met,p}}$	width of p-metal finger	m
x_{pitch}	pitch distance	m
x_{SCR}	expansion of the space charge region	m
y_{met}	metal finger length	m
z_{front}	depth relative to the front side	m
z_{L}	absorption length	m
z_{rear}	depth relative to the rear side	m
α_{L}	absorption length	m^{-1}
ε	dielectric constant in a material	-
ε_0	dielectric constant in vacuum	-
ϕ_{n}	capture cross section for electrons	m^2
ϕ_{p}	capture cross section for holes	m^2

Symbol	Description	Unit
η	conversion efficiency	-
λ	wave length	m
μ_n	mobility of electrons	$\text{m}^2\text{V}^{-1}\text{s}^{-1}$
μ_p	mobility of holes	$\text{m}^2\text{V}^{-1}\text{s}^{-1}$
ρ_{base}	specific base resistivity	Ωm
$\rho_{\text{base,T}}$	specific base resistivity after co-diffusion	Ωm
$\rho_{\text{C,BSF}}$	contact resistivity at interface BSF/electrode	Ωm
$\rho_{\text{C,E}}$	contact resistivity at interface emitter/electrode	Ωm
$\rho_{\text{C,met}}$	specific resistivity of metal electrodes	Ωm
σ	electrical conductivity	$\Omega^{-1}\text{m}^{-1}$
σ_n	electrical conductivity of electrons	$\Omega^{-1}\text{m}^{-1}$
σ_p	electrical conductivity of holes	$\Omega^{-1}\text{m}^{-1}$
$\tau_{\text{Aug,ex}}$	extrinsic Auger limitation of life time	s
$\tau_{\text{Aug,int}}$	intrinsic Auger limitation of life time	s
τ_n	life time of electrons	s
τ_h	life time of holes	s
τ_{bulk}	bulk life time	s
τ_{eff}	effective life time	s
ξ	electrical field	Volt m^{-1}

Acronym	Description
Al_2O_3	aluminum oxide
ALD	atomic layer deposition
Al-Si	aluminum silicon alloy
AM1.5G	reference solar spectral irradiance: air mass 1.5
APCVD	atmospheric pressure chemical vapor deposition
AR	anti-reflection
Au	gold
B	boron
B_2H_6	diborane
BC-BJ	back-contact back-junction
BSF	back surface field
BSG	boron-doped silicate glass
BRL	boron rich layer
CH_3	methyl
Cl_2	chlorine

Acronym	Description
COC	contact opening coverage
Cr	chromium
CVD	chemical vapor deposition
Cz	Czochralski
D1	diode 1
D2	diode 2
DI	deionized
D-in	drive-in
DoD	drop on demand
EC	emitter coverage
EDX	energy dispersive X-ray measurement
EP-setup	PECVD setup featuring an electrical power source
Fe	iron
FSF	front surface field
FTIR	Fourier transform infrared (spectroscopy)
FZ	float zone
g	gaseous
Ga	gallium
GaAs	gallium arsenide
H ₂ O	water
H ₂ O ₂	hydrogen peroxide
HCl	hydrochloric acid
HF	hydrofluoric acid
HNF	cleaning procedure with HNO ₃ and HF
IEC	international electrotechnical commission
IPA	isopropyl alcohol
KNaC ₄ H ₄ O ₆	potassium sodium tartarate
KOH	potassium hydroxide
l	Liquid
LTO	low-temperature oxidation
Mo	molybdenum
MPP	maximum power point
MW-setup	PECVD setup featuring power source emitting micro waves
<i>n</i> ⁺ -Si	heavily doped silicon (<i>n</i> -type)
N ₂	nitrogen
N ₂ O	nitrous oxide

Acronym	Description
NaOH	sodium hydroxide
NH ₃	ammonia
<i>n</i> -Si	lowly doped silicon (<i>n</i> -type)
O ₂	oxygen
OC	open circuit
P	phosphorus
<i>p</i> ⁺ -Si	heavily doped silicon (<i>p</i> -type)
P ₂ O ₅	phosphorus pentoxide
PECVD	plasma enhance chemical vapor deposition
POCl ₃	phosphoryl chloride
POCl ₃ , O ₂ ↑	POCl ₃ process with a high oxygen content
POCl ₃ , O ₂ ↓	POCl ₃ process with a low oxygen content
PSG	phosphorus-doped silicate glass
<i>p</i> -Si	lowly doped silicon (<i>p</i> -type)
PVD	physical vapor deposition
QE	quantum efficiency
RCA	radio corporation of america
s	solid
Sb	Antimony
SC	short circuit
SC1	standard clean 1
SC2	standard clean 2
SCR	space charge region
SDE	saw-damage etched
SEM	scanning electron microscopy
Si	silicon
SiH ₄	silane
SIMS	secondary ion mass spectroscopy
SiN _x	PECVD siliconnitride
SiO	passivation scheme: SiO ₂ layer on both sides
SiO ₂	Silicon dioxide (thermally grown)
SiO-AlO	passivation scheme: SiON _x at front and Al ₂ O ₃ at rear side
SiON _x	PECVD silicon oxynitride
SiO _x	PECVD silicon oxide
SRH	Shockley Read Hall
SR-LBIC	spectrally resolved light beam induced current

Acronym	Description
Ti	titanium
TMAI	trimethylaluminium
TMPI	trimethylphosphite
V	vanadium
Z1-5	temperature zones
Zn	zinc
ZnO	zinc oxide

List of Publications

Refereed journal papers

- A. Fallisch, D. Wagenmann, **R. Keding**, D. Trogus, M. Hofmann, J. Rentsch, H. Reinecke, and D. Biro, *Analysis of phosphorus-doped silicon oxide layers deposited by means of PECVD as a dopant source in diffusion processes*, IEEE Journal of Photovoltaics, vol. 2, pp. 450-6, (2012).
- **R. Keding**, D. Stüwe, M. Kamp, C. Reichel, A. Wolf, R. Woehl, D. Borchert, H. Reinecke, and D. Biro, *Co-diffused back-contact back-junction silicon solar cells without gap regions*, IEEE Journal of Photovoltaics, vol. 3, pp. 1236-1242, (2013).
- P. Rothhardt, **R. Keding**, A. Wolf, and D. Biro, *Co-diffusion from solid sources for bifacial n-type solar cells*, physica status solidi (RRL) – Rapid Research Letters, vol. 7, pp. 623-626, (2013).
- M. Kamp, J. Bartsch, G. Cimiotti, **R. Keding**, A. Zogaj, C. Reichel, A. Kalio, M. Glatthaar, and S. W. Glunz, *Zincate processes for silicon solar cell metallization*, Solar Energy Materials and Solar Cells, vol. 120, pp. 332-8, (2014).
- M. Padilla, C. Reichel, N. Hagedorn, A. Fell, B. Michl, **R. Keding**, M. Kasemann, W. Warta, and M. C. Schubert, *Contact fault characterization of IBC silicon solar cells: a guideline based on current voltage characteristics and luminescence imaging*, Progress in Photovoltaics: Research and Applications, accepted for publication, 2015.
- N. bin Tanvir, **R. Keding**, P. Rothhardt, S. Meier, A. Wolf, H. Reinecke, and Daniel Biro, *Co-Diffusion Sources and Barriers for the Assembly of Back-Contact Back-Junction Solar Cells*, IEEE Journal of Photovoltaics, accepted for publication, 2015.

Refereed papers presented at international conferences

- N. Mingirulli, **R. Keding**, J. Specht, A. Fallisch, D. Stüwe, and D. Biro, *Hot-melt inkjet as masking technology for back-contacted cells*, in Proceedings of the 34th IEEE Photovoltaic Specialists Conference, Philadelphia, pp. 1064-8, (2009).
- N. Mingirulli, D. Stüwe, J. Specht, **R. Keding**, R. Neubauer, A. Fallisch, and D. Biro, *18.8% EWT-cells with screen-printed metallization and single step side selective emitter formation*, in Proceedings of the 24th European

- Photovoltaic Solar Energy Conference, Hamburg, Germany, pp. 1979-84, (2009).
- A. Fallisch, **R. Keding**, G. Kästner, J. Bartsch, S. Werner, D. Stüwe, J. Specht, R. Preu, and D. Biro, *Sinto EWT silicon solar cells*, in Proceedings of the 25th European Photovoltaic Solar Energy Conference and Exhibition, Valencia, Spain, pp. 1991-6, (2010).
 - A. Fallisch, D. Stüwe, R. Neubauer, D. Wagenmann, **R. Keding**, J. Nekarda, R. Preu, and D. Biro, *Inkjet structured EWT silicon solar cells with evaporated aluminum metallization and laser-fired contacts*, in Proceedings of the 35th IEEE Photovoltaic Specialists Conference, Honolulu, Hawaii, USA, (2010).
 - **R. Keding**, R. Woehl, D. Stüwe, A. Fallisch, A. Hofmann, J. Rentsch, and D. Biro, *Diffusion and characterization of doped patterns in silicon from prepatterned boron- and phosphorus-doped silicate glasses*, in Proceedings of the 26th European Photovoltaic Solar Energy Conference and Exhibition, Hamburg, Germany, pp. 1385-9, (2011).
 - R. Müller, P. Löper, D. Hiller, S. Gutsch, **R. Keding**, C. Reichel, M. Bivour, M. Hermle, S. Janz, J. C. Goldschmidt, M. Zacharias, and S. W. Glunz, *Calculation of the quasi fermi-level splitting in an ideal superlattice of silicon nanocrystals*, in Proceedings of the 26th European Photovoltaic Solar Energy Conference and Exhibition, Hamburg, Germany, pp. 465-9, (2011).
 - R. Woehl, **R. Keding**, M. Rüdiger, H. Gentischer, F. Clement, J. Wilde, and D. Biro, *20% efficient screen-printed and aluminium-alloyed back-contact back-junction cells and interconnection scheme of point-shaped metalized cells*, in Proceedings of the 37th IEEE Photovoltaic Specialists Conference, Seattle, Washington, USA, pp. 48-52, (2011).
 - **R. Keding**, P. Rothhardt, C. Roters, A. Fallisch, S. Hohage, M. Hofmann, R. Woehl, D. Borchert, and D. Biro, *Silicon doping performed by different diffusion sources aiming co-diffusion*, in Proceedings of the 27th European Photovoltaic Solar Energy Conference and Exhibition, Frankfurt, Germany, pp. 1906-11, (2012).
 - P. Rothhardt, T. Stoffels, **R. Keding**, U. Belledin, A. Wolf, and D. Biro, *Control of phosphorus doping profiles for co-diffusion processes*, in Proceedings of the 27th European Photovoltaic Solar Energy Conference and Exhibition, Frankfurt, Germany, pp. 1917-20, (2012).
 - D. Stüwe, **R. Keding**, D. Hahn, M. Jahn, A. Fallisch, F. Clement, M. Hofmann, R. Woehl, D. Biro, C. Tueshaus, O. Doll, W. Stockum, and I.

- Koehler, *Inkjet-printed diffusion barrier for structured doping areas from doped PECVD silicate glasses*, in Proceedings of the 27th European Photovoltaic Solar Energy Conference and Exhibition, Frankfurt, Germany, pp. 1802-5, (2012).
- **R. Keding**, R. Bock, A. Bochow, K. Katkhouda, D. Stüwe, C. Reichel, F. Clement, R. Woehl, H. Reinecke, and T. Geppert, *Study of the electrical insulation of dielectric passivation layers and stacks for back-contact back-junction silicon solar cells*, in Proceedings of the 28th European Photovoltaic Solar Energy Conference and Exhibition, Paris, France, pp. 1321-6, (2013).
 - **R. Keding**, D. Stüwe, M. Kamp, C. Reichel, A. Wolf, R. Woehl, D. Borchert, H. Reinecke, and D. Biro, *Co-diffused back-contact back-junction silicon solar cells*, in Proceedings of the 28th European Photovoltaic Solar Energy Conference and Exhibition, Paris, France, (2013).
 - D. Stüwe, P. Hartmann, **R. Keding**, F. Clement, R. Woehl, and D. Biro, *Etching of PVD metal layers for contact separation of back contact silicon solar cells using inkjet-printing*, in Proceedings of the 29th International Conference on Digital Printing Technologies and Digital Fabrication, Seattle, USA, (2013).
 - D. Stüwe, **R. Keding**, D. Hahn, F. Clement, M. Hofmann, R. Woehl, D. Biro, J. Korvink, C. Tüshaus, O. Doll, W. Stockum, and W. Köhler, *Inkjet-gedruckte Diffusionsbarriere gegen Diffusion aus dotierten PECVD-Silikatgläsern*, in Mikrosystemtechnik Kongress 2013, Aachen, Germany, (2013).
 - M. Hendrichs, **R. Keding**, A. Spribille, T. Fellmeth, S. Nold, F. Clement, A. Wolf, and D. Biro, *Optimization of multi-layer metallization for large-area back-contact back-junction solar cells*, in Proceedings of the 29th European Photovoltaic Solar Energy Conference and Exhibition, Amsterdam, Netherlands, (2014).
 - M. Kamp, J. Bartsch, **R. Keding**, M. Jahn, R. Müller, M. Glatthaar, S. W. Glunz, and I. Krossing, *Plating processes on aluminum and application to novel solar cell concepts*, in Proceedings of the 4th International Conference on Crystalline Silicon Photovoltaics SiliconPV, 's-Hertogenbosch, Netherlands, (2014).
 - **R. Keding**, M. Hendrichs, D. Stüwe, M. Jahn, C. Reichel, D. Borchert, A. Wolf, H. Reinecke, and D. Biro, *POCl₃-based co-diffusion process for n-type back-contact back-junction solar cells*, in Proceedings of the 29th European

- Photovoltaic Solar Energy Conference and Exhibition, Amsterdam, Netherlands, (2014).
- M. Padilla, B. Michl, C. Reichel, N. Hagedoren, S. Kluska, S. Haag, **R. Keding**, A. Fell, M. Kasemann, W. Warta, and M. C. Schubert, *Characterizing local contact resistances of interdigitated back-contact silicon solar cells*, in Proceedings of the 29th European Photovoltaic Solar Energy Conference and Exhibition, Amsterdam, Netherlands, (2014).
 - D. Stüwe, **R. Keding**, A. Salim, M. Jahn, R. Efinger, F. Clement, B. Thaidigsmann, J. Korvink, C. Tüeshaus, S. Barth, O. Doll, and D. Biro, *Inkjet-printed diffusion sources*, in Proceedings of the 29th European Photovoltaic Solar Energy Conference and Exhibition, Amsterdam, Netherlands, (2014).

Oral presentations

- *Co-diffused back-contact back-junction silicon solar cells*, 28th European Photovoltaic Solar Energy Conference and Exhibition, Paris, France, (2013).
- *$POCl_3$ -based co-diffusion process for n-type back-contact back-junction solar cells*, in Proceedings of the 29th European Photovoltaic Solar Energy Conference and Exhibition, Amsterdam, Netherlands, (2014).

Danksagung

Die Durchführung der vorliegenden wissenschaftlichen Arbeit wurde auf vielfältige Art und Weise von verschiedensten Personen mitgetragen. Bei diesen Personen möchte ich mich an dieser Stelle herzlichst bedanken.

An erster Stelle gilt mein Dank Prof. Dr. Holger Reinecke, der, neben der Abnahme des Erstgutachtens dieser Arbeit, viel Interesse und Motivation ausgestrahlt und durch konstruktive Kritik wesentlich zu der Entwicklung der Solarzelle beigetragen hat.

Es stand außer Frage, dass Prof. Dr. Gerhard Willeke, nach Begutachtung von Bachelor- und Masterarbeit, auch die Abnahme des Zweitgutachtens der vorliegenden Dissertation übernehmen würde. So auch geschehen. Vielen Dank dafür und auch für die kniffligen Fragen im Rahmen des Diplomanden-Doktoranden Seminars.

Vielen Dank an meinen Bereichsleiter Dr. Ralf Preu, Abteilungsleiter Dr. Daniel Biro und Gruppenleiter Dr. Andreas Wolf für die herzliche Aufnahme in dem Bereich „PV Production Technology and Quality Assurance, PTQ“, für die Organisation des Bereichs und für die hartnäckige Akquise von Projekten ohne die eine Finanzierung der vorliegenden Arbeit unmöglich gewesen wäre.

Sehr dankbar bin ich Dr. Robert Woehl und nochmals Dr. Andreas Wolf für die Betreuung meiner Arbeit, für viele intensive, konstruktive, wissenschaftliche Diskussionen und für die wissenschaftlichen Entfaltungsmöglichkeiten in den Gruppen „Back-Contact Solar Cells / Inkjet and PVD Technology“ und „Thermal Processes / Passivated Solar Cells“.

Für die Einweisung in die Kunst der Herstellung einer Rückseitenkontakt-Solarzelle und für Inspiration möchte ich mich herzlichst bei Dr. Nicola Mingirulli, nochmals Dr. Robert Woehl, Dr. Arne Fallisch und Dr. Christan Reichel bedanken.

Besonderer Dank gilt Christian Roters und Nauman bin Tanvir, die mir, durch ihre sorgfältig durchgeführten und sehr gut dokumentierten Bachelor- und Masterarbeiten, in jeglicher Hinsicht sehr viel Arbeit abgenommen haben.

Eine hocheffiziente Solarzelle ist im hohen Maße von der Prozessumgebung, der Prozesse als Solche und der Arbeitsweise von Prozessverantwortlichen abhängig. In diesem Sinne bedanke ich mich bei Albrecht Weil (PV-TEC), Rainer Neubauer (Fertigungslabor) und Daniel Trogus (Technikum) für die Einhaltung hochwertiger Standards in den Laboratorien, sowie - um nur einige zu nennen – nochmals Rainer Neubauer, Heike Furtwängler (Nasschemie), Rupprecht Ackermann, Nicole Hoffmann (PECVD), Stefan Maier, Udo Belledin, Dr. Sebastian Mack (Diffusion/Oxidation), Philip Hartmann, Felix Schätzle (PVD), Albrecht Weil, Christian Harmel (Laser), sowie Mathias Kamp und Dr. Jonas Bartsch (Galvanik) für die sorgfältige, hochpräzise

und aufmerksame Durchführung von Prozessen. Des Weiteren gilt mein großer Dank Dr. Dietmar Borchert und Stefan Hohage für die Möglichkeit PECVD Prozesse im Labor und Servicecenter (LSC) in Gelsenkirchen zu entwickeln und für die großartige Unterstützung bei der Umsetzung.

Die präzise Anwendung der Inkjet Technologie zur Herstellung von hochauflösenden Strukturen ist allesentscheidend für die Rückseitenkontakt Solarzelle. Für die tatkräftige Unterstützung möchte ich mich an dieser Stelle herzlichst bei Mike Jahn, David Stüwe, Raphael Efinger und Jan Specht bedanken.

Vielen Dank an Elisabeth Schäffer für unzählige Solarzellenmessungen an der großen Sonne im Solarzellen-Messlabor und Thomas Hultsch für die Messung ausgewählter Top-Zellen im „Fraunhofer ISE CalLab PV cells laboratory“.

Viele Zellmodifikationen wurden in der Rückseitenkontakt Kompetenzrunde, dem BC-BJ Treffen, erarbeitet. Vielen Dank für die regelmäßige Teilnahme und für die anregenden Diskussionen in dieser Veranstaltung an Milan Padilla, Dr. Sven Kluska, Ralph Müller, Julia Kumm, Max Hendrichs, Achim Kimmerle und nochmals Dr. Christian Reichel.

Rohdaten werden erst durch eine nachvollziehbare Darstellung in Text und Bild zu einem wissenschaftlichen Ergebnis. In diesem Sinne möchte ich mich bei Dr. Philip Rothhardt, Dr. Tobias Fellmeth, nochmals Dr. Christian Reichel und nochmals Dr. Andreas Wolf für die sorgfältigen Korrekturlesungen dieser Thesis bedanken. Auch vielen Dank an Lennart Keding und Tony Kosar für die aufschlussreiche Englischkorrektur.

Schließlich bedanke ich mich bei meinen treuen Freunden und meiner Fußballtruppe „Frisch auf Bölkstoff“, die das Leben in meiner Wahlheimat Freiburg in höchstem Maße lebenswert gemacht haben. Vielen Dank an den SC Freiburg und den Stadionsprecher, der durch die schallende Ansage im ausverkauften Schwarzwald-Stadion „Roman, gib mal endlich deine Diss ab, damit Du dich mehr auf den SC konzentrieren kannst. Man!“ die Schreibgeschwindigkeit signifikant beeinflusst hat.

Unterm Strich.

Neben dem Wandel gibt es im Leben für mich noch eine weitere Konstante. Liebe Familie, vielen Dank für all das was ich bin und dafür, dass es euch gibt.

The driving force in photovoltaics is the reduction of the ratio between device costs and conversion efficiency. The present research study introduces a highly innovative diffusion process, called co-diffusion, which allows for a drastic decrease in process costs, on the one hand, and the assembly of a highly efficient solar cell device, the back-contact back-junction (BC-BJ) silicon solar cell, on the other. The co-diffusion approach is based on pre-patterned layers, which contain dopants, deposited by means of plasma enhanced chemical vapor deposition and diffusion in a tube furnace, which contains dopant gases in the process atmosphere. The solar cells are built on n-type silicon which features a high potential in achieving a high silicon life time, which is a necessary requirement of highly efficient BC-BJ solar cells. Fundamental knowledge in terms of co-diffusion processes can be gained from this research study. The processes allow for the fabrication of BC-BJ solar cell devices with a conversion efficiency exceeding 21%.

